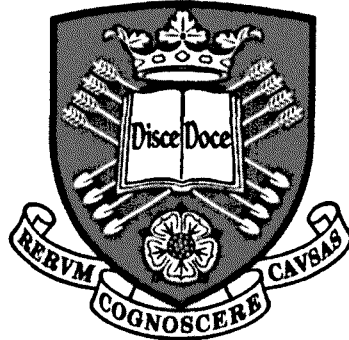


**SEISMIC BEHAVIOUR OF DEFICIENT
EXTERIOR RC BEAM-COLUMN
JOINTS**



by

Yaser Jemaa

A thesis submitted to
the Faculty of Engineering
of The University of Sheffield
in partial fulfilment of the requirements for
the degree of Doctor of Philosophy



Department of Civil and Structural Engineering
THE UNIVERSITY OF SHEFFIELD

March 2013

Copyright © 2013

UNIVERSITY
OF SHEFFIELD
LIBRARY



IMAGING SERVICES NORTH

Boston Spa, Wetherby

West Yorkshire, LS23 7BQ

www.bl.uk

BEST COPY AVAILABLE.

VARIABLE PRINT QUALITY



IMAGING SERVICES NORTH

Boston Spa, Wetherby

West Yorkshire, LS23 7BQ

www.bl.uk

**PAGE NUMBERING AS
ORIGINAL**

بِسْمِ اللَّهِ الرَّحْمَنِ الرَّحِيمِ

﴿اقرأ باسم ربك الذي خلق (1) خلق الإنسان من علق (2) اقرأ وربك الأكرم (3) الذي علم بالقلم (4) علم الإنسان ما لم يعلم﴾ (5) العلق

To My Parents

And My Beloved Country SYRIA

إهداء

إلى نبع الحنان الذي لا ينضب.....إلى أمي

إلى شعلة العطاء التي لا تنطفئ.....إلى أبي

ABSTRACT

Post-earthquake reconnaissance and results of previously conducted experiments show that stiffness and strength deterioration of beam-column joints can have a detrimental effect on the integrity and vulnerability of reinforced concrete frame structures, especially in older buildings in developing countries. As a result, there is a need to develop efficient structural evaluation techniques that are capable of accurately estimating the strength and deformability of existing buildings to facilitate the development of safer, simpler, and lower cost retrofit solutions and thus contributing to risk mitigation.

The current research is part of a general effort that is being carried out at the University of Sheffield to quantify and develop strategies for the mitigation of seismic risk in developing countries. The primary aim of this work is to improve the current understanding of the seismic behaviour of deficient exterior reinforced concrete beam-column joints. Seven full-scale isolated exterior beam-column joints were tested under quasi-static cyclic loading to investigate and quantify the effects of using different types of beam reinforcement anchorages and low column axial loads on the seismic shear performance of exterior beam-column joints with no shear reinforcement.

Contrary to what is reported in the literature, the test results show that increasing the column axial load even at very low levels ($<0.2f_c A_{g_c}$) can enhance the joint shear strength of deficient exterior joints (exhibiting pure shear failure) by up to 15%. The test results also show that, for the same joint panel geometry and column axial load, the type of beam anchorage detail, whether it is a straight bar, long or short hook, can influence the joint shear strength by up to 34%.

A new analytical model that predicts the shear strength of deficient exterior beam-column joints in both loading directions and takes into account the column axial load and bond conditions within the joint is developed. The model predicts with good accuracy the strength of the tested specimens in addition to other specimens reported by other researchers. Furthermore, a spring-based exterior beam-column joint model for finite element analysis of deficient RC frames is proposed. The model development includes a joint shear stress-strain constitutive model based on the developed strength model. The simulated response using the proposed model shows good agreement with the experimentally observed response.

ACKNOWLEDGMENTS

I would like to express my sincere thanks and deepest gratitude to my supervisor Professor Kypros Pilakoutas for his continuous guidance, encouragement and support throughout the preparation of this thesis.

I am also very grateful to Dr Maurizio Guadagnini for his invaluable contributions and help. It would not have been possible without his support.

I also want to thank all my friends for all their help and support during the various stages of my PhD years, but most importantly for their invaluable friendship.

I would also like to thank the Concrete and Earthquake Engineering Group and the Department of Civil and Structural engineering at the University of Sheffield for supporting the experimental part of this research.

Finally, I would like to express my sincere love and gratitude to my beloved family, especially my mother and father. Their endless love, support and prayers helped me get through the difficult times and achieve this work.

TABLE OF CONTENTS

CHAPTER 1	INTRODUCTION.....	1
1.1	BACKGROUND AND PROBLEM STATEMENT	1
1.2	RESEARCH AIMS AND OBJECTIVES	5
1.3	THESIS LAYOUT	6
CHAPTER 2	BACKGROUND AND STATE OF THE ART.....	8
2.1	INTRODUCTION	8
2.2	BACKGROUND	8
2.3	GEOMETRY AND DETAILING	9
2.4	BEHAVIOUR OF DEFICIENT EXTERIOR JOINTS	11
2.4.1	Joint Shear Resistance Mechanisms	11
2.4.2	Joint Shear Strength	13
2.4.3	Deficient Joint Failure Mechanisms	15
2.5	KEY INFLUENCE PARAMETERS	16
2.5.1	Effect of Concrete Compressive Strength	17
2.5.2	Effect of Joint Aspect ratio	17
2.5.3	Effect of Beam Reinforcement	18
2.5.4	Effect of Column Axial Load	19
2.6	PREVIOUS EXTERIOR BEAM-COLUMN JOINT TESTS	20
2.6.1	Hanson and Connor (1967)	20
2.6.2	Uzumeri (1977)	20
2.6.3	Clyde et al. (2000)	21
2.6.4	Pantelides et al. (2002)	22
2.6.5	Ghobarah and Said (2001)	23
2.6.6	Antonopoulos and Triantafillou (2003)	24
2.6.7	Wong (2005)	25
2.6.8	Karayannis et al. (2008)	26
2.7	ANALYTICAL JOINT STRENGTH MODELS	26
2.7.1	ASCE/SEI 41 JOINT STRENGTH	27

2.7.2	Strut-and-Tie Joint Models	28
2.7.3	Spring-Based Joint Models for FE Frame Analysis	46
2.8	RECAP AND CONCLUSIONS	55
CHAPTER 3	EXPERIMENTAL PROGRAMME.....	58
3.1	INTRODUCTION	58
3.2	TEST PARAMETERS	58
3.2.1	Concrete compressive strength	59
3.2.2	Column axial load ratio	59
3.2.3	Beam longitudinal bar bond demand	59
3.2.4	Joint Shear Reinforcement	60
3.3	TEST SPECIMENS	60
3.3.1	DESCRIPTION OF MODEL STRUCTURE	60
3.3.2	DESIGN AND FABRICATION OF TEST SPECIMENS	61
3.3.3	SPECIMEN CONSTRUCTION	69
3.4	MATERIALS	69
3.4.1	CONCRETE	69
3.4.2	STEEL REINFORCEMENT	72
3.5	INSTRUMENTATION	74
3.5.1	INTERNAL INSTRUMENTATION: Strain Gauges	74
3.5.2	EXTERNAL INSTRUMENTATION	79
3.5.3	JOINT PERFORMANCE PARAMETERS	81
3.6	TEST SETUP	89
3.6.1	THE LOADING FRAME	89
3.6.2	TESTING PROCEDURE	90
CHAPTER 4	EXPERIMENTAL OBSERVATIONS AND DISCUSSION.....	93
4.1	INTRODUCTION	93
4.2	DAMAGE CRITERIA	93
4.3	PERFORMANCE CHARACTERISTICS	94
4.4	GENERAL CYCLIC BEHAVIOUR OF TEST SPECIMENS	96
4.4.1	SPECIMEN JA-1 & 2	96

4.4.2 SPECIMEN JA-3	102
4.4.3 SPECIMEN JB-1	106
4.1.1 SPECIMEN JB-2	112
4.1.2 SPECIMEN JC-1	115
4.1.3 SPECIMEN JC-2	124
4.2 PERFORMANCE INDICATORS	126
4.2.1 AXIAL LOAD CAPACITY	126
4.2.2 STIFFNESS DEGRADATION	127
4.2.3 SHEAR STRESS-STRAIN RESPONSE CURVE	128
4.2.4 JOINT SHEAR DEFORMATION	131
4.2.5 DISSIPATED ENERGY	132
4.2.6 BEAM BAR STRAINS	133
4.5 EVALUATION OF TEST VARIABLES	135
4.5.1 EFFECT OF AXIAL LOAD LEVEL	135
4.5.2 ANCHORAGE TYPE	142
4.6 RECAP AND CONCLUSIONS	146
CHAPTER 5 JOINT SHEAR STRENGTH MODEL.....	150
5.1 INTRODUCTION	150
5.2 JOINT DATABASE	150
5.3 ASSESSMENT OF PREVIOUS JOINT STRENGTH MODELS	152
5.3.1 Hwang and Lee Model	152
5.3.2 Vollum and Newman Model	153
5.3.3 Tsonos Model	155
5.3.4 Park and Mosalam Model	155
5.3.5 Hassan Model	156
5.4 PROPOSED STRENGTH MODEL	157
5.4.1 Model Development and Background	157
5.4.2 Assumptions and Equilibrium	161
5.4.3 Joint Shear Capacity	172
5.5 VERIFICATION OF THE PROPOSED MODEL	173

5.6	MODEL LIMITATIONS	174
5.7	RECAP AND CONCLUSIONS	174
CHAPTER 6	RC JOINT MODEL FOR FE FRAME ANALYSIS	177
6.1	INTRODUCTION	177
6.2	CONSTITUTIVE SHEAR MODEL	177
6.2.1	Development of Shear Envelope Model	177
6.2.2	Proposed Shear Stress-Strain Envelope	179
6.2.3	Predicted Shear Envelope	182
6.3	SELECTION OF THE ANALYTICAL TOOL	183
6.4	NONLINEAR JOINT MODELLING	184
6.4.1	Background and Previous Models	184
6.4.2	Proposed Joint Panel Zone Model	186
6.4.3	Beam Anchorage Slip Modelling	191
6.4.4	Simulation Results and Comparisons	193
6.5	RECAP AND CONCLUSIONS	198
CHAPTER 7	CONCLUSIONS AND FUTURE RECOMMENDATIONS	200
7.1	LITERATURE REVIEW AND CURRENT KNOWLEDGE	200
7.2	EXPERIMENTAL PROGRAMME	201
7.3	SHEAR STRENGTH MODELS FOR DEFICIENT EXTERIOR JOINTS	204
7.4	JOINT MODELS FOR FE FRAME ANALYSIS	205
7.5	RECOMMENDATIONS FOR FUTURE WORK	207
REFERENCES		209
APPENDICES		219

LIST OF FIGURES

Figure 1.1 Moments and shear forces during earthquakes, after CEB-fip BN 231 (1996).....	1
Figure 1.2 Total and partial building collapse due to failure of deficient beam-column connections after the 1994 Northridge, California earthquake, a) (Moehle, 2008), b) (NISEE, 2012)	2
Figure 1.3 Partial building collapse due to severe damage in beam-column connections after the 1999 Izmit, Turkey earthquake, (NISEE, 2012).....	2
Figure 1.4 Observed damage in deficient beam-column joints (Moehle, 2008)	3
Figure 1.5 Deficient beam-column joints, 2009 L'aquila, Italy earthquake (Verderame et al., 2009)	4
Figure 2.1 Typical exterior beam-column joint of a RC frame building.....	10
Figure 2.2 Common anchorage detailing types of older exterior beam-column joints	10
Figure 2.3 Forces acting on joint core and shear resisting mechanisms of confined exterior beam-column joint (Paulay & Scarpas, 1981).....	12
Figure 2.4: Exterior unconfined joint: a) Interface Forces, b) Diagonal strut mechanism, after Hwang and Lee (1999).....	12
Figure 2.5 Joint effective area (ACI 318-08, 2008)	14
Figure 2.6 a) Free body diagram, b) column global equilibrium, c) shear force distribution of a typical exterior beam-column joint	15
Figure 2.7 Effect of joint aspect ratio on joint shear strength coefficient γ	18
Figure 2.8 Cyclic load-beam tip displacement response curve of specimen SP5 (Uzumeri, 1977)	21
Figure 2.9 Test setup and specimen dimensions (Clyde et al., 2000)	22
Figure 2.10 Reinforcement details of the specimens (Pantelides et al., 2002).....	23
Figure 2.11 Reinforcement details and cyclic load-beam tip displacement response curve of specimen T1 (Ghobarah & Said, 2001).....	24
Figure 2.12 Reinforcement details and measured response of specimen C1 (Antonopoulos & Triantafillou, 2003)	24
Figure 2.13 Dimensions and detailing of unconfined exterior joints (Wong, 2005).....	25
Figure 2.14 Dimensions and reinforcement details of control specimens (Karayannis et al., 2008)	26
Figure 2.15 General nonlinear load-deformation envelope for beam-column joints, (ASCE/SEI 41, 2006) and (ACI 369R, 2011).....	28
Figure 2.16 The proposed joint shear resisting mechanisms of SST model (Hwang & Lee, 1999)	29
Figure 2.17 Joint shear distribution among resisting mechanisms of SST model (Hwang & Lee, 1999)	30

Figure 2.18 Concrete constitutive model (Hwang & Lee, 1999)	31
Figure 2.19 Compatibility conditions of cracked concrete (Hwang & Lee, 1999)	32
Figure 2.20 SAT model for exterior beam-column joints without stirrups a) boundary forces; b) geometry (Vollum & Newman, 1999)	33
Figure 2.21 Assessment of the simplified empirical model proposed by Vollum and Newman (1999) for unconfined exterior beam-column joints	35
Figure 2.22 Strut and truss shear resisting mechanisms of exterior beam-column joints (Tsonos, 2008)	36
Figure 2.23 Proposed Strut and Tie joint shear model (Park & Mosalam, 2012a)	40
Figure 2.24 Fraction factor function of strut ST1 (Park & Mosalam, 2012a)	42
Figure 2.25 Direct Strut and Tie joint shear model (Hassan, 2011)	44
Figure 2.26 One-component nonlinear beam-joint model, Giberson (1967)	46
Figure 2.27 Two-component nonlinear beam-joint model, Otani (1974)	47
Figure 2.28 Panel-zone joint models: a) scissors model by Krawinkler and Mohasseb (1987), b) Krawinkler model by Krawinkler (2001)	48
Figure 2.29 Multi rotational spring joint model (Biddah & Ghobarah, 1999)	49
Figure 2.30 Beam-Column joint model by Youssef and Ghobarah (2001)	50
Figure 2.31 Beam-Column joint model by Lowes and Altoontash (2003)	51
Figure 2.32 Interior Beam-Column joint model by Shin and LaFave (2004)	52
Figure 2.33 Interior Beam-Column joint model by Mitra (2007)	53
Figure 2.34 Exterior Beam-Column joint model by Sharma et al. (2011)	54
Figure 3.1: Ecoleader no.2 frame structure fixed to the shaking table (Chaudat et al., 2005)	60
Figure 3.2: Geometry of Ecoleader no.2 frame structure, after Chaudat et al. (2005)	61
Figure 3.3 Beam cross section	62
Figure 3.4 Columns cross section	62
Figure 3.5 Columns cross section of JA-1	63
Figure 3.6: Anchorage details of the test specimens	64
Figure 3.7 Dimensions and reinforcement details of the pilot specimen JA-1	65
Figure 3.8 Reinforcement detailing of the joint core of Group A specimens	65
Figure 3.9 Dimensions and reinforcement details of group B specimens	66
Figure 3.10 Dimensions and reinforcement details of group C specimens	67
Figure 3.11 Details for development length of standard hooks (ACI 318-08, 2008)	68
Figure 3.12 Concrete compressive stress-strain relationship for batch No. 2&3	72
Figure 3.13 Stress-strain relationship for the specimens' longitudinal reinforcement	73
Figure 3.14 Stress-strain relationship for the specimens' shear reinforcement	74
Figure 3.15 Types of waterproofing material for strain gauges (a Rubber sealant, (b Araldite ..	75
Figure 3.16 Strain gauge locations of the pilot specimen JA-1	76
Figure 3.17 Strain gauge locations: the old and the revised distribution	77

Figure 3.18 Strain gauge locations for JA-2 & JA-3	78
Figure 3.19 Strain gauge locations for JB-1 & JB-2	78
Figure 3.20 Strain gauge locations for JC-1 & JC-2	79
Figure 3.21 LVDT configuration	80
Figure 3.22 Displacement transducers configuration	81
Figure 3.23 LVDT configuration for joint shear strain measurement and method of calculation	82
Figure 3.24 DT configuration for joint global rotation measurement	83
Figure 3.25 LVDT configuration for the measurement of beam rotation relative to the joint....	84
Figure 3.26 Anchorage-Slip mechanism at the joint interface	85
Figure 3.27 Bond-Slip measurement.....	86
Figure 3.28 Strain distribution of beam bottom bar	87
Figure 3.29 Definition of Peak-to-Peak stiffness	88
Figure 3.30 Definition of energy dissipation per one load-drift cycle	89
Figure 3.31 Loading apparatus.....	90
Figure 3.32 Loading history	91
Figure 4.1: Definition of drift.....	94
Figure 4.2: Progression of cracking for specimen JA-2	97
Figure 4.3: Lateral load-drift response for specimen JA-2.....	98
Figure 4.4: Specimen JA-2 after one cycle at 0.5% drift	99
Figure 4.5: Specimen JA-2 after three cycles at 0.5% drift.....	99
Figure 4.6: Specimen JA-2 after one cycle at 0.75% drift	100
Figure 4.7: Specimen JA-2 after one cycle at 1.5% drift	101
Figure 4.8: Specimen JA-2 after one cycle at 2.0% drift	101
Figure 4.9: Progression of cracking for specimen JA-3	103
Figure 4.10: Lateral load-drift response for specimen JA-3.....	104
Figure 4.11: Specimen JA-3 after three cycles at 4.0% drift.....	105
Figure 4.12: Specimen JA-3 at the first positive peak to 5.0% drift	105
Figure 4.13: Progression of cracking for specimen JB-1	106
Figure 4.14: Lateral load-drift response for specimen JB-1.....	107
Figure 4.15: Specimen JB-1 after one cycle at 0.5% drift.....	108
Figure 4.16: Specimen JB-1 cracks at the third negative peak to 0.5% drift	109
Figure 4.17: Specimen JB-1 after three cycles at 0.75% drift.....	109
Figure 4.18: Specimen JB-1 after one cycle at 1.5% drift.....	110
Figure 4.19: Specimen JB-1 after three cycles at 2.0% drift.....	111
Figure 4.20: Specimen JB-1 after three cycles at 3.0% drift.....	111
Figure 4.21: Specimen JB-1 after three cycles at 4.0% drift.....	112
Figure 4.22: Progression of cracking for specimen JB-2	113

Figure 4.23: Lateral load-drift response for specimen JB-2.....	114
Figure 4.24: Specimen JB-2 at 5.0% drift	115
Figure 4.25: Progression of cracking for specimen JC-1	116
Figure 4.26: Lateral load-drift response for specimen JC-1	117
Figure 4.27: Specimen JC-1 after one cycle at 0.35% drift.....	118
Figure 4.28: Specimen JC-1 after one cycle at 0.5% drift.....	118
Figure 4.29: Specimen JC-1 after two cycles at 0.5% drift.....	119
Figure 4.31: Specimen JC-1 after three cycles at 0.75% drift.....	120
Figure 4.32: Specimen JC-1 after one cycle at 1.0% drift.....	120
Figure 4.33: Specimen JC-1 after three cycles at 1.5% drift.....	121
Figure 4.34: Specimen JC-1 after three cycles at 2.0% drift.....	121
Figure 4.35: Specimen JC-1 after three cycles at 3.0% drift.....	122
Figure 4.36: Specimen JC-1 after one cycle at 4.0% drift.....	122
Figure 4.37: Concrete spalling in specimen JC-1 after 4.0% drift cycles	123
Figure 4.38: Exposed rebar in specimen JC-1 after 4.0% drift cycles	123
Figure 4.39: Progression of cracking for specimen JC-2	124
Figure 4.40 Lateral load-drift response for specimen JC-2	125
Figure 4.41: Specimen JC-2 after one cycle at 5.0% drift.....	126
Figure 4.42 Applied axial load history of specimen JA-2.....	127
Figure 4.43 Peak-to-peak and half-cycle secant stiffness degradation of specimen JA-2.....	128
Figure 4.44 Peak-to-peak and half-cycle secant stiffness degradation of specimen JA-3.....	128
Figure 4.45 Joint shear stress-shear strain of specimen JA-2.....	129
Figure 4.46 Joint shear stress-shear strain of specimen JA-3.....	129
Figure 4.47 Peak-to-peak Shear Modulus Degradation of specimen JA-2	130
Figure 4.49 Contribution of joint shear deformation of group A specimens to total drift	131
Figure 4.50 Contribution of joint shear deformation of group B specimens to total drift.....	131
Figure 4.51 Contribution of joint shear deformation of group C specimens to total drift.....	132
Figure 4.52 Cumulative energy dissipation of specimen JA-2 and specimen JA-3	133
Figure 4.53 Dissipated energy per cycle for specimen JA-2 and specimen JA-3	133
Figure 4.54 Investigated strain gauges of beam top and bottom bars	134
Figure 4.55 Strain distribution of top beam bar at first positive peak of each drift level.....	134
Figure 4.56 Strain distribution of bottom beam bar at first negative peak of each drift level..	134
Figure 4.57 Top bar measured strains of specimen JA-2 in comparison to section analysis prediction.....	135
Figure 4.58 Normalised load-drift envelope curves of group A specimens.....	137
Figure 4.59 Normalised load-drift envelope curves of group B specimens	137
Figure 4.60 Normalised load-drift envelope curves of group C specimens	137
Figure 4.61 Load-drift envelope curves of group A specimens	139

Figure 4.62 Load-drift envelope curves of group B specimens	139
Figure 4.63 Load-drift envelope curves of group C specimens	139
Figure 4.64 Normalised Peak-to-Peak stiffness degradation of group A specimens	140
Figure 4.65 Normalised Peak-to-Peak stiffness degradation of group B specimens.....	140
Figure 4.66 Normalised Peak-to-Peak stiffness degradation of group C specimens.....	141
Figure 4.67 Half-cycle secant stiffness degradation of group A specimens	141
Figure 4.68 Half-cycle secant stiffness degradation of group B specimens.....	142
Figure 4.69 Half-cycle secant stiffness degradation of group C specimens.....	142
Figure 4.70 Normalised load-drift envelope curves of group I specimens	143
Figure 4.71 Load-drift envelope curves of Group I specimens.....	144
Figure 4.72 Normalised shear stress-strain envelope curves of Group I specimens	144
Figure 4.73 Normalised load-drift envelope curves of Group II specimens	145
Figure 4.74 Load-drift envelope curves of Group II specimens	146
Figure 4.75 Normalised shear stress-strain envelope curves of Group II specimens.....	146
Figure 5.1 Verification of SST Model (Hwang & Lee, 1999)	152
Figure 5.2 Assessment of Hwang and Lee (1999) model for unconfined exterior joints.....	153
Figure 5.3 Assessment of Vollum and Newman (1999)model for unconfined exterior joints..	154
Figure 5.4 Assessment of Tsonos (2007) model for unconfined exterior joints	155
Figure 5.5 Assessment of Park & Mosalam (2009) model for unconfined exterior joints.....	156
Figure 5.6 Assessment of Hassan (2011) model for unconfined exterior joints	157
Figure 5.7: Idealised compression strut in exterior beam-column joints	158
Figure 5.8:Crack pattern of JA-2 showing an extended compression strut.....	159
Figure 5.9: Proposed Strut and Tie joint shear model (Park & Mosalam, 2012a)	159
Figure 5.10: Strut and Tie in a joint with straight bars according to the model by Park & Mosalam (2009; 2012a)	160
Figure 5.9: Extension and stress distribution of the assumed diagonal compressive strut.....	162
Figure 5.12: Extended nodal zone due to the presence of a tension force (ACI 318-08, 2008)	162
Figure 5.13: Types of anchored ties as defined in ACI 318-08 (2008).....	163
Figure 5.14: Assumed anchored tie in deficient exterior joints.....	164
Figure 5.15: The outer nodal zone in the assumed strut.....	164
Figure 5.16: Influence of transverse pressure on bond stress.....	166
Figure 5.13: Definition of anchorage length and bar covers	167
Figure 5.14 a) Free body diagram, b) global equilibrium, c) shear force distribution of a typical test specimen	168
Figure 5.15: Definition of l_s for beam straight bars.....	170
Figure 5.16: Definition of hook contribution to the tie reinforcement.....	171
Figure 5.17: Local bond stress of 90° hook bar (Shima & Fukuju, 2008)	172
Figure 5.18 Verification of the proposed Strut-and-Tie joint shear strength model	174

Figure 6.1 Shear stress-strain of specimen JC-2 and proposed envelope.....	178
Figure 6.2 Proposed exterior joint shear stress-strain envelope curve	178
Figure 6.3 Comparison of measured and predicted strain at the peak joint shear stress	181
Figure 6.4 Shear stress-strain of specimen JA-3 and predicted envelope	182
Figure 6.5 Shear stress-strain of specimen JB-1 and predicted envelope	183
Figure 6.6 Shear stress-strain of specimen JC-1 and predicted envelope	183
Figure 6.7 Panel zone joint model.....	185
Figure 6.8 Modified Scissors joint model with translational shear hinges.....	186
Figure 6.9 Proposed Krawinkler-type panel zone joint model.....	186
Figure 6.10 DRAIN-2DX exterior beam-column joint model: Geometry and Elements.....	187
Figure 6.11 DRAIN-2DX Element 10: connection types, after Foutch et al. (2003).....	188
Figure 6.12 DRAIN-2DX Element 10: concrete connection hysteresis model, after Foutch et al. (2003)	188
Figure 6.13 Decomposition of shear hinge quad-linear envelope.....	189
Figure 6.14 DRAIN-2DX Element 15 description, after Powell (1993).....	190
Figure 6.15 Calculations of slip induced rotation at a cross-section.....	192
Figure 6.16 Application of the adopted Sezen model on exterior joints.....	193
Figure 6.17 Comparison of rigid joint model response with measured response of specimen JC-1	194
Figure 6.18 Comparison of rigid joint model response with measured response of specimen JC-2.....	194
Figure 6.19 Simulation results of Joint specimen JA-2.....	195
Figure 6.20 Simulation results of Joint specimen JA-3.....	195
Figure 6.21 Simulation results of Joint specimen JB-1	195
Figure 6.22 Simulation results of Joint specimen JB-2.....	196
Figure 6.23 Simulation results of Joint specimen JC-1	196
Figure 6.24 Simulation results of Joint specimen JC-2.....	196
Figure 6.25 Prediction of Wong (2005) specimen BS-U	197
Figure 6.26 Prediction of Wong (2005) specimen BS-L.....	197
Figure 6.27 Prediction of Clyde et al. (2000) specimen #2.....	198
Figure 6.28 Prediction of Clyde et al. (2000) specimen #6.....	198

LIST OF TABLES

Table 2-1 Average Parameters for Pre-1967 Buildings (Mosier, 2000).....	9
Table 2-2 Average Parameters for 1967-1979 Buildings (Mosier, 2000).....	9
Table 3-1 Joint steel details in comparison to the current ACI code.....	68
Table 3-2 Concrete compressive strength of specimen JA-1 (Pilot test)	70
Table 3-3 Concrete tensile strength of specimen JA-1 (Pilot test).....	70
Table 3-4 Concrete compressive strength and modulus of elasticity of batch 2 specimens.....	70
Table 3-5 Concrete tensile strength of batch 2 specimens	71
Table 3-6 Concrete compressive strength and modulus of elasticity of batch 3 specimens.....	71
Table 3-7 Concrete tensile strength of batch 3 specimens	71
Table 3-8 Test specimens main reinforcement properties.....	73
Table 3-9 Test Specimens shear reinforcement properties.....	73
Table 3-10 Test Specimens axial load ratio	91
Table 3-11 Drift Levels and beam tip displacement	92
Table 4-1 Joint nominal shear strength and beam shear, according to ASCE 41 (2006).....	95
Table 4-2 Modelling parameters for test specimens according to ASCE 41 and ACI 369R	96
Table 4-3 Description of observed damage of specimen JA-3.....	104
Table 4-4 Description of observed damage of specimen JB-2.....	114
Table 4-5 Description of observed damage of specimen JC-2.....	125
Table 4-6 Maximum joint shear stress-strain of specimen JA-3	129
Table 4-7 Applied axial load level	135
Table 4-8 Joint shear strength of the test specimens	136
Table 4-9 Positive to negative direction strength ratios of the test specimens.....	138
Table 5-1 Database of exterior deficient beam-column joints	151

LIST OF SYMBOLS

a_b	depth of beam compression zone
a_c	depth of column compression zone
a_s	effective strut width
a_{pr}	horizontal projection of strut extended width
A_g	gross area of column cross section
A_j	effective joint area
A_s	area of steel reinforcement
A_{st}	area of compressive strut
b_b	beam width
b_c	column width
b_j, b_{je}	effective joint width
D	compressive strut capacity
d_b	beam effective depth
E_c	concrete modulus of elasticity
h_b	beam depth
h_c	column depth
h_j	joint depth
f'_c	compressive cylinder strength of concrete
f_{ce}	effective compressive strength of inclined strut
f_y	yield strength of steel reinforcement
f_s	average stress in beam bars at column face
G_c	theoretical elastic shear modulus
H	column height; measured between the roller supports at the end of top and bottom columns

jd_b	lever arm of beam moment at column face
K_p	peak-to-peak stiffness per load-drift hysteretic loop
K_{sec}	secant stiffness of each half cycle positive and negative
L, L_b	beam length; measured between the point where cyclic load is applied to column face
l_{anc}	recommended bar development length within nodal zone for development of tie reinforcement, as defined in ACI 318
l_b	horizontal projection of embedment length measured from joint interface to end of bar
l_{dh}	horizontal projection of embedment length as defined in ACI 318; measured from joint interface to end of bar.
l_s	length of beam bar under transverse pressure within original length of inclined strut a_c
M_b	beam moment at column face
n	number of beam longitudinal bars in tension
T_b	tension force in beam reinforcement at column face
V_b	beam shear force
V_c	column shear force
V_j	joint shear in the vertical or horizontal directions
V_{jh}	joint shear strength in the horizontal direction
w_t	effective tie width
Δ_b	total beam tip displacement
Δ_j	contribution of joint shear deformation to beam tip displacement
γ	joint shear stress normalised by $\sqrt{f'_c}$; and denoted here as “ <i>joint shear strength coefficient</i> ”
γ_{cr}	cracking shear strain
γ_j	joint shear strain
$\Omega_{p,tr}$	enhancing factor of bond stress due to transverse pressure
τ_E	bond stress distribution at elastic stage (before yielding)

τ_b	average bond stress distribution
τ_{cr}	cracking shear stress
τ_j	joint shear stress
θ_s	angle of inclination of inclined strut; measured between outer side of inclined strut and outer face of column

LIST OF ABBREVIATIONS

<i>BJ-Type</i>	joint shear failure after yielding in longitudinal reinforcement
DT	displacement transducers
<i>J-Type</i>	joint shear failure without yielding in longitudinal reinforcement
LVDT	linear variable differential transducers
MCFT	the modified compression field theory
RC	reinforced concrete
SAT	strut-and-tie approach
SST	softened strut-and-tie model

CHAPTER 1

INTRODUCTION

1.1 BACKGROUND AND PROBLEM STATEMENT

Reinforced concrete (RC) beam-column connections are the most important parts of moment resisting frame structures. During severe earthquakes, beam-column joints are subjected to a combination of high shear forces and moments (see Figure 1.1). Failure to withstand these imposed actions can yield severe damage, which in turn may jeopardise the integrity of the whole structure.

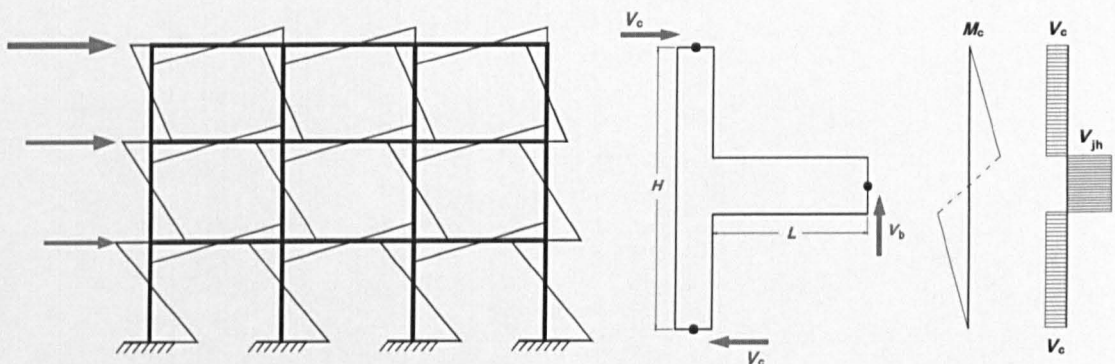


Figure 1.1 Moments and shear forces during earthquakes, after CEB-fip BN 231 (1996)

While joints designed according to current seismic codes can easily sustain the imposed seismic forces, the same is not true for joints found in older existing buildings. Reconnaissance reports of recent destructive earthquakes such as El-Ansam, Algeria, 1980; Northridge, California, 1994; Tehuacan, Mexico, 1999; Athens, Greece, 1999; 1999 Chi-Chi, Taiwan, Izmit, Turkey, 1999; L'aquila, Italy, 2009; and Haiti, 2010 demonstrated the high vulnerability level of older existing RC buildings (EERI, 1999a; EERI, 1999b; EERI, 1999c; Moehle, 2000; Sezen et al., 2000; Taciroglu & Khalili-Tehrani, 2008; Verderame et al., 2009). In many of the reported cases beam-column joints were severely damaged causing a total or partial building failure. Figure 1.2 through Figure 1.4 show examples of some of the reported buildings in which severe

distortion (i.e. failure) in beam-column joints is believed to have contributed to the total or partial collapse of these buildings.



(a)



(b)

Figure 1.2 Total and partial building collapse due to failure of deficient beam-column connections after the 1994 Northridge, California earthquake, a) (Moehle, 2008), b) (NISEE, 2012)



Figure 1.3 Partial building collapse due to severe damage in beam-column connections after the 1999 Izmit, Turkey earthquake, (NISEE, 2012)



Figure 1.4 Observed damage in deficient beam-column joints (Moehle, 2008)

Previous earthquakes, as shown in the above figures, also demonstrated the high vulnerability of exterior joints in comparison to interior joints. This is because the sudden change in the geometry of exterior joints (i.e. discontinuity of the beam and slab) leads to higher and unbalanced moments (both flexural and torsional), lower confinement and weaker bond conditions for the anchored beam bars (i.e. increased bond demand), (Novák et al., 2008; Engindeniz, 2008).

The observed failure in exterior beam-column joints is attributed to the structural deficiencies present in the majority of these older structures. In general, the reported joints were mainly lacking shear links within the joint (i.e. unconfined), inadequate beam bar anchorage, and/or the presence of lap splices (EERI, 1999a; EERI, 1999b; EERI, 1999c; Sezen et al., 2000). Figure 1.5 shows some of the deficiencies observed in older exterior joints after the 2009 L'aquila, Italy earthquake (Verderame et al., 2009).



Figure 1.5 Deficient beam-column joints, 2009 L'aquila, Italy earthquake (Verderame et al., 2009)

Over the past five decades, a great deal of the conducted research focused on improving the seismic design of RC beam-column joints for moment resisting frames. In contrast, less research studies aimed to study the performance of older buildings with seismically substandard exterior beam-column joints (despite being the majority of the existing building stock).

The earthquake engineering community has a major concern that many of these old buildings represent potential death traps in future seismic events. In addition to the lack of financial resources, low level of public awareness in developing countries makes retrofitting such buildings a major challenge. The only currently available option for researchers is to raise the public awareness and to develop efficient evaluation approaches that are capable of accurately estimating the strength of existing buildings, and thus achieve safer, simpler, and lower cost options for retrofitting.

Performance evaluation of older structures for the purpose of strengthening has always been a huge challenge for engineers, as the current seismic and retrofitting codes lack the transparency required to allow the engineer to fully understand and control the evaluation process (D'Ayala & Charleson, 2002; Novák et al., 2008; Hassan, 2011; Soyluk & Harmankaya, 2012; Park & Mosalam, 2012b). Most of these codes, when addressing any potential structural deficiencies, aim to evaluate the structure's performance as a whole rather than on a local level. This reflects the lack of proper understanding of the effect of each of the different design parameters on joint seismic behaviour. As a result, using these codes can lead to the underestimation of the structure's real strength, which in turn may result in a more expensive strengthening solutions than what is really needed (D'Ayala & Charleson, 2002; Soyluk & Harmankaya, 2012).

To address the above issue there is an urgent need to develop a rational yet transparent procedure that is capable of accurately simulating the real behaviour of deficient beam-column joints and their effect on the global response during seismic events. This will only be feasible

through an analytical model that accounts for all structural deficiencies typical of older buildings.

Several attempts were made to simulate the behaviour of older beam-column joints. The majority of these attempts focused on interior joints and varied in their inclusion of nonlinear characteristics such as the pinching effect, stiffness degradation, and strength degradation. The common problem between all these previous attempts is that the shear strength and failure mechanisms are predicted based on shear constitutive models developed specifically for confined RC elements such as the modified compression-field theory MCFT (Vecchio & Collins, 1986). This is because, until recently, there were no dedicated shear strength models for deficient joints except for some attempts based on parametric studies such as Mitra (2007). However, these recent attempts (mostly based on the Strut-and-Tie model approach) assume proper beam reinforcement embedment length within the joint area (i.e. standard hook). The cases between very short anchorage and full standard hook have not been explored yet.

A joint model that is capable of estimating the hysteretic shear behaviour of deficient exterior beam-column joints and its impact on the global behaviour is therefore required. Moreover, the current understanding of issues such as brittle shear failure in comparison to less brittle (joint shear failure after beam yielding), different beam anchorage types in comparison to standard hooks, and low column axial load levels as opposed to high levels is relatively scarce/limited and should therefore be addressed via an experimental programme. The experimental results can be used to calibrate a shear stress-strain constitutive model for deficient exterior joints.

The current research is part of a general effort that is being carried out at the University of Sheffield (Kythreoti, 2007; Kyriakides, 2008; Khan, 2011; Ahmad, 2011), with the aim to develop an analytical seismic vulnerability assessment tool to mitigate the seismic risk in developing countries.

1.2 RESEARCH AIMS AND OBJECTIVES

The primary aim of this research is to develop an analytical model capable of predicting the shear strength and failure mechanism of deficient exterior RC beam-column joints taking into account all the possible affecting parameters, and in turn employ it to evaluate and achieve better strengthening design for RC older existing buildings. Only exterior beam-column joints with no transverse reinforcement and with no stub beams, but with different beam anchorage details, are considered in this study.

This is achieved through the following objectives:

- 1- Conducting an extensive literature review that includes the following tasks

- a) Defining the main structural deficiencies of exterior joints in older existing buildings, especially in developing countries by reviewing past and recent post-earthquake reconnaissance reports.
 - b) Establishing the current understanding/knowledge of the different aspects of the seismic behaviour of deficient exterior beam-column joints, in terms of force transfer mechanisms, strength calculations, and failure modes.
 - c) Identifying the key influencing parameters and their effects on the joint shear strength of deficient exterior beam-column joints.
 - d) Establishing a database of all the available deficient exterior beam-column joint tests that exhibited joint shear failure.
 - e) Reviewing all the available joint shear strength models that might be applicable to deficient exterior joints.
 - f) Reviewing the available element-based joint models for FE computer simulations and establishing drawbacks and advantages of each model.
- 2- Experimentally investigating the effect of low axial load level, column lap splices, and different beam bar anchorages on the shear strength and failure mode of deficient exterior joints.
 - 3- Analytically evaluating the accuracy and the applicability of available shear strength models to deficient exterior joints.
 - 4- Developing a simple analytical approach capable of estimating the strength of deficient exterior joints taking into account the bond conditions of the anchored beam bars within the joint.
 - 5- Proposing a shear stress-shear strain constitutive model for deficient exterior joints.
 - 6- Developing a simple element-based joint model incorporating the proposed shear constitutive model for the purpose of FE frame simulations.

1.3 THESIS LAYOUT

This thesis is divided into seven chapters. The following is a brief overview of each chapter.

Chapter 2 gives a brief background of the key research problem and a review of the observed damage and common structural deficiencies found in older buildings in developing countries. In addition, this chapter presents the current understanding of the vital aspects of the seismic behaviour of deficient exterior RC beam-column joints, in terms of force transfer mechanisms, strength calculations, and failure modes. Moreover, previous experimental test results of deficient exterior beam-column joints failing in shear are presented and key parameters that

influence the seismic behaviour of such joints are discussed. Finally, Chapter 2 offers a critical and extensive review of the available shear strength and computer based joint models that might be applicable for shear-critical deficient exterior joints.

Chapter 3 presents the details of the experimental programme and methodology used of the current research carried out at the Heavy Structures Laboratory of The University of Sheffield. The experimental programme comprises testing seven full scale deficient exterior RC beam-column joints. A description of the test specimens and the investigated parameters is given in this chapter along with a discussion on the construction of the specimens, material properties and instrumentation.

Chapter 4 describes in detail the observed response in terms of hysteretic behaviour and progression of damage for each of the tested specimens. The damage criteria and performance characteristics of the hysteretic behaviour are defined and explained. This includes a description of the lateral load-drift hysteretic response and backbone curve, stiffness degradation, shear stress-strain response curve, and dissipated energy. The effects of test variables on the seismic performance and hysteretic behaviour of deficient exterior beam-column joints, such as low column axial load variation and beam reinforcement anchorage types, are also presented.

In Chapter 5, the most recent joint shear strength models that were reviewed in Chapter 2 are evaluated and criticized in terms of their accuracy and applicability to shear-critical deficient exterior beam-column joints. Based on the drawbacks of the reviewed models, a new analytical model that predicts the shear strength of exterior deficient beam-column joints in both loading directions and takes into account column axial load and anchorage conditions within the joint is developed. This chapter gives the details of the development for the proposed strut-and-tie joint shear strength model. Finally, verification of the model against 24 deficient exterior beam-column joints is presented and discussed.

Chapter 6 presents the development of an exterior beam-column joint model for finite element analysis of deficient RC frames. The development of the model includes the proposal of a quad-linear shear stress-strain constitutive model for the representations of joint panel zone, selection of the analytical tool, and description of the model structure in terms of the included elements and hysteretic properties. Finally, an evaluation of the accuracy of the simulated response using the proposed model and conventional rigid-zone joint models of the current and other reported joint test specimens is presented and discussed.

Chapter 7 presents the concluding remarks of the current research based on the findings of each part of the work. Recommendations for future research are also included in Chapter 7.

CHAPTER 2

DEFICIENT EXTERIOR BEAM-COLUMN JOINTS: BACKGROUND AND STATE OF THE ART

2.1 INTRODUCTION

Defining the research problem requires establishing a good understanding of the vulnerability of deficient exterior beam-column joints and the impact of such joints on the global behaviour of older RC buildings during seismic events. The following chapter presents a comprehensive overview of the current understanding on some of the vital aspects of seismic behaviour of deficient exterior beam-column joints (i.e. joints with no shear reinforcement in the core area). This includes definition of failure mechanisms, types of deficient joint reinforcement detailing (commonly found in older buildings in developing countries), and joint shear force transfer mechanisms. This chapter also presents a summary of previous experimental test results on deficient exterior beam-column joints failing in shear and key parameters that influence the seismic behaviour of such joints. Finally, this chapter includes a critical review of the available shear strength and computer based joint models that could be used for shear-critical deficient exterior joints.

2.2 BACKGROUND

The high seismic vulnerability of beam-column joints in buildings constructed prior to 1980 comes from that fact that even though the first seismic design provisions for beam-column joints were introduced in the 1960s, they were not officially adopted as part of the main design requirements for ductile frames until the late 1970s (FEMA 313, 1998). The first US design code to include seismic design provisions/requirements for beam-column joints, such as the requirement of transverse reinforcement in the joint area, was the 1976 edition of the Uniform Building Code (UBC 1976). It is only rational therefore to assume that most, if not all buildings, built before the 1980s suffer from some kind of seismic deficiency, and in turn are highly vulnerable to the risk of seismic collapse during severe earthquakes. This problem is even more pronounced in developing countries located in high seismicity regions, especially since such

provisions for ductile design were not adopted into the main design codes of some of these countries until the late 1980s and sometimes the 1990s (Soyluk & Harmankaya, 2012).

Mosier (2000) conducted a survey on a wide range of pre-1979 buildings in the US. The survey identified joint characteristics such as strong beam-weak column design, short lap splices and the absence of joint shear reinforcement that were present in that era's buildings, as shown in Table 2-1 and Table 2-2. The consequences of joint failure are well documented (EERI, 1999a; EERI, 1999b; EERI, 1999c; Moehle, 2000; Sezen et al., 2000; Taciroglu & Khalili-Tehrani, 2008; Verderame et al., 2009) and are briefly shown in Chapter 1.

Table 2-1 Average Parameters for Pre-1967 Buildings (Mosier, 2000)

	Axial Load	Column Lap	v_j/f'_c **	Vol. Joint	
	Ratio	Splice Length (l_{dc}) (in)*		Reinforcement	$\sum M_c / \sum M_b$
				Ratio	
Average	0.12	28	0.21	0.000	2.2
Standard Deviation	0.07	8	0.09	0.000	2.8
Minimum	0.03	20	0.03	0.000	0.2
Maximum	0.28	38	0.37	0.002	9.4

* = typically spliced above floor.

** v_j is average joint shear stress.

Table 2-2 Average Parameters for 1967-1979 Buildings (Mosier, 2000)

	Axial Load	Column Lap	v_j/f'_c	Vol. Joint	
	Ratio %	Splice Length (in)		Reinforcement	$\sum M_c / \sum M_b$
				Ratio	
Average	0.17	Variable	0.15	0.009	2.04
Standard Deviation	0.10	in location	0.06	0.008	1.29
Minimum	0.03	and length	0.06	0.000	0.70
Maximum	0.33		0.29	0.021	5.18

2.3 GEOMETRY AND DETAILING

Figure 2.1 shows an idealisation of a reinforced concrete frame building. For the reasons pointed out in Chapter 1 (page 3), the current study focuses only on isolated exterior beam-column joints of a typical floor building, such as the one shown in Figure 2.1 without the transverse beam. Exterior beam-column joints in older buildings are generally considered to be the most vulnerable joints but yet the least studied.

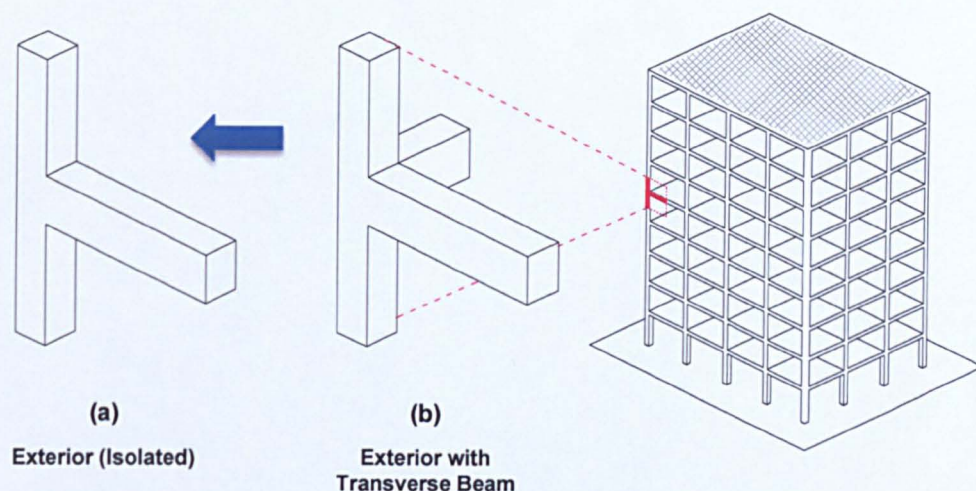


Figure 2.1 Typical exterior beam-column joint of a RC frame building

Seismic deficiencies related to reinforcement detailing of exterior beam-column joints of older buildings vary according to the adopted design guidelines. Some of the most common types of deficient details found in older buildings are shown in Figure 2.2. As can be seen, the shared deficiency between all types is the lack of shear reinforcement within the joint area. Other reported deficiencies include short lap splices in top columns and the use of plain bars. Type (a) and type (b), shown in Figure 2.2, are the most common in older frames, whereas type (c) can be found in more important buildings. The other two types (d, e), reported by Wong (2005), are rarely found, as they are regarded as impractical and difficult to execute.

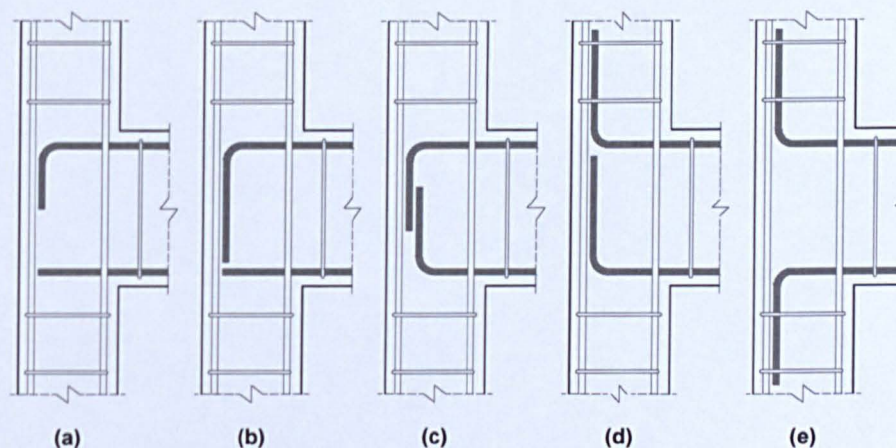


Figure 2.2 Common anchorage detailing types of older exterior beam-column joints

In the current research, only the most common types of exterior joints such as a, b and c will be considered. Any joint with type a, b or c and with no transverse reinforcement in the joint area is denoted in this research as “*unconfined*” or “*deficient*” exterior joint.

2.4 BEHAVIOUR OF DEFICIENT EXTERIOR JOINTS

2.4.1 Joint Shear Resistance Mechanisms

During earthquakes, and due to beam and column moment reversal, the adjoining beam-column joints are left with internal shear stresses and bond demands usually much higher than those within the adjoining frame members. Therefore, to avoid any failure in the joint panel, joints must be able to withstand the demands that correspond to the adjoining beam and columns whilst developing their full flexural capacity.

In general, it is assumed that RC exterior beam-column joints resist joint shear through two basic mechanisms: a diagonal compressive strut and a truss mechanism (Paulay et al., 1978). These two mechanisms control how the joint core behaves during a seismic event, in terms of maximum shear strength and expected failure mechanism. The transmitted internal forces from the adjacent framing beam and columns, subject the joint core to a state of high diagonal stresses. In other words, each joint face is subjected to a combination of shear, compressive, and tensile forces. Under these imposed forces, a state of equilibrium is established, in which the imposed forces are resisted by the two resisting mechanisms.

The joint truss mechanism, as shown in Figure 2.3, is assumed to form within the joint panel as a result to the combined effect of beam and column forces transmitted to the joint core by means of bond stress transfer along the beam and column longitudinal bars and the tensile resisting forces that develop within the joint transverse reinforcement (i.e. shear links), which work as ties for the formed truss mechanism (Paulay & Scarpas, 1981; Paulay & Priestley, 1992; Uma & Parsad, 2004). Therefore, for joints with no transverse reinforcement in the joint area, the same truss mechanism cannot be formed. Instead, the forces transmitted along the beam and column longitudinal bars (by means of bond stress transfer) offer limited contribution to enhance the joint shear resistance (Paulay & Priestley, 1992). These bond induced forces mostly help either stabilise the strut ends or increase its width. However, once bond deterioration initiates within the core, this small contribution rapidly diminishes.

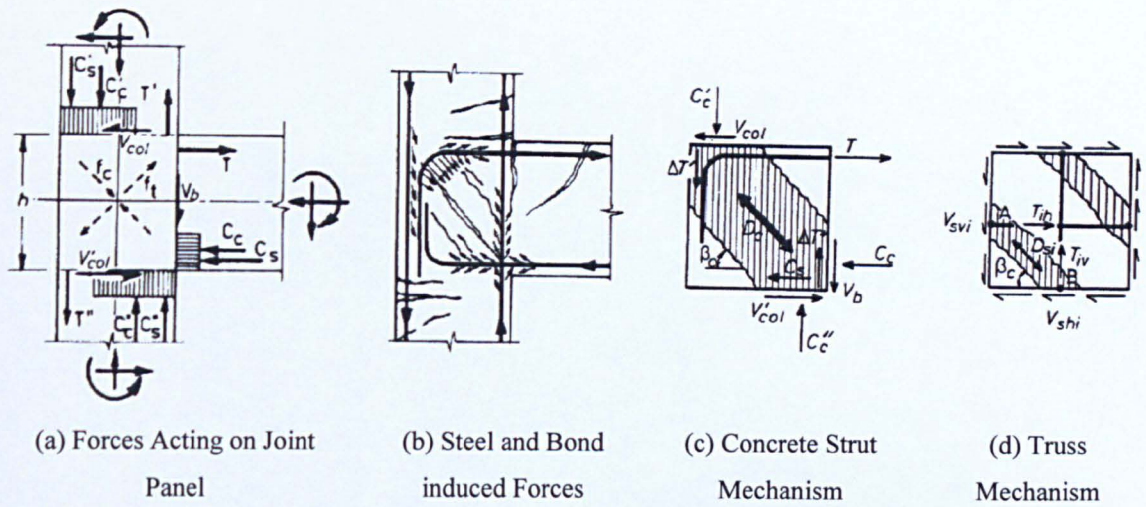


Figure 2.3 Forces acting on joint core and shear resisting mechanisms of confined exterior beam-column joint (Paulay & Scarpas, 1981)

Based on the above, the only effective shear resisting mechanism for unconfined exterior joints is the diagonal compressive strut that forms within the core between the beam and column compression zones. Figure 2.4 shows the internal forces and the diagonal compressive strut of a RC unconfined exterior beam-column joint.

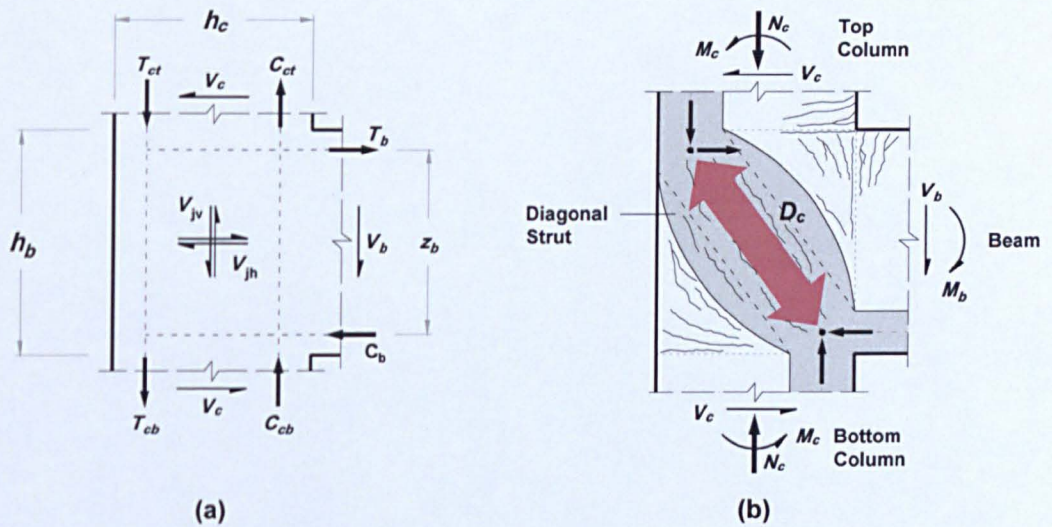


Figure 2.4: Exterior unconfined joint: a) Interface Forces, b) Diagonal strut mechanism, after Hwang and Lee (1999)

The efficiency of the diagonal strut mechanism depends on the state and capacity of the adjoining beam and columns. This can be attributed to the fact that yield penetration of beam longitudinal bars and in turn bond deterioration, together with perpendicular diagonal cracks and full depth interface shear cracks tend to weaken the compressive strength of the diagonal strut, which in turn weakens the joint shear resistance (Naeim, 2001).

Due to the complex stress state of the joint core, the effective compressive strength of the concrete within the joint is different from that of a normal concrete under just compression (i.e. uniaxial compression). The reason is that concrete in joint panels and under reversed actions exhibit tensile stresses acting perpendicular to the axis of the compressive strut. The concrete panel behaviour under biaxial tension-compression stresses was experimentally studied by many researchers such as Vecchio and Collins (1986), Belarbi and Hsu (1995), and Stevens et al. (1991). Furthermore, Stevens et al. (1991) reported that cyclic loading has additional detrimental effects on joint cores which cause further reduction to the concrete strength. This is due to the continuous opening and closing of cracks and the fact that tensile cracks are formed in both loading directions and not just limited to one direction, as in the case of monotonic loading.

Based on experimental studies, many concrete models to predict the softened compressive behaviour of joint concrete were proposed. However, in deficient exterior joints, and due to the lack of joint shear reinforcement, the effects of principal tensile strains and cyclic loading on the compressive strength of the strut's concrete are much more pronounced. Therefore, the strut width, angle of inclination, and concrete strength are the main factors that define the strut strength and in turn the shear strength of exterior joints with no reinforcement. There are several different approaches to estimate these factors and their applicability to exterior joints with no shear links is explored/discussed in section 2.7.2.

2.4.2 Joint Shear Strength

The joint shear strength V_j , in both vertical and horizontal directions can be defined in terms of the normalised joint shear stress, γ as follows:

$$\gamma = \frac{V_j}{\sqrt{f'_c} A_j} \quad (2.1)$$

where γ is denoted here as the “joint shear strength coefficient” and f'_c is the concrete compressive (cylinder) strength

The effective joint area A_j , as shown in Figure 2.5, is defined by ACI 318-08 (2008) as follows:

$$A_j = b_j h_c \quad (2.2)$$

where h_c is the joint depth which is equal to the column depth and b_j is the joint effective width (average of the beam and column widths), as defined by ACI 318-08 (2008) in Figure 2.5.

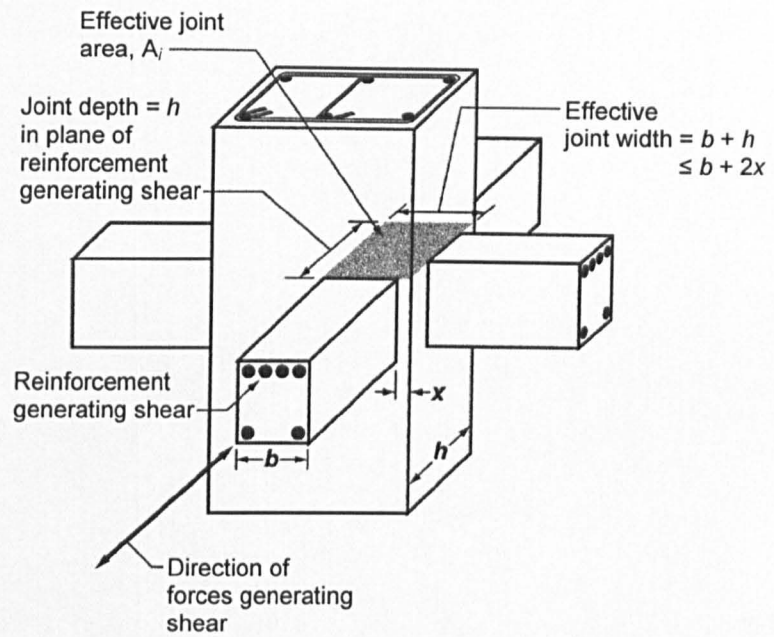


Figure 2.5 Joint effective area (ACI 318-08, 2008)

Figure 2.6 shows the geometry and applied forces on a typical exterior beam-column subassembly taken from a typical frame structure at beam and column mid-spans (i.e. moment contra-flexure points).

From global equilibrium, the column shear force, V_c can be calculated as follows:

$$V_c = V_b \frac{L + \frac{h_c}{2}}{H} \quad (2.3)$$

where:

- V_b is beam shear
- H and L are the column height and the beam length, respectively.

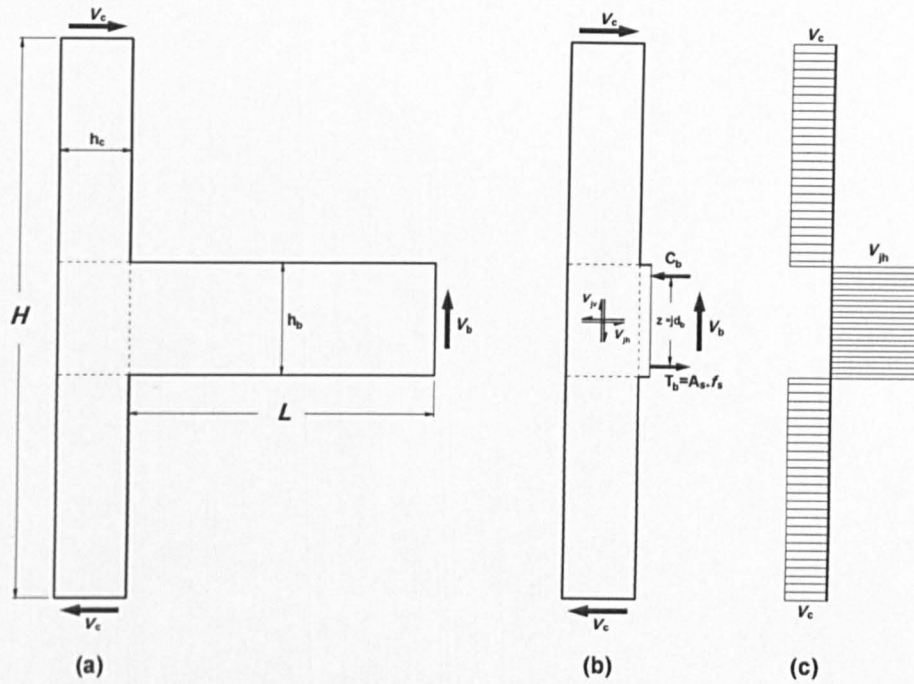


Figure 2.6 a) Free body diagram, b) column global equilibrium, c) shear force distribution of a typical exterior beam-column joint

Similarly, from beam internal equilibrium (see Figure 2.6.b), the beam moment and internal forces at the column face can be calculated as follows:

$$M_b = V_b \times L = T_b \times jd_b \quad (2.4)$$

where:

- T_b is the tension force in beam reinforcement at the column face
- jd_b is the beam moment lever arm, in which d_b is the beam effective depth

By using the column shear force V_c given in Eq (2.3) and the beam internal force T_b given in Eq (2.4), the joint shear V_j can be expressed as follows:

$$V_j = T_b - V_c \quad (2.5)$$

2.4.3 Deficient Joint Failure Mechanisms

Several beam-column joint studies, such as the studies conducted by Pigni and Lowes (2003), Kim and LaFave (2007), and Hassan (2011) focused on identifying the types of failure mechanisms that can be sustained by deficient joints typical of older RC buildings. Based on these studies the following failure mechanisms were identified:

J-Type Failure

In this type of failure mechanism, the maximum shear capacity of the joint is reached without any yielding in beam or column longitudinal reinforcement (i.e. pure shear failure). This type of failure mechanism is typical of deficient beam-column joints where the adjoining beam and column are well reinforced and, hence, stronger than the joint panel itself. This means that when the shear capacity of the joint panel is reached, the corresponding forces on the beam and column are less than the flexural capacity of these members. It also means that the corresponding forces that develop in the beam anchored bars within the joint are less than those required to cause anchorage failure (i.e. bar pull-out).

BJ-Type Failure

In this type of failure mechanism, the maximum shear capacity of the joint is reached shortly after yielding is initiated in beam top or bottom longitudinal reinforcement. This type of failure can occur in cases of deficient joints where beam yielding strength is equal or slightly less than joint shear strength. When beam reinforcement yields at the column face, yield penetrates into the joint causing rapid bond deterioration within the joint which, coupled with excessive joint panel cracking, eventually leads to joint shear failure. This failure mechanism is considered more ductile than the previous *J-Type* failure (due to beam yielding). Beam-column joints sustaining such failure type are typical of strong column-weak beam connections.

P-Type Failure

In this type of failure mechanism, the maximum shear capacity of the joint is not fully developed due to bar pull-out of beam bottom reinforcement. This failure mechanism is typical of deficient beam-column joints where the anchorage of beam bottom bars within the joint is short and straight (i.e. not a hook anchorage). Under seismic excitation, when the developed forces in the beam bottom bars at the column face become larger than the bar bond strength, bar pull-out occurs (i.e. bond-slip failure).

J-Type, *BJ-Type*, and *P-Type* are the most common joint failure mechanisms sustained by deficient beam-column joint tests. Other but less common joint failure mechanisms that were reported by researchers include joint failure after column yielding (*CJ-Type*) and joint failure after beam and column simultaneous yielding (*CBJ-Type*).

2.5 KEY INFLUENCE PARAMETERS

Previous beam-column joint tests showed that the behaviour of unconfined exterior joints is affected by several key parameters; some having a direct effect and some indirect to the overall behaviour. Recent parametric studies conducted by Kim and LaFave (2007), Park and Mosalam

(2009), and Hassan (2011) tried to identify these influential parameters and quantify their effects. Each study compiled an extensive database of confined (Kim & LaFave, 2007) and unconfined (Park & Mosalam, 2009; Hassan, 2011) exterior joints which experienced shear failure with and without beam yielding (i.e. *J-Type* and *BJ-Type* failures). The studied parameters included concrete compressive strength, joint aspect ratio, column axial load, and beam reinforcement ratio. The following sub-sections summarise the findings of these studies.

2.5.1 Effect of Concrete Compressive Strength

The concrete compressive strength of the reviewed joints ranged between 19 to 89 MPa. Kim and LaFave (2007), based on their database of joint tests, concluded that the concrete compressive strength is the governing influence parameter in terms of joint shear strength. In fact, it was established that the square root of the concrete compressive strength is proportional to the joint shear stress and strain. In addition, it was found that increasing the concrete compressive strength is beneficial in terms of improving joint shear resistance, as it improves the load bearing of column and beam compression zones as well as the bond strength of beam bars within the joint area.

2.5.2 Effect of Joint Aspect ratio

For confined exterior joints with *BJ-Type* failure, Kim and LaFave (2007) found the normalised joint shear stress (and strain) to be little influenced by the beam depth to column depth ratio (h_b/h_c) when it ranges from 1.0 to 1.6 or beam width to column width ratio (b_b/b_c) when it ranges from 0.56 to 1.0. In other words, no clear relationship was established between joint aspect ratio and joint shear behaviour. Whereas, for *J-Type* failure joints, Kim and LaFave (2007) found that increasing the joint aspect ratio can cause only a slight reduction in the joint shear strength. Based on that, Kim and LaFave concluded that the ACI 352R-02 (2002) recommendations for defining the design joint shear strength based on beam to column width ratio, are rather unjustified.

On the other hand, and based on the test results of unconfined exterior joints having joint aspect ratios between 1.0 and 2.0, Wong (2005) reported that the joint aspect ratio has an inverse relationship with the joint shear strength coefficient γ [see Eq (2.1)]. A similar conclusions was drawn by Vollum and Newman (1999) and Bakir and Boduroğlu (2002) after analysing a large database of monotonic exterior joint tests.

This inverse relationship can be attributed to the fact that in the Strut-and-Tie approach (SAT), for unconfined exterior joints, the only effective resisting joint shear mechanism is the diagonal compressive strut mechanism. However, due to the nature of the formed strut, the angle of inclination has a huge impact on the effectiveness of the strut shear resistance. This means that when the joint aspect ratio is large the strut becomes steeper and, hence, its ability to equilibrate

the horizontal joint shear force is lower, which in turn means lower shear strength. Park and Mosalam (2009) and Hassan (2011) supported this observation with plots of the joint shear strength coefficient γ with the joint aspect ratio for a large set of unconfined exterior joint tests under monotonic and cyclic loadings (see Figure 2.7). After thorough inspection of the two plots, a trend of some sort can be observed for *J-Type* failure joints only. However, the observed relationship is not so definite to be signified as linearly adverse. This in turn indicates that the relationship between the joint shear strength and joint aspect ratio is dependent on other factors, such as axial load and beam and column reinforcement ratios. Therefore, more joint tests are required to investigate this relationship.

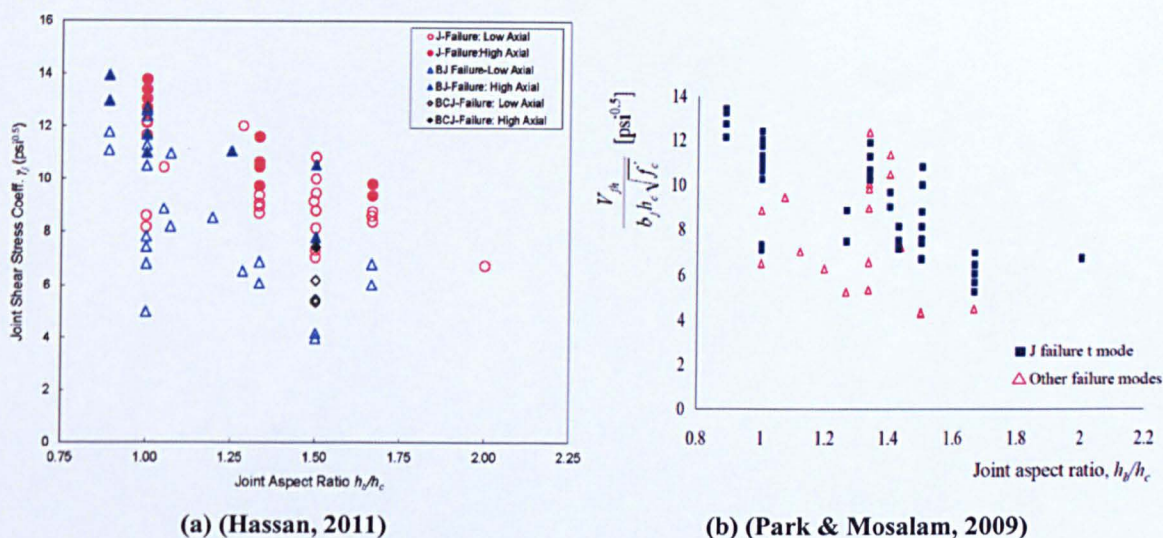


Figure 2.7 Effect of joint aspect ratio on joint shear strength coefficient γ

2.5.3 Effect of Beam Reinforcement

The relationship between the joint shear strength and beam reinforcement ratio was studied experimentally by many researchers. Research studies on unconfined interior and exterior beam-column joints conducted by Walker (2001), Alire (2002) and Wong (2005) showed that joints having identical geometries and column axial load, but different amounts of beam reinforcement, can exhibit shear failure at different levels of joint shear demand, indicating the dependency of joint shear strength on the amount of beam reinforcement. Bakir and Bodurođlu (2002), after investigating test results of unconfined exterior joints, came to the same conclusion that there is a relationship between beam reinforcement and normalised joint shear strength. On the other hand, other researchers such as Anderson et al. (2008) and Moehle (2008) assumed that joint shear strength and failure mode is defined based on the framing member flexural capacity, especially beams. Accordingly, joints with high reinforcement ratios are expected to exhibit a brittle behaviour (*J-Type* failure), whereas joints with less beam reinforcement are expected to exhibit a more ductile behaviour (*BJ-Type* failure), as beam yielding, and in turn yield penetration and bond deterioration, hinders the diagonal strut from developing its full compressive strength.

Park and Mosalam (2009) and Hassan (2011), after investigating the test results of unconfined exterior joints with *BJ-Type* failure, found the relationship between the normalised joint shear strength and the beam reinforcement ratio to be almost linearly proportional, provided other design variables are identical. This, however, is valid provided the beam bars are well anchored in the framing joints and the joint aspect ratio, as suggested by Park and Mosalam (2009), is between 0.89 and 1.33. Moreover, Park and Mosalam (2009), for the case of unconfined joints, attributed the enhancement of joint shear strength when increasing the amount of beam reinforcement to the improved bond conditions of beam bars within the joint. This improved bond is assumed to increase the transmitted shear force within the joint which in turn requires extending the compressive strut area to enable it to resist this enhanced shear force (see section 2.7.2.5 for further details).

2.5.4 Effect of Column Axial Load

The relationship between the column axial load level and the shear strength of beam-column joints is, in general, deemed to be too complex and not well defined. According to Kim and LaFave (2007), for confined joints, the column axial load has little influence on the overall joint shear behaviour (i.e. shear stress and shear strain). However, when analysing the test results of joints with weak column-strong beam design, Kim and LaFave (2007) found that increasing the column axial load somehow improves the column moment strength up to the balanced condition point (on the P-M diagram). In other words, the presence of column axial load is more favourable as it helps increase the neutral axis depth, thus reducing the stress demand on the column longitudinal reinforcement, and hence contributes towards achieving strong column-weak beam behaviour. In addition, reducing the tensile stress in the column longitudinal reinforcement within the joint delays yielding and in turn prevents bond deterioration from occurring at an early stage. The better bond conditions for both beam and column bars lead to a more effective strut mechanism in resisting shear, which means better shear strength.

For the case of unconfined exterior beam-column joints, Park and Mosalam (2009) and Hassan (2011) found the influence to be insignificant in joints where the column axial load is less than $0.2f'_cA_g$. On the other hand, for joints with higher column axial load ($>0.2f'_cA_g$), many researchers (Uzumeri, 1977; Beres et al., 1992; Clyde et al., 2000; Pantelides et al., 2002; Barnes et al., 2008; Park & Mosalam, 2009; Hassan, 2011; Park & Mosalam, 2012b) tend to describe the effect on joint shear strength and stiffness as mostly beneficial up to the point of joint shear strength, and detrimental afterwards (i.e. rapid deterioration). Therefore, more joint tests are required to investigate this relationship, especially at low levels of column axial load.

2.6 PREVIOUS EXTERIOR BEAM-COLUMN JOINT TESTS

Over the past four decades many experimental studies focused on understanding and improving the behaviour of beam-column joints under seismic excitations. However, only a limited number of these studies highlighted the behaviour of deficient exterior joints and provided shear stress-shear strain data that can be utilised for developing new shear models. This section summarises all previous research projects which included tests of isolated unconfined RC exterior beam-column joints (i.e. no transverse beams or slab). All reported tests exhibited either joint shear failure (J-Type failure) or shear failure after beam reinforcement yielding (BJ-Type failure). In addition, specimens failing primarily due to anchorage failure (bar pull-out) are not included.

2.6.1 Hanson and Connor (1967)

The first experimental study investigating the seismic behaviour of RC beam-column joints was conducted by Hanson and Connor (1967). Seven exterior beam-column joints were tested, among which only two were with no joint transverse reinforcement; specimen V and specimen VA. Test variables included joint shear reinforcement ratio, column axial load and column cross section.

Specimen V experienced joint shear failure with no reinforcement yielding, whereas in specimen VA beam reinforcement yielded, but no failure mechanism was observed. The applied axial load level was $0.86f_c A_g$ for specimen V and $0.54f_c A_g$ for specimen VA. Based on these test results, it was concluded that joint shear links must be provided in isolated exterior beam-column joint and corner joints in order to insure a satisfactory shear resistance.

2.6.2 Uzumeri (1977)

Uzumeri (1977) conducted a study at the University of Toronto, in which three unconfined beam-column joints were tested. Two of the specimens (SP1 & SP2) were corner joints with a transverse beam, whereas the third specimen (SP5) was an isolated exterior joint. The dimensions and reinforcement detail were the same for all specimens. In addition, in all specimens the column was subjected to a constant axial load level of 520 Kips or $0.48f_c A_g$.

All three specimens exhibited joint shear failure after beam reinforcement yielding (BJ-Type failure). The observed damage at failure included total exposure and buckling of column bars within the joint area, whereas the beam, apart from a limited initial yielding, remained intact. Figure 2.8 shows the cyclic load-deflection response curve for one of the tested specimens. In general, the three specimens behaved similarly, as no clear confinement effect of the added transverse beams was observed. In addition, based on the test results, Uzumeri (1977) concluded the following: a) loading history has a significant effect on stiffness, but no effect at all on the strength of beam-column joints; b) large axial compressive force can be helpful at the early stages before reaching the maximum strength, and detrimental at the later stages; c) in nonlinear

structural analysis of RC frame buildings the assumption of rigid beam-column connection can yield invalid results.

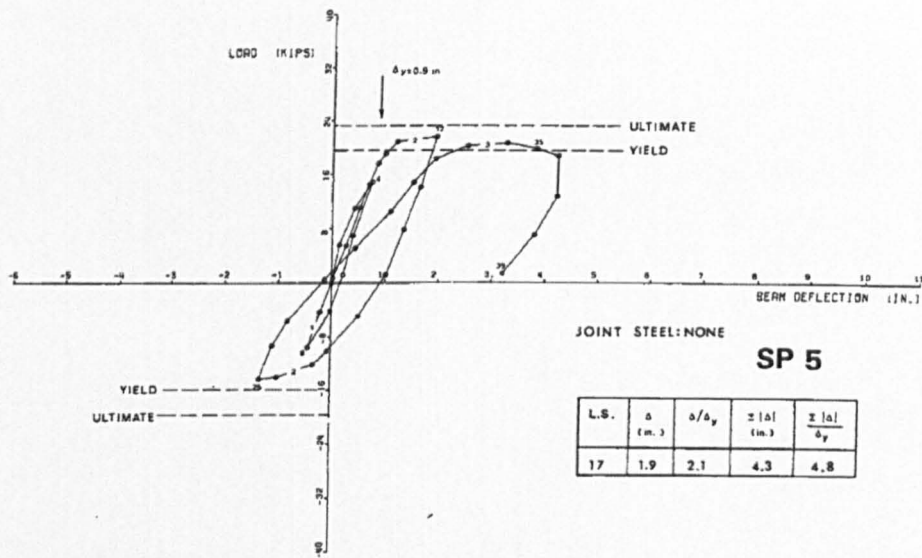


Figure 2.8 Cyclic load-beam tip displacement response curve of specimen SP5 (Uzumeri, 1977)

2.6.3 Clyde et al. (2000)

Clyde et al. (2000) conducted a study at the University of Utah, in which four half-scale RC exterior beam-column joints with no shear links and inadequate beam bar anchorages were tested. The main aim of the study was to investigate the behaviour of joints typically found in 1960s frame buildings in a shear critical condition. Beam and columns were well designed in order to force the joint specimens to fail in shear (i.e. J-Type failure). All four specimens had the same detailing and dimensions, as can be seen in Figure 2.9.

The column was subjected to two axial load levels $0.1f_c A_g$ and $0.25f_c A_g$, and the concrete compressive strength ranged between 37.0 and 46.2 MPa. The tests were performed using a loading frame in which the column was placed horizontally. Cyclic loads were applied at the end of the beam while axial loads were applied to the end of the column (see Figure 2.9).

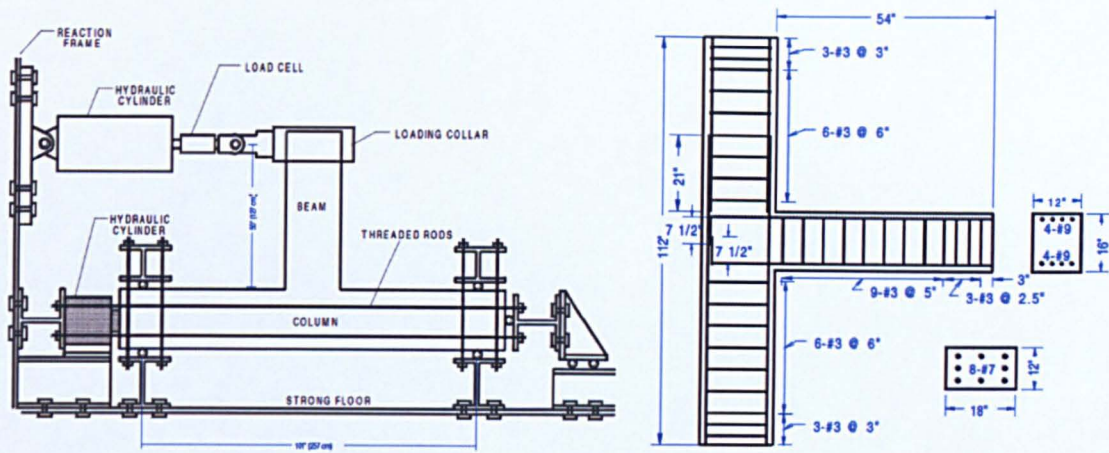


Figure 2.9 Test setup and specimen dimensions (Clyde et al., 2000)

All joint specimens failed in shear after yielding of beam longitudinal bars. Increasing column axial load from $0.1f_c A_g$ to $0.25f_c A_g$ caused the joint shear strength to increase by 8% and the principal tensile stress by 50%. On the other hand, the displacement ductility of the $0.1f_c A_g$ specimens was 1.5 times higher than that of the other specimens.

2.6.4 Pantelides et al. (2002)

In a similar manner, Pantelides et al. (2002) conducted a study at the University of Utah, in which six full-scale RC exterior beam-column joints with no shear reinforcement were tested under cyclic loading. The adopted design of the specimens represented buildings designed before the 1970, which are known to have serious structural deficiencies. In order to evaluate the effect of column axial load, two levels were used, $0.1f_c A_g$ and $0.25f_c A_g$.

The beam and columns were designed with sufficient flexural and shear strength to ensure a J-Type failure in the joint. All six specimens had the same dimensions; however three different types of beam bottom reinforcement were used (Figure 2.10). The beam top longitudinal bar, in all specimens, ended with a 180° hook. In the first two specimens (units 1&2), beam bottom bars extended (15.25 cm) into the joint from the face of the column which resulted in an overlap of (6.35 cm) between top and bottom bars. In the second group of specimens (units 3&4), bottom bars extended (35.56 cm) from the face of the column. Finally, in the last two specimens (units 5&6), a 180° hook was used for both bottom and top bars. The concrete compressive strength was about 31.9 MPa for all specimens. The tests were performed using a loading frame in which the column was mounted vertically. Cyclic loads were applied at the end of the beam while axial loads were applied to the end of the column. Two different levels of column axial load were used, $0.1f_c A_g$ and $0.25f_c A_g$.

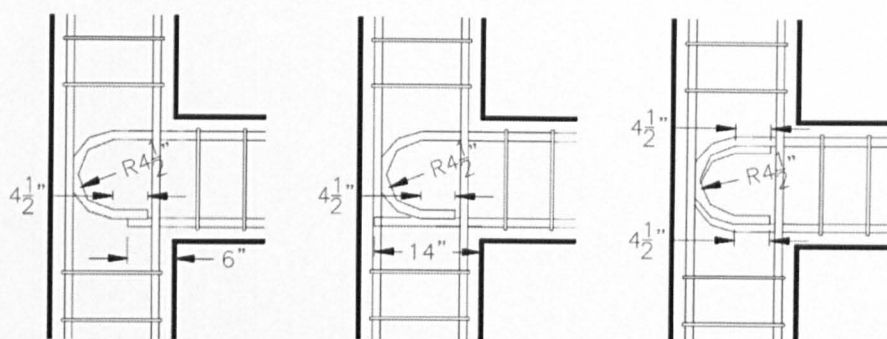


Figure 2.10 Reinforcement details of the specimens (Pantelides et al., 2002)

Based on the test results, Pantelides et al. (2002) concluded that joints with substandard details exhibit either bond slip failure, or joint shear failure. The first two specimens with the short bottom beam bar anchorage exhibited bond-slip failure, whereas the remaining specimens sustained joint shear failure after reinforcement yielding. Increasing column axial load from $0.1f_c A_g$ to $0.25f_c A_g$ enhanced the joint shear strength by 35% for the short anchorage specimen, whereas the enhancement was only 15% for the other two anchorage types. Similarly, the increased axial load increased the principal tensile stress in the joint by 117% for the short anchorage and by 69% for the other specimens. However, higher axial load was found to be detrimental in terms of energy dissipation and displacement ductility. No major differences were found between specimens of the second and the third reinforcement detailing. Joints with shear failure exhibited axial failure at the end of the test.

2.6.5 Ghobarah and Said (2001)

Ghobarah and Said (2001) conducted an experimental study, at the University of McMaster, to evaluate the nonlinear behaviour of non-ductile RC exterior beam-column joints with and without FRP strengthening. All specimens were full-scale isolated exterior joints with no shear reinforcement within the joint area and with 90° hooks bent into the joint at the end of beam top and bottom reinforcement. Two of the specimens (T1, T2) were tested as control specimens in bare condition (i.e. without strengthening). Both specimens were tested under cyclic loading. The applied column axial load on specimen T1 and specimen T2 was $0.19f_c A_g$ and $0.1f_c A_g$, respectively.

Both specimens sustained joint shear failure after limited yielding in the beam reinforcement. The joint core was severely damaged and cracks extended to the top and bottom columns. The overall joint behaviour of the joint was brittle, as a significant degradation in strength occurred at ductility factor of 2, whereas at 2.5 ductility factor the strength of the specimen had dropped to only 30% of the maximum sustained strength by the specimen. Increasing column axial load from $0.1f_c A_g$ to $0.19f_c A_g$ enhanced the joint shear strength by 15%. Figure 2.11 shows the reinforcement details and the cyclic load-beam tip displacement response curve of specimen T1.

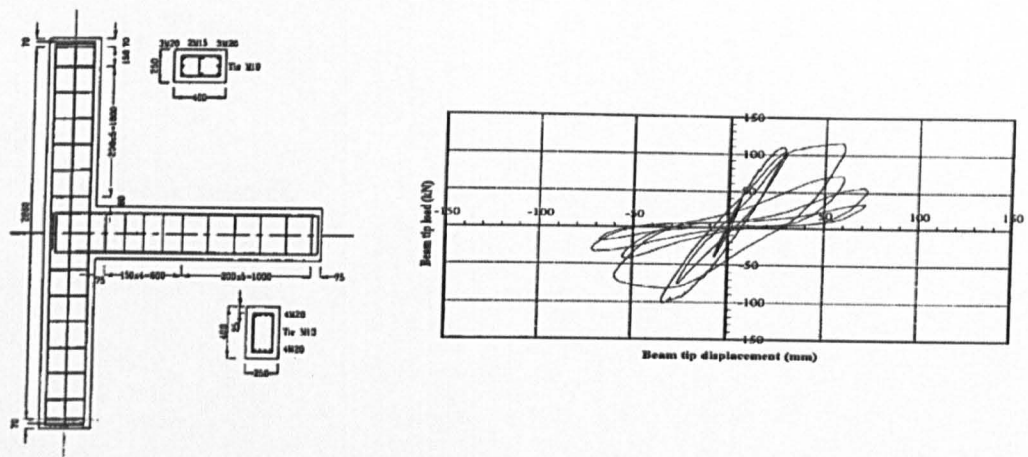


Figure 2.11 Reinforcement details and cyclic load-beam tip displacement response curve of specimen T1 (Ghobarah & Said, 2001)

2.6.6 Antonopoulos and Triantafillou (2003)

Antonopoulos and Triantafillou (2003) carried out an experimental study at the University of Patras to investigate the effectiveness of FRP strengthening to enhance the shear capacity of shear critical RC exterior beam column joints. A total of 18 specimens were tested, two of which were tested in bare condition as control specimens, specimen C1 and specimen C2. Both control specimens were 2/3 scale RC T-beam-column joints with no joint shear reinforcement and 90° hooks for the beam reinforcement. The applied column axial load was 46kN, equating to $0.06f_c A_g$ and $0.05f_c A_g$ for specimen C1 and specimen C2, respectively. As designed, both specimens sustained joint shear failure without any reinforcement yielding (i.e. J-Type failure), see Figure 2.12. The observed damage was typical x-shaped with diagonal cracks extending to the top and bottom columns.

In general, the study highlighted the shear vulnerability of unconfined exterior joints. In addition, it was found that transverse beams and transverse reinforcement can enhance the shear capacity of such joints by an average of 9% and 16%, respectively.

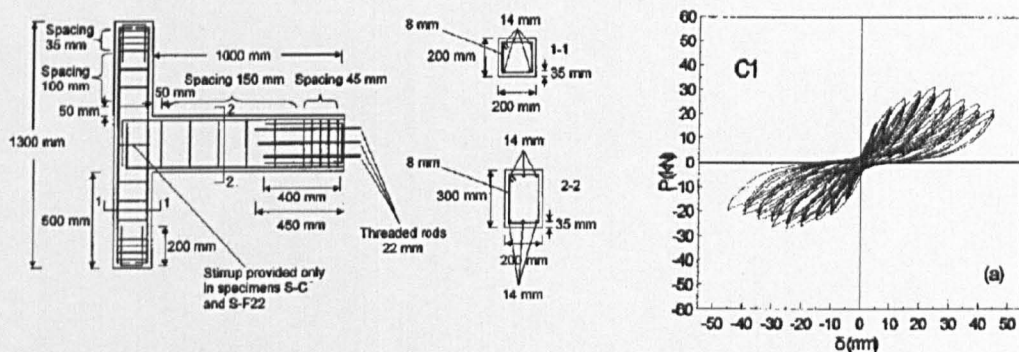


Figure 2.12 Reinforcement details and measured response of specimen C1 (Antonopoulos & Triantafillou, 2003)

2.6.7 Wong (2005)

Wong (2005) conducted a study at the University of Science and Technology, Hong Kong, in which 12 full-scale RC exterior beam-column joints with no transverse reinforcement were tested (see Figure 2.13). The study investigated the seismic performance of deficient exterior beam-column joints in terms of the effect of column intermediate longitudinal bars, column lap splice, axial load level, beam depth to column depth ratio, and beam reinforcement anchorage.

Two axial load levels were investigated $0.03f_c A_g$ and $0.15f_c A_g$, and the concrete compressive strength ranged between 28 and 46 MPa. The tests were performed using a loading frame in which the columns were placed horizontally.

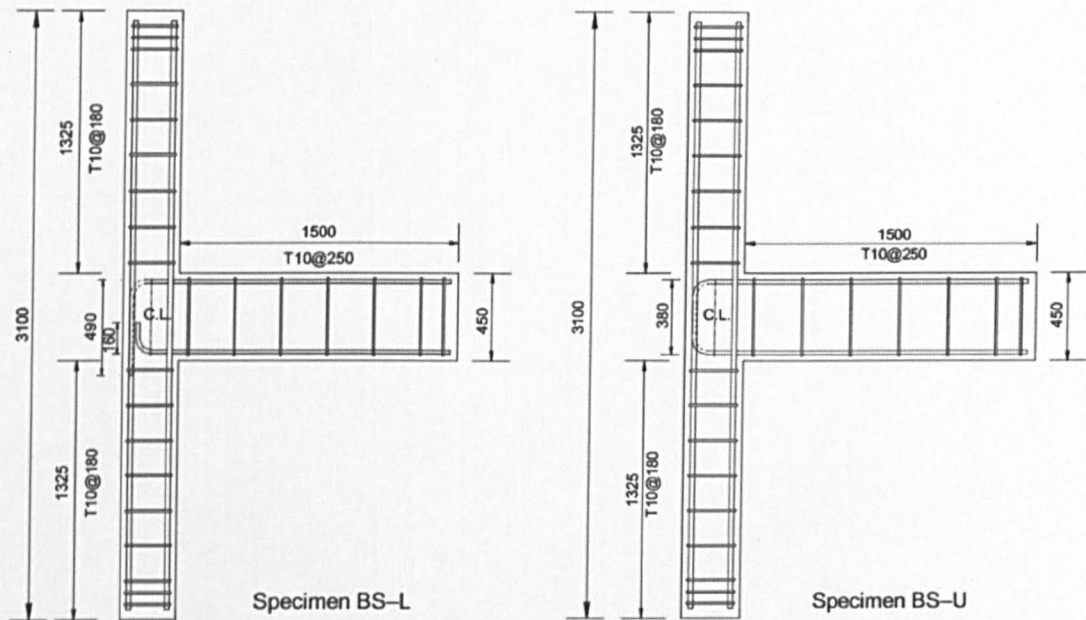


Figure 2.13 Dimensions and detailing of unconfined exterior joints (Wong, 2005)

The specimens exhibited two types of failure; joint shear failure with no reinforcement yielding (*J-Type* failure) was observed in nine specimens, whereas the remaining three specimens exhibited shear failure after reinforcement yielding (*BJ-Type* failure). Increasing column axial load from $0.03f_c A_g$ to $0.15f_c A_g$ was found to enhance the joint shear strength by a mere 4%. On the other hand, the effect of increasing the beam depth, h_b resulted in inconsistent results, as in one group of specimens increasing h_b showed no change in joint shear strength, whereas in another group it resulted in a decrease of 46%. The effect of intermediate column longitudinal bars was found to be beneficial to a certain extent, as adding 4T10 to the column increased joint shear strength by 24%, whilst adding 8T10 resulted in an increase of only 33%. On the other hand, no change was observed in the specimen with column lap splice, as joint shear failure occurred at an early stage.

2.6.8 Karayannis et al. (2008)

Karayannis et al. (2008) conducted an experimental study at University of Thrace to evaluate the seismic performance of non-ductile RC exterior beam-column joints strengthened with thin RC jackets. A total of 10 specimens were tested, three of which had no reinforcement in the joint area and were tested as control specimens, specimens A0, B0, and C0, as shown in Figure 2.14. The concrete compressive strength for all specimens was 31.6 MPa and the column axial load was $0.05f_c A_g$. Other test parameters included: amount of shear reinforcement in the joint area, joint aspect ratio, and amount of column intermediate longitudinal bars.

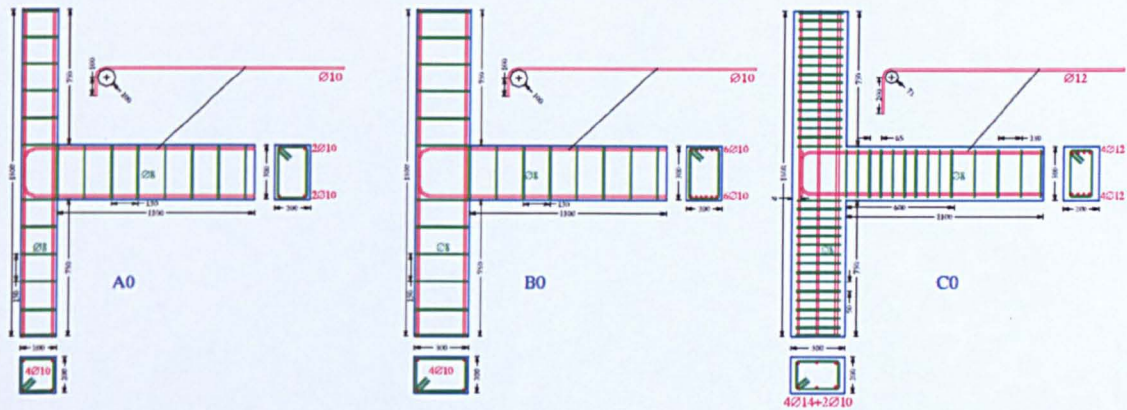


Figure 2.14 Dimensions and reinforcement details of control specimens (Karayannis et al., 2008)

All control specimens sustained joint shear failure after yielding in beam reinforcement (BJ-Type failure). The observed damage was concentrated in the joint area (x-shaped diagonal cracks) and also extended to top and bottom columns, especially in specimens A0 and C0. Based on the test results, it was concluded, similarly to previous research projects, that the increase of variables such as column depth, column intermediate longitudinal bars, and column axial load can enhance the joint shear capacity of deficient RC exterior beam-column joints.

2.7 ANALYTICAL JOINT STRENGTH MODELS

Over the years, many analytical joint strength models were proposed. The main focus of the majority of these models was to represent the nonlinear behaviour of well-designed beam-column joints. However, some of these models include special provisions that extend their applicability to include exterior beam-column joints with no joint shear reinforcement. This section reviews existing strength models that can be used for shear-critical exterior beam-column joints. In addition, this section presents a summary of the limitations and the applicability of spring-based joint models that were developed for the purpose of RC frame simulations.

2.7.1 ASCE/SEI 41 JOINT STRENGTH

2.7.1.1 Joint Shear Strength

The ASCE/SEI 41 (2006) provisions provide a simple and practical approach to predict the nominal joint shear strength taking into account the joint geometry and the joint shear reinforcement ratio. These provisions have been widely used to evaluate the shear strength of older buildings beam-column joints (Park & Mosalam, 2012b). The nominal joint shear strength, V_n , is defined according to ASCE 41 as follows:

$$V_n = \lambda \gamma \sqrt{f'_c} A_j \text{ psi} \quad (2.6)$$

where λ is taken as 1 for normal weight aggregate concrete, γ (as defined in Table 6-10 in ASCE 41) is the joint shear strength coefficient and can be calculated by normalising the joint shear stress v_j as follows:

$$\gamma = \frac{v_j}{\sqrt{f'_c}} \quad (2.7)$$

The effective joint area A_j , can be defined as follows

$$A_j = b_{je} h_j \quad (2.8)$$

where h_j is the joint depth which is equal to the column depth h_c and b_{je} is the joint effective width (see Figure 2.5), as defined by ACI 318-08 (2008).

According to ASCE 41 Table 6-10, the joint shear strength coefficient γ is 6 ($\sqrt{\text{psi}}$) or 0.5 ($\sqrt{\text{MPa}}$) for exterior joints without transverse beams and with a volumetric ratio of transverse reinforcement within the joint area of less than 0.3%. However, the same strength applies for corner joints (i.e. exterior joints with one transverse beam). In addition, the ASCE 41 provisions do not account for the amount of beam reinforcement or the type of beam bar anchorage within the joint. Based on this, the joint shear strength of two identical joints but with different beam bar anchorage, such as a standard hook and straight bar, is the same.

2.7.1.2 ASCE 41 Joint Shear Stress-Strain Envelope

Figure 2.15 shows the generalised load-deformation envelope curve proposed by ASCE 41 and ACI 369R-11 to describe the shear stress-shear strain of beam column joints in nonlinear conditions.

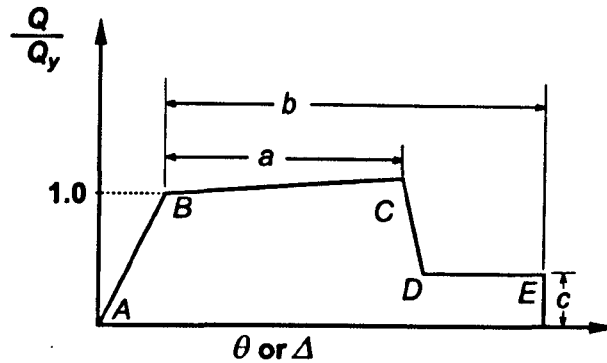


Figure 2.15 General nonlinear load-deformation envelope for beam-column joints, (ASCE/SEI 41, 2006) and (ACI 369R, 2011)

The model parameters denoted in Figure 2.15 can be calculated following the procedure outlined in ASCE 41, Table 6-9.

Park and Mosalam (2012b) and Hassan (2011) evaluated the predictions of the ASCE 41 joint shear strength approach against a large data set of unconfined exterior and corner beam-column joints. The approach was found to be over-conservative and produces unrealistic results in terms of strength degradation. Further evaluation of the joint shear strength model and the shear stress-strain envelope of the ASCE 41 provisions is provided in Chapter 4.

2.7.2 Strut-and-Tie Joint Models

2.7.2.1 Hwang and Lee Model

Hwang and Lee (1999) proposed a method named “Softened Strut-and-Tie Model (SST)” to predict the shear strength of isolated exterior beam-column joints. This model was developed with emphasis on confined exterior beam-column joints, in which joint hoops and column intermediate longitudinal reinforcement are present. The model was derived based on the Strut-and Tie concept by satisfying not only the stress equilibrium within the joint but also strain compatibility and material constitutive laws at ultimate loading stage (i.e. cracked reinforced concrete section). According to the SST model, the joint shear force is resisted by three basic mechanisms; diagonal strut mechanism, horizontal mechanism (horizontal tie plus two inclined struts), and vertical mechanism (column intermediate longitudinal bar and two struts), as shown in Figure 2.16.

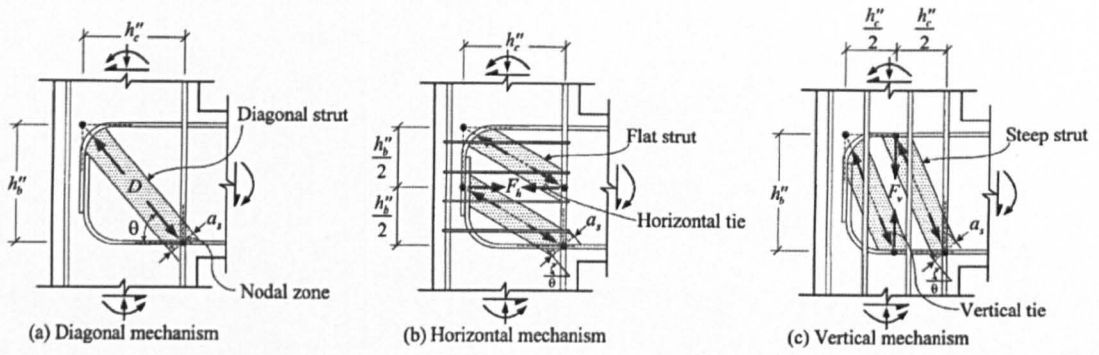


Figure 2.16 The proposed joint shear resisting mechanisms of SST model (Hwang & Lee, 1999)

The area of the diagonal strut is

$$A_{str} = a_s b_s \quad (2.9)$$

The strut depth b_s is taken as the joint effective width b_j as defined by ACI 318-95 (1995). The diagonal strut depth a_s is taken as the depth of the column compression zone a_c , based on the assumption that the compression zone depth in beams with yielding reinforcement is negligible. Therefore, this initial assumption limits the applicability of this model to only exterior beam-column joints where yielding of beam reinforcement occurs prior to joint shear failure. The column compression zone depth a_c is approximated by Eq (2.10), as proposed by Paulay and Priestley (1992).

$$a_c = (0.25 + 0.85 \frac{N}{f_c' A_g}) h_c \quad (2.10)$$

From force equilibrium, the horizontal joint shear force, V_{jh} , is

$$V_{jh} = D \cos \theta + F_h + F_v \cot \theta \quad (2.11)$$

D is the diagonal strut compression force, F_h and F_v are the tension force in the horizontal tie and vertical tie, respectively. The diagonal strut angle θ is calculated based on the joint aspect ratio and reinforcement details as follows:

$$\theta = \tan^{-1} \left(\frac{h_b''}{h_c''} \right) \quad (2.12)$$

where h_b'' is the distance between the top and bottom beam bars and h_c'' is the distance between the column inner bar and the end of the beam 90° hook anchorage, as shown in Figure 2.16.

Based on the diagonal strut angle, the ratios of the joint horizontal shear V_{jh} assigned to each of the three resisting mechanisms is defined as follows:

$$D \cos \theta = \frac{R_d}{(R_d + R_h + R_v)} \times V_{jh} \quad R_d = \frac{(1 - \gamma_h)(1 - \gamma_v)}{1 - \gamma_h \gamma_v} \quad (2.13.a)$$

$$F_h = \frac{R_h}{(R_d + R_h + R_v)} \times V_{jh} \quad R_h = \frac{\gamma_h(1 - \gamma_v)}{1 - \gamma_h \gamma_v} \quad (2.13.b)$$

$$F_v \cot \theta = \frac{R_v}{(R_d + R_h + R_v)} \times V_{jh} \quad R_v = \frac{\gamma_h(1 - \gamma_v)}{1 - \gamma_h \gamma_v} \quad (2.13.c)$$

$$\gamma_h = \frac{2 \tan \theta - 1}{3} \quad \gamma_v = \frac{2 \cot \theta - 1}{3} \quad (2.13.d)$$

where R_d , R_h , and R_v are the shear ratios of the diagonal, horizontal, and vertical mechanisms, respectively (see Figure 2.17).

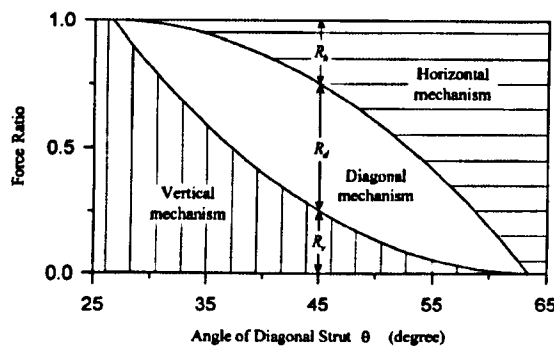


Figure 2.17 Joint shear distribution among resisting mechanisms of SST model (Hwang & Lee, 1999)

The joint shear strength is reached when the bearing stress of the nodal zone where the forces from the three mechanisms meet is reached. The maximum compressive stress acting on the outer nodal zone of the diagonal compressive strut is given as follows:

$$\sigma_{d,max} = \frac{1}{A_{str}} \left\{ D + \frac{\cos\left(\theta - \tan^{-1}\left(\frac{h_b''}{2h_c''}\right)\right)}{\cos\left(\tan^{-1}\left(\frac{h_b''}{2h_c''}\right)\right)} F_h + \frac{\cos\left(\tan^{-1}\left(\frac{2h_b''}{h_c''}\right) - \theta\right)}{\sin\left(\tan^{-1}\left(\frac{2h_b''}{h_c''}\right)\right)} F_v \right\} \quad (2.14)$$

The strength of the concrete diagonal strut is estimated based on the softening concrete model (see Figure 2.18) proposed by Belarbi and Hsu (1995) as follows:

$$\sigma_d = \xi f'_c \left[2 \left(\frac{\varepsilon_d}{\xi \varepsilon_o} \right) - \left(\frac{\varepsilon_d}{\xi \varepsilon_o} \right)^2 \right] \text{ for } \frac{\varepsilon_d}{\xi \varepsilon_o} \leq 1 \quad (2.15.a)$$

$$\xi = \frac{5.8}{\sqrt{f'_c}} \frac{1}{\sqrt{1 + 400\varepsilon_r}} \leq \frac{0.9}{\sqrt{1 + 400\varepsilon_r}} \quad (2.15.b)$$

$$\varepsilon_o = -0.002 - 0.001 \left(\frac{f'_c - 20}{80} \right) \text{ for } 20 \leq f'_c \leq 100 \text{ MPa} \quad (2.15.c)$$

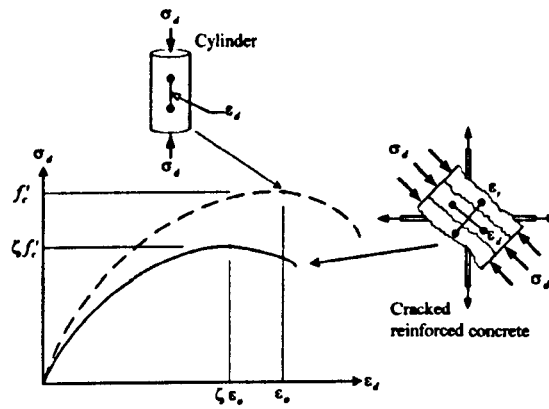


Figure 2.18 Concrete constitutive model (Hwang & Lee, 1999)

According to the STT model, the joint shear capacity is reached when the compressive stress and strain of the diagonal strut become as follows

$$\sigma_d = \xi f'_c \quad \text{and} \quad \varepsilon_d = \xi \varepsilon_o \quad (2.16)$$

The steel reinforcement constitutive law is elastic-perfectly-plastic (i.e. with no tension stiffening) and is formulated as follows:

$$f_s = E_s \varepsilon_s \quad \text{for } \varepsilon_s < \varepsilon_y \quad (2.17.a)$$

$$f_s = f_y \quad \text{for } \varepsilon_s \geq \varepsilon_y \quad (2.17.b)$$

Based on Eq (2.17), the relationship between forces and strains of the vertical and horizontal tension ties is formulated as follows:

$$F_h = A_{th} E_s \varepsilon_h \leq F_{yh} \quad (2.18.a)$$

$$F_v = A_{tv} E_s \varepsilon_v \leq F_{yv} \quad (2.18.b)$$

Accepting the principal compressive stress predetermined direction, the two-dimensional compatibility strain condition (see Figure 2.19) relates the average strains in the joint panel as follows:

$$\varepsilon_r = \varepsilon_h + (\varepsilon_h - \varepsilon_d) \cot^2 \theta \quad (2.19.a)$$

$$\varepsilon_r = \varepsilon_v + (\varepsilon_v - \varepsilon_d) \tan^2 \theta \quad (2.19.b)$$

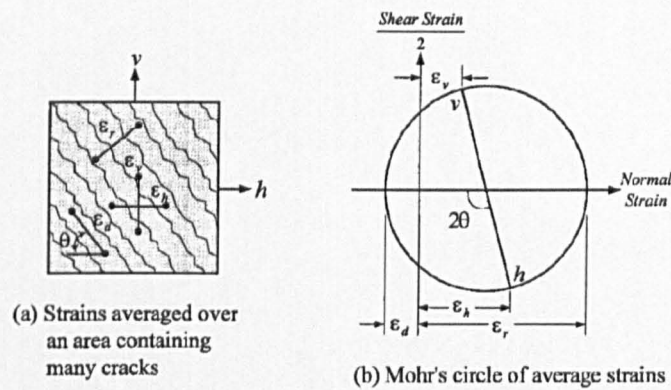


Figure 2.19 Compatibility conditions of cracked concrete (Hwang & Lee, 1999)

The joint shear strength is calculated using an iterative solver. The iterative solver calculates the joint capacity by controlling the softening coefficient based on the strain state in the vertical and the horizontal ties. For unconfined exterior joints, one of the ties is ignored whereas the other is considered yielding. Therefore, this model is not able to predict the joint shear capacity when no yielding occurs before failure. A detailed evaluation of the applicability of the solution algorithm of this model to shear-critical exterior beam-column joints is provided in Chapter 5.

2.7.2.2 Vollum Model

Vollum (Vollum & Newman, 1999) developed a Strut-and-Tie model to predict the shear capacity of RC exterior beam-column joints with and without transverse reinforcement (see Figure 2.20). The dimensions of the top and bottom nodes at the end of the diagonal compressive strut are defined based on beam and column bar forces and widths of concrete compression zones.

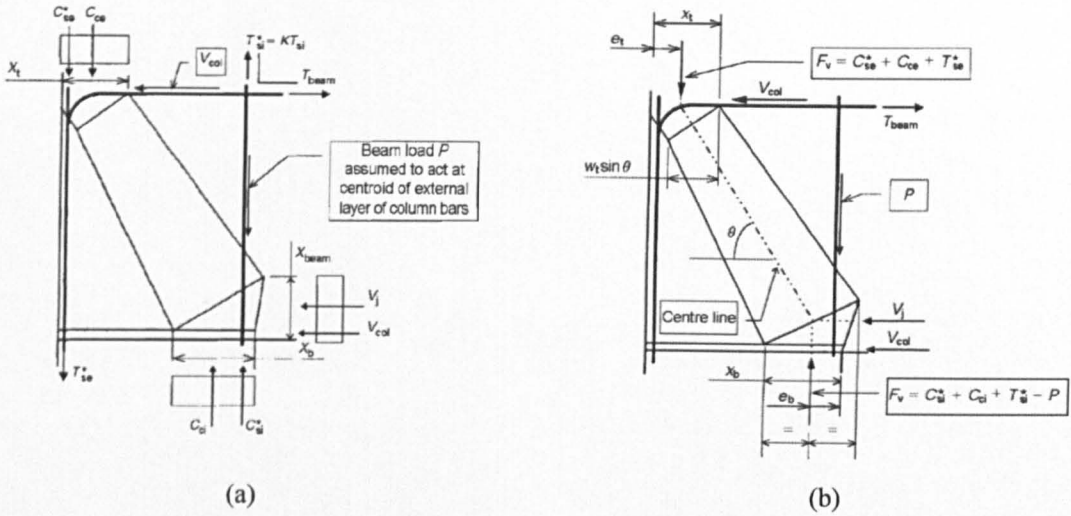


Figure 2.20 SAT model for exterior beam-column joints without stirrups a) boundary forces; b) geometry (Vollum & Newman, 1999)

According to the model, joint shear failure initiates around the top node when the strut compressive strength is reached. The maximum concrete compressive stress σ_d acting on the outer nodal zone of the diagonal strut is

$$\sigma_d = f[2(\varepsilon_2/\varepsilon'_c) - (\varepsilon_2/\varepsilon'_c)^2] \tag{2.20}$$

where ε_2 is the concrete principal tensile strain, ε'_c is the concrete compressive strain in the diagonal strut; and f is estimated based on the softening concrete model proposed by Collins and Mitchell (1991) as follows:

$$f = \frac{f'_c}{0.8 - 0.34(\varepsilon_1/\varepsilon'_c)} < f'_c \tag{2.21.a}$$

$$\varepsilon_1 = \varepsilon_t + (\varepsilon_t - \varepsilon'_c) \cot^2 \theta \tag{2.21.c}$$

where ε_1 is the concrete principal compressive strain, ε_t is the tensile strain in the transverse direction (stirrup).

For joints with no stirrups, ε_t at failure is assumed to be 0.003, which is equivalent to typical yield strain ε_y of high strength reinforcement. Based on previous analysis of exterior beam-column joint tests, Vollum and Newman (1999) found that the shear strength of joints with no stirrups is proportional to $\sqrt{f'_c}$. Moreover, in Eq (2.20) and Eq (2.21.a), ε'_c is assumed to be -0.002 when the maximum compressive stress is reached (i.e. strut failure). Given these assumptions, Eq (2.21.a) can be modified as follows:

$$f = \frac{5.92\sqrt{f'_c}}{0.8 + 170\varepsilon_1} < f'_c \quad (2.22)$$

The joint shear strength V_j calculated at the top node is formulated as follows:

$$V_j = b_e w_t \sigma_d \cos \theta \quad (2.23)$$

where b_e is the effective joint width and w_t is the strut width at the top node.

Vollum and Newman (1999) acknowledged the difficulty of establishing the forces and concrete compression zones at the joint boundaries. Therefore, to make this feasible, forces in concrete and reinforcement at the joint boundaries were calculated from conventional section analysis (using Euler–Bernoulli assumption that plane sections remain plane), and by using concrete rectangular stress blocks, as defined in Eurocode 2 (BSI, 1992), at a maximum stress of $0.85f'_c(1 - f'_c/250)$. In addition, the column axial force was taken as zero.

To further simplify the procedure of determining the strut width, Vollum and Newman calibrated the proposed model based on test results, reported by Reyes (1993), of exterior joints with no stirrups that failed in shear. The calibration process was performed at the top column by multiplying the inner bar tensile force T_{si} by a factor $K (>1)$. Equilibrium was established with each new K value by only adjusting the width of the concrete stress block and not the tensile force of the outer bar. The resulting strut width from calibration is

$$w_t = 0.4 h_c / \sin \theta \quad (2.24)$$

The proposed function of $h_c / \sin \theta$ in Eq (2.24) takes into account the observed reduction in joint shear strength with joint aspect ratio. Furthermore, three methods were investigated to study the effect of adjusting column bar forces on the predicted joint shear strength when the strut width is $0.4 h_c / \sin \theta$. The difference between the three methods was found to be small. However, due to its simplicity and accuracy, the method in which equilibrium is found by only adjusting the tensile force in the inner bar was adopted.

The proposed model managed to predict the joint shear strength of previous monotonic exterior joint tests with good accuracy. However, Vollum and Newman (1999) believed that a simple strut-and-tie model does not offer a realistic representation of the complex behaviour of beam-column joints. This is due to the difficulties that accompany developing a strut-and-tie joint model, in terms of defining node dimensions and strut width as well as establishing the neutral axes and determining the forces in the column longitudinal bars at the joint interface. For these reasons, Vollum and Newman (1999) further simplified their SAT model and developed an empirical joint strength model, in which beam anchorage detail and joint aspect ratio are

considered as the main influence parameters. The model was developed to predict the shear strength of exterior beam-column joints with and without transverse reinforcement. The joint shear strength of unconfined exterior joints is given as follows:

$$V_j = 0.624\beta(1 + 0.555(2 - h_b/h_c))b_e h_c \sqrt{f'_c} \quad (2.25)$$

where V_j , as before, is the joint shear strength and β is a factor taking into account the beam anchorage detail and is taken as 1.0 for hooked bars (L bars) and 0.9 for U bars.

Vollum and Newman (1999) recommended using their simplified empirical model when a simple design procedure is required for exterior beam-column joints with and without transverse reinforcement. Park and Mosalam (2009) and Hassan (2011) evaluated the accuracy of this simplified model against a large database of shear-critical unconfined exterior beam-column joints tested under cyclic loading, as shown in Figure 2.21.

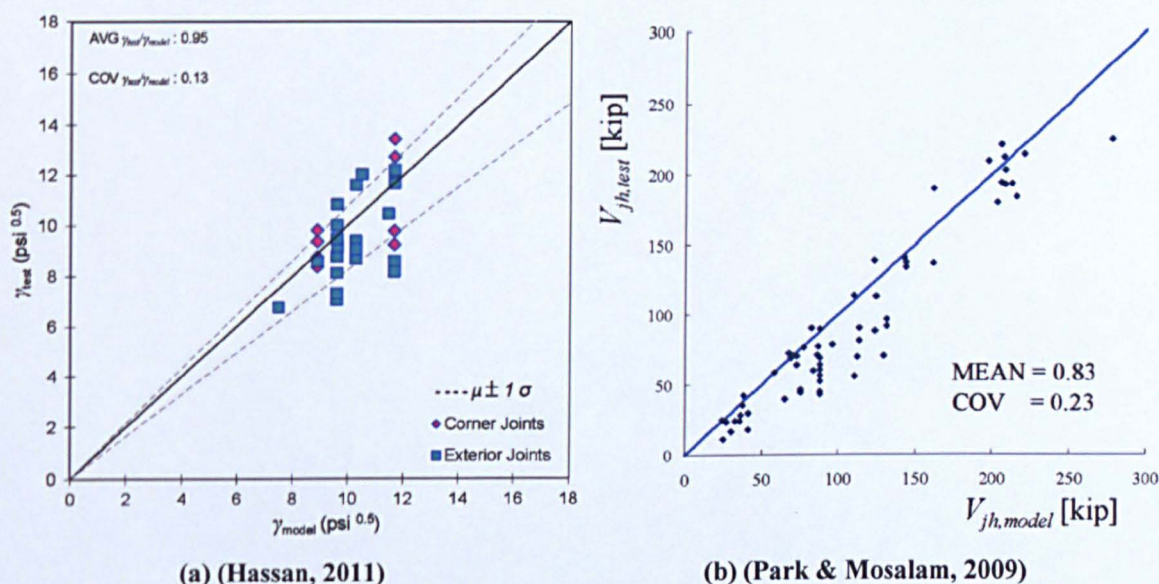


Figure 2.21 Assessment of the simplified empirical model proposed by Vollum and Newman (1999) for unconfined exterior beam-column joints (Notes: 1 Ksi = 6.90 MPa; 1 Kip = 4.45 kN)

As can be seen, the model, in general, predicted with good accuracy the shear strength of the joints used in their databases. Hassan (2011) argued that the adopted detrimental effect of the joint aspect ratio, which is taken as a 25% linear reduction of the joint shear strength when the joint aspect ratio changes from 1 to 2, is based on the test results of monotonic exterior beam-column joints and therefore might not be applicable to exterior joint tested under cyclic loading or joints with higher axial load levels. Hassan (2011) also acknowledged that the model does not account for column axial load of unconfined exterior beam-column joints, whereas the model for confined joints addresses this issue by introducing a factor $\alpha = 0.2$. Furthermore, Park and Mosalam (2009) found the joint shear strength predictions of the model to be accurate for exterior joints exhibiting *J-Type* failure and overestimating for exterior joints exhibiting *BJ-*

Type failure. Park and Mosalam (2009) attributed this to the lack of the effect of beam reinforcement ratio in the model, especially since the shear strength of *J-Type* failure joints is little influenced by the beam reinforcement ratio in comparison to *BJ-Type* failure joints.

Further evaluation of the accuracy and applicability of this simplified model to unconfined exterior beam-column joints with different beam anchorage details including straight bars is provided in Chapter 5.

2.7.2.3 Tsonos Model

Tsonos (1999; 2007; 2008) proposed a new model to predict the ultimate shear strength of RC exterior beam column joints. The model assumes joint shear is resisted by two mechanisms; a diagonal compressive strut and truss mechanism, as shown in Figure 2.22.

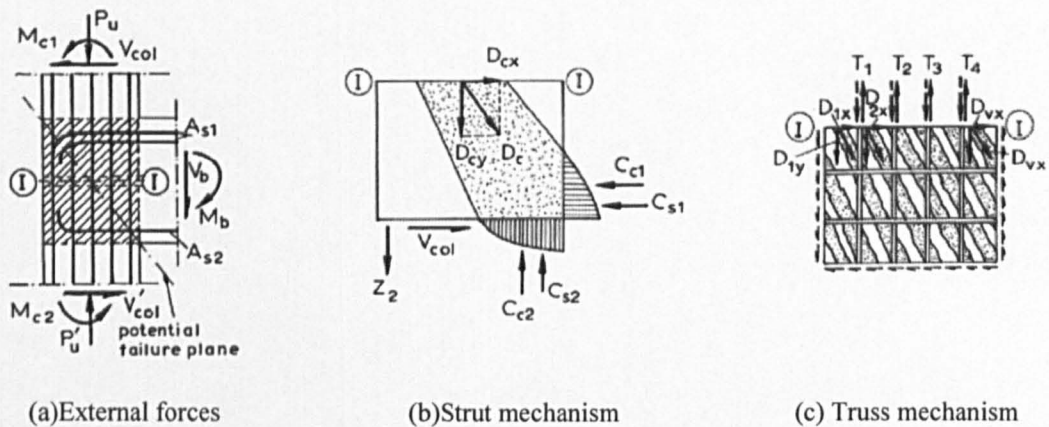


Figure 2.22 Strut and truss shear resisting mechanisms of exterior beam-column joints (Tsonos, 2008)

Given these assumptions, joint shear strength is measured by the maximum concrete strength of the joint panel under biaxial loading. Moreover, at the joint mid-height section (I-I), the two proposed mechanisms are assumed to generate vertical and horizontal forces equal and opposing to the vertical and horizontal shear forces acting on the joint as follows:

$$D_{cy} + (T_1 + T_2 + \dots) = D_{cy} + D_{sy} = V_{jv} \quad (2.26)$$

$$D_{cx} + (D_{1x} + D_{2x} + \dots) = D_{cx} + D_{sx} = V_{jh} \quad (2.27)$$

where D_{cx} , D_{cy} are components of the compression strut force, and T_i , D_{ix} are the tension and compression forces that develop in the truss mechanism, see Figure 2.22 (a & b).

The stress state at the mid-height joint section (I-I), can be expressed by the uniformly distributed shear stress τ and the normal compressive stress in the vertical direction σ as follows:

$$\sigma = \frac{D_{cy} + D_{sy}}{h_c' b_c'} = \frac{V_{jv}}{h_c' b_c'} \quad (2.28.a)$$

$$\tau = \frac{V_{jh}}{h_c' b_c'} \quad (2.28.c)$$

where h_c' , h_b' are the dimensions of the joint core.

From Eq (2.28) and based on joint aspect ratio $\alpha = h_b/h_c$, the relationship between the normal compressive stress σ and the average joint shear stress τ is expressed as follows:

$$\sigma = \frac{V_{jv}}{V_{jh}} \tau = \frac{h_b}{h_c} \tau \quad (2.29)$$

where h_c , h_b are the column depth and the beam depth, respectively.

The maximum principal stresses (σ_I , σ_{II}) are formulated using the Mohr's circle of stress as follows:

$$\sigma_{I,II} = \frac{\sigma}{2} \pm \frac{\sigma}{2} \sqrt{1 + \frac{4\tau^2}{\sigma^2}} \quad (2.30)$$

Unlike the models by Wong (2005) and Hwang and Lee (1999), a fifth degree parabola is adopted in this model to represent the concrete behaviour of the joint core under biaxial stresses as follows:

$$-10 \frac{\sigma_I}{f_c} + \left[\frac{\sigma_{II}}{f_c} \right]^5 = 1 \quad (2.31)$$

where f_c is the joint compressive strength taking into account the confining effect of joint shear hoops, and is given as follows:

$$f_c = K f_c' \quad , \quad K = 1 + \frac{\rho_s f_{yh}}{f_c'} \quad (2.32)$$

From the above equations and by taking $\tau = \gamma \sqrt{f_c'}$, Eq (2.31) becomes

$$\left[\frac{\alpha \gamma}{2\sqrt{f_c'}} \left(1 + \sqrt{1 + \frac{4}{\alpha^2}} \right) \right]^5 + \frac{5\alpha \gamma}{\sqrt{f_c'}} \left(\sqrt{1 + \frac{4}{\alpha^2}} - 1 \right) = 1 \quad (2.33)$$

By solving equation (2.33), the normalised joint shear strength γ can be determined. For the case of exterior beam-column joints without shear reinforcement, the effect of confinement to

increase the joint compressive strength f_c is ignored by taking $K=1$. A detailed evaluation of the applicability of this model to shear-critical exterior beam-column joints is provided in Chapter 5.

2.7.2.4 Wong Model

Wong (2005) developed a shear strength model for shear membrane elements, named “Modified Rotating-Angle Softened-Truss Model (MRA-STM)”. The model was further extended to include exterior beam-column joints. The proposed MRA-STM model was developed based on three existing models; modified compression field theory (MCFT), rotating-angle softened-truss model (RA-STM), and fixed-angle softened-truss model (FA-STM). The main assumption of the developed model is that the angle of cracks that develops in the concrete does not coincide with the concrete principal stress angle. The model satisfies stress equilibrium, strain compatibility, and constitutive laws of material similar to the STT model by Hwang and Lee (1999).

In the MRA-STM model, by using the Mohr’s circle of stress, the average stresses of cracked concrete are expressed as follows:

$$f_{cx} = f_{c1} - v_{cxy} \cot \theta \quad (2.34.a)$$

$$f_{cy} = f_{c1} - v_{cxy} \tan \theta \quad (2.34.b)$$

$$v_{cxy} = \frac{f_{c1} - f_{c2}}{2} \sin 2\theta \quad (2.34.c)$$

where f_{cx}/f_{cy} is average stress of concrete in the x/y direction, f_{c1}/f_{c2} average principal stresses of concrete, v_{cxy} average concrete shear stress, and θ is the concrete principal compressive stress angle of inclination.

In the same way, by using the Mohr’s circle of strain, the cracked concrete average strains are:

$$\varepsilon_{cx} = \frac{\varepsilon_{c1} - \varepsilon_{c2}}{2} (1 - \cos 2\theta) + \varepsilon_{c2} \quad (2.35.a)$$

$$\varepsilon_{cy} = \varepsilon_{cx} + (\varepsilon_{c1} - \varepsilon_{c2}) \cos 2\theta \quad (2.35.b)$$

$$\gamma_{cxy} = 2(\varepsilon_{cy} - \varepsilon_{c2}) \tan \theta \quad (2.35.c)$$

where $\varepsilon_{cx}/\varepsilon_{cy}$ is average strain of concrete in x/y direction, $\varepsilon_{c1}/\varepsilon_{c2}$ average principal strains of concrete, and γ_{cxy} average concrete shear strain.

The adopted concrete average compressive stress-strain relationship follows the softening concrete model proposed by Belarbi and Hsu (1995) as follows:

$$f_{c2} = \xi f'_c \left[2 \left(\frac{\varepsilon_{c2}}{\xi \varepsilon_0} \right) - \left(\frac{\varepsilon_{c2}}{\xi \varepsilon_0} \right)^2 \right] \text{ for } \varepsilon_{c2}/\xi \varepsilon_0 \leq 1 \quad (2.36.a)$$

$$f_{c2} = \xi f'_c \left[1 - \left(\frac{\varepsilon_{c2}/\xi \varepsilon_0 - 1}{4/\xi - 1} \right)^2 \right] \text{ for } \varepsilon_{c2}/\xi \varepsilon_0 > 1 \quad (2.36.b)$$

The cracked concrete softening coefficient ξ and the concrete strain at the peak maximum compressive stress ε_0 are estimated as follows:

$$\xi = \frac{5.8}{\sqrt{f'_c}} \frac{1}{\sqrt{1 + 400\varepsilon_{c1}}} \leq \frac{0.9}{\sqrt{1 + 400\varepsilon_{c1}}} \quad (2.37.a)$$

$$\varepsilon_0 = -0.002 - 0.001 \left(\frac{f'_c - 20}{80} \right) \text{ for } 20 \leq f'_c \leq 100 \text{ MPa} \quad (2.37.b)$$

The average concrete tensile stress-strain relationship is formulated as follows:

$$f_{c1} = E_c \varepsilon_{c1} \quad \text{for } \varepsilon_{c1} \leq \varepsilon_{cr} \quad (2.38.a)$$

$$f_{c1} = f_{cr} \left(\frac{0.00008}{\varepsilon_{c1}} \right)^{0.4} \quad \text{for } \varepsilon_{c1} \leq \varepsilon_{cr} \quad (2.38.b)$$

$$f_{cr} = 0.31 \sqrt{f'_c} \quad \text{and} \quad \varepsilon_{cr} = 0.00008 \quad (2.38.c)$$

The MRA-STM model assumes the resisting shear element in exterior beam-column joints to be similar to the one in deep beams with direct supports. The empirical results of shear span-to-depth ratio of deep beams were used to define the effective vertical and horizontal stresses of the shear element. The size of the assumed shear element is dependent on the concrete bounded by beam and column longitudinal reinforcement. Based on this, joints with different joint detailing but with the same joint aspect ratio, will have identical shear elements.

The joint shear strength can be predicted using an extensive iterative procedure (flow chart) that incorporates the above equations. Similarly to the STT model developed by Hwang and Lee (1999), the iterative solution estimates joint shear capacity from the updated stress/strain state in the vertical and the horizontal directions by following the adopted softening model. Results from unconfined beam-column joints were used to calibrate and evaluate this model. Nonetheless, the model was found extremely difficult to follow and implement and, hence, has not been used in this research.

2.7.2.5 Park and Mosalam Model

Park and Mosalam (2009; 2012a) proposed a new SAT model to predict the shear strength of RC exterior beam-column joints without shear reinforcement in the joint area. The model takes into account differences in joint shear strength due to variation in joint aspect ratios and longitudinal reinforcement ratios. The main difference between this model and previously proposed SAT models is that this model assumes a shear resisting mechanism consisting of two inclined struts in the joint rather than just one, see Figure 2.23. In addition, the model is able to predict the joint shear strength without the need to estimate the area of the diagonal strut A_{str} .

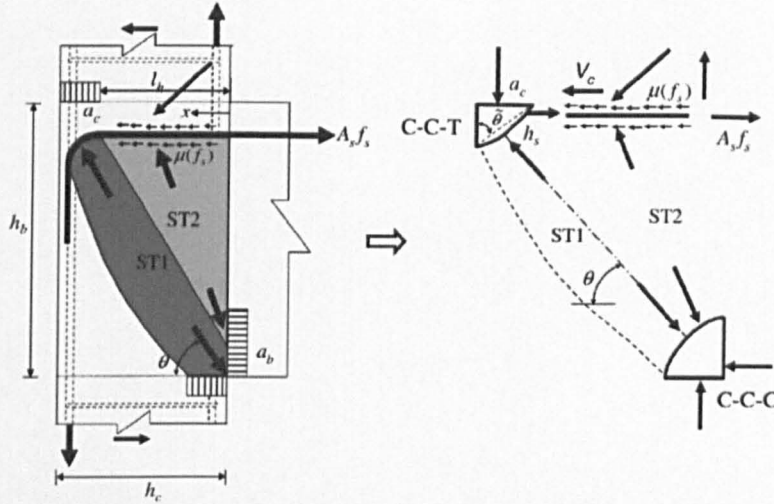


Figure 2.23 Proposed Strut and Tie joint shear model (Park & Mosalam, 2012a)

The model assumes that the first inclined strut ST1 is developed by the effect of the 90° hook, whereas the second strut ST2 is developed due to bond forces between the joint concrete and the straight part of the hook, as shown in Figure 2.23. Consequently, the horizontal joint shear force V_{jh} is resisted by the horizontal component of the first and the second struts ($V_{jh,ST1}$, $V_{jh,ST2}$). Furthermore, the model assumes that joint failure initiates around the top end of the first strut. The authors attributed this to the effect of the anchored tie and on the observed crack patterns of previously tested unreinforced exterior beam-column joints.

The model defines joint shear failure as when the applied stress at the C-C-T node at the end of ST1 reaches the maximum stress of the joint softening concrete model. The joint panel cracked concrete strength σ is estimated based on the softening concrete model proposed by Vollum (1998)

$$\sigma = \frac{5.9\sqrt{f'_c}}{0.8 + 170\varepsilon_1} \text{ MPa} \tag{2.39}$$

Park and Mosalam (2009) found that strain compatibility equations adopted in many analytical joint shear models for average strain calculations are not suitable for exterior joints without transverse reinforcement. Thus, they suggested that the principal tensile strain ε_1 at shear failure can be estimated as follows:

$$\varepsilon_1 = 0.003 + 0.0005(h_b/h_c) \quad (2.40)$$

where h_b , h_c are the beam and column heights, respectively.

From equilibrium, the beam moment M_b and column shear force V_c can be calculated as follows:

$$M_b = V_b L = j d_b A_s f_s \quad (2.41.a)$$

$$V_c = \frac{L + h_c/2}{H} V_b \quad (2.41.b)$$

where L is the beam length to the column face; H is the column height; d_b is the beam effective depth; and j is the moment lever arm factor.

The horizontal joint shear force V_{jh} is

$$V_{jh} = A_s f_s - V_c = A_s f_s \left(1 - \frac{L + h_c/2}{H} \frac{j d_b}{L} \right) \quad (2.42)$$

By considering $d_b \approx 0.9h_b$ and j equal to 0.875 at yielding, the previous equation can be simplified as follows:

$$V_{jh} \approx A_s f_s \left(1 - 0.85 \frac{h_b}{H} \right) \quad (2.43)$$

The fraction of the horizontal joint shear force resisted by each of the inclined struts is calculated as follows:

$$V_{jh} = V_{jh,ST1} + V_{jh,ST2} \quad (2.44.a)$$

$$V_{jh,ST1} = A_s f_s - n\pi\phi_b \int_0^{l_h} \mu(f_s) dx = \alpha V_{jh} \quad (2.44.b)$$

$$V_{jh,ST2} = n\pi\phi_b \int_0^{l_h} \mu(f_s) dx - V_c = (1 - \alpha) V_{jh} \quad (2.44.c)$$

where n , ϕ_b are the number and diameter of beam longitudinal bars, and $\mu(f_s)$ is bond stress distribution as a function of beam bar tensile stress.

The fraction factor α is a tri-linear function of beam reinforcement tensile stress taking into account bond deterioration, as shown in Figure 2.24. By substituting Eq (2.42) into Eq (2.44.b), the fraction factor α becomes:

$$\alpha = \frac{H}{H - 0.85h_b} \left(1 - \frac{4}{\Phi_b} \frac{\int_0^{l_h} \mu(f_s) dx}{f_s} \right) \quad (2.45)$$

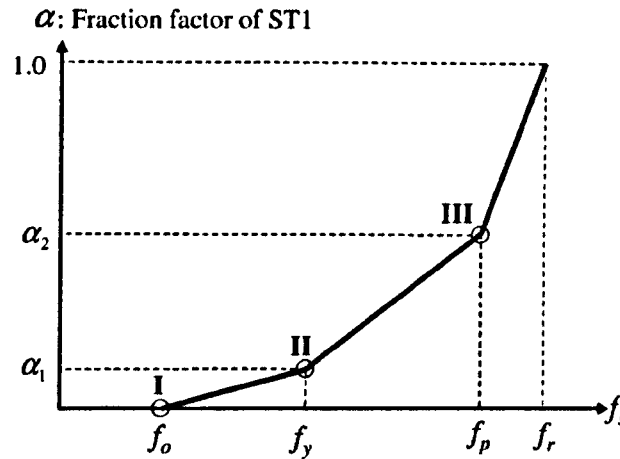


Figure 2.24 Fraction factor function of strut ST1 (Park & Mosalam, 2012a)

The first point of the fraction factor (i.e. point I in Figure 2.24) represents the case when the developed bond strength of strut ST2 is enough on its own to resist the entire horizontal joint shear force V_{jh} . In this case, the model assumes the contribution of ST1 and α as 0. The beam reinforcement tensile stress at this point, f_o is expressed as follows:

$$f_o = \frac{4}{\Phi_b} \mu_E l_h \quad (2.46)$$

where μ_E is the elastic bond strength, and l_h is the horizontal projection of ST2.

Point II of the fraction factor relationship represents yielding of beam reinforcement at the beam-joint interface. The fraction factor at this point, α_1 , is given as follows:

$$\alpha_1 = \frac{H}{H - 0.85h_b} \left(1 - \frac{4}{\Phi_b} \frac{\mu_E l_h}{f_y} \right) \quad (2.47)$$

Point III of the fraction factor relationship represents the case when yielding reaches the end of strut ST2 width l_h . At this point, the tensile stress of beam reinforcement at the beam-joint interface, f_p is expressed as follows:

$$f_p = f_y + \frac{4}{\Phi_b} \mu_y l_h \quad (2.48)$$

where μ_y is the inelastic bond strength and taken as $0.5\mu_E$.

The fraction factor at point III, α_2 is given as follows:

$$\alpha_2 = \frac{H}{H - 0.85h_b} \left(1 - \frac{4}{\Phi_b} \frac{\mu_y}{f_y + \frac{4}{\Phi_b} \mu_y l_h} l_h \right) \leq 1 \quad (2.49)$$

Finally, the tensile stress of beam longitudinal bars when the fraction factor α is equal to 1 is given as follows:

$$f_r = \frac{4}{\Phi_b} \frac{H}{0.85h_b} \int_0^{l_h} \mu(f_r) dx \geq f_p \quad (2.50)$$

According to the model, joint shear strength, V_n is defined as the joint horizontal shear force, V_{jh} that corresponds to the strut ST1 reaching its maximum shear capacity, $V_{jh,ST1,max}$. This is expressed as follows:

$$V_{jh,ST1,max} = c_0 D \cos \theta, \quad D = \sigma b_j h_s, \quad \text{and} \quad \theta = \tan^{-1}(h_b/h_c) \quad (2.51)$$

where c_0 is a constant that can be determined based on experimental results, and b_j is the joint effective width.

The ST1 strut width h_s , similarly to Hwang and Lee (1999), is assumed to be equal to the strut ST1 horizontal projection, a_c . Based on this assumption, and from Eq (2.39), Eq (2.40), and Eq (2.51), the maximum shear capacity of ST1 becomes:

$$V_{jh,ST1,max} = \bar{c} \frac{b_j h_c \sqrt{f'_c} \cos \theta}{1.31 + 0.085 \left(\frac{h_b}{h_c} \right)}; \quad \bar{c} = 2.07\gamma \quad (2.52)$$

In the previous equation, the constant \bar{c} can be defined when the fraction factor is 1 and $V_{jh,ST1} = V_{jh}$ or as the minimum joint shear strength at which ST1 is capable of resisting the applied joint shear force alone. The authors used one test specimen to calibrate the value of \bar{c} . In this specimen $\gamma = V_{jh}/h_c b_j \sqrt{f'_c} = 4 \text{ psi}^{0.5} [0.33 \text{ MPa}^{0.5}]$, $h_b/h_c = 1.1$ and $\theta = \pi/3.8 \text{ Rad}$.

The final joint shear strength is determined using an iterative procedure, in which assuming an initial value for the tensile stress of beam longitudinal bars is required. A detailed evaluation of the model accuracy and applicability to exterior beam-column joints with different reinforcement detailing is provided in Chapter 5.

2.7.2.6 Hassan Model

Hassan (2011) proposed a new simple Strut-and-Tie model to predict the shear capacity of RC exterior beam-column joints without transverse reinforcement (see Figure 2.25). The model formulations are based entirely on the ACI 318-08 (2008) direct strut-and-tie approach.

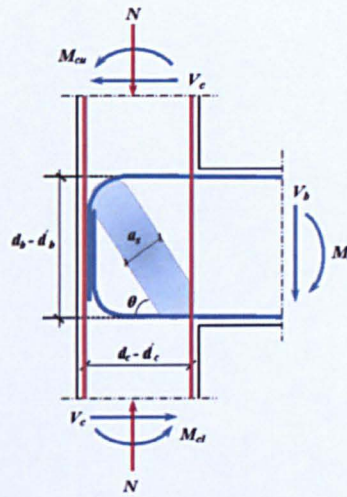


Figure 2.25 Direct Strut and Tie joint shear model (Hassan, 2011)

According to the model, the diagonal strut effective capacity D is calculated based on the strut compressive strength f_{cu} as follows:

$$f_{cu} = 0.85\beta_s f'_c \quad (2.53.a)$$

$$D = f_{cu} A_{str} \quad (2.53.b)$$

where β_s is concrete softening coefficient, and can be taken as 0.6 for bottle-shaped struts with no shear reinforcement (ACI 318-08, 2008).

The area of the concrete compressive strut A_{str} is calculated based on the joint effective width b_j and the strut depth a_s as follows:

$$A_{str} = a_s b_j \quad (2.54.a)$$

$$a_s = \beta_1 \sqrt{a_b^2 + a_c^2} \quad (2.54.b)$$

$$\beta_1 = 1 - 0.05(f'_c - 4) \quad f'_c: \text{Ksi} \quad (2.54.c)$$

where a_c and a_b are the depth of the column and beam compression zones, respectively, and β_1 is a reduction factor for concrete strengths (>4Ksi).

Hassan (2011) assumed that in joints with J-Type failure, beam reinforcement remains elastic. Hence, beam compression zone depth a_b is estimated from transformed linear beam section after cracking as follows:

$$a_b = k d_b \quad (2.55.a)$$

$$k = \left[(\rho + \rho')^2 n^2 + 2 \left(\rho + \rho' \frac{d'_b}{d_b} \right) n \right]^{1/2} - (\rho + \rho') n \quad (2.55.b)$$

where n is the modular ratio, and ρ, ρ' are beam reinforcement ratios.

The column compression zone depth, similar to the model by Hwang and Lee (1999), is estimated as follows:

$$a_c = \left(0.25 + 0.85 \frac{P}{f'_c A_g} \right) h_c \leq 0.4 h_c \quad (2.56)$$

The upper bound limit of $0.4 h_c$ in the previous equation was adopted to limit the increase in joint shear strength due to column axial load.

The joint shear strength which is based solely on the strength of concrete compressive strut is given as follows:

$$V_j = D \cos \theta \quad (2.57.a)$$

$$\theta = \tan^{-1} \left(\frac{d_b - d'_b}{d_c - d'_c} \right) \quad (2.57.b)$$

$$\gamma = \frac{V_j}{h_c b_j \sqrt{f'_c}} \quad (2.57.c)$$

where d_c, d'_c are depths measured from the concrete extreme compression fibre to the centre of tension and compression reinforcement bars in the column, respectively. The same goes for d_b and d'_b in the beam.

The model is extended to include joints failing in shear after beam yielding (i.e. BJ-Type failure). Hassan (2011) assumes that the gain in joint strength after beam yielding is small and

hence; joint shear strength can be taken as the joint shear corresponding to beam yielding (i.e. beam flexural capacity). A detailed evaluation of the accuracy of this model to unconfined exterior beam-column joints is provided in Chapter 5.

2.7.3 Spring-Based Joint Models for FE Frame Analysis

Accurate predictions of the behaviour of RC frames under lateral load excitations is still a challenge. This is mainly attributed to the complex behaviour of beam-column joints. Over the years, many attempts were made to model joint shear deformations and beam bar-slip induced rotation using simple spring elements. These models ranged in their complexity from one spring element to models consisting of several springs with rigid links. The following section presents a brief overview of these past attempts.

2.7.3.1 Nonlinear Beam-Joint Models

In one of the early attempts to account for the nonlinear behaviour of beam-column joints, Giberson (1967) proposed a simple “one-component” beam model to be used for computer simulations of tall buildings. The model consisted of one perfectly elastic beam element and two nonlinear zero-length rotational springs, as shown in Figure 2.26. The nonlinear hysteretic moment-rotation relationship of the two rotational springs account for all nonlinear actions caused by the beam and joint inelastic deformations. One of the main limitations of the proposed model is that the initial slope of the spring moment-rotation hysteretic relationship at both ends of the beam must be the same. This was due to the assumed moment distribution which fixes the point of moment contra-flexure at the centre of the member.

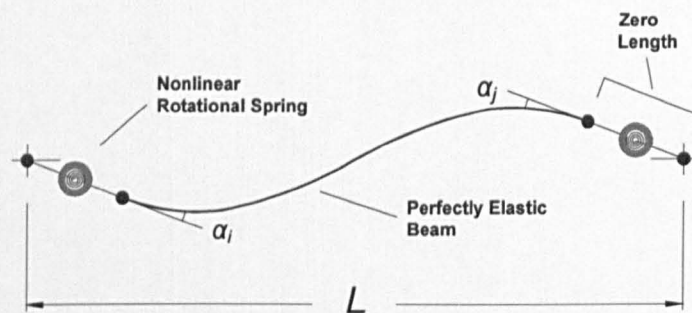


Figure 2.26 One-component nonlinear beam-joint model, Giberson (1967)

In a later study, Otani (1974) proposed a new frame element model consisting of two infinitely rigid elements representing beam-column joint core, two inelastic rotational springs representing beam end rotation caused by bond-slip of beam longitudinal reinforcement at the column face, two parallel elements, one fully elastic and one inelastic, as shown in Figure 2.27. In this model, and unlike the model by Giberson (1967), inelastic deformations can extend beyond the member ends, as the location of moment contra-flexure point is not fixed at the centre. A simplified bilinear curve based on the hysteretic rule proposed by Takeda et al. (1970)

was used to represent the response of the nonlinear rotational springs. In addition, the model accounted for concrete cracking, yielding and strain hardening of reinforcement, and stiffness degradation due to cyclic loading by calibrating a modified version of Takeda hysteretic rule for the inelastic line element. However, joint shear deformations were not accounted for in this model.

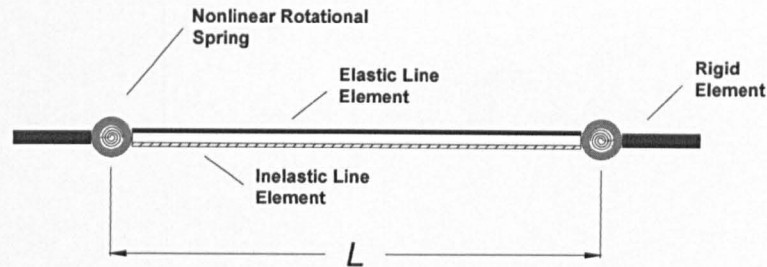


Figure 2.27 Two-component nonlinear beam-joint model, Otani (1974)

Anderson and Townsend (1977) conducted a study reviewing many of the previously proposed analytical hysteretic models. The authors found that proper simulation of the inelastic behaviour of RC beam-column joints requires the inclusion of stiffness and strength degradation in the material model representing the joint region. Based on experimental evaluations, the authors modified Otani's model to take into account the contribution of joint shear deformation. Despite the improvement, the model still cannot identify the various failure modes such as joint failure due to shear. Another drawback is the assumption of constant bond and no slip for beam reinforcement within the joint, which can yield inaccurate local demands.

2.7.3.2 Nonlinear Panel-Zone Joint Models

Krawinkler and Mohasseb Model

Krawinkler and Mohasseb (1987) proposed a new joint model, denoted as "*Scissors model*", capable of simulating the effect of joint panel zone shear distortion on the global response of moment-resisting steel frames. The model represents joint panel zones using two rigid elements connecting through a hinge that allows free rotation between the rigid elements and one nonlinear rotational spring to represent joint panel zone shear deformations, as shown in Figure 2.28. The length of the horizontal rigid element is taken as the column depth, whereas the length of the vertical rigid element is taken equal to the beam depth. The rotational spring properties are defined as the relationship between joint shear force and panel zone shear deformations. This is represented as moment-rotation, in which the moment is considered at the face of the column. In a later study, the scissors model was further developed by proposing a more accurate panel zone representation (Krawinkler, 2001). The new model, denoted as "*Krawinkler model*", consists of four rigid links connected by hinges. Owing to their simplicity,

both models (i.e. Scissor and Krawinkler) were adopted by many researchers, as the following shows.

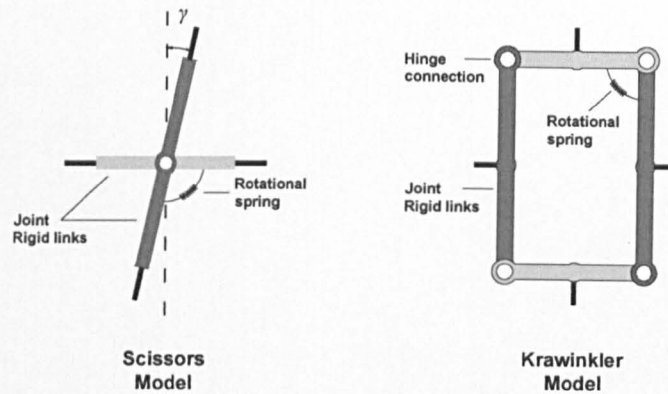


Figure 2.28 Panel-zone joint models: a) scissors model by Krawinkler and Mohasseb (1987), b) Krawinkler model by Krawinkler (2001)

El-Metwally and Chen Model

El-Metwally and Chen (1988) proposed a new joint model, in which the nonlinear behaviour within the beam-column joint is represented by a concentrated rotational spring. The rotational spring properties are defined based on three parameters: the initial stiffness computed by assuming all materials are perfectly elastic, the ultimate moment strength computed by assuming all materials are perfectly plastic, and an internal variable that represents the connection dissipated energy. The model attributes energy dissipation to bond deterioration within the joint, concrete cracks at the face of the column and inelasticity of materials. The model is a step forward in comparison to the aforementioned models (in section 2.7.3.1), especially since it accounts for bond deterioration in the joint region. However, like the previous models, this model is unable to address stiffness and strength loss due to the panel zone shear deformations. Another drawback is its failure to capture the softening behaviour of the joint after yielding of the reinforcement. This is due to the assumption that yielding of reinforcement is accompanied by the formation of a plastic hinge at the joint interface which controls the behaviour of the connection afterwards. In other words, this model is formulated to model ductile joints where beam flexural plastic hinges are expected to form.

Alath and Kunnath Model

Alath and Kunnath (1995) proposed a joint model that accounts for the additional shear deformations of the joint panel-zone. The model consists of one zero-length rotational spring and rigid links representing the joint panel zone dimensions, similar to the scissors model proposed by Krawinkler and Mohasseb (1987). The model assumes the joint panel to be under pure shear and that panel moments are the beam and column moments at the joint interface. The rotational spring's nonlinear shear-deformation relationship is defined based on an empirically

modified hysteretic model by Umemura and Aoyama (1969) that includes degrading effects. The main drawback of this model is that the inelastic deformations due to bond-slip within the joint region are not accounted for in the model formulations.

Uma and Prasad Model

Uma and Prasad (1996) proposed a joint model, in which the joint core is represented by two rigid shear beam elements, whereas elastic beam line elements are used for beams and columns. The concrete model proposed by Sheikh and Uzumeri (1982) is adopted to represent confined concrete while the effect of reversed cyclic loading is accounted for by applying the softening factor of the MCFT (Vecchio & Collins, 1986). A calibration procedure employing the softened truss theory (Belarbi & Hsu, 1995) is used to define the joint shear capacity and the nonlinear shear stress-strain relationship of the rigid beam elements. The model is capable of accounting for hysteretic properties such as pinching effect, strength degradation, and stiffness degradation.

Biddah and Ghobarah Model

Biddah and Ghobarah (1999) proposed a new model in which the joint consists of two types of zero-length rotational springs. The first type accounts for the additional shear deformations of the joint panel zone, whereas the second represents the additional rotation due to bond-slip of beam reinforcement within the joint core (see Figure 2.29). The shear stress-strain relationship of the joint panel zone is a tri-linear curve defined based on the softened truss model (Hsu, 1998). A hysteresis relationship with degrading effects, but with no pinching, is used to simulate the cyclic response of the joint panel zone (i.e. the shear spring). Experimental results reported by Morita and Kaku (1984) were adopted to compute the moment-rotation bilinear relationship of the bond-slip spring, whereas cyclic response was simulated by a hysteresis model with pinching effect developed by Chung et al. (1987). Despite accounting for degradation in addition to pinching, the model does not properly address these hysteretic properties.

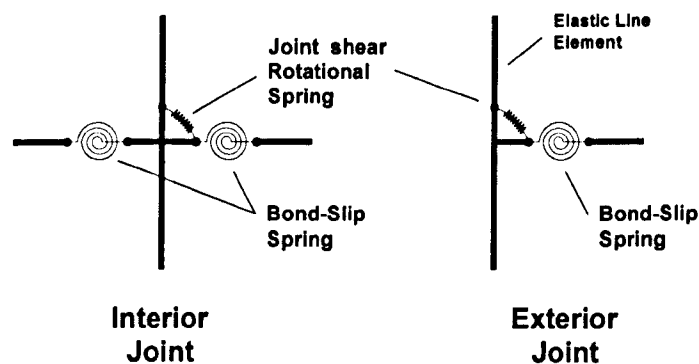


Figure 2.29 Multi rotational spring joint model (Biddah & Ghobarah, 1999)

Youssef and Ghobarah Model

Youssef and Ghobarah (2001) proposed a joint model that is capable of simulating joint shear deformations, bond-slip, and flexural deformations in the plastic hinge zones. The joint panel is represented by four pin-connected rigid elements and two diagonal translational shear springs, as shown in Figure 2.30. Beams and columns are represented by elastic line elements which connect to the joint panel zone through 12 translational concrete and steel springs (i.e. three springs at each joint panel interface). Each steel spring represents the bond strength-slip relationship of steel bars within the joint, whereas the concrete spring represents concrete crushing at the joint interface. The nonlinear response curve of the shear springs is defined based on MCFT (Vecchio & Collins, 1986), whereas the cyclic response is simulated by a hysteresis model by Ghobarah and Youssef (1999). Similarly to the model by Ghobarah and Youssef (1999), this model does not address well the hysteretic properties such as degradation and pinching effects.

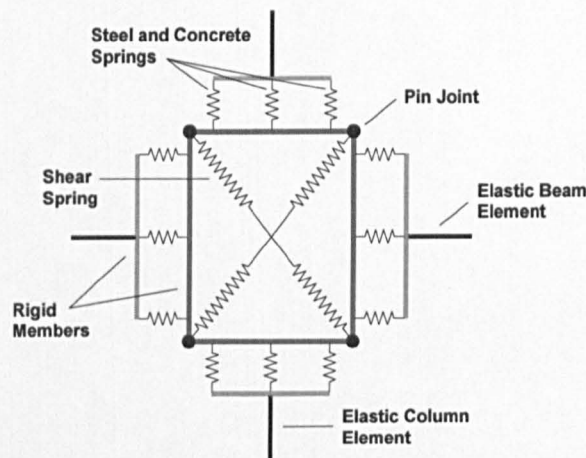


Figure 2.30 Beam-Column joint model by Youssef and Ghobarah (2001)

Lowes and Altoontash Model

Lowes and Altoontash (2003) proposed a joint model capable of simulating all primary inelastic joint actions such as strength and stiffness degradation due to panel zone shear distortion, slippage of steel bars within the joint core, and interface shear transfer failure due to crack opening. The model represents the joint by four rigid elements that connect through eight zero-length bond-slip springs and four zero-length interface shear springs to a shear panel, as shown in Figure 2.31.

The shear stress-strain response curve of the shear panel is defined based on the MCFT (Vecchio & Collins, 1986). The cyclic response of the shear panel is simulated by the one-dimensional hysteretic material model in OpenSees (Mazzoni et al., 2006). The constitutive model and cyclic properties of the bond-slip interface spring was determined from experimental

studies (Viathanatepa et al., 1979; Eligenhausen et al., 1983; Lowes & Moehle, 1999) under the assumption that bond stress is constant within the joint and that slip is only due to elongation. The shear stress vs. slip envelope of the interface-shear spring was defined by employing a calibration procedure developed based on the findings of previous research (Walraven, 1981; Walraven, 1994). When defining the hysteretic behaviour and the unloading-reloading characteristics of the model, strength and stiffness deterioration were neglected (Lowes et al., 2003). The model showed good correlation with experimental results of ductile joints.

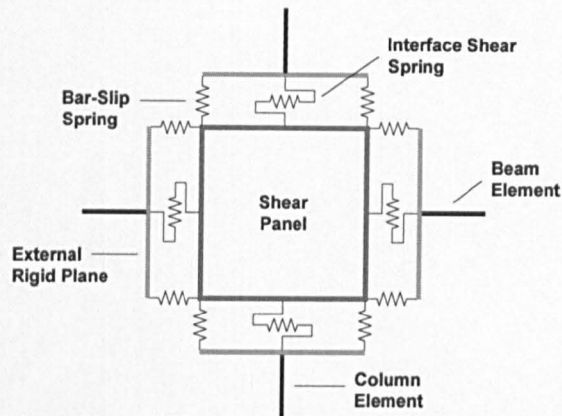


Figure 2.31 Beam-Column joint model by Lowes and Altoontash (2003)

Shin and LaFave Model

Shin and LaFave (2004) proposed a new joint model capable of simulating the hysteretic shear behaviour of joint panel zones under seismic excitations. The model was implemented in DRAIN-2DX and consisted of four rigid links, one at each side of the joint perimeter (Krawinkler-model). These rigid links are connected to one another through hinges with one of the hinges having three parallel rotational springs (see Figure 2.32). Each nonlinear rotational spring is a Drain-2DX element 10 developed by Foutch et al (2003). The element is a modified version of element 04, which is a simple zero-length spring element included in the original DRAIN-2DX library (Prakash et al., 1993).

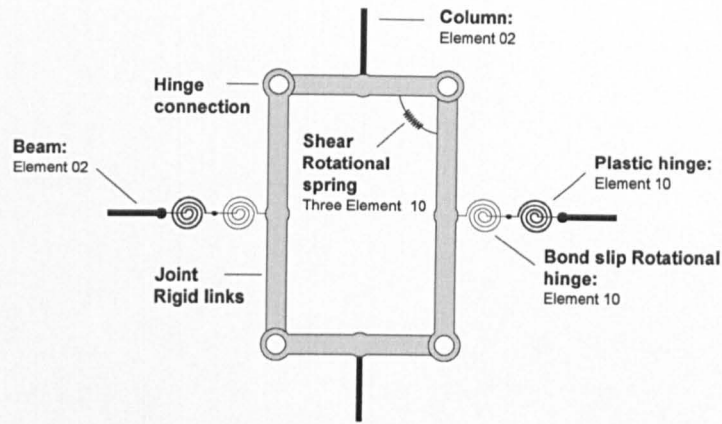


Figure 2.32 Interior Beam-Column joint model by Shin and LaFave (2004)

In this model, the nonlinear shear-deformation relationship of the joint panel zone is represented by placing three rotational springs (Element 10) in parallel to produce a quad-linear moment-rotation envelope, as each Element 10 can only express a bi-linear curve. An analytical procedure employing the MCFT (Vecchio & Collins, 1986) is utilised to define the shear stress-strain envelope curve of the three parallel springs.

Beams and columns are modelled using DRAIN-2DX element 02 which is an elastic element that accounts for strain hardening and axial force-moment interaction. Furthermore, beam ends are modelled using two Element 10 placed in series, one accounts for rotations caused by the inelastic deformations in the plastic hinge region, while the other accounts for fixed end rotations caused by bond slip or yielding of longitudinal reinforcement passing through the joint core. The formulation of the bond-slip model proposed by Morita and Kaku (1984) was adopted to define the bilinear moment-rotation relationship of the bond-slip spring. Some modifications were applied to the original model to simplify the calibration procedure.

Element 10 is capable of representing many hysteretic response characteristics, such as strength degradation, stiffness degradation, and pinching behaviour. The rotational shear springs included all the aforementioned characteristics, while the bond-slip springs excluded only pinching. Results of previously conducted experiments were used to calibrate the hysteretic response parameters of the model. The model predicted with good accuracy the overall cyclic response of ductile joints.

Mitra and Lowes Model

Mitra and Lowes (2007) proposed a beam-column joint capable of simulating the response of a wide range of RC joints. The model is a modified version of the previously proposed model by Lowes and Altoontash (2003) which can be considered as a special case of the new model. The model is a multi-element joint model that is intended for 2D structural analysis. Similar to the model by Lowes and Altoontash (2003), the new model consists of the exact elements, one

shear panel, eight bar-slip springs, and 4 interface shear springs. The primary modification in comparison to the old model formulation is the position of interface bar-slip springs. The bar-slip springs were shifted to the centre of the compression and tension zones of beams and columns rather than being at the perimeter of the joint (see Figure 2.33). A new calibration procedure was developed for the shear panel element based on the assumption that joint shear is resisted by a diagonal compressive strut. The strut forms between beams and columns compression zones, assuming full development of beam flexural capacity. The concrete compressive strength of the strut follows a new softening concrete model proposed based on the results of 13 interior beam-column joints. The new model showed good correlation with experimental results.

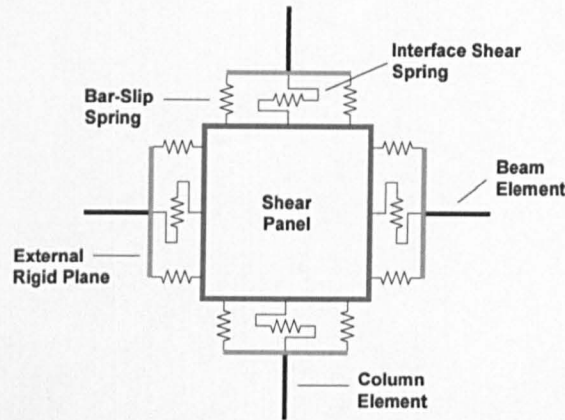


Figure 2.33 Interior Beam-Column joint model by Mitra (2007)

Favvata et al. Model

Favvata et al. (2008) proposed a model to simulate the inelastic response of exterior beam-column joints in multi-storey RC frame structures. The model is a zero-length rotational spring element incorporated in the nonlinear program ADAPTIC (Izzuddin, 1991). The rotational spring accounts for all nonlinear actions of the joint area, whereas the rigid zones at the end of beam and columns represent the core of the joint. The moment-rotation envelope curve of the rotational spring is a tri-linear curve with a hysteresis model that accounts for strength and stiffness degradation in addition to the pinching effect. An evaluation procedure was developed to define the behaviour of the joint model based on the exhibited failure mechanism, whether it is joint shear failure, anchorage failure due to bar pull-out, or beam flexural failure. The ultimate joint shear strength is estimated based on the iterative procedure proposed by Hwang and Lee (1999) which showed a tendency to over-estimate when applied to joints with no shear links. The model was used to model an eight storey RC building. The model emphasised the importance of modelling joints as flexible for seismic simulations of RC moment-resisting frames.

Sharma et al. Model

Sharma et al. (2011) proposed a new (scissors-type) joint model to simulate the shear behaviour of RC exterior beam-column joints under seismic loading. The model consists of six nonlinear hinges. The panel zone is represented using one rotational shear hinge connected to the beam and two translational shear hinges connected to the top and bottom columns, as shown in Figure 2.34. Outside the panel zone, beam and columns are modelled using elastic line elements with a rotational hinge that connects the frame element to the panel zone. Unlike previous joint models, in this model, joint shear failure is determined based on the principal tensile stress in the joint core. Spring characteristics are defined based on experimentally calibrated plots of principal tensile stress vs. joint shear deformation suggested by Priestley (1997) and Pampanin et al. (2003). The model is capable of simulating the shear response of exterior beam-column joints with 90° hooks and short beam anchorage, but only if bar pull-out occurs. Extending the model to other types of joint detailing other than the investigated is uncertain, such as joints with straight bar anchorage and sustaining J-type failure. The model correlated with acceptable accuracy with the investigated experimental results.

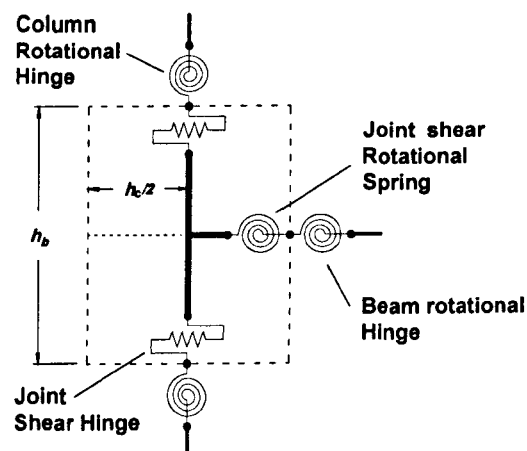


Figure 2.34 Exterior Beam-Column joint model by Sharma et al. (2011)

2.7.3.3 Discussion of Beam-Column Joint Models for FE Frame Analysis

In the previous section, many of the proposed beam-column joint models for FE structural analysis were reviewed. Early attempts accounted for joint deformations implicitly, whereas the more recent attempts tried to simulate the behaviour of beam-column joints more realistically by proposing joint models with explicit panel zone representation, whether they consist of a single spring or multi-spring elements. While multi-spring models may seem like the better option, they are not always the most accurate or efficient, as they tend to overcomplicate the analysis and cause problems related to numerical convergence, especially when used for multi-storey buildings. In addition, multi-spring models require a significant amount of initial calculations to define the characteristics of each spring. Some of the proposed methods for estimating the

characteristics of joint panel zone shear springs were based on calibrating tests of confined interior beam-column joints. Thus, using these approaches to cases other than the ones included in the calibration might yield inaccurate results. An example of this is the MCFT by Vecchio and Collins (1986), which showed good accuracy predicting the shear strength of well confined beam-column joints (Lowe et al., 2003; Shin & LaFave, 2004; Kim & LaFave, 2007), whereas for beam-column joints with little or no shear reinforcement it was found to be unconservative (Mitra, 2007; Celik & Ellingwood, 2008). This can be attributed to the fact that the average strain state in RC beam-column joints with no transverse reinforcement is very different to that of shear membrane elements having vertical and horizontal reinforcement for which the MCFT was developed.

Based on the above, it can be concluded that any of the reviewed joint panel-zone representations can be adopted in frame analysis and can adequately represent the complexity of joint deformation. However, the main factor that influences the accuracy of predictions is not just the number of the included springs, but rather the adopted constitutive models that define the behaviour of these springs, and in turn the behaviour of the joint panel zone. Therefore, choosing one model over the other, provided the same constitutive model is adopted in both models, should be judged solely based on the purpose of the model, whether a more global or local behaviour is required. In addition, weighing the computational cost in comparison to the expected improvement should be another intrinsic factor for the selection process.

Celik and Ellingwood (2008) investigated the accuracy and the applicability of some of these spring-based models to represent RC exterior beam-column joints without shear reinforcement in fragility assessments of RC frames designed for gravity loads. They concluded that, when adopting an accurately calibrated shear stress-strain constitutive model based on experimental results, a simple representation for the joint panel zone using scissors type rigid links and a rotational spring can produce sufficiently accurate results in comparison to the predictions of a more sophisticated model.

In this research, for the purpose of developing a more practical representation of deficient exterior joints in RC frame analysis, the scissors model and the Krawinkler model representations are considered and further explored in Chapter 6.

2.8 RECAP AND CONCLUSIONS

Based on the comprehensive literature review and the current understanding of the seismic behaviour of deficient exterior RC beam-column joints presented in this chapter the following conclusions can be drawn:

- 1- RC beam-column joints of building constructed prior to 1980, especially in developing countries, are seismically deficient and therefore highly prone to sustain joint shear failure under seismic excitations. This is highly established based on findings from beam-column joint tests and post-earthquake reconnaissance reports.
- 2- The seismically deficient details of exterior beam-column joints of older existing building vary based on the adopted design guidelines, but the most common type of deficiency found in the majority of these joints is the lack of shear reinforcement within the joint area.
- 3- The current seismic and retrofitting codes are mostly over-conservative and lack the transparency required to allow the designer to fully understand and control the evaluation process. This is due to the lack of proper understanding of the effect of each of the different design parameters on the seismic behaviour of beam-column joints.
- 4- There is increasing need to accurately assess, evaluate, and strengthen older existing buildings to help overcome and mitigate any potential threats these older-buildings pose to the society in terms of public safety and economic risk.
- 5- It is assumed in deficient exterior joints, and due to the lack of shear reinforcement, that the only effective shear resisting mechanism is the diagonal compressive strut that forms within the core between the beam and column compression zones. The strut strength, and in turn the joint shear strength, is a function of the stress and strain state within the joint panel.
- 6- Concrete compressive strength within the joint panel is reduced due to tensile cracks that form parallel to the axis of compressive loading. Load reversal causes extra reduction to the concrete strength due to the continuous opening and closing of cracks.
- 7- Several types of failure mechanisms that can be sustained by deficient joints typical of older RC buildings are identified. These types include joint shear failure without reinforcement yielding (*J-Type*), shear failure shortly after reinforcement yielding (*BJ-Type*), and failure due to bar pull-out (*P-Type*). Other failure types are identified but are less common.
- 8- The seismic behaviour of deficient exterior beam-column joints is affected by several key parameters. The parameters identified as most influential include concrete compressive strength, joint panel geometry, beam reinforcement ratio, and column axial load.
- 9- Concrete compressive strength is the governing influence parameter in terms of joint shear stress and strain. The square root of the concrete compressive strength is

- proportional to the joint shear stress and increasing the concrete strength can improve the joint shear strength.
- 10- Higher joint aspect ratio (h_b/h_c) reduces the normalised joint shear strength of deficient exterior joints. The adverse effect is slightly clearer for *J-Type* failure exterior deficient joints in comparison to *BJ-Type* failure joints. This relationship is dependent on other parameters such as axial load and beam reinforcement.
 - 11- Joint shear strength is a function of the amount of beam reinforcement. For deficient exterior joints of joint aspect ratio between 0.89 and 1.33, the relationship between the normalised joint shear strength and beam reinforcement ratio can be denoted as linearly proportional, provided other design parameters remained unchanged.
 - 12- The effect of column axial load on the joint shear strength of deficient exterior joints is mostly unclear. The influence is insignificant in joints where the column axial load is less than $0.2f'_cA_g$. The effect is assumed to be mostly beneficial up to the point of joint shear strength and detrimental afterwards for joints with a column axial load level higher than $0.2f'_cA_g$.
 - 13- Many experimental studies focused on improving the behaviour of beam-column joints under seismic excitations. However, only a limited number of these studies highlighted the behaviour of deficient exterior joints and provided shear stress-shear strain data that can be utilised for developing new shear models.
 - 14- Until recently, there were no joint shear strength models for deficient exterior beam column joints. Most proposed joint strength models are developed and calibrated for well-designed beam-column joints.
 - 15- Many attempts were made to account for joint shear deformations and beam bar-slip induced rotation in RC FE frame simulations using simple spring elements. These attempts ranged in their complexity from one spring element to models consisting of several springs with rigid links
 - 16- Based on an analytical study by Celik & Ellingwood (2008), it was found that modelling the panel zone as a rigid zone yields inaccurate results in terms of strength and stiffness. They also found that a simple representation for the joint panel zone using scissors type rigid links and a rotational spring can produce sufficiently accurate results in comparison to the predictions of a more sophisticated model (i.e. super-element panel zone joint mode), provided an accurately calibrated shear stress-strain constitutive model is adopted in both models.

CHAPTER 3

EXPERIMENTAL PROGRAMME

3.1 INTRODUCTION

Previous experimental research on different aspects of the seismic performance of beam-column joints was presented in Chapter 2. Much of this work focused on improving the seismic performance of ductile joints detailed according to current design codes. The few that reported specimens with low or standard strength concrete from older existing buildings focused on strengthening techniques and lacked the basic data required for developing shear strength models for such joint cases. To fill this gap, the experimental program of this research was designed to study the shear performance of existing deficient RC beam-column joints in cyclic loading.

This chapter presents full details of the experimental programme that was carried out at the heavy structures laboratory at the University of Sheffield for the purposes of this study. The experimental programme investigated the seismic performance of older existing buildings by testing seven full scale exterior RC beam-column joints. The specimens were designed to simulate different joint details found in pre-1980 (seismically deficient) buildings. Specimens were tested under quasi-static cyclic loading to the point of total collapse. Description of the test specimens and the investigated parameters in addition to the construction of the specimens and the utilised instrumentation are described in this chapter.

3.2 TEST PARAMETERS

Based on previous joint research presented in Chapter 2, several parameters that had a significant effect on the seismic performance of exterior joints were selected for this research:

- Concrete compressive strength
- Column axial load ratio
- Beam longitudinal bar bond demand (i.e. type of beam anchorage detailing)
- Joint shear reinforcement

A brief description of these parameters is given below.

3.2.1 Concrete compressive strength

It was established in Chapter 2 that the concrete compressive strength is the governing influence parameter in terms of joint shear stress and strain. In addition, reviewing previous research on beam-column joints, showed how these studies offer limited information when it comes to joints with low strength concrete. This is despite that fact that the majority of older existing buildings, especially those in developing countries, were constructed using low strength concrete $f_c < 15$ MPa (Koru, 2002; Bedirhanoglu et al., 2010; Ahmad, 2011). Therefore, and to fill this gap, this research was aimed to study the effect of varying the concrete compressive strength, from low to normal, on the seismic shear performance of existing deficient exterior joints. The targeted concrete strength was designed to range between $f_c = 10$ to 18MPa. Detailed description of the obtained strengths is reported in 3.4.1.

3.2.2 Column axial load ratio

Mosier (2000) based on his survey of pre-1967 existing structures, presented in Chapter 2, reported that the average axial load ratio of columns ranged between 3% of the column axial capacity ($f_c A_g$) in higher stories and 28% in lower stories, as shown in Table 2-1. Therefore, to investigate the effect of column axial load on the bond demand of beam longitudinal bars within the joint along with the effect on the shear strength of poorly detailed joints, lower levels of axial load are selected. This is because, as mentioned in Chapter 2, high levels of column axial load ($>0.2f_c A_g$) were found to offer beneficial effects, whereas the effects of lower levels are still not well defined. The two levels of column axial load adopted in this research are 150kN (7%) and 250kN (12%), as shown in Table 3-10.

3.2.3 Beam longitudinal bar bond demand

As previously discussed in Chapter 2, the beam reinforcement ratio within the joint and in turn the bond stress demand of beam longitudinal bars may have a significant impact on the overall joint seismic behaviour. However, this impact is expected to be more pronounced when the development length l_d of beam bars is not adequate enough to allow for the bar strength to be fully developed. Such cases can lead to rapid strength degradation and a hysteresis response with prominent pinching.

Current design codes, such as ACI 318-11 (2011), control this problem by limiting the column depth to bar diameter h_c/d_b to 20. In order to investigate the effect of bond demand of beam longitudinal bars on joint seismic performance, three different configurations of beam anchorage are used in the current test programme, none of which complies with the seismic provisions of current design codes, as explained in 3.3.2.3.

3.2.4 Joint Shear Reinforcement

Studies and surveys on older existing buildings, presented in Chapter 2, established how the absence of joint shear links is considered to be the single most common deficiency in buildings constructed prior to the 1980s. This is usually attributed to the lack of seismic detailing requirements in pre-1980s design codes such as the American Concrete Institute design code (ACI) and the Uniform Building Code (UBC). Therefore, and to recreate the same conditions of old practice buildings, the adopted beam-column design for the current test programme has no joint shear reinforcement.

3.3 TEST SPECIMENS

3.3.1 DESCRIPTION OF MODEL STRUCTURE

The design of the test specimens was initially based on the first-storey corner joint extracted from the Ecoleleader no.2 frame structure shown in Figure 3.1 and Figure 3.2. The structure was designed according to old European design codes to simulate Pre-1980 seismically deficient joint configurations. The main deficiencies included a strong beam-weak column joint design. The structure was tested in Saclay, France between October and November 2004 on the AZALEE shaking table (Chaudat et al., 2005).

The typical storey height (floor to floor) was 3.3 m, and the typical beam span was 4 m. The original dimensions were adjusted for practical reasons, to account for the available space in the laboratory and dimensions of the testing frame.

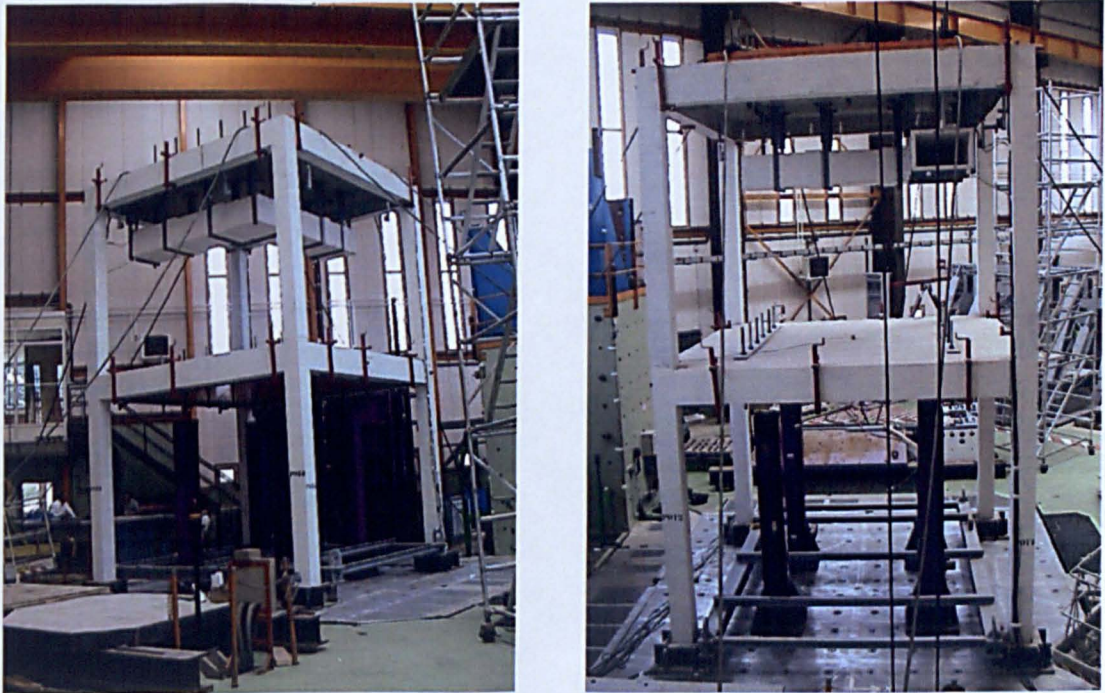


Figure 3.1: Ecoleleader no.2 frame structure fixed to the shaking table (Chaudat et al., 2005)

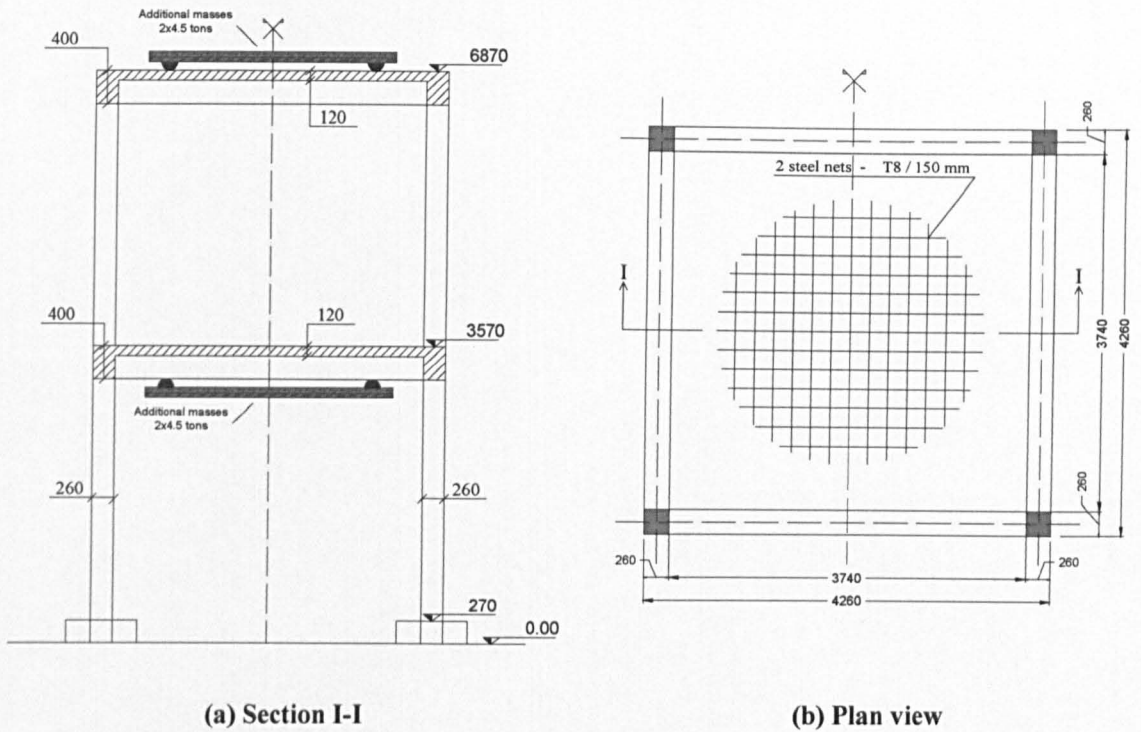


Figure 3.2: Geometry of Ecoleader no.2 frame structure, after Chaudat et al. (2005)

3.3.2 DESIGN AND FABRICATION OF TEST SPECIMENS

All seven specimens shared the same dimensions and cross sections. Initial joint shear strength was estimated based on FEMA 273, Table (6-9) (FEMA 273, 1997). The reinforcement detailing of both beam and column was based on joint shear stress calculations. The shear reinforcement in beam and columns was made sufficient to avoid shear failure in these elements. Similarly, the longitudinal reinforcement of beams and columns was designed to avoid early degradation and force the joint to fail either due to shear or a combination of shear and anchorage slip. Details of the initial calculations and the predicted strengths can be found in Appendix A

This sub-section summarises the design and the reinforcement details of the test specimens. In addition, the studied parameters are quantified and detailed.

3.3.2.1 Beam Design

In all seven specimens, the cross section of beams is identical except for the pilot specimen JA-1. Beams are 260 mm wide and 400 mm deep with identical top and bottom longitudinal reinforcement of 4T16, as shown in Figure 3.3.

The beam shear reinforcement starts 50 mm from the face of the column and comprises one link T8 every 150 mm over the whole length of the beam except at the end where the distance between links is reduced to 75 mm, as shown in Figure 3.9. The reason for closer spacing was to

avoid concrete crushing due to the concentrated stress caused by the actuator's applied force during testing.

As for the pilot specimen JA-1, T10 is used instead of T8 for the shear reinforcement due to unavailability, as shown in Figure 3.7. Additionally, and in order to replicate old construction practice, all shear links end with a 90° bent on both ends and a 70 mm extension starting from the corner, as shown in Figure 3.3 and Figure 3.4.

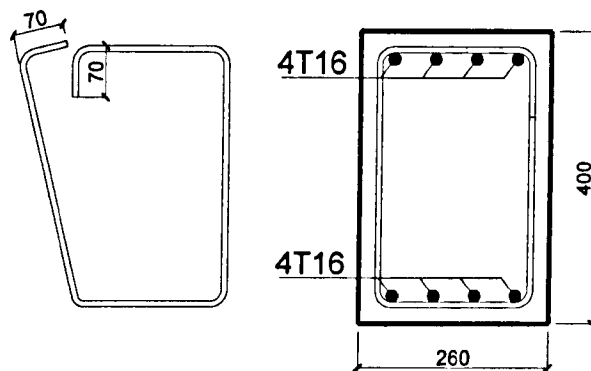


Figure 3.3 Beam cross section

3.3.2.2 Column Design

Similarly to the beams, the cross section of columns is identical except for the pilot specimen JA-1. Columns have a square section of 260 mm x 260 mm. The longitudinal reinforcement of the bottom column comprises 8T16 uniformly distributed around the column faces, as shown in Figure 3.4. In addition, the longitudinal reinforcement of the bottom column continues through the joint core to the top column where it stops at a distance equals to $25d_b$ (400 mm) from the top column-joint interface, as can be seen in Figure 3.7.

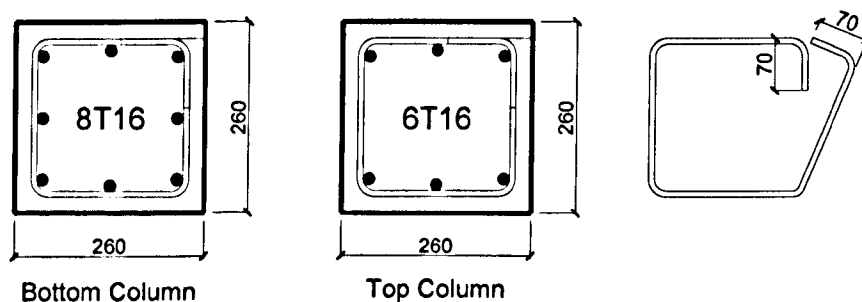


Figure 3.4 Columns cross section

The top column longitudinal reinforcement is reduced to 6T16 instead of the original 8 bars of the bottom column. The steel bars start from the joint interface leaving a 400 mm overlap between the bottom and top longitudinal reinforcement. This $25d_b$ (400 mm) overlap between

the column spliced bars is insufficient according to current design guidelines (ACI 318-08, 2008; ACI 318-11, 2011).

As for the pilot specimen, the column longitudinal reinforcement is slightly different than the rest of the specimens. The bottom column is reinforced with 6T16 while the top column has only 4 bars as shown in Figure 3.5. The two extra bars were added to avoid the possibility of premature spalling in the joint core.

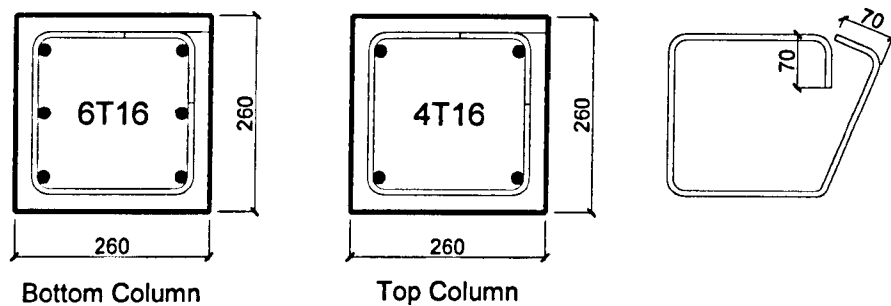


Figure 3.5 Columns cross section of JA-1

The shear reinforcement of all columns starts 70 mm from the joint interface, 50 mm for the case of JA-1, and comprises one link T8 every 150 mm over the whole length of the column. However, at the end of the columns the spacing is reduced to 50 mm (see Figure 3.7).

The beam cross section is intentionally designed stronger than the column to represent common state of old practice buildings. Consequently, the sum of the resisting bending moments of the columns is less than the resisting bending moment of the beam, which according to Eurocode 8 (BSI EC8, 2004) should comply with the following requirement:

$$\sum M_{Rc} \geq 1.3 \sum M_{Rb} \quad (3.1)$$

where $\sum M_{Rc}$ and $\sum M_{Rb}$ are the sum of the resisting bending moment of the adjoining columns and beams, respectively (BSI EC8, 2004).

In this case, columns are expected to fail before beams, provided that the joint core is strong enough to allow the framing beam and columns to develop their flexural strengths. In case of deficient exterior joints, joint failure can be the primary failure mechanism. However, this is dependent on the type of anchorage and the flexural strengths of the framing beams and columns, whether the joint is stronger or weaker.

3.3.2.3 Joint Design

The specimens are categorized into groups A, B and C. Each group consists of two specimens with a different anchorage detailing for the beam longitudinal bars. These different details were

selected based on previous observations and reconnaissance reports of prior earthquakes (as mentioned in Chapter 2). Figure 3.6 shows the different configurations of joint detailing utilised in the test specimens and denotes the naming of each group.

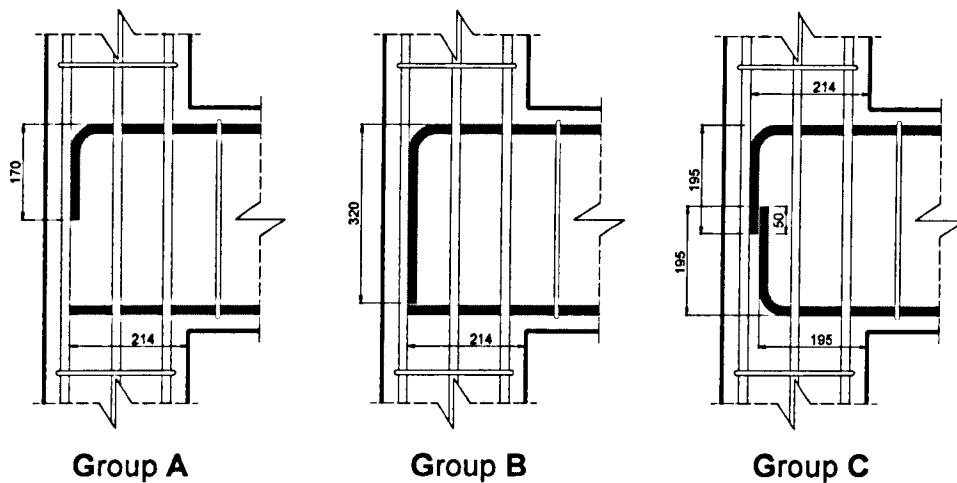


Figure 3.6: Anchorage details of the test specimens

The dimensions and the reinforcement details of the pilot specimen, Joint JA-1, are shown in Figure 3.7. It can be noted from Figure 3.7 that the beam bottom longitudinal bars are straight and extend inside the joint till reaching the outer longitudinal bars of the column reinforcement; while the beam top bars are hooks bent 90° into the joint, and stop at the mid-height of the joint.

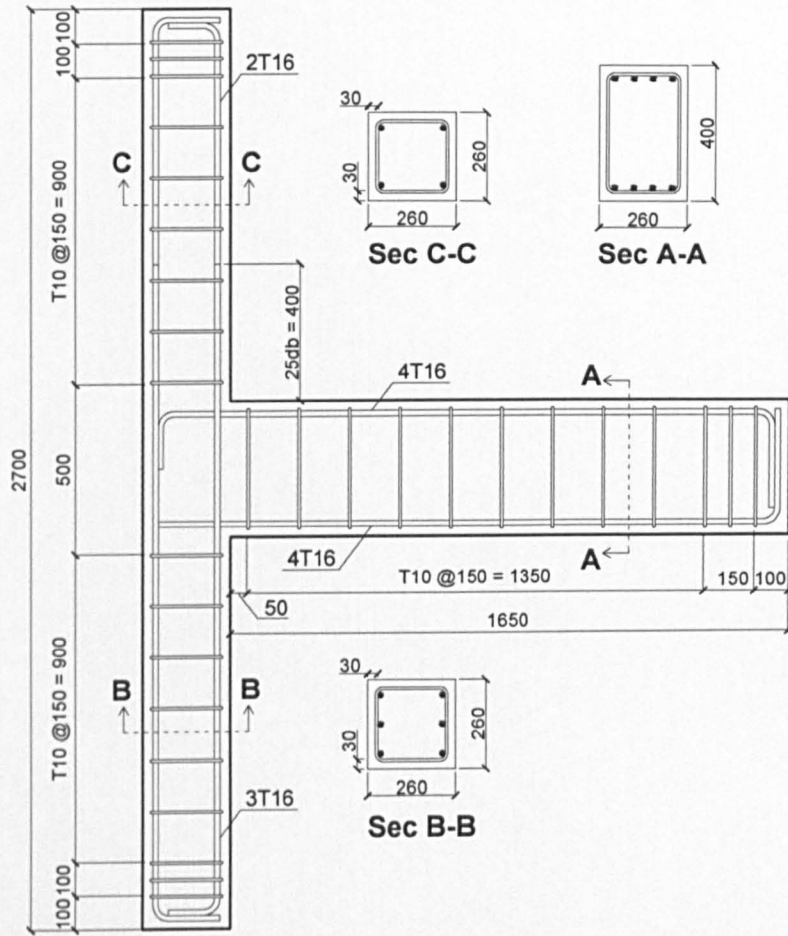


Figure 3.7 Dimensions and reinforcement details of the pilot specimen JA-1

For specimens JA-2 and JA-3, the reinforcement detailing of the joint core is practically the same as in JA-1 except for the extra two bars added to the bottom column reinforcement parallel to the casting face. Figure 3.8 outlines the differences between the pilot specimen JA-1 and JA-2 & JA-3.

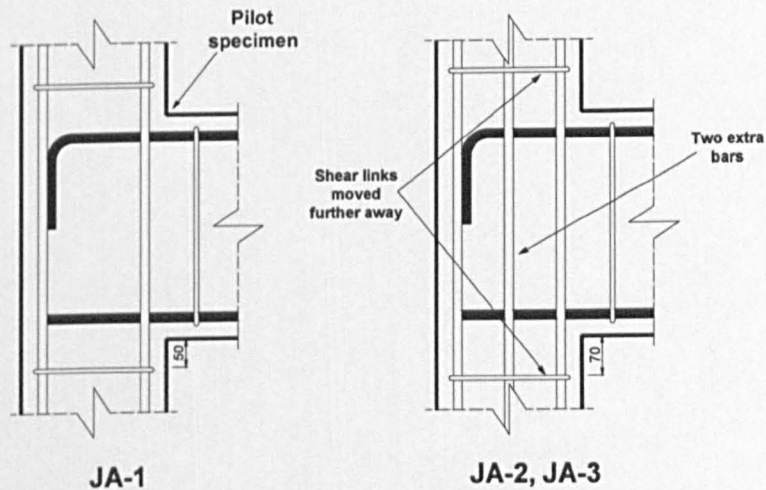


Figure 3.8 Reinforcement detailing of the joint core of Group A specimens

The dimensions and the reinforcement details of group B which includes specimens JB-1 and JB-2 are shown in Figure 3.9. In these specimens, the same detailing of group A is adopted except for the beam top bars, where the 90° hook rather than stopping at the mid-height of the joint continues further down inside the joint till reaching the beam bottom longitudinal bar.

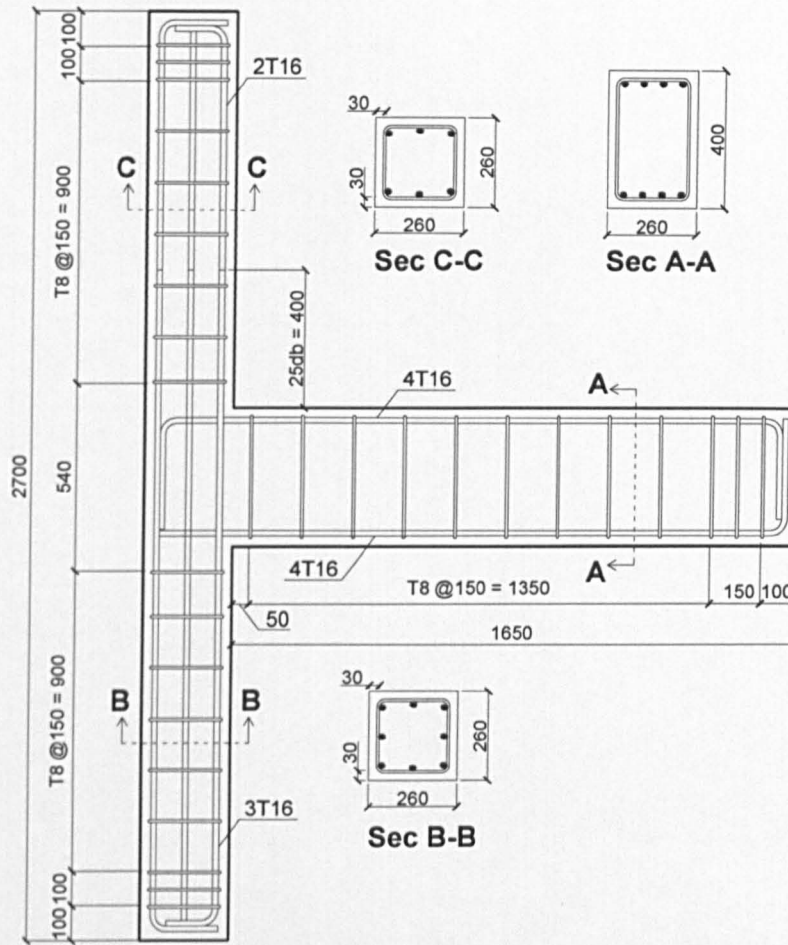


Figure 3.9 Dimensions and reinforcement details of group B specimens

Furthermore, Figure 3.10 shows the dimensions and the reinforcement details of group C which is consisted of JC-1 and JC-2. In this case, both the beam bottom and top longitudinal reinforcement are hooks bent 90° into the joint, leaving a 50 mm overlap between the hooks, as shown in Figure 3.6.

As for the joint transverse reinforcement, all seven joints (including the pilot test) have no shear links within the joint region, as shown in Figure 3.7 to Figure 3.10.

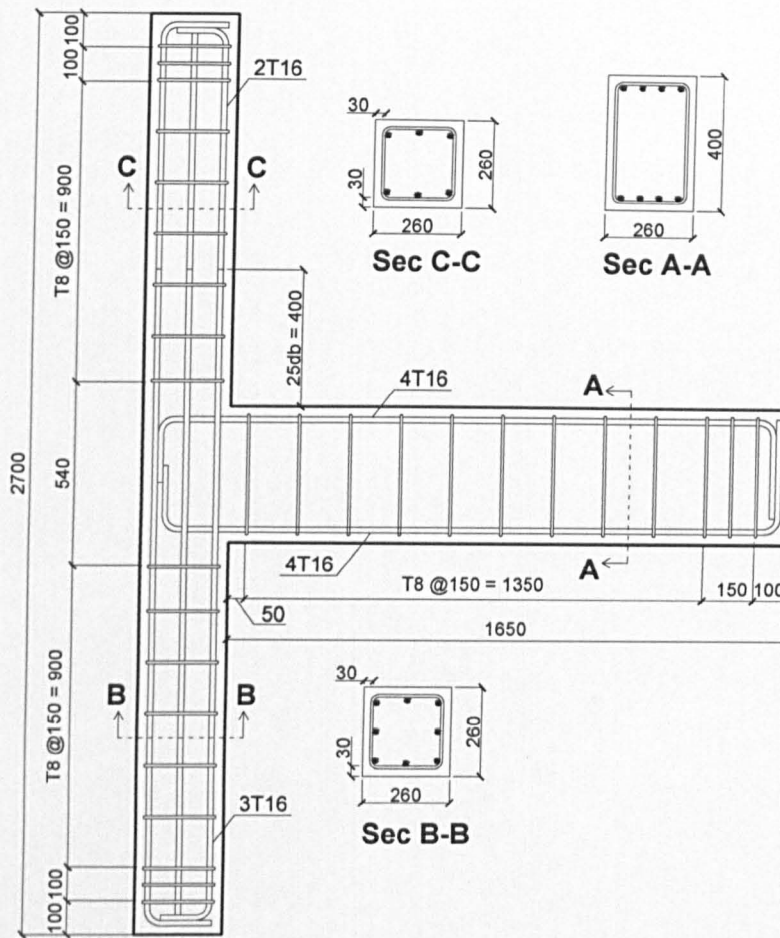


Figure 3.10 Dimensions and reinforcement details of group C specimens

As previously mentioned in section 3.3.2.2, the spliced bars at the top column have a development length l_d equal to 400 mm ($25d_b$). For such a case (i.e. spliced bars), ACI 318-11 recommends the development length for deformed bars in tension to be not less than $47d_b$. This is true when a minimum clear spacing of $2d_b$ along with a minimum concrete cover of d_b is provided. However, when the cover or spacing is less than the recommended value then the development length should be at least $72d_b$ (ACI 318-08, 2008; ACI 318-11, 2011).

Moreover, the three configurations of beam anchorage are deficient and lack the appropriate development length according to current seismic design codes. The beam bottom bars in group A and group B are straight and have a development length l_d equal to 210 mm ($\approx 13d_b$). However, ACI 318-11 requires this bar to end with a standard hook.

Similarly, the 90° hooks, in all used configurations are also deficient. According to ACI 318-11 standard hooks are bent 90° plus a $12d_b$ extension measured from the free end of the bar, as shown in Figure 3.11. Furthermore, the development length l_{dh} from the joint interface should be taken as the larger of:

$$l_{dh} = \begin{cases} \left(\frac{0.24 f_y}{\sqrt{f'_c}} \right) d_b \\ (0.043 f_y) d_b \end{cases} \quad (3.2)$$

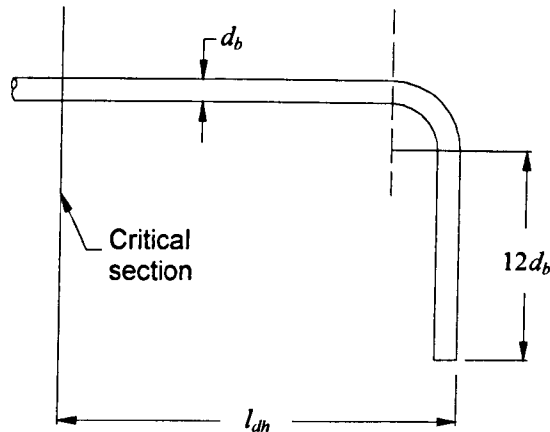


Figure 3.11 Details for development length of standard hooks (ACI 318-08, 2008)

The initial shear and flexural calculations for both beams and columns considered f_y to be 500MPa, f'_c to be 18MPa and d_b to be 16mm. This corresponds to a hook development length (required) within the joint, l_{dh} equal to $\approx 28d_b$ (450 mm). Table 3-1 compares the joint steel details for all the test specimens with the current ACI code requirements (it should be noted that the ACI 318-11 requirements are the same as the ACI 318-08).

Table 3-1 Joint steel details in comparison to the current ACI code

			l_d (mm)	Extension (mm)	Notes	
Beam	A	top	90° hook	214	122	
		bottom	Straight	214	-	**
	B	top	90° hook	214	272	
		bottom	Straight	214	-	**
	C	top	90° hook	214	147	
		bottom	90° hook	195	147	
Top Column		lap splices	$25d_b = 400\text{mm}$	-		
ACI 318-11		90° hook	Eqn. (3.2) $\approx 28d_b = 453\text{mm}^*$	$12d_b = 192\text{mm}$		
		lap splices	$47d_b = 752\text{mm}$	-		

* l_{dh} reduces when using the actual f'_c .

** Not satisfied: A standard hook is required.

Furthermore, the adopted weak column strong beam design, along with the selected bar size, adds a new deficiency to the joint design with regard to the bond demand from the beam longitudinal bars within the joint. As the column depth to bar size ratio h_c/d_b for all joints is around 16, whereas ACI318-11, as previously mentioned in 3.2.3, limits this ratio to 20. Therefore, additional inelastic deformations related to bond deterioration were expected during these tests.

3.3.3 SPECIMEN CONSTRUCTION

The steel cages of all specimens were constructed according to the drawings shown in Figure 3.7 to Figure 3.10. The cages were assembled horizontally on a special table then transferred to the wooden forms in one piece. To avoid honeycombing during casting, a high frequency vibrator was used to consolidate the concrete. The specimens were covered after casting with wet hessian to avoid rapid evaporation of water and surface cracking. The specimens were allowed to cure for 5 days then removed from their moulds.

3.4 MATERIALS

3.4.1 CONCRETE

A special concrete mix was developed by Ahmad (2011) at the University of Sheffield to replicate the low strength concrete usually found in older buildings, especially in developing countries. However, due to the small capacity of the available concrete mixer, three full batches of concrete were needed to complete one specimen and that on its own is a major obstacle as it leads to inconsistent concrete throughout the specimen. Hence, concrete was ordered from a ready mix concrete company. Despite their best intentions, restrictions on the available resources, such as strength of aggregates and cement grades, prevented the goal strength from being achieved.

The first specimen was cast separately as a pilot test, in which the ordered mix was of grade C16/ 20, target slump S3, and the maximum aggregate size was 10mm. The main specimen along with sample cubes and cylinders were cast, cured, prepared and tested according to BS EN 12390-3 (2009). Initial uniaxial compressive tests on the sample cubes and cylinders after 3, 7 and 14 days, showed the expected concrete compressive strength to be within the acceptable range. However, due to many problems faced during the assembling of the loading apparatus, the test was delayed for six months resulting in a higher strength at the day of testing.

The sample cubes and cylinders underwent two types of tests to determine the concrete properties. Uniaxial compression tests were performed according to BS EN 12390-3 (2009) to determine the concrete compressive strength, whereas tensile splitting tests were performed according to BS EN 12390-6 (2000) to determine the concrete tensile strength. Table 3-2 shows

the test results of three 150x300 mm cylinders from concrete batch No.1 tested in uniaxial compression on the day of testing. Table 3-3 shows the concrete tensile strength for the pilot specimen JA-2 from four 150x300 mm cylinders.

Table 3-2 Concrete compressive strength of specimen JA-1 (Pilot test)

Sample №	f_c (MPa)	f_c [Mean] (MPa)	Standard deviation
1	25.2		
2	23.0	24.3	1.2
3	24.7		

Table 3-3 Concrete tensile strength of specimen JA-1 (Pilot test)

Sample №	f_{ct} (MPa)	f_{ct} [Mean] (MPa)	Standard deviation
1	2.9		
2	2.6	2.6	0.18
3	2.6		
4	2.4		

After testing the pilot test, two extra more moulds were constructed in order to cast the specimens in batches of three rather than casting them separately. This allows having specimens with comparable if not identical concrete strengths. The second batch had the same mix characteristics as the first batch. Three specimens were cast with plenty of sample cubes and cylinders to monitor the progress of concrete strength over time. Similarly to the pilot specimen, the average concrete compressive strength for each joint specimen was determined from three 150x300 mm cylinders on the day of testing, as shown in Table 3-4. The tensile splitting strength was determined from nine 150x300 mm cylinders, as shown in Table 3-5.

Table 3-4 Concrete compressive strength and modulus of elasticity of batch 2 specimens

Specimen №	f_c [Mean] (MPa)	Standard deviation	E_c (GPa)
JC-1	27.2	0.9	24.5
JB-1	31.1	1.8	26.2
JB-2	30.8	0.5	26.1

Table 3-5 Concrete tensile strength of batch 2 specimens

Sample №	f_{ct} (MPa)	f_{ct} [Mean] (MPa)	Standard deviation
1	2.5		
2	2.5		
3	2.4		
4	2.2		
5	2.2	2.4	0.22
6	2.9		
7	2.4		
8	2.6		
9	2.2		

In an attempt to achieve the desired lower strength, the third batch, which was used to cast the remaining three specimens, was ordered of grade C12/16. Despite using a lower concrete grade, the obtained results were still higher than the target strength. Table 3-6 shows the average strength of each of the remaining specimens based on three 150x300 mm cylinders on the day of testing. The tensile splitting strength like in batch No.2 was determined from nine 150x300 mm cylinders, as shown in Table 3-7.

Table 3-6 Concrete compressive strength and modulus of elasticity of batch 3 specimens

Specimen №	f_c [Mean] (MPa)	Standard deviation	E_c (GPa)
JA-2	31.0	0.3	26.2
JA-3	32.4	0.7	26.8
JC-2	32.6	0.6	26.8

Table 3-7 Concrete tensile strength of batch 3 specimens

Sample №	f_{ct} (MPa)	f_{ct} [Mean] (MPa)	Standard deviation
1	2.47		
2	2.36		
3	2.30		
4	2.16		
5	2.44	2.4	0.16
6	2.44		
7	2.55		
8	2.50		
9	2.74		

The concrete modulus of elasticity was determined according to BS EN 1992-1-1 (BSI EC2, 2004) from uniaxial compressive tests and results were verified according to ACI 318-08 (2008). Sample cylinders which were subjected to uniaxial compression tests were equipped with three LVDTs mounted parallel to their longitudinal axis. This setup was utilised for concrete batch No. 2 and 3 only. Table 3-4 and Table 3-6 show the modulus of elasticity for concrete batch No.2 and concrete batch No.3 specimens, respectively. Figure 3.12 shows the concrete compressive stress-strain relationship of two sample cylinders BN2 and BN3 from batch No. 2 and batch No. 3, respectively.

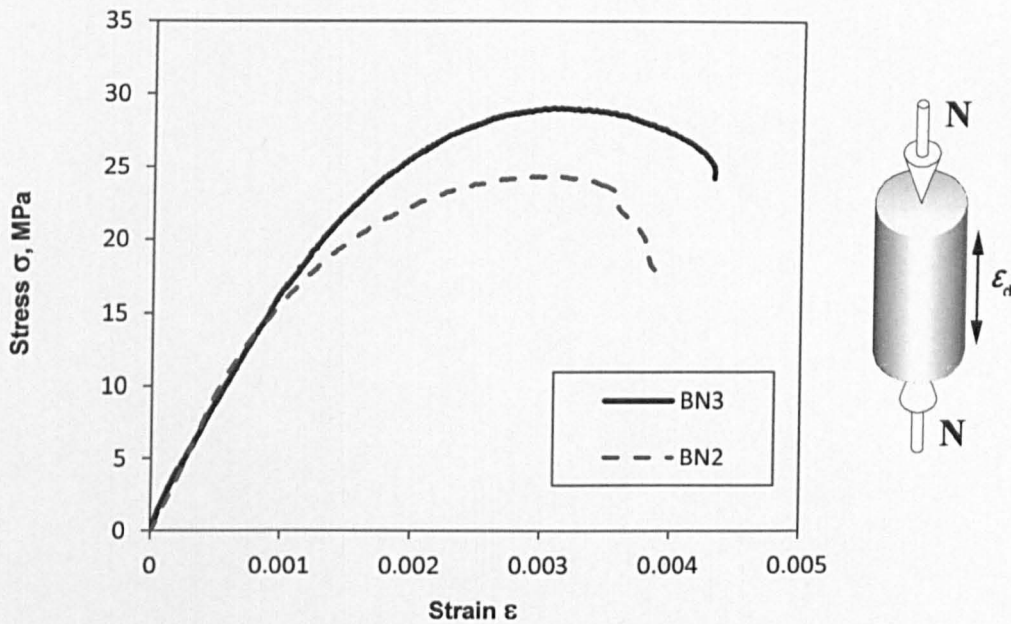


Figure 3.12 Concrete compressive stress-strain relationship for batch No. 2&3

A detailed description of the concrete properties of all the tested sample cylinders is reported in Appendix A.

3.4.2 STEEL REINFORCEMENT

Two different sizes of steel rebar were used in the test specimens. T16 rebar was used as the longitudinal reinforcement for both columns and beams, whereas T8 was used for the shear links. Due to the time gap between the construction date of the pilot specimens and the construction date of the rest of the specimen, two different batches of T16 rebar were used. Moreover, the shear design of both the column and the beam called for T8; however the only available option at the time of fabrication of the pilot specimen JA-1 was T10 and thus was used.

The yield strength (f_y) and the ultimate strength (f_u) of the main longitudinal reinforcement are shown in Table 3-8, in which (A) denotes the reinforcement of the pilot specimen while (B) refers to the main reinforcement of the remaining six specimens. Figure 3.13 shows the typical stress-strain relationship of the main longitudinal reinforcement.

Table 3-8 Test specimens main reinforcement properties

Bar size (mm)	f_y (MPa)	ϵ_y	ϵ_{sh}	ϵ_u	f_u (MPa)	E_s (GPa)
16A	478	0.0024	0.023	0.09	616	198
16B	554	0.0024	0.020	0.10	756	230

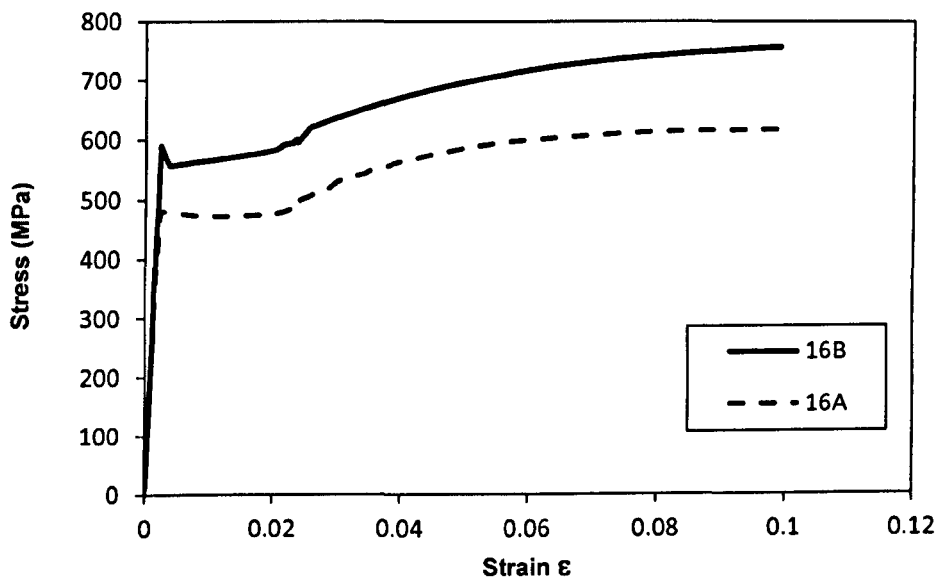


Figure 3.13 Stress-strain relationship for the specimens' longitudinal reinforcement

Table 3-9 shows the yield (f_y) and the ultimate (f_u) strengths of the shear reinforcement used in the six remaining specimens. Figure 3.14 shows the typical stress-strain relationship of the specimen's shear reinforcement.

Table 3-9 Test Specimens shear reinforcement properties

Bar size (mm)	f_y (MPa)	ϵ_y	ϵ_u	f_u (MPa)	E_s (GPa)
8	616	0.0028	0.11	758	220
10	533	0.0027	0.09	654	197

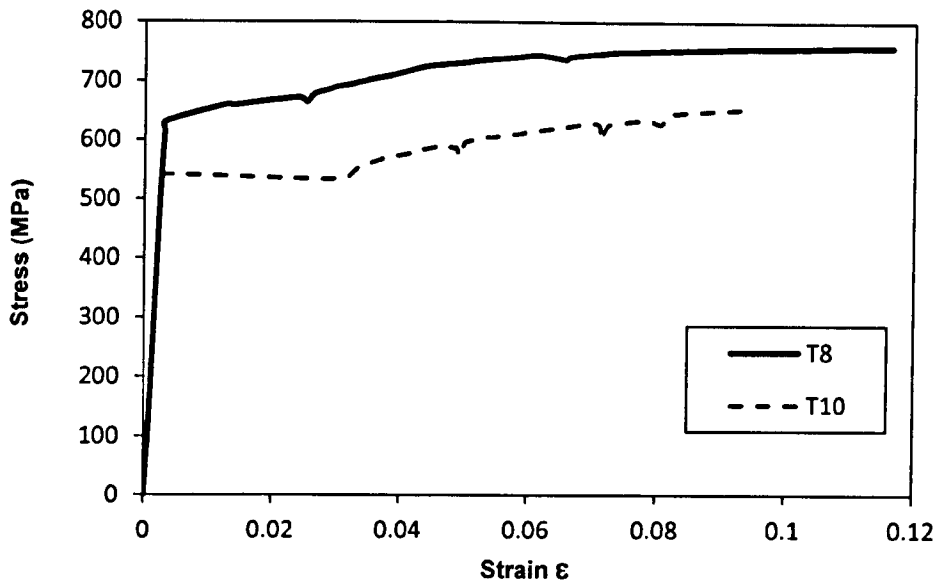


Figure 3.14 Stress-strain relationship for the specimens' shear reinforcement

Full properties and test results are shown in Appendix A.

3.5 INSTRUMENTATION

3.5.1 INTERNAL INSTRUMENTATION: Strain Gauges

Strain gauges were positioned at selected locations on the longitudinal and transverse reinforcement of both beam and columns. All locations were chosen to be within and around the perimeter of the joint core to accurately capture the behaviour of the joint during testing, through strain, stress and bond distributions.

The steel cage of each specimen was assembled and placed in the wooden form to accurately mark the locations of the strain gauges. Two types of strain gauges were used, 10mm for the longitudinal bars and 5mm for the transverse reinforcement. The location of each strain gauge was prepared by creating a smooth flat surface on the rebar's surface that was wider than the gauge's width and extended at least 3mm beyond the ends of the strain gauge. To create the smooth surface, filing was performed with different grades of metal files and sanding papers. The metal files were utilised to remove the first layers of coarse surface including part of the external ribs. Extra care was taken to minimise the reduction of cross sectional area.

Once the surface was well prepared and cleaned, the gauge was fixed using a special adhesive. An external twisted wire was attached to each strain gauge through a small connector located at the end of each strain gauge. These wires were bundled together and ran along the main reinforcement to the nearest end, whether it was a column or a beam. Moreover, to avoid disturbing the bond between the concrete and the steel reinforcement, the bundles were run a bit

loosely rather than tightly around the rebar. Extra care was taken during the casting process to avoid damaging or snapping any wire.

Two types of waterproofing materials were utilised in this experimental programme to keep the gauges free from moisture. A rubber sealant was used to cover the strain gauges and their connectors in the pilot specimens JA-1, as shown in Figure 3.15.a. However, it was found that this type of material was difficult to apply. Therefore, and to avoid covering a larger area than intended, Araldite was used for the rest of the specimens, as can be seen in Figure 3.15.b.

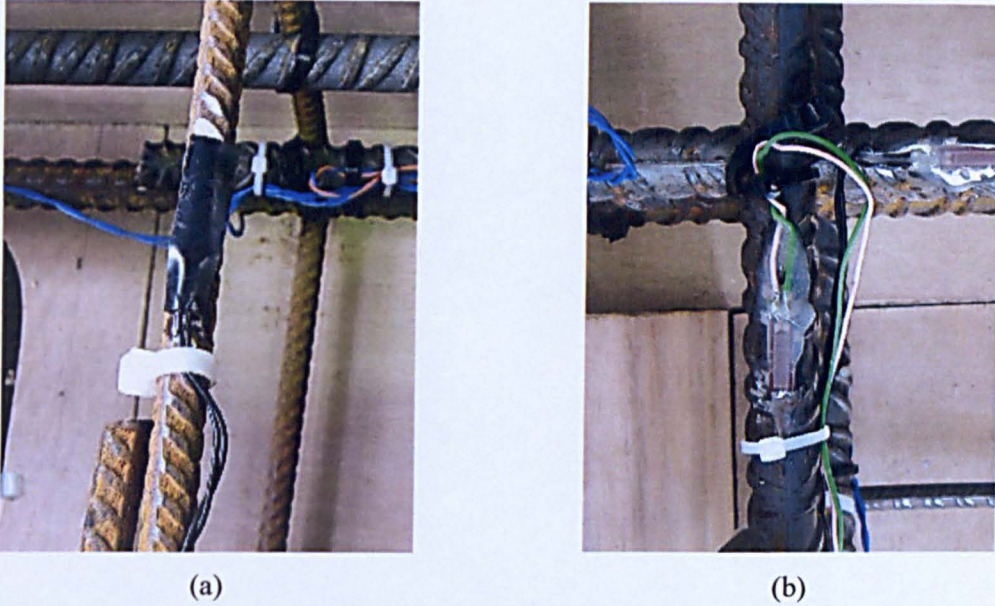


Figure 3.15 Types of waterproofing material for strain gauges (a Rubber sealant, (b Araldite)

In order to study which locations represent best the joint nonlinear behaviour, and to provide the necessary redundancy to compensate for any case of gauge failure, extra strain gauges were utilised in the pilot specimen. A total of 50 strain gauges were used. Figure 3.16 shows the locations of strain gauges of the pilot specimen JA-1, in which C and B refer to the longitudinal reinforcement of the column and beam, respectively. Moreover, for the case where two strain gauges are placed at the same location but on two parallel bars, the strain gauge is denoted with two sequential numbers, as shown in Figure 3.16.

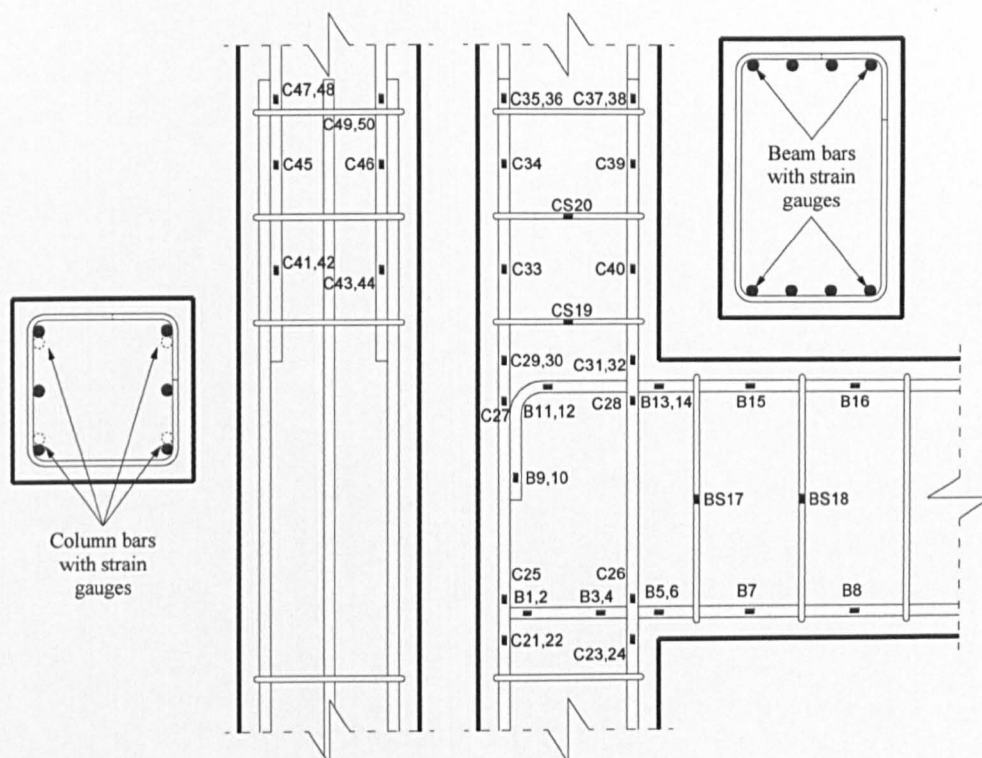


Figure 3.16 Strain gauge locations of the pilot specimen JA-1

After completing the pilot test and studying the response captured through the utilised strain gauges, some gauges and their locations were found to be unnecessary. Consequently, for the rest of the specimens, the total number of strain gauges was reduced. Furthermore, it was found that placing the strain gauges on the interface plane between the beam and the column led to a premature failure in some of the strain gauges. Therefore, and to avoid losing the data of such crucial gauges, some modifications to the locations were introduced. This was done by moving the gauges in question slightly away from the interface plane. The main changes to the strain gauge locations between the original distribution of the pilot test and the revised one for JA-2 & JA-3 are pointed out in Figure 3.17.

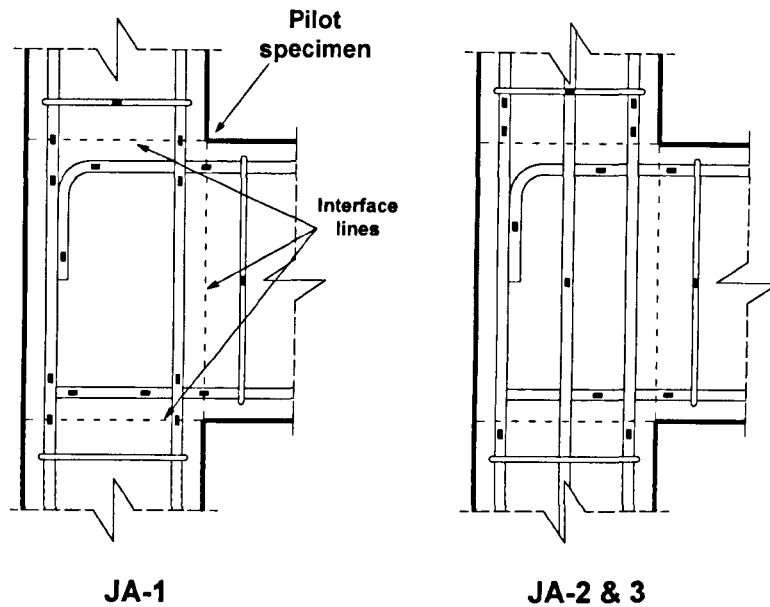


Figure 3.17 Strain gauge locations: the old and the revised distribution

Figure 3.18 shows the locations of the strain gauges of specimens JA-2 and JA-3. The total number of installed gauges was 35. The beam longitudinal bars and the spliced bars of the top column were heavily equipped with strain gauges. In addition, four small strain gauges were installed on the shear links around the joint core.

Strain gauges were numbered in an ascending manner for each face starting from the bottom column. The same rule applies for gauges located on the column shear links. Moreover, the beam strain gauges were numbered in a horizontal manner where numbers increased from right to left. However, for the beam shear links, numbers increased from left to right, as shown in Figure 3.18.

Similarly to JA-2 and JA-3, Figure 3.19 shows the distribution of the strain gauges of specimens JB-1 and JB-2. This distribution is identical to JA-2 and JA-3. The only difference between the two is the location of gauges C29/30 which was moved down due to the extended length of the 90° hook.

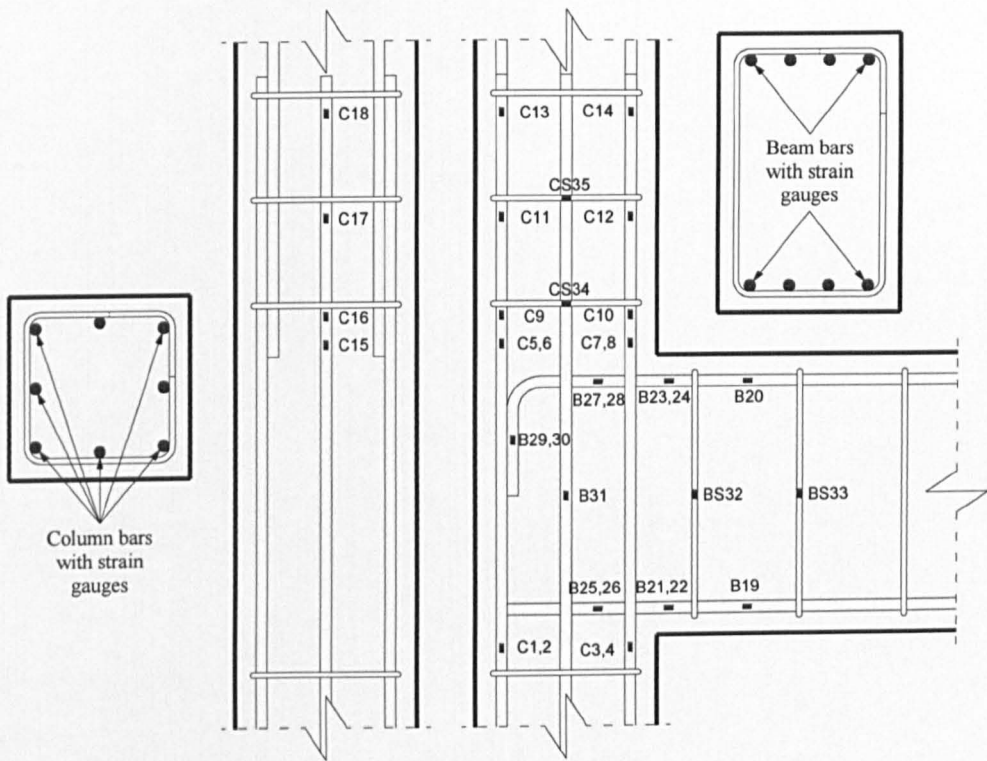


Figure 3.18 Strain gauge locations for JA-2 & JA-3

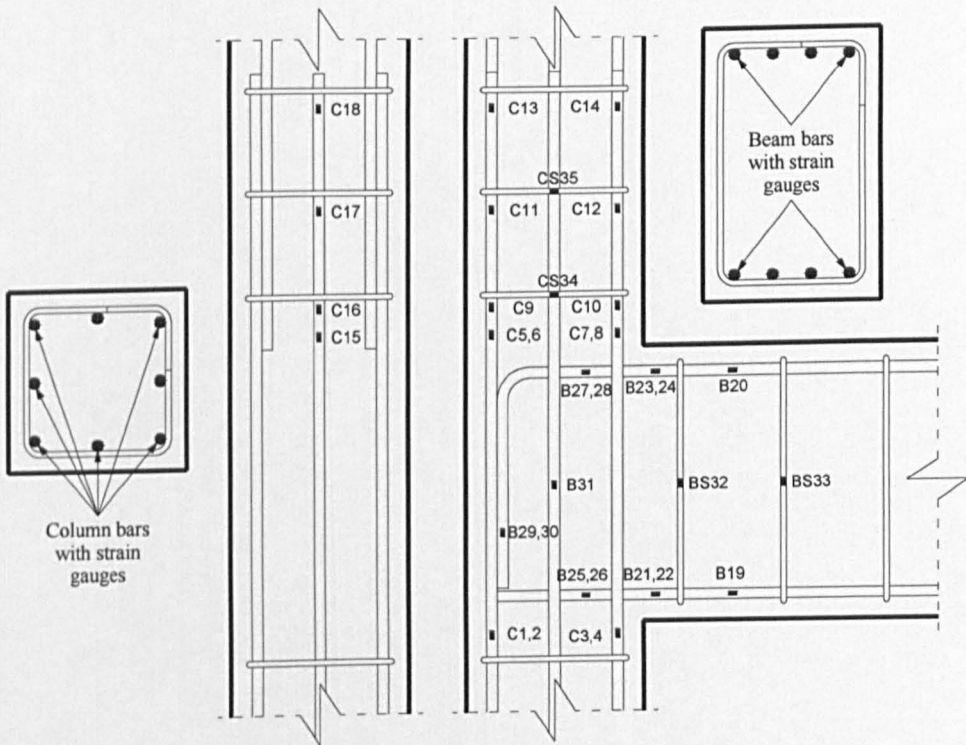


Figure 3.19 Strain gauge locations for JB-1 & JB-2

Figure 3.20 shows the locations of the strain gauges of specimens JC-1 and JC-2. The specimens were equipped with a total number of 37 strain gauges. This distribution is identical to the strain gauges distribution of specimens JA-2 and JA-3. The two extra strain gauges were placed near the end of the bottom beam hook, as shown in Figure 3.20.

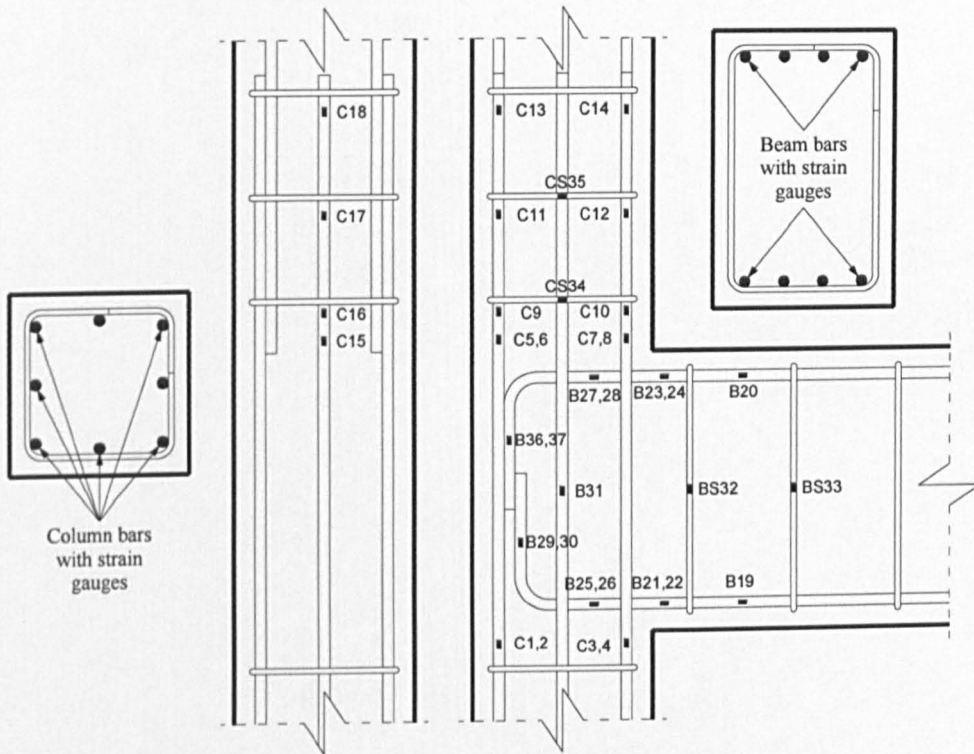


Figure 3.20 Strain gauge locations for JC-1 & JC-2

3.5.2 EXTERNAL INSTRUMENTATION

3.5.2.1 LVDTs

A total of 16 linear variable differential transducers (LVDT) were positioned on the front face of each of the seven specimens. Steel angles with extended steel rods were used to mount the LVDTs on the specimens. The angles were fixed to the specimen's side faces via two, equally distanced from the centre, threaded rods that were anchored 10 cm deep in the concrete.

The LVDTs were arranged in order to monitor the joint core, the beam-end region, and the lap splice region of the upper column. Figure 3.21 shows the LVDT configuration used for all the specimens.

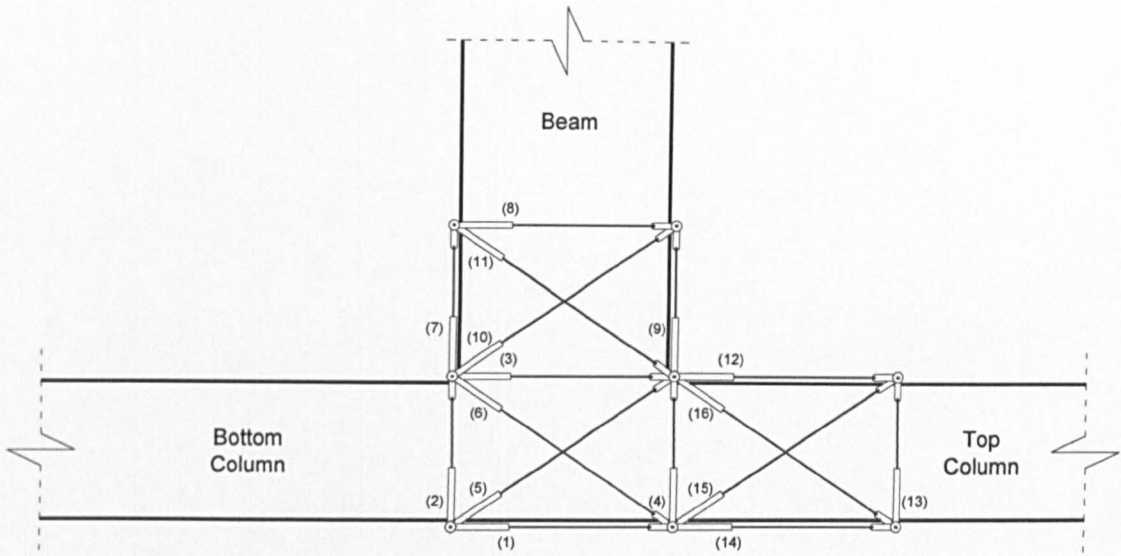


Figure 3.21 LVDT configuration

3.5.2.2 Displacement Transducers

Displacement transducers (DT) were installed on the surface of all seven specimens in the configuration shown in Figure 3.22. Two types of displacement transducers were used in this configuration. The first type was a 20 cm stroke displacement transducer and this was installed at the end of the beam to measure the beam end deflection. The second type of displacement transducers had a 10 cm stroke and was utilised to measure beam average curvature, rotation along the whole length of the beam, beam tip deflection, joint rotation, and the rigid body movement of the whole specimen. To avoid friction, for each displacement transducer, either a steel angle or a steel plate was fixed on the concrete at the point of contact. However, when spalling or extensive concrete damage was expected, like in the case of the two vertical displacement transducers at the bottom of the specimen, a different setup was used, as explained in 3.5.3.2.

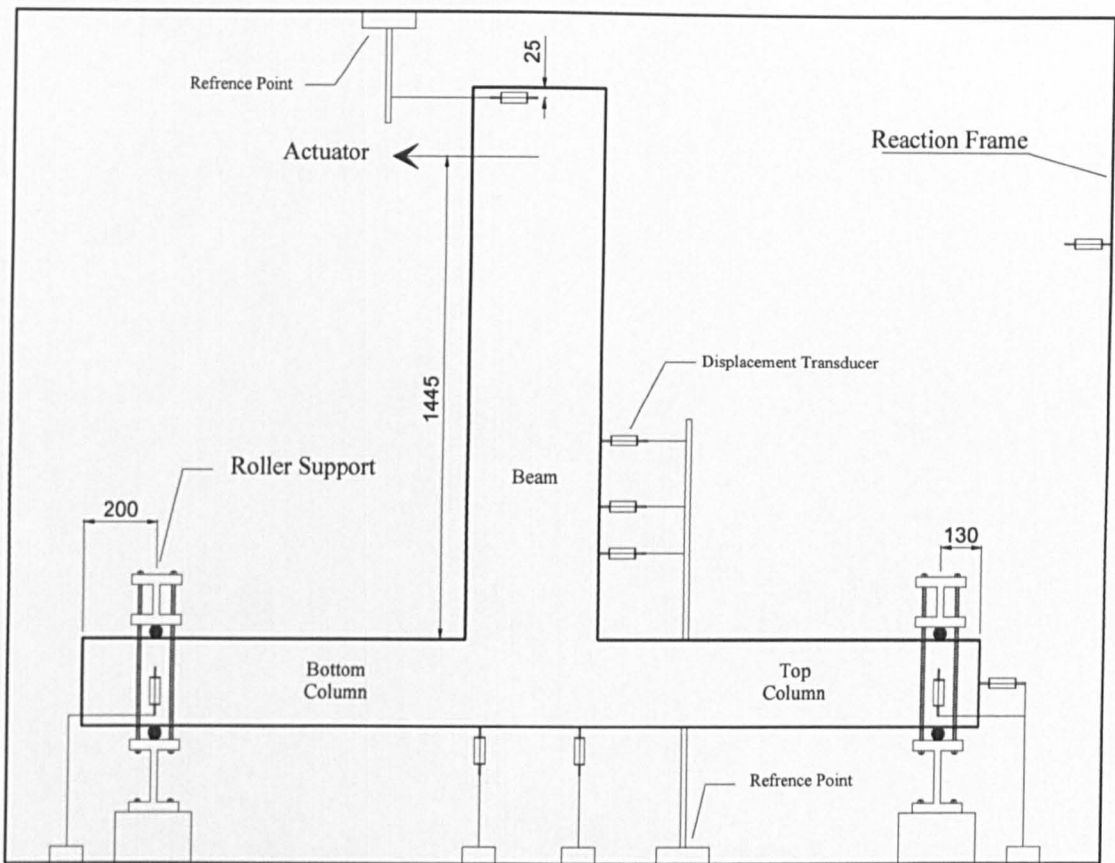


Figure 3.22 Displacement transducers configuration

3.5.3 JOINT PERFORMANCE PARAMETERS

3.5.3.1 JOINT SHEAR STRAIN

A joint shear rig consisting of six LVDTs were used to measure joint shear strains in all the tested specimens. By applying the Law of Cosines on this LVDT configuration, four values of joint shear strain can be calculated. The method is based on decomposing the shear rig into four different triangles. Each triangle has a diagonal, vertical and a horizontal LVDT. Figure 3.23 shows a typical LVDT configuration and the method of calculation.

By using the original lengths of the triangle sides and the new deformed lengths after adding the LVDT readings, the joint shear strain from this triangle can be calculated using the following equations:

The Law of Cosines

$$D^2 = H^2 + V^2 - 2HV \cos \theta \quad (3.3)$$

By rearranging the previous equation, the angle of the original triangle between the horizontal and vertical LVDT can be calculated as follows

$$\theta = \cos^{-1} \left(\frac{H^2 + V^2 - D^2}{2HV} \right) \quad (3.4)$$

Similarly, the angle of the deformed triangle will be

$$\theta_d = \cos^{-1} \left(\frac{H_d^2 + V_d^2 - D_d^2}{2H_dV_d} \right) \quad (3.5)$$

where H, V and D are the horizontal, vertical and the diagonal lengths of the original triangle, respectively, while H_d, V_d and D_d are the new lengths of the deformed triangle.

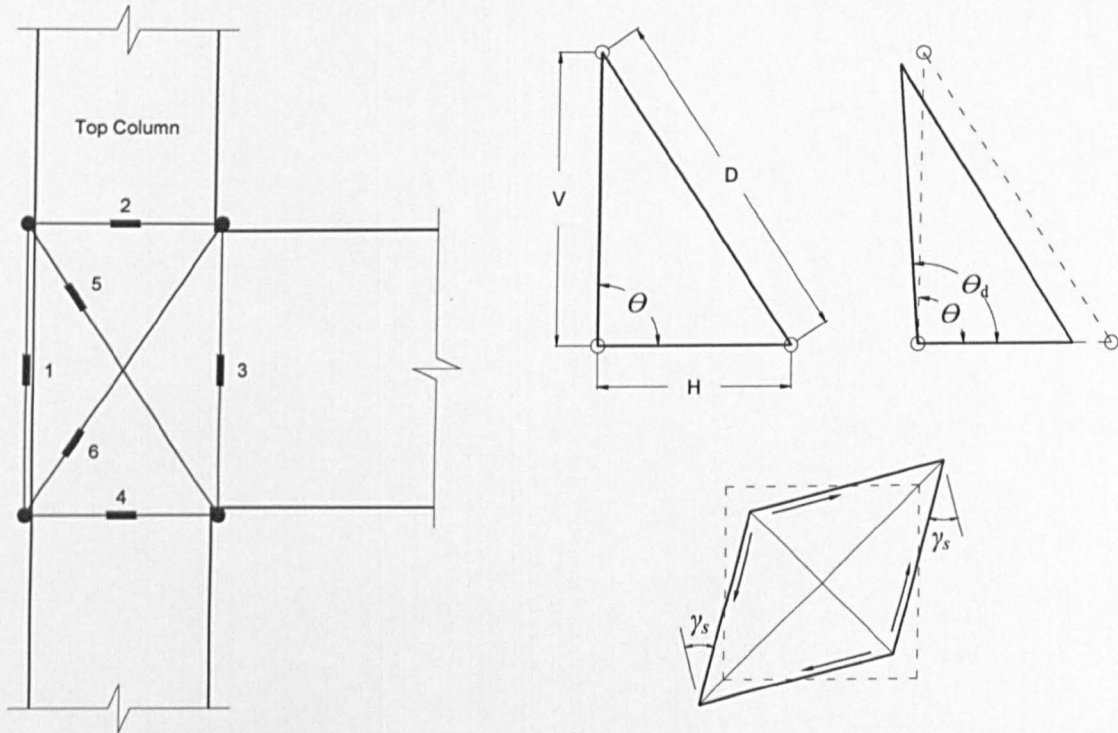


Figure 3.23 LVDT configuration for joint shear strain measurement and method of calculation

The joint shear strain, γ_s for each triangle can then be calculated as follows

$$\gamma_s = \theta_d - \theta \quad (3.6)$$

By repeating the same procedure for all the four triangles, the final joint shear strain value can then be obtained by averaging these four values.

3.5.3.2 Joint Global Rotation

Joint global rotation (θ_{gR}) for all the tested specimens was measured, during the tests, using the readings of two vertically positioned displacement transducers (DT). These displacement transducers were mounted on a fixed reference frame and connected to the centreline of the joint bottom face at a distance a (5 cm) from the top and bottom column-joint interfaces, as shown in

Figure 3.24. In order to avoid friction between the LVDT and the concrete surface, threaded steel rods with thin steel plate ends were anchored to a depth c (6 cm) into the concrete at the point of connection. Based on this configuration, the joint global rotation can be calculated as follows

$$\theta_{gR} = \frac{\Delta L}{h_b - 2a} \quad (3.7)$$

where ΔL is the difference between the two LVDT measurements, h_b is the beam height, and a is the distance between the LVDT and the joint interface.

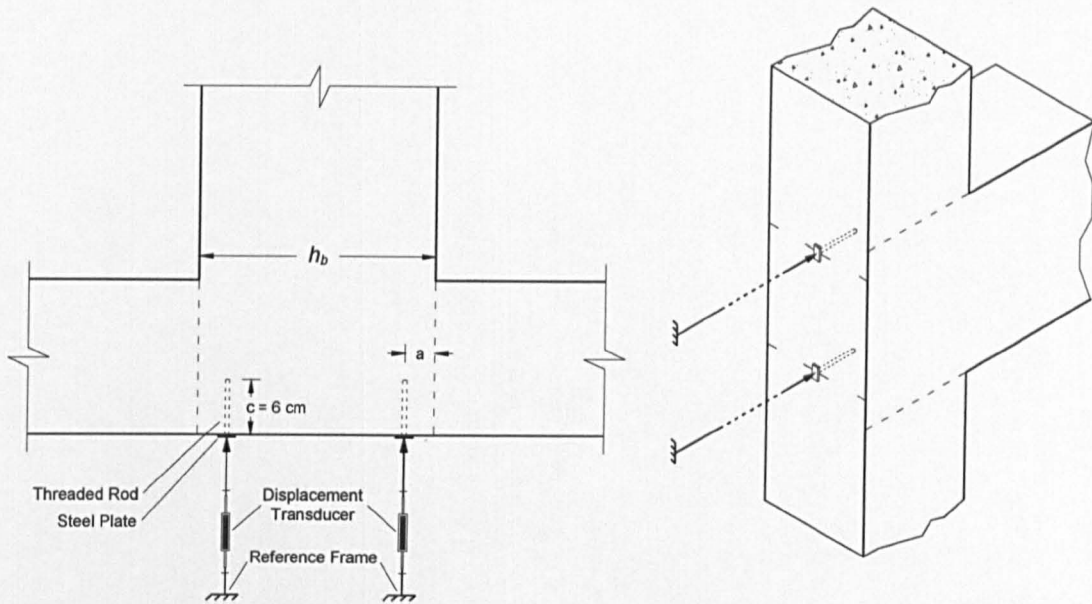


Figure 3.24 DT configuration for joint global rotation measurement

3.5.3.3 Beam Relative Rotation

Beam relative rotation to the joint (θ_{bR}) was measured using the readings of two LVDTs parallel to the beam's main axis, as shown in Figure 3.25. The LVDTs were connected to the beam side faces using steel angles with anchored threaded steel rods, as explained in section 3.5.2.1, at a distance equal to the column depth h_c from the joint-beam interface. Similarly, the LVDTs were connected to the top and bottom columns at a distance b ($=12\text{mm}$) from the beam faces. By neglecting the joint effect within the bottom and top (b) distances, the beam relative rotation to the joint was calculated as follows:

$$\theta_{bR} = \frac{\Delta L}{h_b + 2b} \quad (3.8)$$

where ΔL is the difference between the readings of the top and bottom LVDTs and h_b is the beam depth.

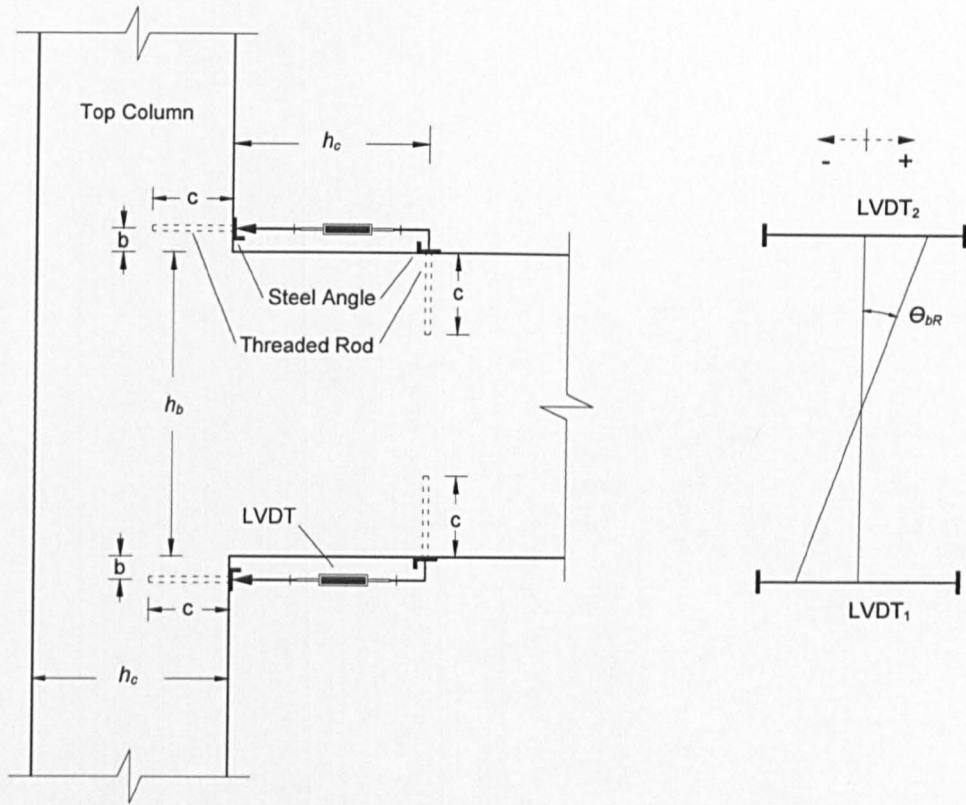


Figure 3.25 LVDT configuration for the measurement of beam rotation relative to the joint

3.5.3.4 Beam Average Curvature

Beam average curvature was measured for the monitored segment adjacent to the beam-column interface. The curvature was calculated by using the readings of the two LVDTs parallel to the main axis of the beam. Based on Eq (3.8), beam average curvature was calculated as follows:

$$\phi_b = \frac{\theta_{bR}}{h_c} \quad (3.9)$$

where θ_{bR} and h_b are as before.

3.5.3.5 Bond-Slip

The two LVDTs mounted parallel to the beam main axis are used as a direct measurement for anchorage-slip of the beam longitudinal reinforcement, as shown in Figure 3.26. The measured anchorage-slip Δ_{slip} consisted of deformations caused by bar pull-out Δ_{pull} and bar elongation $\Delta_{elongation}$, as follows:

$$\Delta_{slip} = \Delta_{pull} + \Delta_{elongation} \quad (3.10)$$

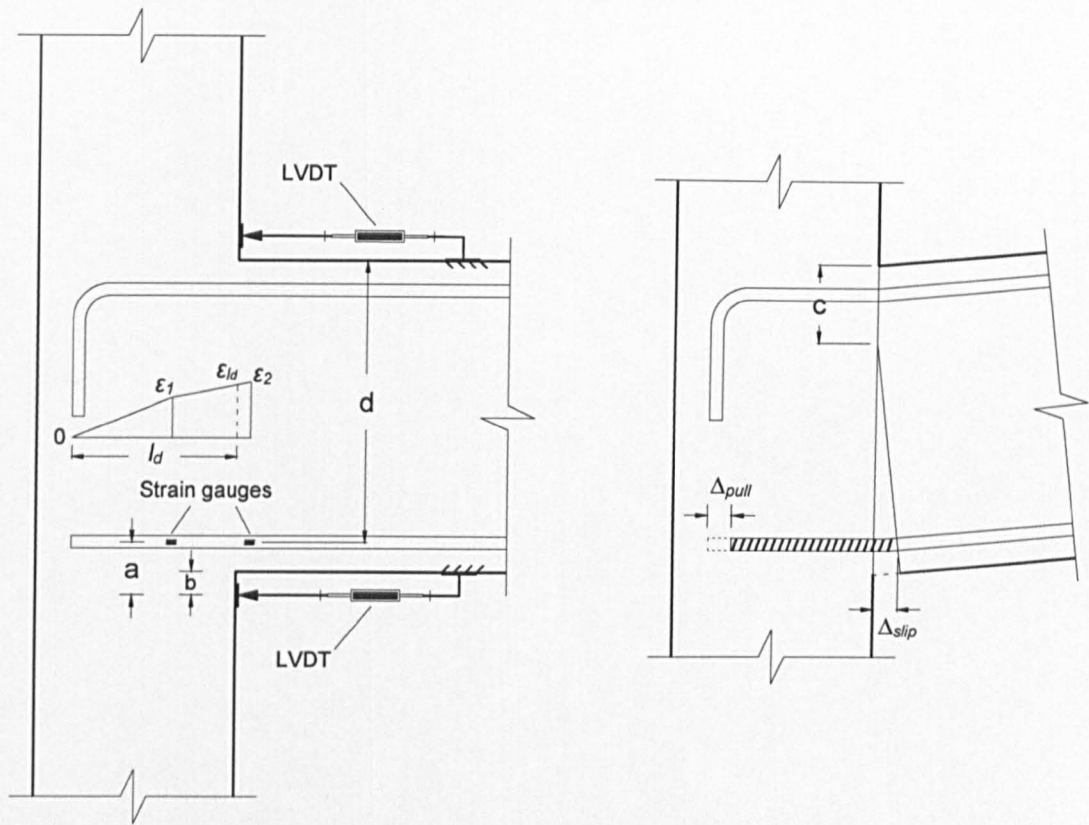


Figure 3.26 Anchorage-Slip mechanism at the joint interface

By using the measurements from the top and bottom beam LVDTs and beam relative rotation (θ_{bR}) from Eq (3.8), the total anchorage-slip deformation can be calculated as follows:

$$\Delta_{slip} = \theta_{bR} \cdot (d + b - c) \quad (3.11)$$

The beam compression zone, c can be calculated from geometry as follows:

$$c = \frac{\Delta_2}{\Delta_2 - \Delta_1} \cdot (h_b + 2b) \quad (3.12)$$

where Δ_1 and Δ_2 are the readings (with their signs) of the first (bottom) and second (top) LVDTs, respectively. Figure 3.27 illustrates the sign convention for the LVDT reading.

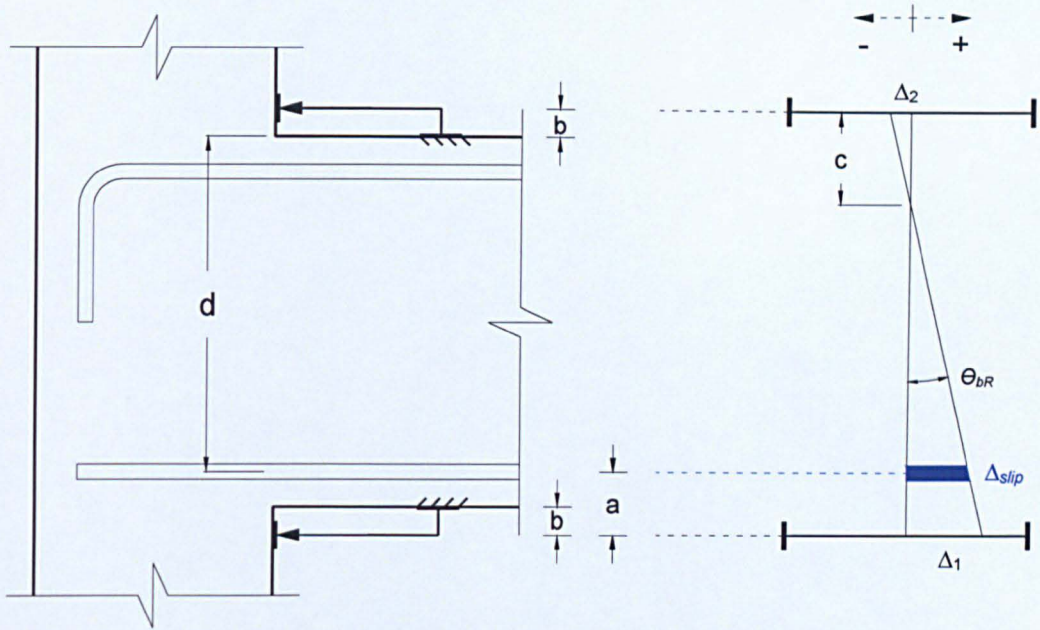


Figure 3.27 Bond-Slip measurement

The adopted method of measurement lacks the ability to separate the contributions of each of the anchorage-slip components. Therefore, in this study, the bar elongation component $\Delta_{elongation}$ is quantified by using the bar strain distribution obtained from strain gauges, as shown in Figure 3.28. The bar elongation can be calculated using the following equation:

$$\Delta_{elongation1} = \int_0^{l_d} \varepsilon (dx) = A_1 + A_2 + \dots \quad (3.13)$$

where ε is the bar strain and l_d is the bar embedment length within the joint core.

Figure 3.28 shows the elastic strain distribution of the beam bottom longitudinal bars in typical group A joint. Since strain gauges were installed on two of the bottom beam longitudinal bars, the final value for bar elongation was taken as:

$$\Delta_{elongation} = (\Delta_{elongation1} + \Delta_{elongation2})/2 \quad (3.14)$$

where $\Delta_{elongation1}$ and $\Delta_{elongation2}$ are the value of bar elongation for the first and fourth beam longitudinal bars, respectively.

It should be noted that this procedure conservatively ignores bar elongation within the monitored length of the beam, on the basis that bar stresses are low. However, if strain gauges are provided within this monitored length, bar elongation within the beam should be calculated and subtracted from the total measured slip.

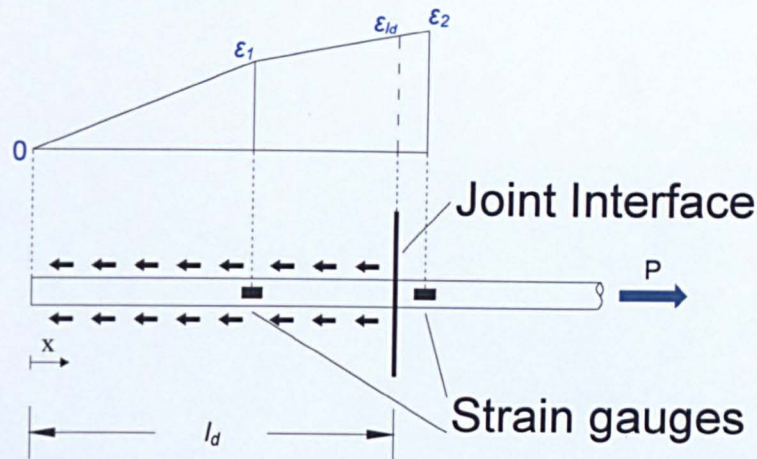


Figure 3.28 Strain distribution of beam bottom bar

The bar pull-out Δ_{pull} is considered to be the difference between the total measured slip and bar elongation, as follows:

$$\Delta_{pull} = \Delta_{slip} - \Delta_{elongation} \quad (3.15)$$

It should be noted that this proposed method assumes a gap opening at the joint-beam interface, as shown in Figure 3.26. For the cases where cracking starts within the joint panel first, this method is no longer valid, as the LVDTs will be measuring the width of the joint shear cracks rather than slip of the bars.

The succeeding Chapter (i.e. Chapter 4) shows that all the tested specimens experienced pure shear failure (*J-Type* failure) and that shear cracks developed at an earlier stage and that no joint-beam interface cracks occurred. Based on this, and as discussed in the preceding paragraph, slip calculation are no longer possible and therefore not included in this research.

3.5.3.6 Stiffness Degradation

The stiffness degradation of a joint can be assessed by calculating the peak-to-peak stiffness (K_p) for every load-drift hysteretic loop. Figure 3.29 shows a line connecting the positive and negative maximum peak drift values for one load-drift cycle. By definition the peak-to-peak stiffness (i.e. secant stiffness) is the angle between this line and the positive x axis.

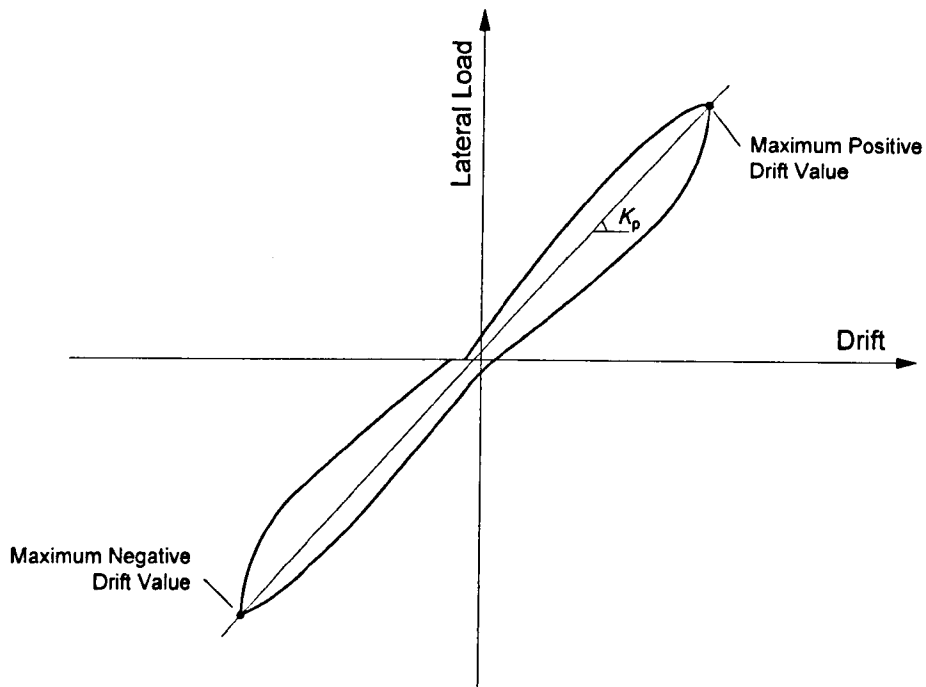


Figure 3.29 Definition of Peak-to-Peak stiffness

The secant stiffness of each half cycle positive and negative ($\pm K_{sec}$) is also assessed in this research. This stiffness is defined by the angle of inclination of the line that connects the point where the response curve intersects with the x axis and the maximum attained drift of that cycle for both negative and positive halves.

3.5.3.7 Energy Dissipation

The energy dissipated during every load-drift hysteretic cycle can be acquired by calculating the area enclosed within that cycle, as shown in Figure 3.30. Therefore, the cumulative dissipated energy for each test specimen can be obtained by integrating the load-drift hysteretic curve or in other words by adding up the dissipated energy of the following cycles throughout the whole test.

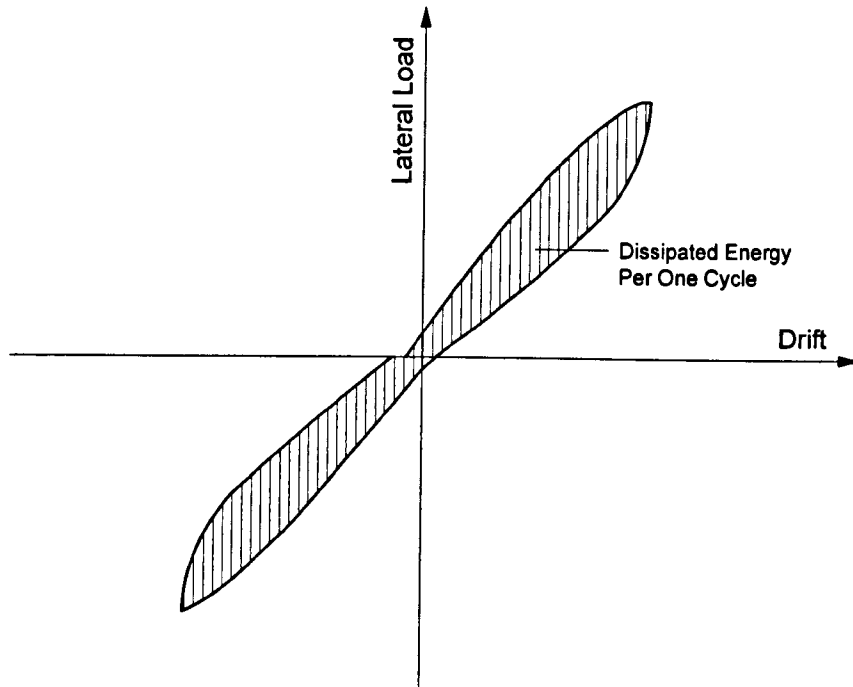


Figure 3.30 Definition of energy dissipation per one load-drift cycle

3.6 TEST SETUP

3.6.1 THE LOADING FRAME

Due to the limitations of the testing frame, the loading apparatus was designed to fit the specimen's column horizontally. The advantage of this, however, is that it allowed the use of a full scale specimen rather than 2/3 or 1/2 scale specimens. Figure 3.31 shows a detailed schematic of the loading apparatus.

Lateral loading was applied to the tip of the beam through a loading collar which consisted of two steel plates connected by two steel rods on each side. A load cell for measuring the applied cyclic load was fitted between the actuator and the loading collar. Moreover, two pins were provided, one before the actuator and one after the load cell, to allow free rotation during testing. A threaded socket was pre-installed before casting at the end of the beam in order to fit a guiding rod after de-moulding. Two angles were attached together and bolted to the top of the reaction frame providing a lateral restraint for the rod to prevent the specimen from going out of plane during testing. The axial load was applied at the end of the top column using a short hydraulic cylinder with a loading cell for load measurement, as shown in Figure 3.31. Roller supports were installed at the two ends of the columns to allow rotation and horizontal movements.

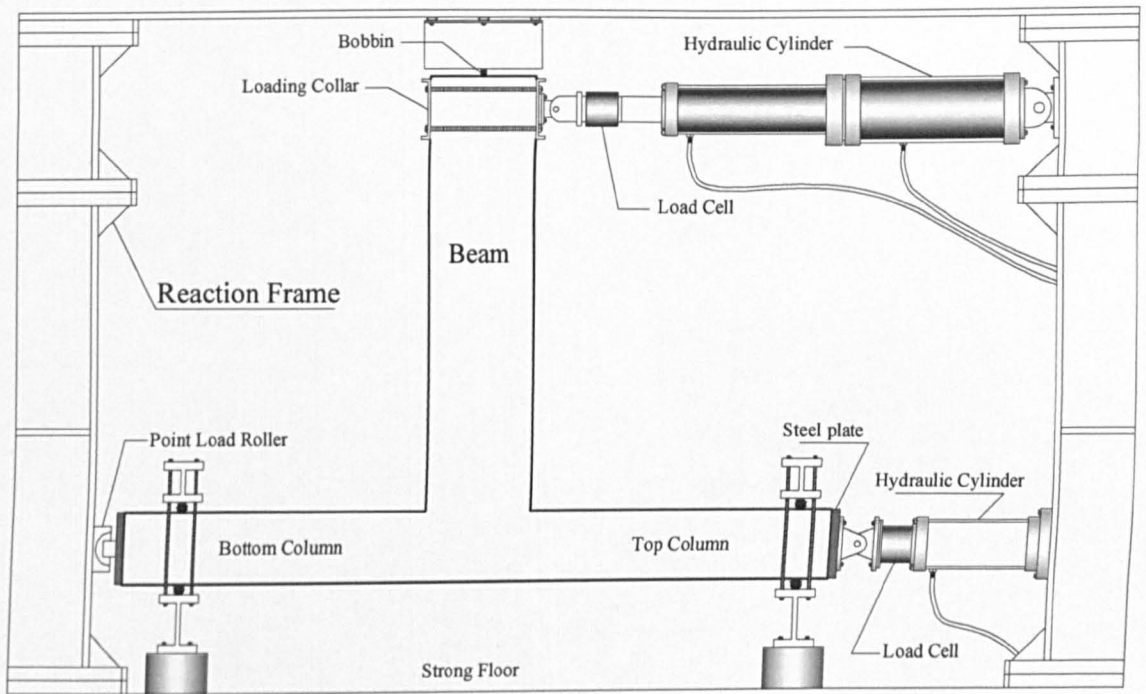


Figure 3.31 Loading apparatus

3.6.2 TESTING PROCEDURE

For all the seven specimens, the tests started by slowly applying the axial load through the small actuator to the end of the column. After reaching the target level of axial load, the load was reduced then increased again to the same level several times. This step was used to eliminate future horizontal rigid body movements and to check the instrumentation.

3.6.2.1 Axial Load

In order to study the effect of axial load on bond and shear stresses within the joint, two levels of axial load were utilised. The pilot test JA-1 and JA-2 were subjected to an axial compressive load equivalent to 150 kN, whereas the next identical specimen JA-3 was subjected to 250 kN. The same pattern of applied axial load was followed for the rest of the specimens. Furthermore, the small actuator was adjusted during the progress of each test to keep the applied axial load around the target level. Table 3-10 summarises the applied axial load levels to all test specimens.

Table 3-10 Test Specimens axial load ratio

Batch №	Specimen №	N (kN)	$\frac{N}{f'_c A_g}$	f'_c (MPa)
1	JA-1	150	0.09	24.30
	JC-1	150	0.08	27.18
2	JB-1	150	0.07	31.05
	JB-2	250	0.12	30.78
3	JA-2	150	0.07	31.03
	JA-3	250	0.11	32.41
	JC-2	250	0.11	32.57

3.6.2.2 Displacement History

The cyclic lateral load was applied in a quasi-static manner at the end of the beam by a long hydraulic actuator, as shown in Figure 3.31. The actuator had a maximum stroke of 21cm. Testing was continued until completing the cycles of all drift levels, or until losing more than 50% of the maximum load carrying capacity with extensive spalling and cracking, whichever happened first.

The tests were conducted in displacement control adopting the procedure outlined by PEER (Pacific Earthquake Research Center). The procedure for all specimens, except the pilot test, began with 0.1% drift cycles then 0.25%, 0.35%, 0.50%, 0.75%, 1.0%, 1.5%, 2.0%, 3.0%, 4.0% and finally 5% drift, as can be seen in Figure 3.32.

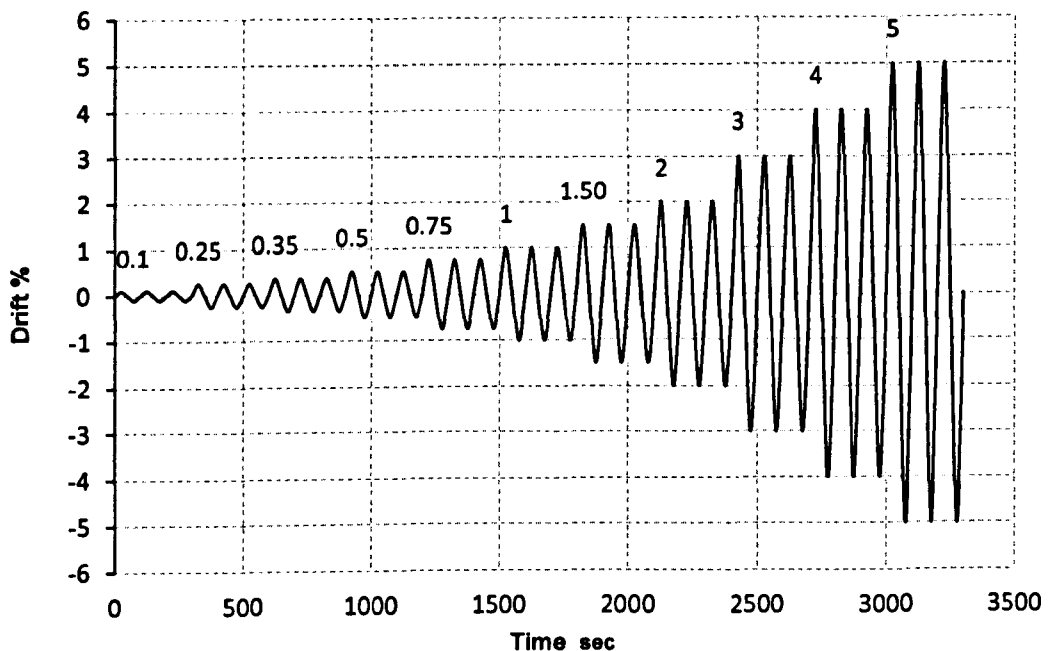


Figure 3.32 Loading history

Table 3-11 summarises the applied drift levels and beam tip displacement. Each drift step consisted of 3 complete cycles. The average time to complete one cycle was between 50 and 60 sec. However, for cycles where significant cracking occurred, extra time was needed for marking and recording the damage. Figure 3.32 shows the displacement history for all specimens except for pilot specimen JA-1.

Table 3-11 Drift Levels and beam tip displacement

Drift %	Beam tip displacement (mm)
0.10	1.7
0.25	4.2
0.35	5.8
0.50	8.4
0.75	12.5
1.00	16.7
1.50	25.1
2.00	33.4
2.50	41.8
3.00	50.1
4.00	66.8
5.00	83.5

For the pilot test, a different approach was applied. This test was intended mainly to check the initial design of the specimen in addition to testing the reliability of the installed instrumentation during testing. Hence, load control was employed for the first part of the pilot test, while displacement control was employed for the second part. The lateral load was applied in small increments of 5 kN.

CHAPTER 4

EXPERIMENTAL OBSERVATIONS AND DISCUSSION

4.1 INTRODUCTION

Seven exterior beam-column joints were subjected to quasi-static cyclic loading in order to study the effects of using different types of beam anchorages on the seismic shear performance of exterior beam-column joints with no shear links (i.e. unconfined).

Knowing the level of damage at each step offers key information that can be used to determine the response of existing buildings with similar joints. The following chapter describes the observed response in terms of hysteretic behaviour and progression of damage throughout the test for each specimen. The damage criteria and performance characteristics of the hysteretic behaviour are defined and explained. This includes description of lateral load-drift hysteretic response and backbone curve, stiffness degradation, shear stress-strain response curve, and dissipated energy. Furthermore, this chapter also discusses the effects of test variables on the seismic performance and hysteretic behaviour of deficient exterior beam-column joints, such as low column axial load variation ($<0.15f_c A_g$) and beam bar anchorage types.

4.2 DAMAGE CRITERIA

The damage progress of every test specimen was monitored and quantified according to the following damage criteria:

- Hairline cracking and first observed main crack
- First diagonal shear crack –significant change in the shear envelope/stiffness
- Maximum load carrying capacity
- Spalling of concrete cover
- Exposure of shear links or longitudinal reinforcement

- Failure: 50% loss in strength from the maximum achieved peak

Yielding of longitudinal reinforcement was excluded from the damage criteria since the test specimens were designed to fail mainly in shear. Tests were controlled manually so as to offer the freedom of stopping the test at any time throughout the test to measure and evaluate the condition of each specimen.

As a general rule, to mark and measure the width of any occurred cracks, the test was stopped at the end of each cycle at both positive and negative peaks of every displacement increment. However, additional stops were introduced whenever a drastic change in the behaviour was observed. The first displacement increment of 0.1% drift was carried out continuously, but fairly slowly to examine the instrumentations and check for any possible faults. All specimens showed no visible cracking during these first three cycles of 0.1% drift.

4.3 PERFORMANCE CHARACTERISTICS

The hysteretic behaviour of each test specimen can be assessed through several key performance characteristics, such as:

- Lateral load-drift response curve
- Stiffness degradation
- Joint shear stress vs. joint shear strain.
- Cumulative dissipated Energy

The lateral cyclic load applied at the tip of the beam is plotted against the drift % of the specimen. The drift, in this research, is defined as the ratio of the beam tip displacement Δ to the length of the beam L_b measured from the beam-joint interface, as shown in Figure 4.1.

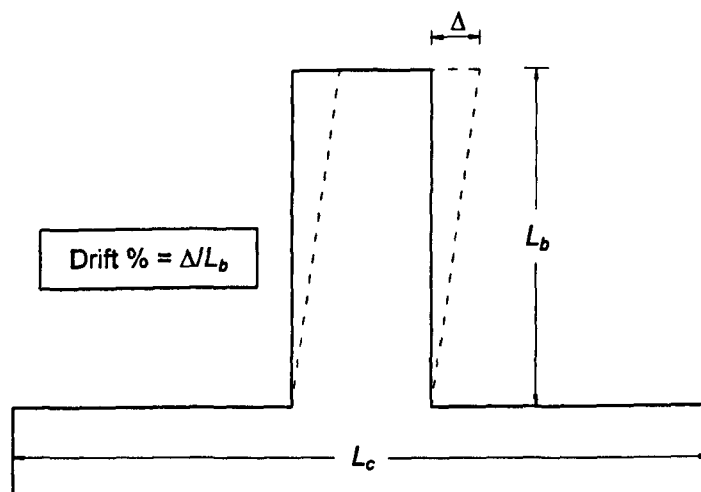


Figure 4.1: Definition of drift

The lateral load-drift response curve for each test specimen is assessed using the equivalent beam shear calculated based on the ASCE 41 shear provisions (see sections 2.4.2 and 2.7.1). Table 4-1 shows the nominal joint shear strength, V_n , and the equivalent beam shear, V_b , for all seven specimens according to ASCE 41 (ASCE/SEI 41, 2006).

Table 4-1 Joint nominal shear strength and beam shear, according to ASCE 41 (2006)

Specimen No	f'_c (MPa)	V_n (kN)	V_b (kN)
JA-1	24.3	166.6	43.5
JA-2	31.0	188.3	48.3
JA-3	32.4	192.4	49.4
JB-1	31.1	188.3	48.0
JB-2	30.8	187.5	47.8
JC-1	27.2	176.2	45.2
JC-2	32.6	192.9	49.2

The stiffness degradation of the test specimens throughout the test was evaluated using two types of stiffness measures (see section 3.5.3.6). The first type, denoted as “peak-to-peak stiffness K_p ”, is calculated for the first cycle of each drift increment. The second type, denoted as “half-cycle secant stiffness K_{sec} ”, is calculated for both halves of the first cycle of each drift increment.

To study the cyclic shear behaviour of the joint, the joint shear stress vs. the joint shear strain relationship is plotted for each test specimen. The average shear stress of each test specimen was calculated from both geometry of the specimen and moment equilibrium, as previously discussed in Chapter 2.

The ASCE 41 shear provisions are used to evaluate the joint shear strength of each test specimen. However, in addition to the nominal joint shear strength, ASCE 41 provisions include a generalised model that describes the overall joint shear stress-shear strain envelope curve under cyclic conditions (see section 2.7.1.2). Table 4-2 shows the model parameters for each test specimen calculated following the procedure outlined in ASCE 41, Table 6-9.

Table 4-2 Modelling parameters for test specimens according to ASCE 41 and ACI 369R

Specimen №	$P/f_c A_g^1$	V/V_n^2	Transverse Reinforcement ³	a (rad)	b (rad)	c
JA-1	0.09	2.4	NC	0.0050	0.0100	0.200
JA-2	0.08	2.1	NC	0.0050	0.0100	0.200
JA-3	0.07	2.1	NC	0.0050	0.0100	0.200
JB-1	0.12	2.1	NC	0.0047	0.0093	0.187
JB-2	0.07	2.1	NC	0.0050	0.0100	0.200
JC-1	0.11	2.2	NC	0.0048	0.0097	0.193
JC-2	0.11	2.1	NC	0.0048	0.0097	0.193

¹ P is the axial load on the top column; A_g is the cross sectional area of the joint

² V is the joint shear force calculated when the beam reaches yielding

³ nonconforming details (i.e. no shear links within the joint)

The energy dissipated by each test specimen is evaluated by plotting the cumulative dissipated energy at every load-drift hysteretic cycle. This can be obtained by adding up the dissipated energy of the consecutive cycles throughout the whole test (see section 3.5.37)

The benefit of evaluating these performance characteristics is that it offers key information on how each testing parameter affects the hysteretic behaviour of each joint. A detailed presentation of these performance characteristics for each test specimen is given in the following sections.

4.4 GENERAL CYCLIC BEHAVIOUR OF TEST SPECIMENS

4.4.1 SPECIMEN JA-1 & 2

In this research, specimen JA-1 is the pilot specimen and it was initially tested to only check the accuracy of the instrumentations and the initial design. The test was load controlled, as mentioned in Chapter 3. The initial behaviour, progression of cracking and peak strength are comparable to JA-2. In the following sub-sections, the description of damage and the hysteretic properties are presented.

4.4.1.1 Description of Damage

As for all the other specimens, specimen JA-2 was subjected to the same displacement history, as shown in Figure 3.32, except for JA-1 (see Chapter 3). The development of cracks for specimen JA-2 during the test, between 0.25% and 2.0% drift levels, are shown in Figure 4.2. The arrows denote the direction of positive loading. In case of specimen JA-1, the progression

of cracking was almost identical to specimen JA-2 up to the 1.5% drift level. Figure 4.3 shows the main damage events denoted on the cyclic load-drift response of specimen JA-2.

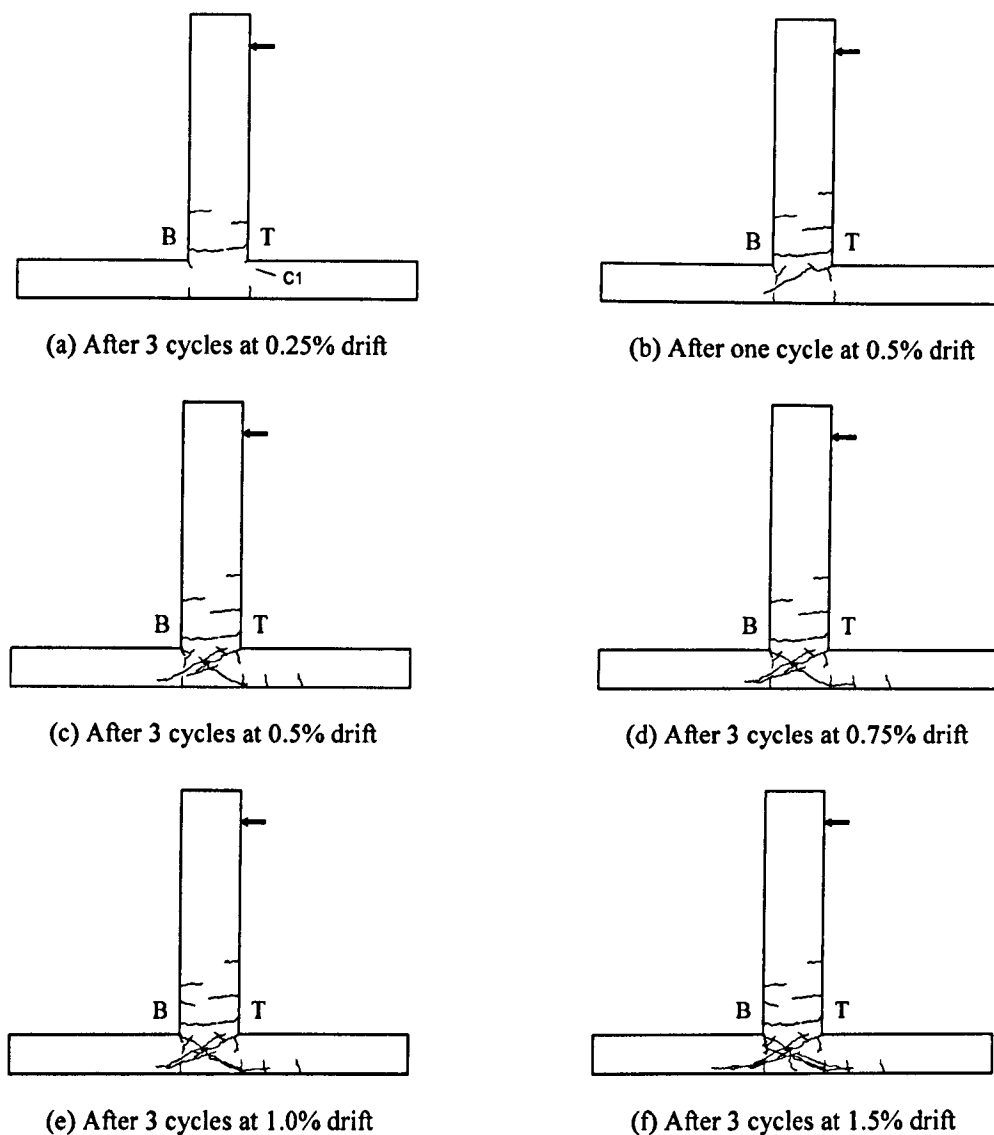


Figure 4.2: Progression of cracking for specimen JA-2

The first displacement increment of 0.1% drift is not presented in Figure 4.2 as no significant damage was recorded. However, hairline cracks of widths less than 0.1 mm appeared at several different locations.

During the first positive cycle at 0.25% drift cracks of width less than 1 mm were observed at the column-joint interface and at the location of the first and second shear links of the beam. In addition, a small inclined crack, denoted as C1, appeared at the corner of the beam-joint interface, (see Figure 4.2.a). A similar crack pattern was observed during the second half of the first cycle. However, the corner crack extended slightly further into the joint. This can be attributed to the difference between the top and bottom anchorage of the beam longitudinal reinforcement. Moreover, as the test continued, no additional cracks were observed.

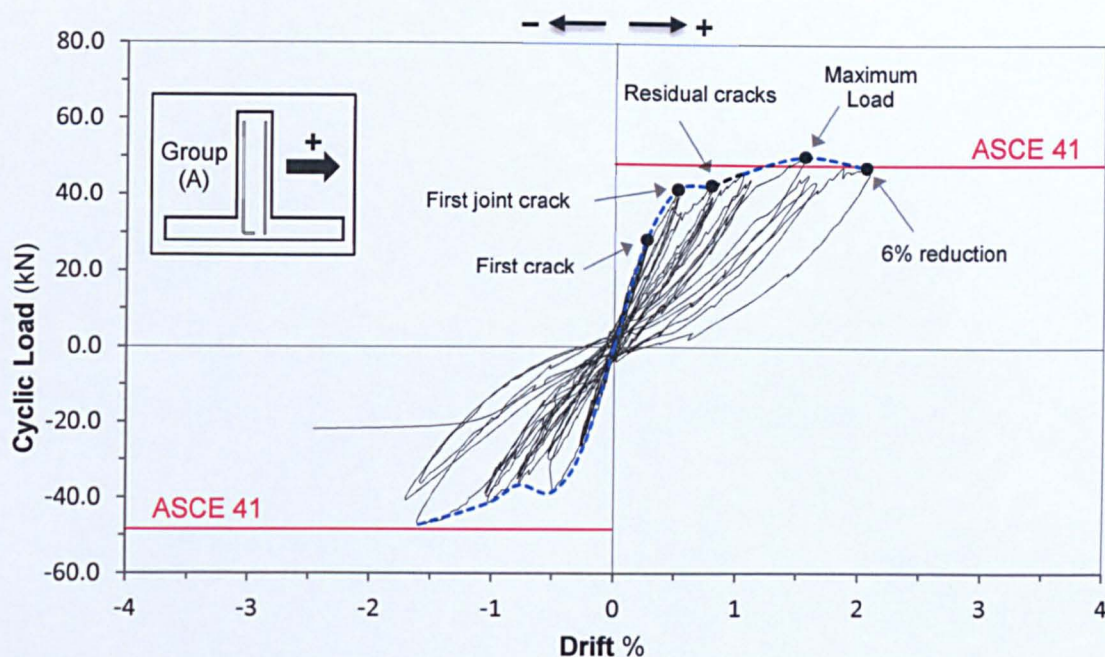
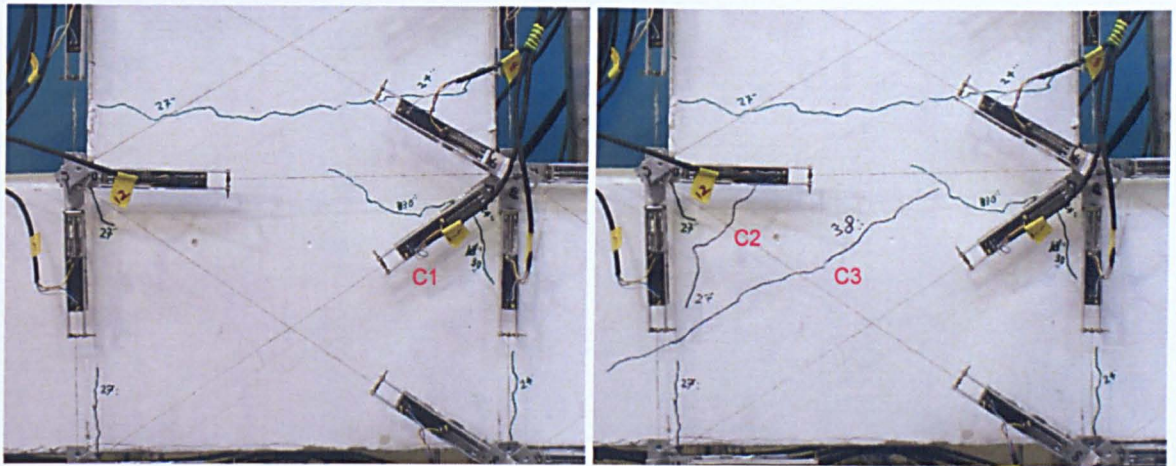


Figure 4.3: Lateral load-drift response for specimen JA-2

The first significant joint crack appeared when displacing the specimen to 0.5% drift. Figure 4.2.b shows the state of specimen JA-2 after completing one full cycle at 0.5% drift. At the first half of the first cycle, the inclined crack (C1) located at the corner of the beam top side extended further into the joint. However, the crack split into two branches following the paths of both the beam and column longitudinal reinforcement, as can be seen in Figure 4.4.a. The second half of the same cycle, however, exhibited far greater damage. As the negative loading increased beyond the previous increment, an inclined crack, denoted as C2, appeared near the bottom corner of the beam-joint interface followed by another diagonal crack (C3) extending from the beam to the bottom column, as can be seen in Figure 4.4.b. The effect of this diagonal crack is evident when comparing the change in the secant stiffness between the negative and the positive halves of the first cycle (see Figure 4.3).

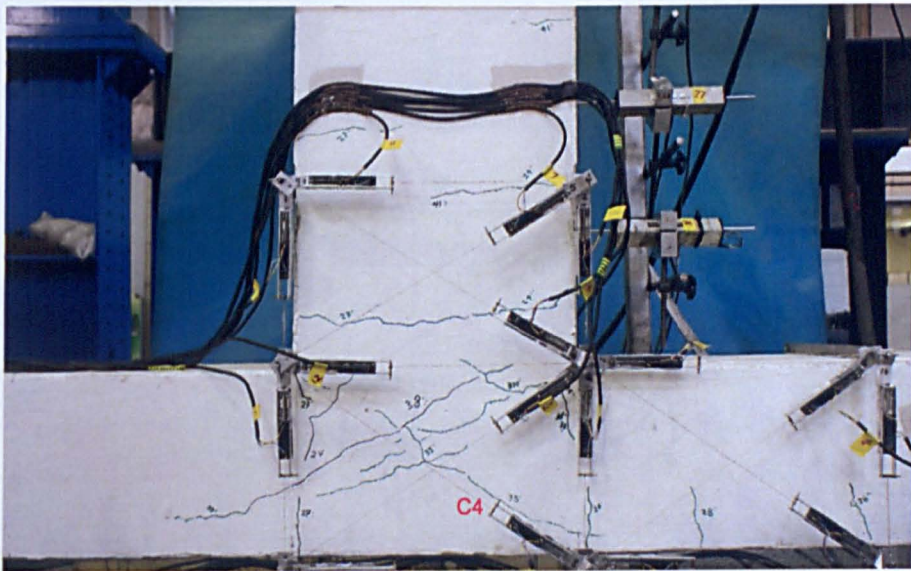


(a) Positive loading

(b) Negative loading

Figure 4.4: Specimen JA-2 after one cycle at 0.5% drift

The specimen continued to exhibit more cracks during the second and the third cycles at 0.5% drift, as shown in Figure 4.2.c. The number and length of cracks formed by negative loading (pulling) were significantly greater than what was caused by positive loading (pushing). Figure 4.5 shows the specimen after completing three cycles at 0.5% drift. Despite the increased damage during the second and the third cycle, the specimen showed no further strength or stiffness degradation beyond that reached during the first cycle (only for positive loading), see Figure 4.3.

**Figure 4.5: Specimen JA-2 after three cycles at 0.5% drift**

While displacing the specimen to 0.75% drift, the diagonal shear crack (C4) extended further from the bottom corner to the top column, as shown in Figure 4.6.a. Similar behaviour was observed during the second half of the first cycle, as the parallel diagonal cracks (C3, C5) widened and extended further into the bottom column, as can be seen in Figure 4.6.b. Moreover, no further damage was observed during the second and the third cycle. However, when the

specimen was brought to 0% drift at the end of the third cycle, residual cracks of widths between 0.5-0.9 mm were observed. Figure 4.2.d shows the crack pattern of specimen JA-2 after three cycles at 0.75% drift.

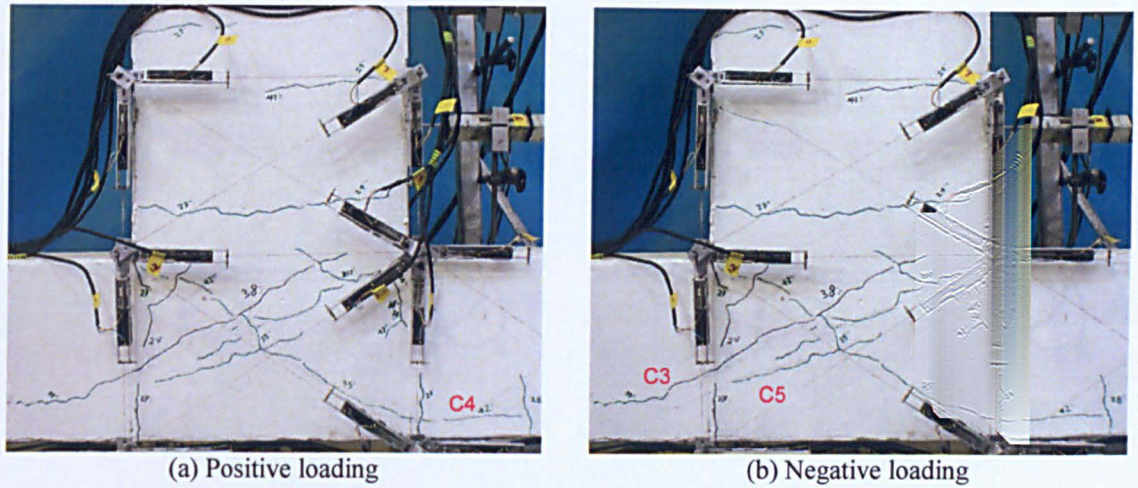


Figure 4.6: Specimen JA-2 after one cycle at 0.75% drift

More joint cracks formed during positive and negative loading of the first cycle at 1.0% drift. Existing cracks increased both in width and length, but when compared to the previous increment of 0.75% drift, the observed damage was rather limited. Although limited, the damage was enough to cause a significant stiffness reduction in the cyclic load-drift response (see. Figure 4.3).

No further damage was recorded during the remaining 2 cycles at 1.0% drift. The measured residual cracks at the end of the third cycle were around 1 to 1.5 mm wide. Figure 4.2.e shows the crack pattern of specimen JA-2 at the end of the 1.0% drift cycles.

Displacing the specimen to 1.5% drift level caused several new joint cracks to form, whereas existing joint cracks widened significantly. Figure 4.7.a shows specimen JA-2 at the first positive half cycle of 1.5% drift. The most notable change during this half cycle is the diagonal shear crack (C6) which started from the centre of the joint and extended into the top column. In addition, the specimen attained its maximum load carrying capacity during this cycle. No reinforcement yielding was observed.

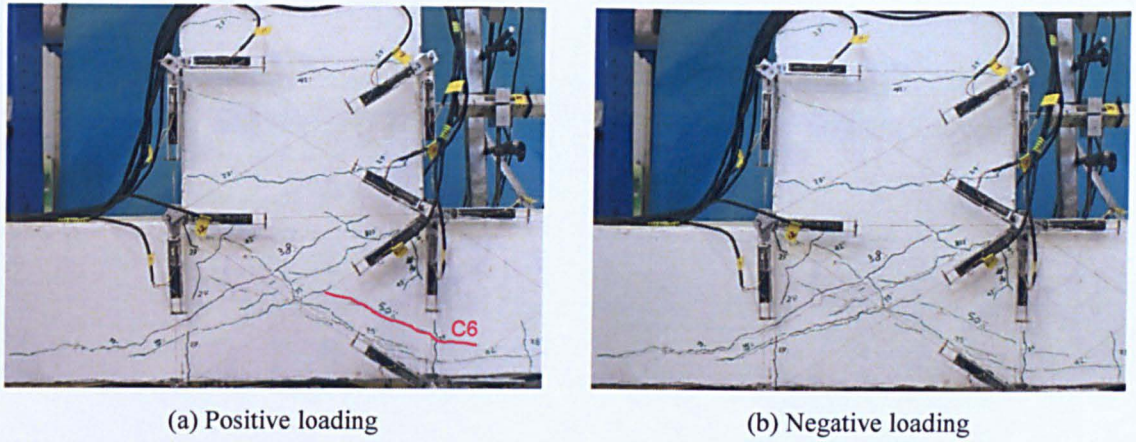


Figure 4.7: Specimen JA-2 after one cycle at 1.5% drift

On the second half of the first cycle, new cracks (in the shape of sub-branches) formed around the diagonal shear cracks. Figure 4.7.b shows the specimen's state after reaching the negative peak of the first cycle. The diagonal shear cracks due to negative loading measured 3mm wide, whereas in the positive loading they measured only 1mm wide.

No further damage was detected during the second and the third cycle. However, as the test continued, the specimen kept becoming softer and a significant reduction in strength was observed (see Figure 4.3). Figure 4.2.f shows the crack pattern of specimen JA-2 after three cycles at 1.5% drift.

More diagonal cracks developed during the positive loading of the first cycle to 2% drift. Strength and stiffness degradation are more evident at this stage, as can be seen in Figure 4.3. However, no reinforcement yielding, concrete flaking or spalling were observed during this half cycle. Figure 4.8.a illustrates the damage attained in specimen JA-2 at the first positive peak of 2.0% drift cycle.

Unfortunately, during the negative half of the first cycle, the control system experienced a malfunction causing the actuator to suddenly shoot to its maximum stroke, which in turn broke the specimen, as shown in Figure 4.8.b. The test was then stopped and concluded.

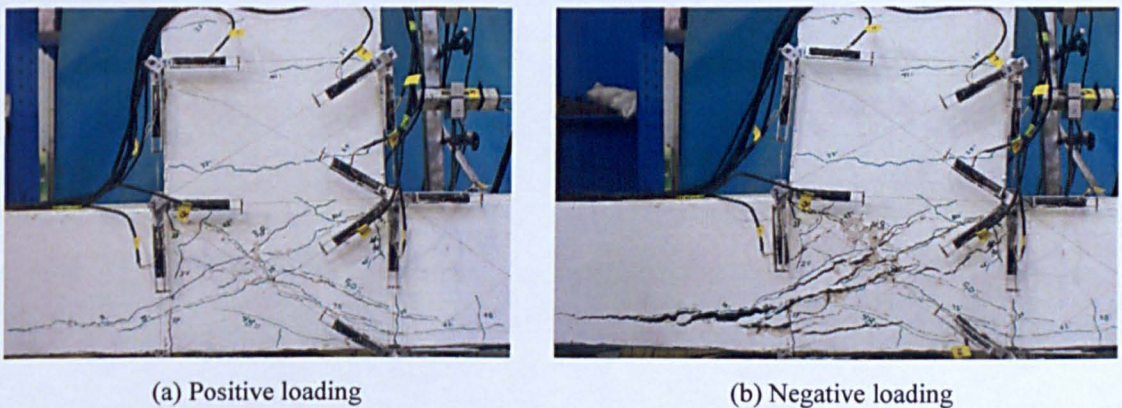


Figure 4.8: Specimen JA-2 after one cycle at 2.0% drift

4.4.1.2 Load Drift Response

Figure 4.3 shows the applied lateral load-drift hysteretic response for joint specimen JA-2 and the equivalent beam shear calculated according to ASCE 41 (see Table 4-1). Positive loading (pushing) corresponds to the beam hooked bars being in tension. It is evident, from Figure 4.3, that specimen JA-2 exhibited weaker resistance in the negative loading direction (pulling). This can be attributed to the poor anchorage detailing of the beam bottom bar, which in this case is a straight bar. The maximum recorded load in the positive direction is 50.6 kN and took place at 1.5% drift level; whereas the maximum recorded load in the negative loading direction is 47 kN and occurred at a drift level equal to 1.5%. The strength of the joint started degrading after reaching the maximum load in both directions. After inspecting the strain gauges of the joint, no reinforcement yielding was found. Based on both the negative and positive direction envelopes, shown in Figure 4.3, and the fact that no yielding was observed, the exhibited mode of failure is considered to be *J-Type* failure (i.e. joint failure due to shear).

4.4.2 SPECIMEN JA-3

4.4.2.1 Description of Damage

Test specimen JA-3 was subjected to the same displacement history as specimen JA-2. However, the applied axial compressive force on the column was 250 kN instead of 150kN as in the case of specimen JA-2. Figure 4.9 shows the crack development for specimen JA-3 during the test between 0.25% and 3.0% drift levels. Arrows denote the direction of positive loading and the top side of the beam. After 3% drift, the damage was difficult to track; therefore, cracks were no longer marked. The cyclic load-drift response of specimen JA-3 and the overall envelope are shown in Figure 4.10. Key changes to the response envelope are marked and denoted.

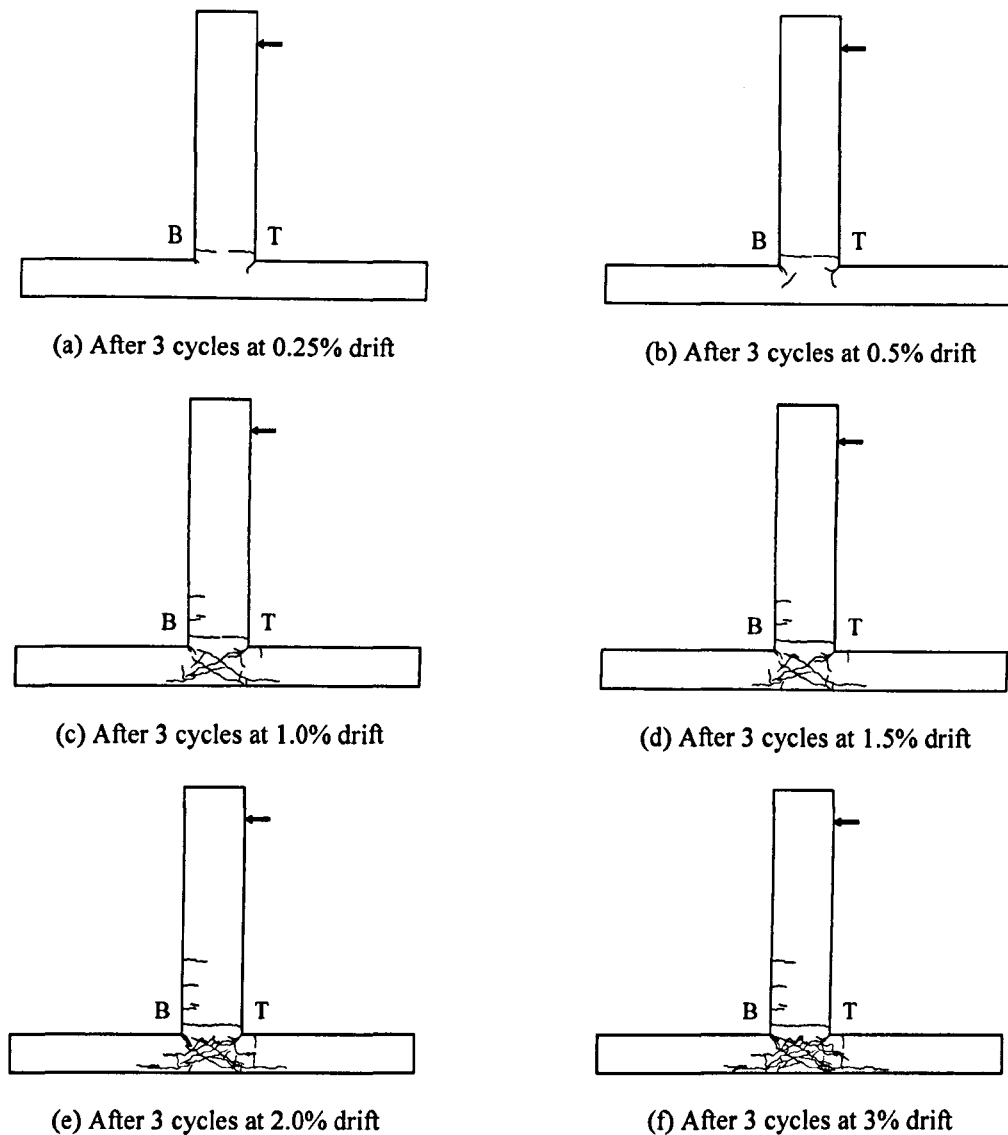


Figure 4.9: Progression of cracking for specimen JA-3

Hairline cracks of widths less than 0.1 mm appeared when displacing the specimen to 0.1% drift level and disappeared once the specimen was brought to the starting point. Apart from these cracks, no significant damage was observed throughout the first three cycles.

In general, the observed crack pattern and the progression of damage up to 2.0% drift level of specimen JA-3 was similar to that of specimen JA-2. However, the intensity of damage at each drift level was always slightly less in JA-3 in comparison to JA-2. For instance, in JA-2, the first diagonal shear crack developed during 0.5% drift cycles, whereas JA-3 developed a similar crack at a drift level equal to 0.78%. The observed difference between the two specimens in terms of damage level may be attributed to the effect of the increased axial load level.

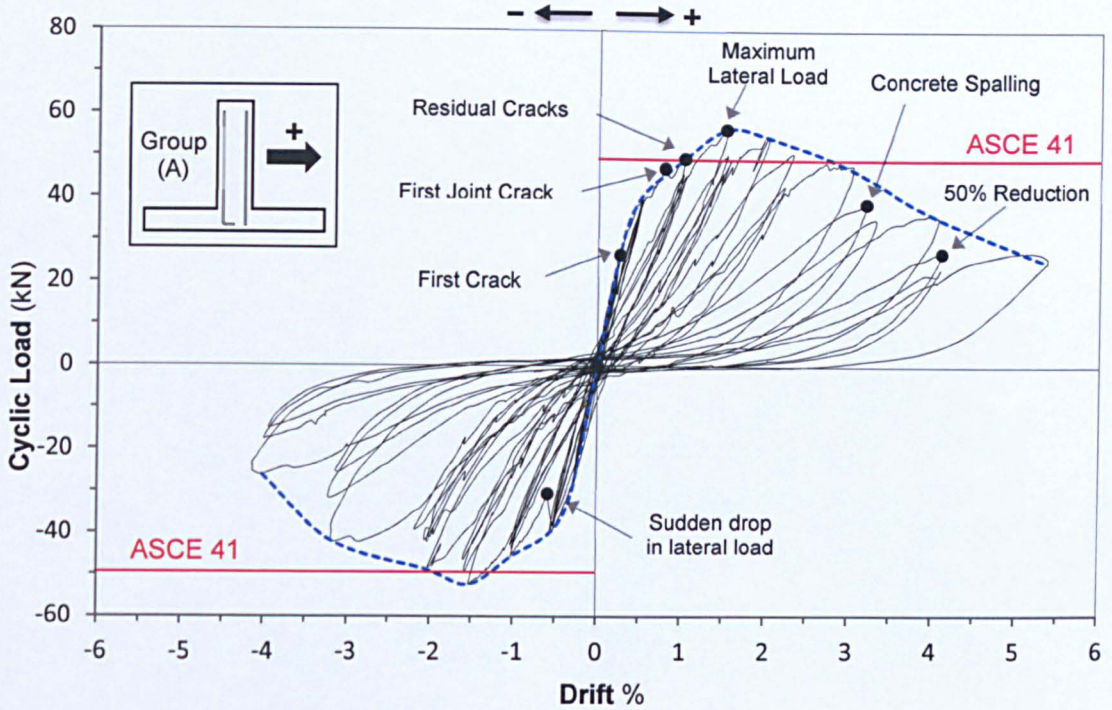


Figure 4.10: Lateral load-drift response for specimen JA-3.

Table 4-3 describes the progress of damage of specimen JA-3 at each drift level. Detailed description of the observed crack pattern and the progress of damage during the test of specimen JA-3 is given in Appendix B.

Table 4-3 Description of observed damage of specimen JA-3

Drift %	Damage description	Crack width (mm)
0.1	Hairline cracks	0.1
0.25	First small corner cracks	<0.5
0.5	Joint cracks	<1
0.75	First diagonal shear crack	1
1.0	x-shaped diagonal cracks - visible residual cracks	1-1.5
1.5	Several diagonal crack extending to columns – peak maximum strength (positive, negative)	3
2.0	Concrete flaking - increased width and length of existing cracks	3-6
3.0	Concrete spalling - extensive damage to the joint core	8-10

Concrete spalling started at 3.0% drift and continued during the 4.0% drift cycles. Specimen JA-3 suffered substantial damage during the 4.0% drift cycles. By the second cycle of 4.0% drift, the specimen had lost 50% of its maximum achieved strength, as shown in Figure 4.10. This point was considered to be joint failure.

At the end of the three cycles, due to the extensive damage, pieces of the centre concrete cover had fallen out. Figure 4.11 shows the level of damage attained by specimen JA-3 after completing three cycles at 4.0% drift.

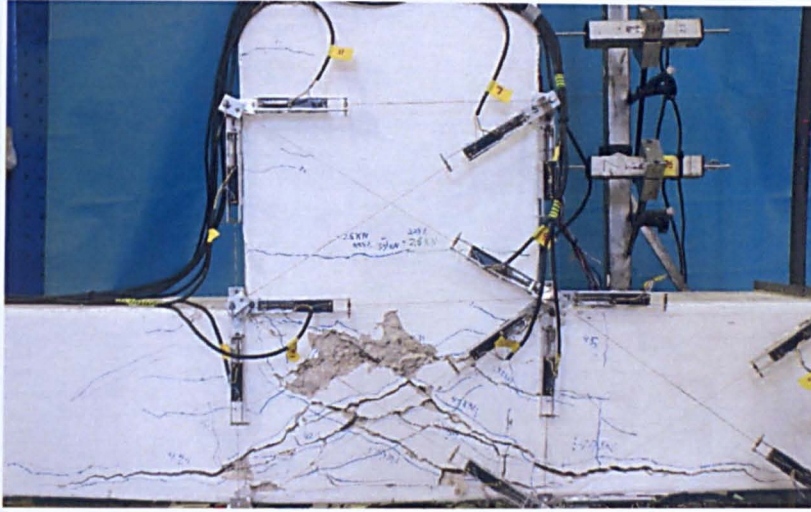


Figure 4.11: Specimen JA-3 after three cycles at 4.0% drift

At 5.0% drift, only half a cycle was performed, as the specimen was deemed to be unstable. Figure 4.12 shows the damage achieved at the first positive peak to 5.0% drift.

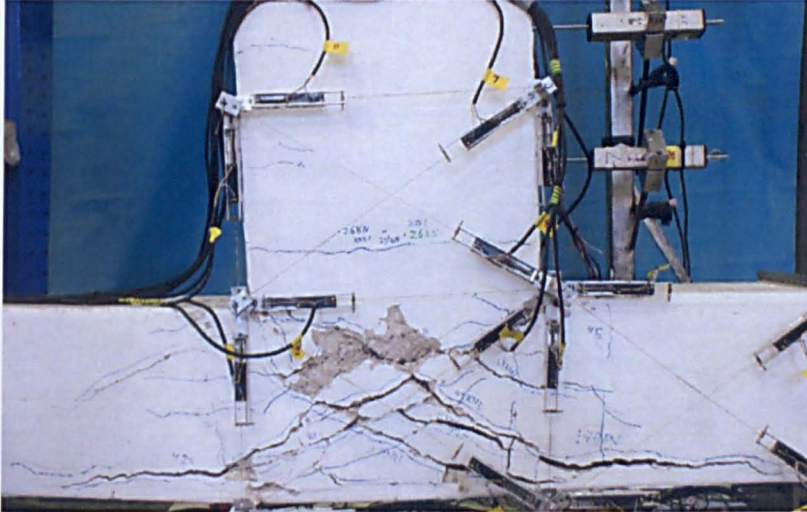


Figure 4.12: Specimen JA-3 at the first positive peak to 5.0% drift

4.4.2.2 Load Drift Response

Figure 4.10 shows the applied lateral load-drift hysteretic response of joint specimen JA-3 and the equivalent beam shear calculated according to ASCE 41 (see Table 4-1). Similarly to JA-2, specimen JA-3 exhibited a weaker resistance in the negative loading direction (pulling) in comparison to the other direction. Since JA-2 and JA-3 share the same detailing, this poor behaviour can be attributed to the same reason, which in this case is the straight bar anchorage. The maximum recorded load in the positive direction is 56.6 kN and 52.3 kN in the negative

loading direction. Both loads occurred at a drift level equal to 1.5% drift. The specimen showed significant degradation in both stiffness and strength after reaching the maximum load in both directions (see Figure 4.10). No reinforcement yielding was found and hence, similarly to JA-2, the exhibited mode of failure is considered to be *J-Type* failure.

4.4.3 SPECIMEN JB-1

4.4.3.1 Description of Damage

Test specimen JB-1 was subjected to the same displacement history as group A specimens. The specimen's column was subjected to a constant axial compressive force equal to 150kN. Figure 4.13 shows the progress of developed cracks for specimen JB-1 up to the 3.0% drift level. Arrows denote the direction of positive loading and the top side of the beam. After the 3% drift level, the damage was so extensive that keeping track of all cracks became very difficult.

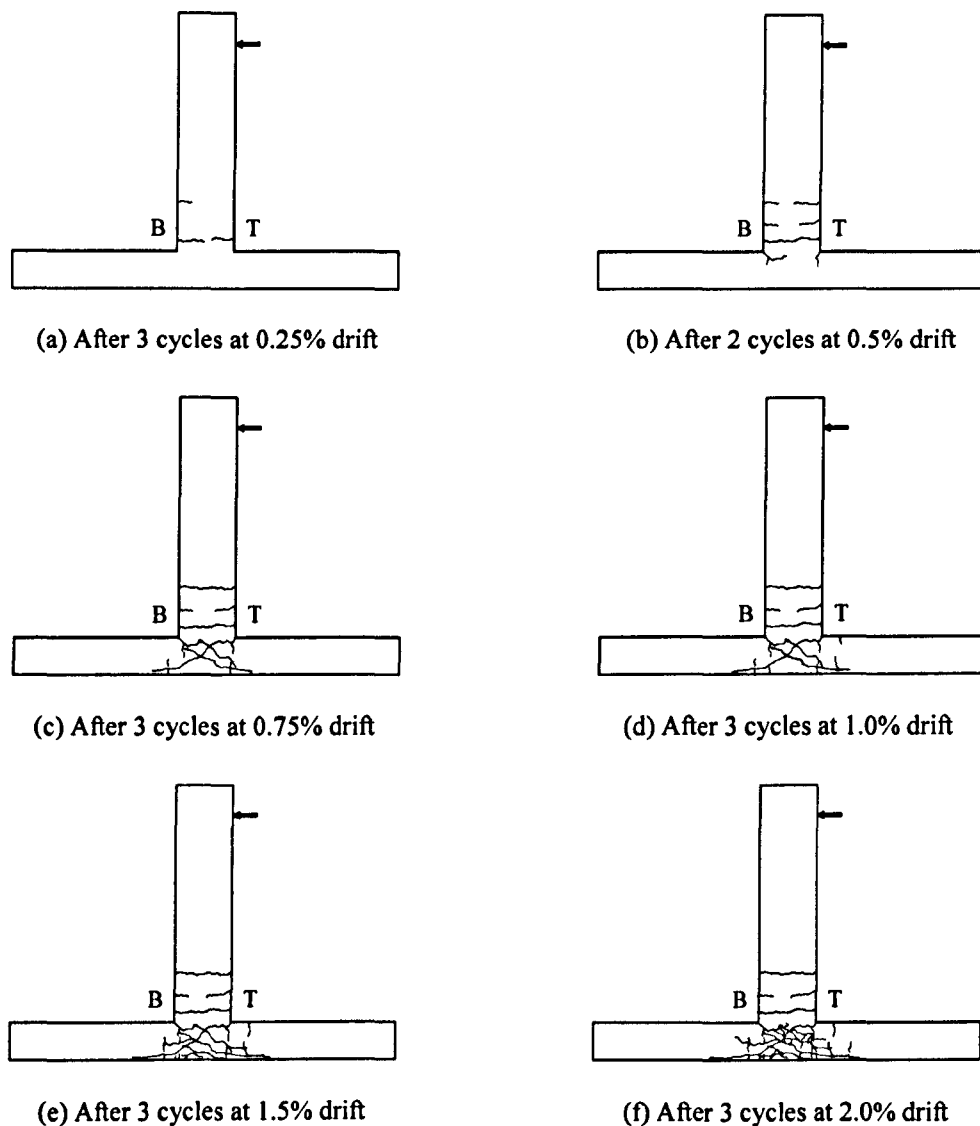


Figure 4.13: Progression of cracking for specimen JB-1

Figure 4.14 shows the cyclic load-drift response of specimen JB-1 and the overall envelope. In addition, key changes to the response envelope are marked and denoted Hairline cracks of widths less than 0.1 mm developed during the first cycle to 0.1% drift level. All hairline cracks disappeared once the specimen was brought to the level of 0% drift. Apart from these cracks, no further damage was observed throughout the first three cycles.

The damage observed during the 0.25% drift cycles, when compared to the damage achieved by group (A) specimens, was small and limited to the beam only. During the first positive loading, a crack was formed at the location of the first beam shear link. A similar crack was observed during the second half of the same cycle. In addition, another horizontal crack was formed in the beam at the third shear link from the beam-column interface. All cracks were of width less than 1mm.

As the test continued, no further damage was observed during the remaining two cycles. Figure 4.13.a shows the crack pattern of specimen JB-1 after three cycles at 0.25% drift.

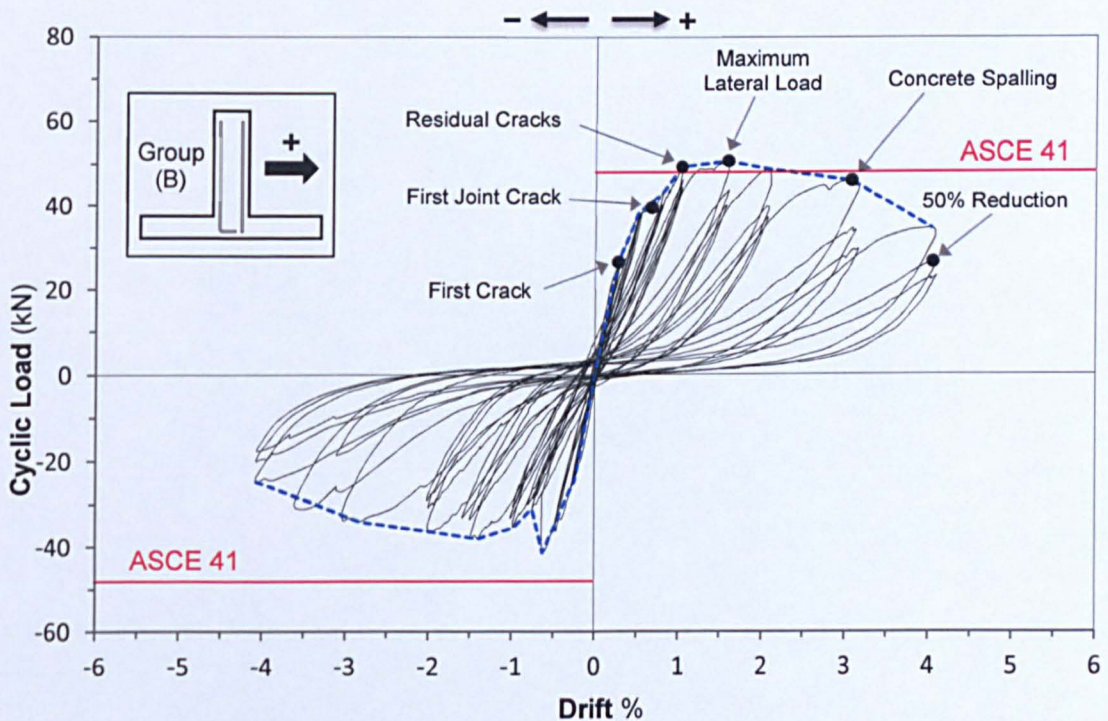


Figure 4.14: Lateral load-drift response for specimen JB-1.

During the first positive loading to 0.5% drift level, several horizontal beam cracks formed at the locations of beam shear links. The first beam crack however, extended further as the test progressed to eventually connect with the opposite crack. These beam cracks were accompanied by an inclined crack, denoted as C1, at the top column-beam corner. The crack started with an angle and then continued by following the path of the beam longitudinal top bars, as can be seen in Figure 4.15.a. The width of all cracks was less than 1mm.

Similarly, the second half of the same cycle showed an almost identical crack pattern. However, the corner crack, denoted as C2, extended into the joint then split into two branches following the paths of both beam and column longitudinal reinforcement, as shown in Figure 4.15.b. This crack is similar to the one developed in both JA-2 and JA-3 but at the opposite corner (see Figure 4.2.b and Figure 4.9.b).

The second cycle of the same drift level showed no further damage. Figure 4.13.b. shows the exhibited crack pattern for specimen JB-2 after two cycles at 0.5% drift.

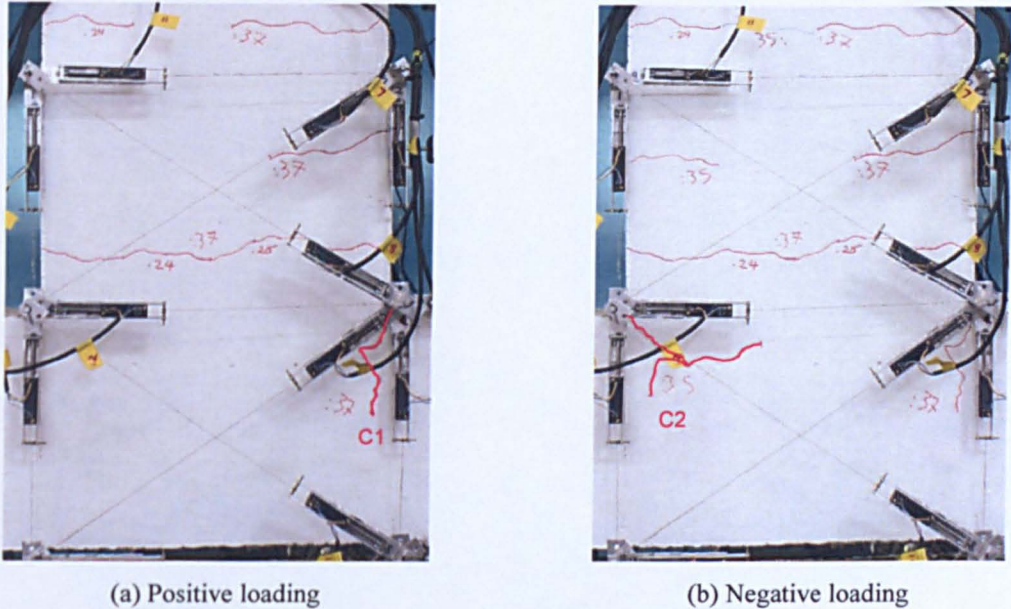


Figure 4.15: Specimen JB-1 after one cycle at 0.5% drift

As the test continued, nothing significant was observed during the first half of the third cycle. The second half of the third cycle, however, exhibited significant damage. The reason for that is because the specimen was displaced further by mistake to a drift level equal to 0.64% drift. At 0.62% drift exactly, the applied cyclic load reached 41.1 kN and a diagonal shear crack, denoted as C3, starting from the top column-beam corner all the way through the joint to the bottom column formed, as can be seen in Figure 4.16. The crack was followed by a massive drop in force from 41.1 to 29 kN at 0.64% drift.

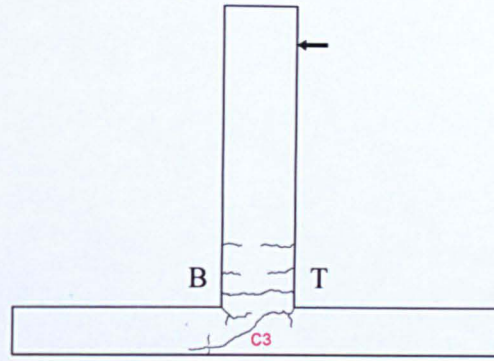


Figure 4.16: Specimen JB-1 cracks at the third negative peak to 0.5% drift

Displacing the specimen to 0.75% drift level caused extra damage to the joint area. During the first positive loading cycle and exactly at 0.67% drift, an inclined shear crack (C4) formed at the centre of the joint and along the joint diagonal. A second parallel diagonal crack (C5) appeared soon after at a drift level equal to 0.78%. Both cracks extended into the top column, as shown in Figure 4.17.

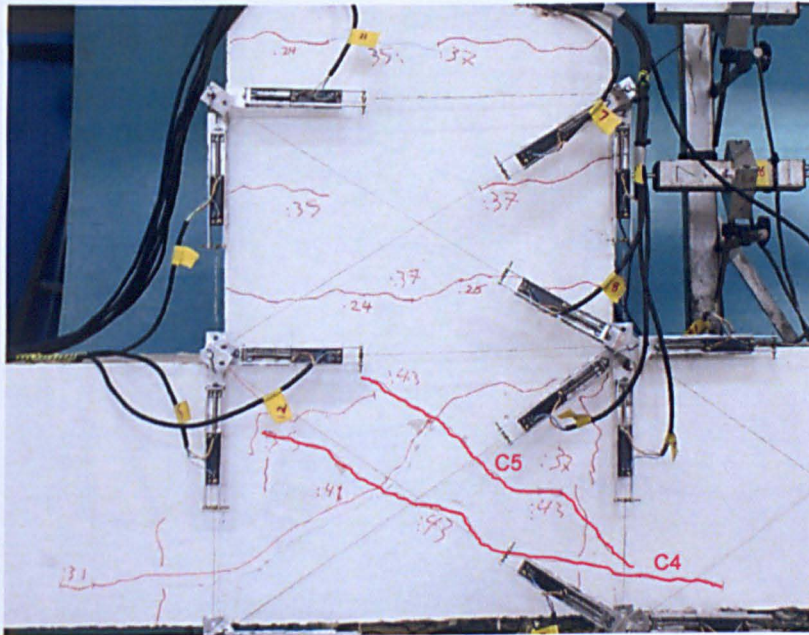


Figure 4.17: Specimen JB-1 after three cycles at 0.75% drift

During the second half of the same cycle, the previously formed diagonal crack (C3) extended further into the bottom column. The level of damage attained during this drift level caused a significant loss in both strength and stiffness, as can be seen in Figure 4.14. As for the previous drift levels, no further damage was observed during the remaining two cycles. Figure 4.13.c shows the exhibited crack pattern of specimen JB-1 at the end of the third cycle at 0.75% drift.

New joint cracks were observed during the positive and negative loading of the first cycle to 1.0% drift. Existing cracks increased in both width and length. Cracks as wide as 2 mm were

observed at both the positive and negative peaks. No further damage was observed during the remaining 2 cycles of 1.0% drift. However, when the specimen was brought to 0% drift level by the end of the third cycle, residual cracks of widths equal to 1 mm were observed. Figure 4.13.d shows the crack pattern of specimen JB-1 after three cycles at 1.0% drift.

The damage observed during the first cycle to 1.5% drift was quite extensive as many new joint cracks formed, whereas existing joint cracks became bigger in both length and width. Diagonal shear cracks due to positive and negative loading measured 1mm and 3mm wide, respectively. Furthermore, the specimen achieved its maximum load carrying capacity during the first half cycle, as can be seen in Figure 4.14. However, no reinforcement yielding or concrete spalling was observed. Figure 4.18 shows specimen JB-1 at the negative peak of the first cycle to 1.5% drift.

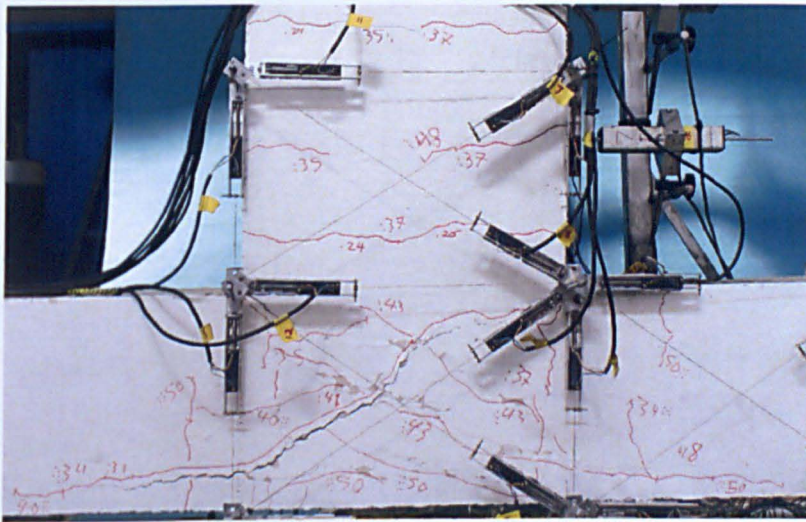


Figure 4.18: Specimen JB-1 after one cycle at 1.5% drift

No further damage was observed during the rest of the remaining cycles. However, as the test progressed, the specimen kept becoming softer (see Figure 4.14). Figure 4.13.e shows the crack pattern of specimen JB-1 after three cycles at 1.5% drift.

Specimen JB-1 was severely damaged during the first cycle at 2.0% drift. Cracks increased in both width and length, especially the diagonal cracks which extended further into the top and bottom columns. Due to this extensive damage, concrete flaking developed around the intersecting diagonal cracks at the centre of the joint, as can be seen in Figure 4.19. This was accompanied by rapid loss in both strength and stiffness (see Figure 4.13). The observed cracks at peaks ranged in width between 3 to 6 mm. Figure 4.13.f shows the crack pattern of specimen JB-1 after three cycles at 2.0% drift.

The test continued and existing cracks became bigger in width and length. The damage at the end of the three cycles left the bottom joint cover barely attached to the longitudinal reinforcement and the joint centre completely deformed with missing pieces of concrete. Figure 4.21 shows the level of damage attained by specimen JB-1 after completing three cycles at 4.0% drift.

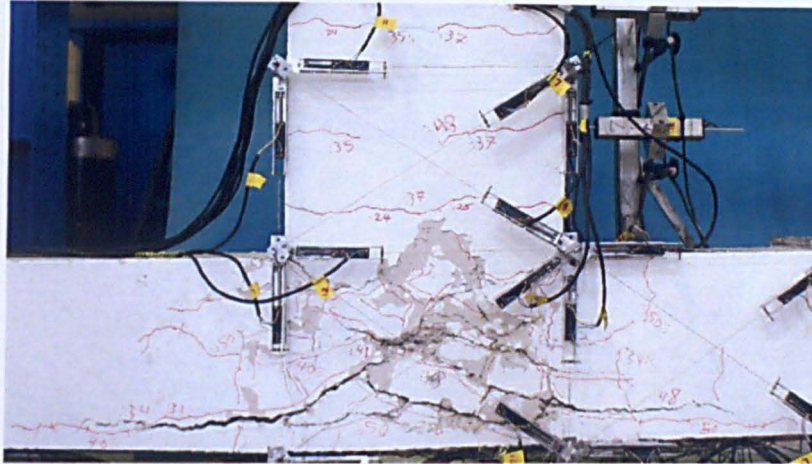


Figure 4.21: Specimen JB-1 after three cycles at 4.0% drift

4.4.3.2 Load Drift Response

Figure 4.14 shows the applied lateral load-drift hysteretic response of joint specimen JB-1 and the equivalent beam shear calculated according to ASCE 41 (see Table 4-1). It is evident, from Figure 4.14, that specimen JB-1 exhibited a weaker resistance in the negative loading direction, in which the beam straight bars are being pulled. The weak performance in the negative loading direction can be attributed to the poor anchorage detailing of the beam bottom bar (straight bar) and also the effect of the elongated top beam hook. The maximum recorded load in the positive direction is 50.8 kN and took place at 1.5% drift level, whereas the maximum recorded load in the negative loading direction is 41 kN and took place at a drift level equal to 0.62%. Stiffness degradation and strength degradation became more pronounced after reaching the maximum load in both directions (see Figure 4.14). The exhibited mode of failure is considered to be *J-Type* failure, as no reinforcement yielding was found.

4.4.4 SPECIMEN JB-2

4.4.4.1 Description of Damage

Specimen JB-2 was subjected to the same displacement history as JB-1. However, the column's axial compression force was increased from 150 to 250 kN. Figure 4.22 shows the progression of cracking for specimen JB-2 between 0.25% and 2.0% drift levels. Similarly to specimen JB-1, the damage observed during 0.1% drift cycles was limited to hairline cracks of width less than 0.1 mm. Apart from these cracks, no further damage was observed. Figure 4.23 shows the

cyclic load-drift response of specimen JB-2 and the overall envelope. In addition, key changes to the response envelope are marked and denoted.

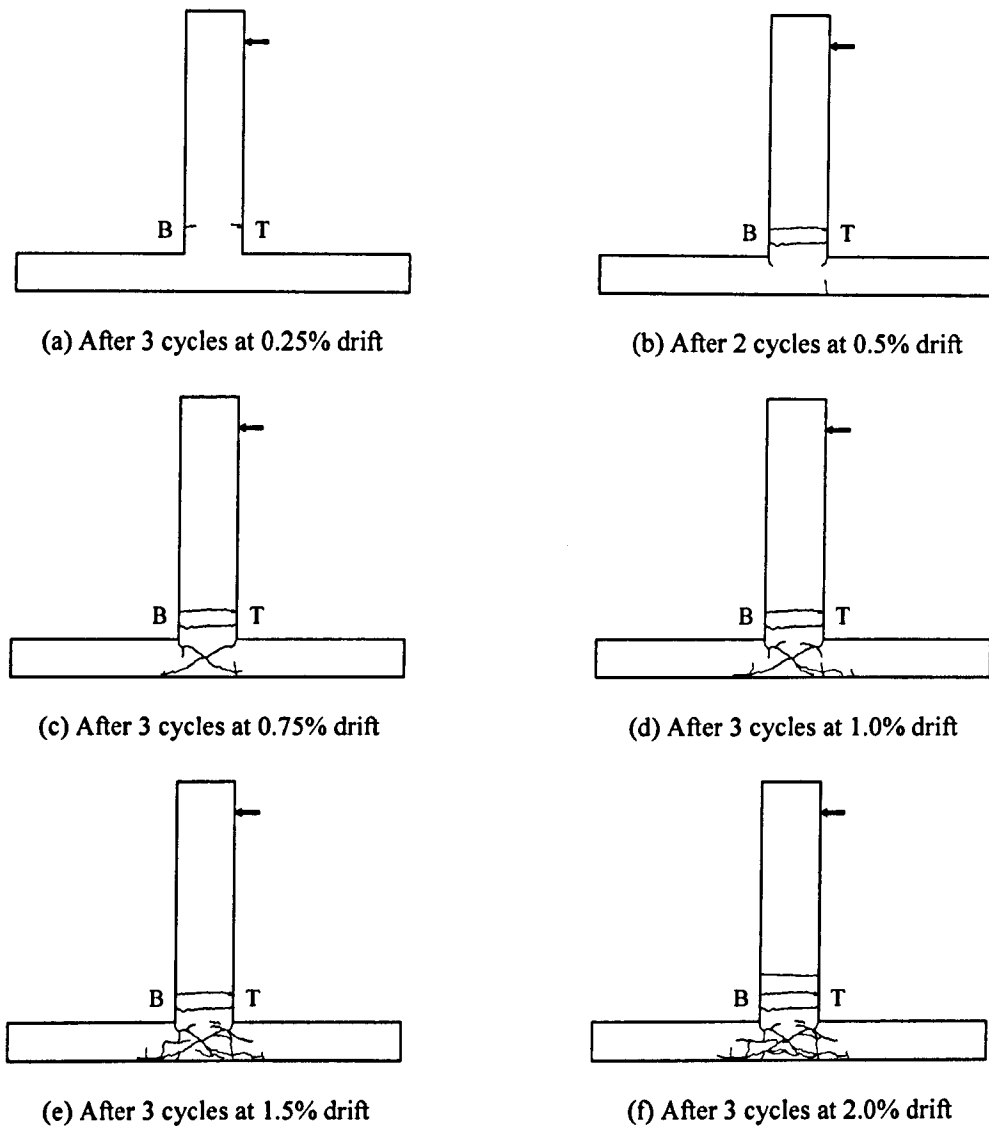


Figure 4.22: Progression of cracking for specimen JB-2

In general, the exhibited crack pattern and the progression of damage of specimen JB-2 during the test was very similar to that of specimen JB-1. However, similarly to the difference between JA-2 and JA-3, the intensity of damage at each drift level was always slightly less in JB-2 when compared to JB-1. For instance, at the end of the 0.75% drift cycles, JB-2 had only two diagonal shear cracks (x-shaped), whereas JB-1 had three diagonal cracks (see Figure 4.22.c and Figure 4.13.c). The difference between these two specimens in terms of damage at each level can be attributed to the positive effect of the increased axial load level in specimen JB-2.

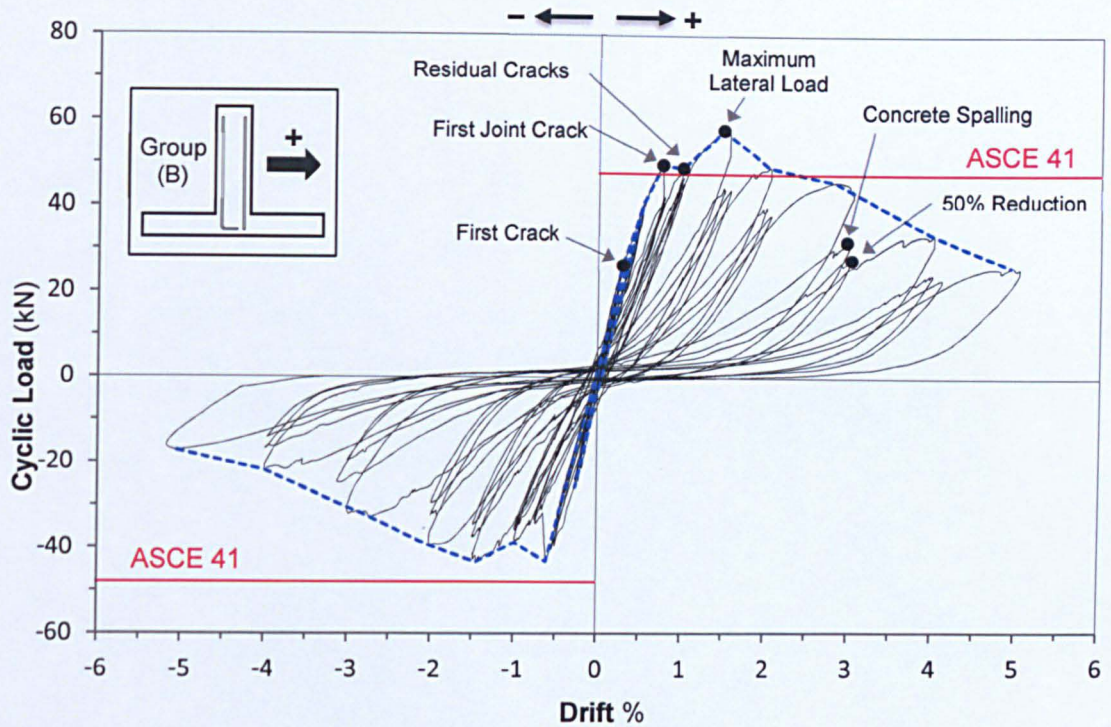


Figure 4.23: Lateral load-drift response for specimen JB-2

Table 4-4 describes the progress of damage of specimen JB-2 at each drift level. The detailed description of the observed crack pattern and progress of damage of specimen JB-2 throughout the test is given in Appendix B.

Table 4-4 Description of observed damage of specimen JB-2

Drift %	Damage description	Crack width (mm)
0.1	Hairline cracks	<0.1
0.25	Limited beam cracks	<0.5
0.5	Extended beam cracks - First small corner cracks	<1
0.75	x-shaped diagonal cracks – peak strength in negative loading	1
1.0	Diagonal; cracks extending to columns - visible residual cracks	2
1.5	Further cracking in the joint – peak maximum strength in positive loading	2-4
2.0	Concrete flaking - increased width and length of cracks – crack along the column outer reinforcement	3-6
3.0	Concrete spalling – bottom concrete cover barely hanging – 50% strength reduction	10-15

Concrete spalling started during the second cycle of the 3.0% drift. By the end of the third cycle, the damage was so extensive that a big chunk of the bottom concrete fell out and 50% of the specimen's maximum achieved strength was lost.

Specimen JB-2 suffered further substantial damage during the 4.0% drift cycles. At the end of the three cycles, the specimen was severely damaged and suffering from extensive expansion in the core area. The test was continued by displacing the joint to 5% drift level. However, the specimen was near the point of total collapse, and therefore only one cycle was performed. Figure 4.24 shows specimen JB-1 after completing one cycle at 5.0% drift.

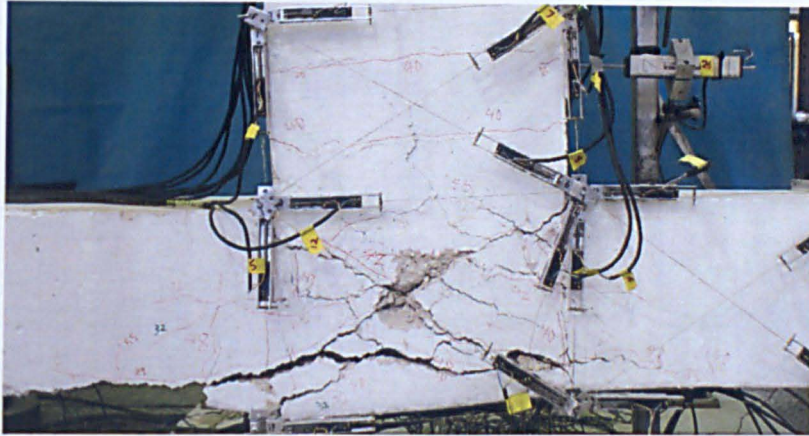


Figure 4.24: Specimen JB-2 at 5.0% drift

4.4.4.2 Load Drift Response

Figure 4.23 shows the applied lateral load-drift hysteretic response of joint specimen JB-2 and the equivalent beam shear calculated according to ASCE 41 (see Table 4-1). Similarly to JB-1, specimen JB-2 exhibited a weaker resistance in the negative loading direction (pulling). The weaker performance, as in JB-1, can be attributed to the poor anchorage detailing of the beam bottom bar (straight bar) and also to the effect of the elongated top beam hook. The maximum recorded load in the positive direction is 58kN and took place at 1.5% drift level; whereas the maximum recorded load in the negative loading direction is 43 kN and took place at a drift level equal to 0.61%.

It should be noted, however, that soon after the negative peak strength was achieved and a drift level equal to 0.64% drift, the specimens experienced a massive drop in strength to 32 kN. The same peak strength (slightly higher 43.3 kN) was achieved once again during the first cycle at 1.5% drift. The specimen showed significant degradation in both stiffness and strength after the 1.5% drift level in both directions (see Figure 4.23). No reinforcement yielding was found and hence, similarly to JB-1, the exhibited mode of failure is considered to be *J-Type* failure.

4.4.5 SPECIMEN JC-1

4.4.5.1 Description of Damage

Specimen JC-1 was the first specimen to be tested after testing the pilot specimen JA-1. Therefore, the specimen was subjected to a slightly different displacement history than the rest

of the specimens. In addition, the specimen's column throughout the test was subjected to an axial compressive force equal to 150kN. Figure 4.25 shows the progression of cracking of specimen JC-1 between 0.25% and 2.0% drift levels. Arrows denote the direction of positive loading and the top side of the beam.

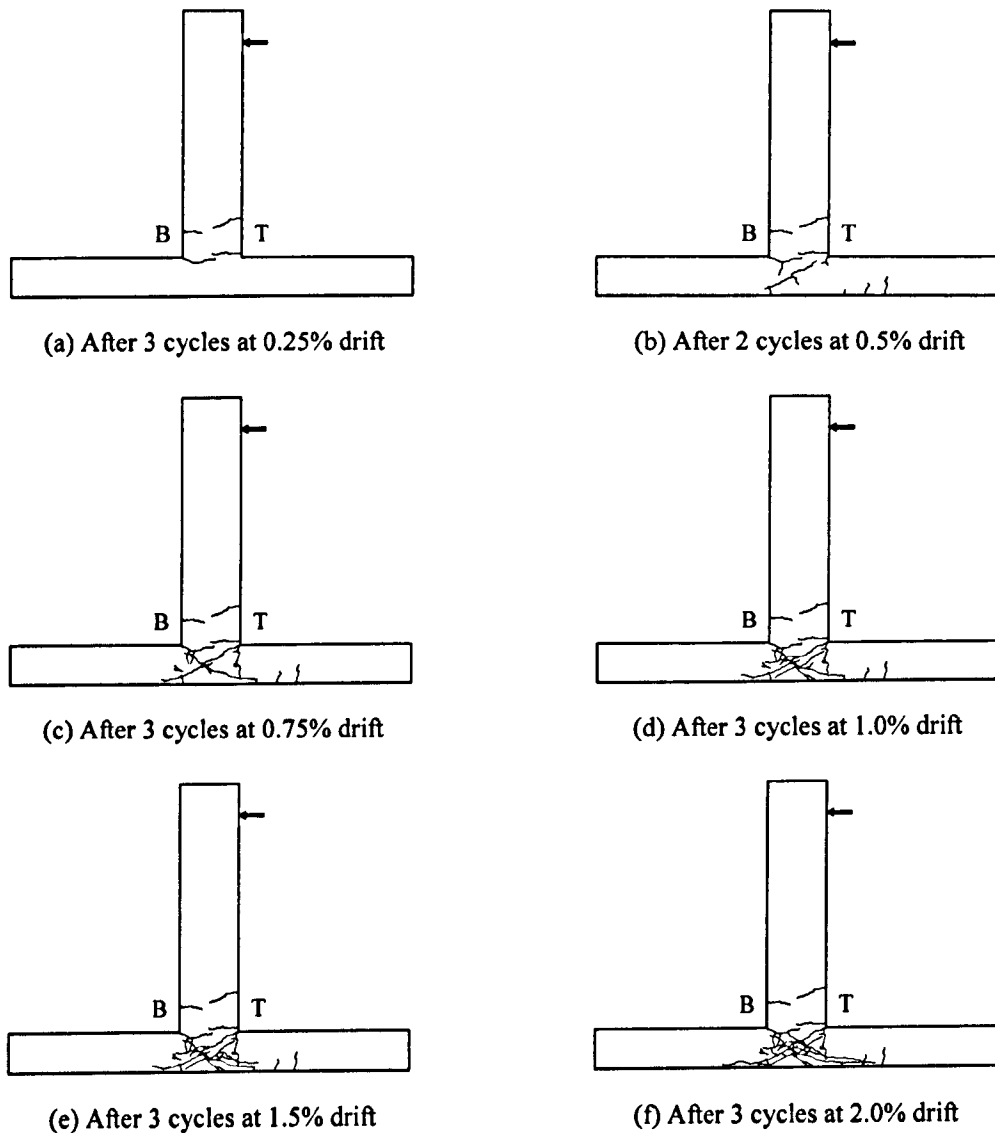


Figure 4.25: Progression of cracking for specimen JC-1

Similarly to the previous specimens, the damage observed during the first cycle to 0.1% drift was limited to hairline cracks, which width measured less than 0.1mm. No further damage was recorded throughout the remaining 0.1% drift cycles. Figure 4.26 shows the cyclic load-drift response of specimen JC-1 and the overall envelope. In addition, key changes to the response envelope are marked and denoted.

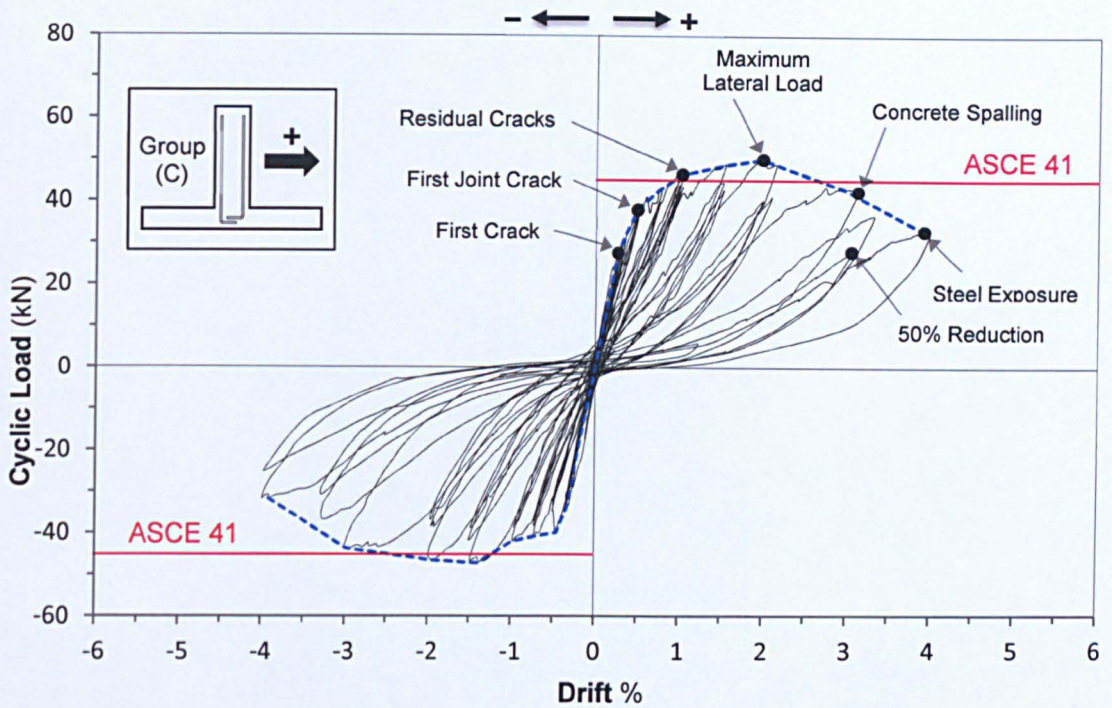


Figure 4.26: Lateral load-drift response for specimen JC-1

A limited level of damage was observed in specimen JC-1 during the 0.25% drift cycles. During the first positive loading, a crack developed around the location of the second beam shear link followed by another crack around the joint-beam interface. A similar crack pattern with slightly different locations was observed during the second half of the same cycle. As the test continued, no further damage was recorded during the remaining two cycles. All observed cracks were of width less than 0.5mm. Figure 4.25.a shows the crack pattern of specimen JB-1 after three cycles at 0.25% drift.

The next displacement increment was displacing the specimen to 0.35% drift level. During the first positive loading to 0.35% drift level, an inclined crack (C1) appeared at the corner between the beam and the top column (see Figure 4.27.a). Similarly, a new crack was observed during the second half of the first cycle. This crack, denoted as C2, started from the interface crack and extended further into the joint core, as shown in Figure 4.27.b. As the test progressed, no further damage was observed during the remaining two cycles.

Due to the limited observed damage, this drift level was deemed redundant and was then removed from the utilised displacement history for the remaining specimens.

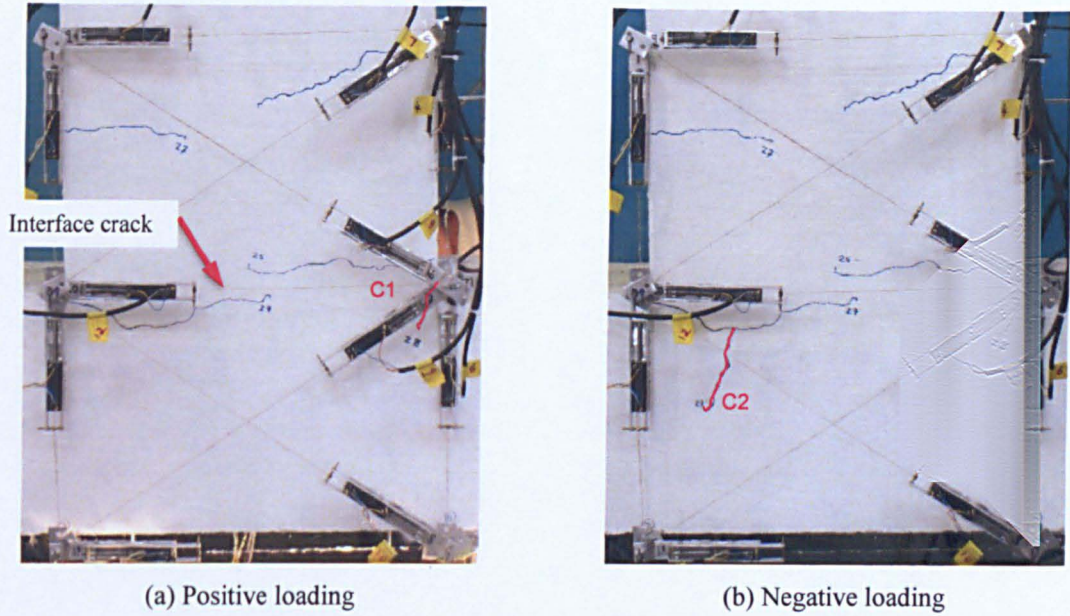


Figure 4.27: Specimen JC-1 after one cycle at 0.35% drift

Several new cracks formed during the 0.5% drift cycles. The inclined joint crack at the beam-top column corner (C1), split into two branches extending further into the joint, as shown in Figure 4.28.a. At the same time, three new vertical cracks appeared in the top column at the locations of the column shear links. The beam cracks, however, remained unchanged.

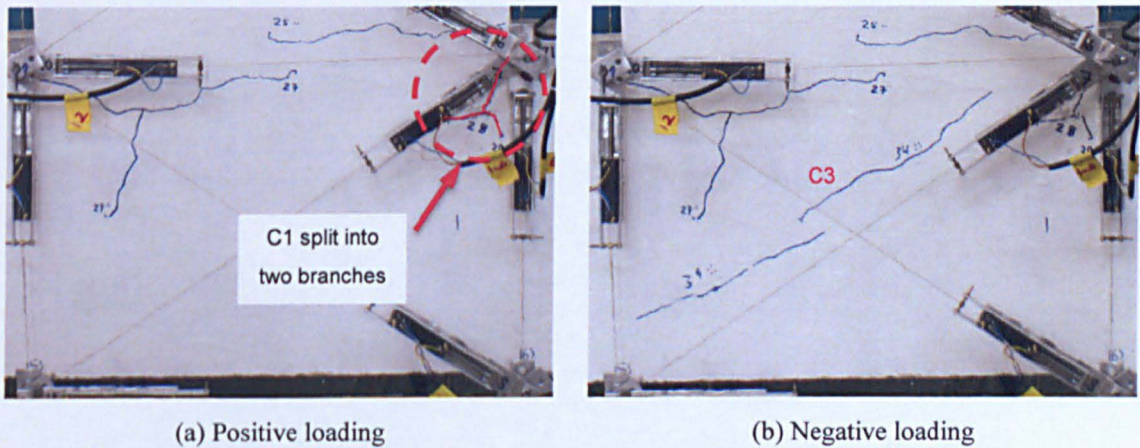


Figure 4.28: Specimen JC-1 after one cycle at 0.5% drift

During the second half of the same cycle, a long diagonal shear crack, denoted as C3, suddenly appeared across the joint core, as shown in Figure 4.28.b. The crack C3 caused a slight stiffness reduction to the lateral load-drift response, as can be seen in Figure 4.26. No other cracks were observed during this half cycle. The width of all cracks was less than 1mm.

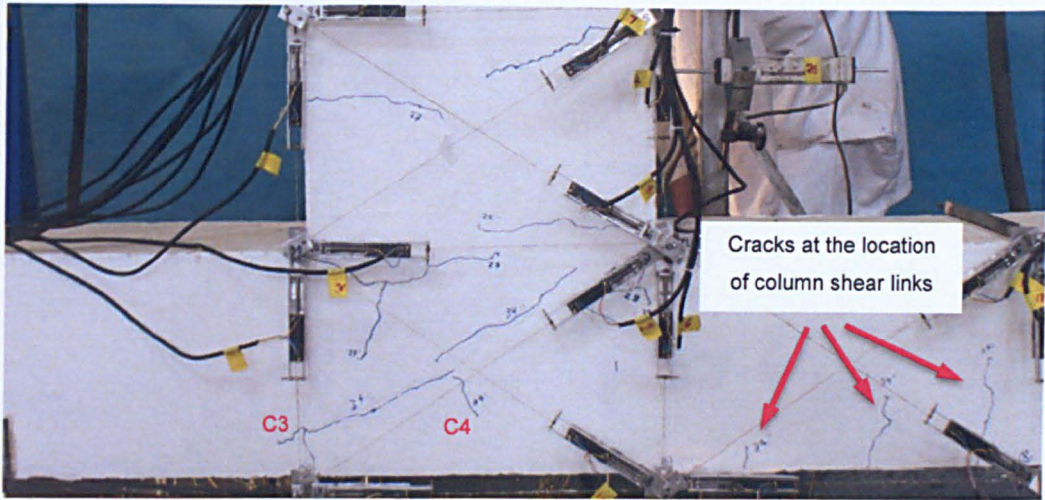


Figure 4.29: Specimen JC-1 after two cycles at 0.5% drift

As the test continued, and during the positive loading of the second cycle, the diagonal shear crack C3 extended further into the bottom column. Similarly, during the negative loading of the same cycle, a small diagonal crack, denoted as C4, perpendicular to the previous diagonal crack formed, as shown in Figure 4.29. No further damage was observed during the third cycle to 0.5% drift level. Figure 4.25.b. shows the exhibited crack pattern for specimen JC-1 after three cycles at 0.5% drift.

Specimen JC-1 exhibited a significant level of damage during the 0.75% drift level. During the first positive loading, and at a drift level equal to 0.6%, a diagonal shear crack (denoted as C5) suddenly appeared extending across the joint, as shown in Figure 4.30.a. The crack caused a sudden drop in the lateral applied load, as can be seen in Figure 4.26. In addition, several new cracks formed in the joint area.

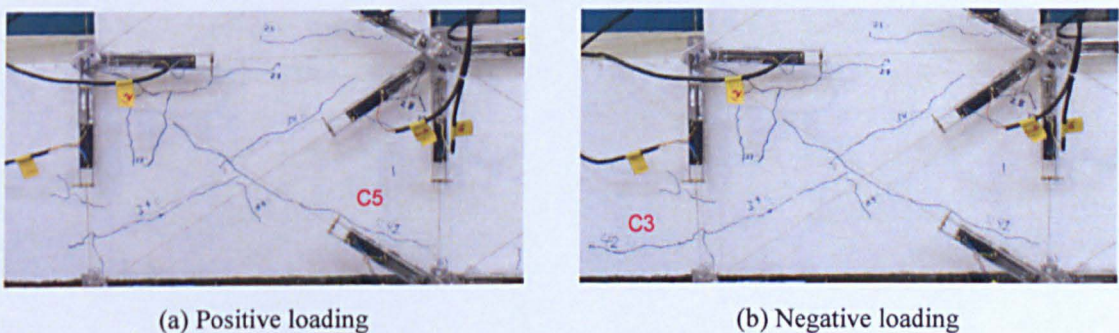


Figure 4.30: Specimen JC-1 after one cycle at 0.75% drift

During the second half of the same cycle, the existing diagonal joint crack C3 extended further into the bottom column, as shown in Figure 4.30.b. However, no further damage was observed during this half cycle. As the test progressed, existing cracks increased in both width and length, as can be seen in Figure 4.31. However, no further stiffness reduction was observed.

Figure 4.25.c shows the crack pattern of specimen JB-2 after completing three cycles at 0.75% drift.

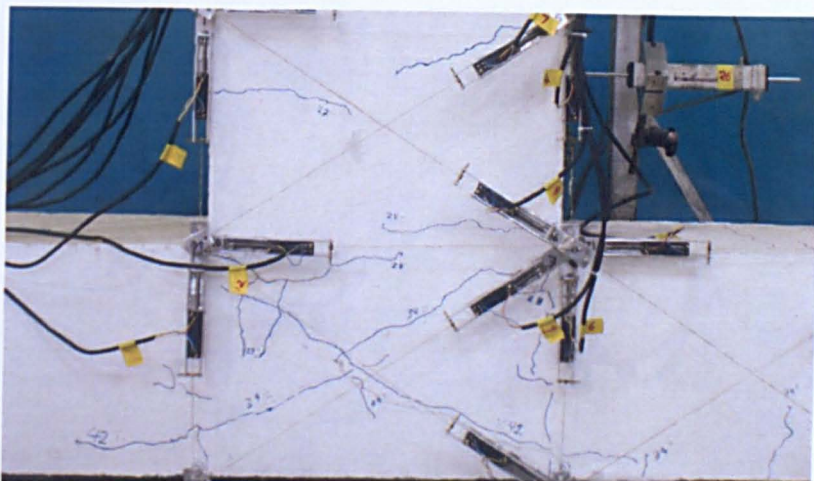


Figure 4.31: Specimen JC-1 after three cycles at 0.75% drift

Two additional cracks developed during the first cycle to 1.0% drift level. Both cracks started from the joint centre and extended to the outer face of the column forming a triangle, as can be seen in Figure 4.32. In addition, existing diagonal cracks increased in both width and length. The measured crack width ranged between 1 to 2 mm at both the positive and negative peaks.

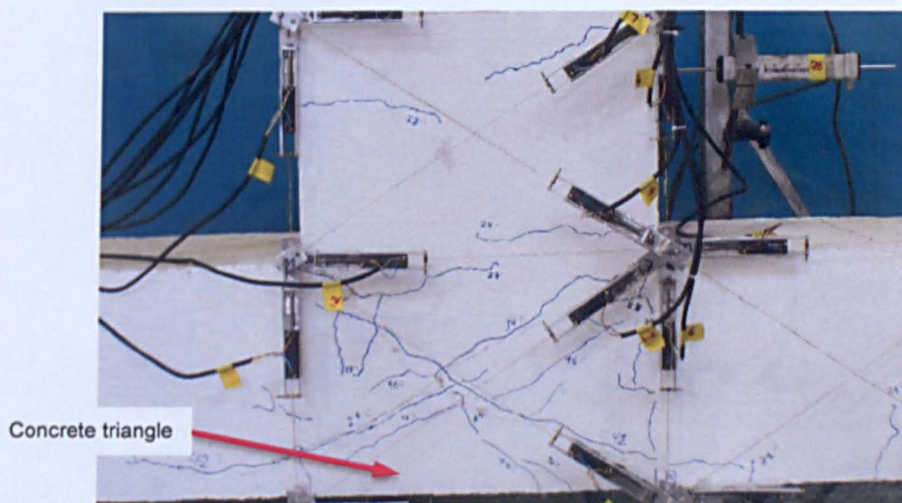


Figure 4.32: Specimen JC-1 after one cycle at 1.0% drift

No more damage was observed during the remaining 2 cycles at 1.0% drift level. The measured residual cracks were approximately 1mm wide by the end of the third cycle. Figure 4.25.d shows the observed crack pattern of specimen JC-1 after three cycles at 1.0% drift.

During the first half cycle to 1.5% drift, several new cracks formed in the joint area and extended into the top column, as shown in Figure 4.33. The cracks, at the centre of the joint, measured 3 mm wide. As the test continued, no further damage was observed during the remaining cycles. However, the specimen suffered a significant stiffness reduction between the

first and second cycle, (see Figure 4.26). Figure 4.25.e shows the final crack pattern of specimen JC-1 at the end of the 1.5% drift cycles.



Figure 4.33: Specimen JC-1 after three cycles at 1.5% drift

Specimen JC-1 suffered significant damage during the first cycle at 2.0% drift level. The diagonal joint cracks extended further into the top and bottom columns following the path of the column longitudinal reinforcement, as can be seen in Figure 4.34. Cracks as wide as 5 mm were measured at both the negative and positive 2.0% drift level. Furthermore, during this drift level the maximum load carrying capacity was reached, as can be seen in Figure 4.26. However, no reinforcement yielding or concrete spalling was observed. As the test progressed, no further damage was observed during the remaining cycles of this drift level. However, the specimen kept exhibiting a softer behaviour which eventually led to a massive 25% strength reduction between the first and the second cycle (see Figure 4.26). Figure 4.25.f shows the crack pattern of specimen JB-2 after three cycles at 2.0% drift.

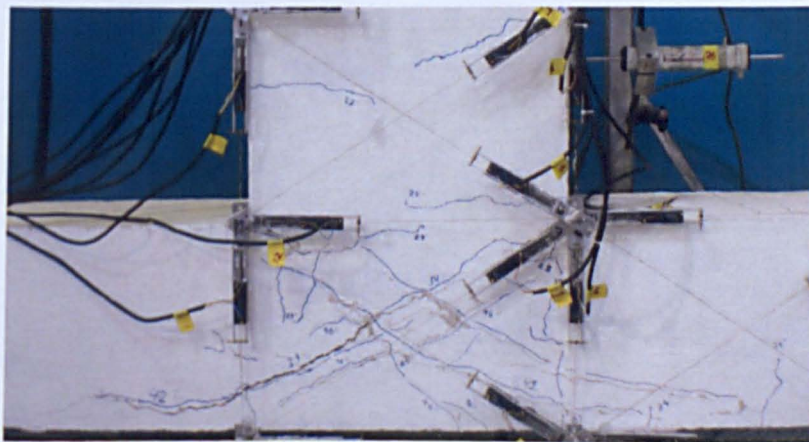


Figure 4.34: Specimen JC-1 after three cycles at 2.0% drift

The specimen was severely damaged during the first cycle to 3.0% drift level. As the existing diagonal cracks opened widely and extended further into the top and bottom columns. In addition, significant concrete spalling was observed around the joint centre. Due to the

extensive damage, the two central diagonal cracks extending into the top and bottom columns joined and formed a concrete cone which left the bottom concrete cover barely hanging. At the peak drift value, the observed diagonal cracks measured around 8 to 12 mm. As the test continued, no change was observed during the remaining cycles. However, the specimen kept becoming weaker with each cycle leading to further loss in both strength and stiffness. The strength reduction was approximately 18% between the first and the second cycle, whereas the total loss by the third cycle was 50% of the maximum lateral load capacity, as can be seen in Figure 4.26. Figure 4.35 shows specimen JC-1 at the end of the 3.0% drift level.



Figure 4.35: Specimen JC-1 after three cycles at 3.0% drift

The test was continued by displacing the joint to 4.0% drift level. At the end of the first complete cycle, the specimen was severely damaged and suffering from extensive expansion in the core area. Figure 4.36 shows the level of damage attained by specimen JC-1 after completing one full cycle at 4.0% drift.

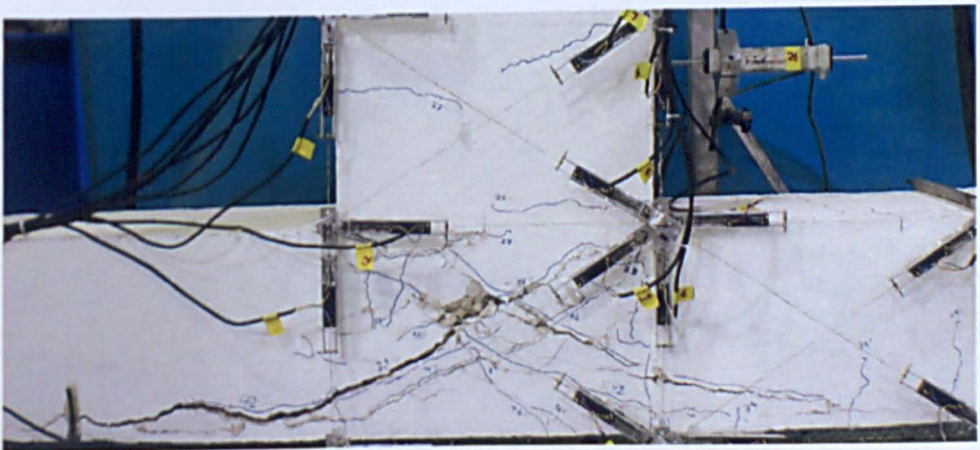


Figure 4.36: Specimen JC-1 after one cycle at 4.0% drift

The second cycle was started with negative loading (pulling), by accident, rather than the usual positive loading. Further expansion was observed during this half cycle. As the test continued to the positive half of the second cycle, the damage was so extensive that a big chunk of the

bottom concrete fell out exposing the bottom longitudinal rebar, as shown in Figure 4.37, and the test was stopped.

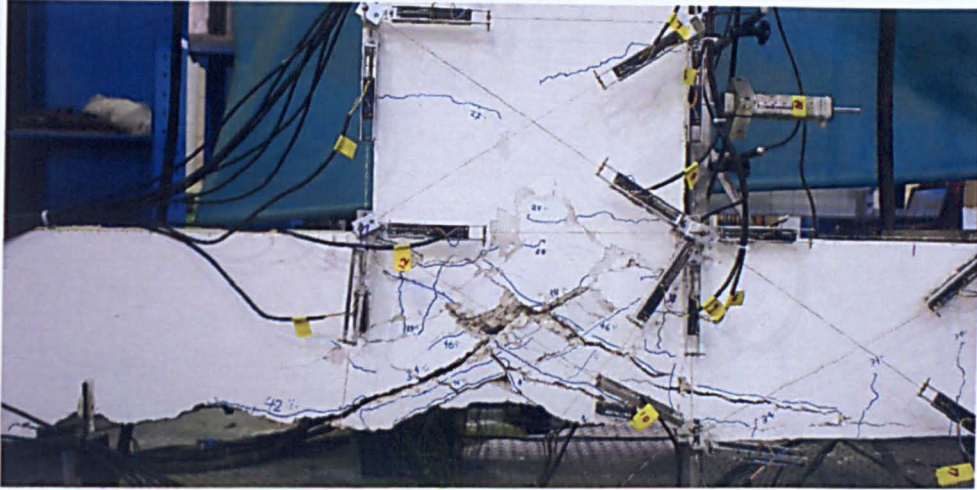


Figure 4.37: Concrete spalling in specimen JC-1 after 4.0% drift cycles

Figure 4.38 shows concrete spalling and the exposed steel rebar at the bottom of specimen JC-1 after completing the 4.0% drift cycles.



Figure 4.38: Exposed rebar in specimen JC-1 after 4.0% drift cycles

4.4.5.2 Load Drift Response

Figure 4.26 shows the applied lateral load-drift hysteretic response of joint specimen JC-1 and the equivalent beam shear calculated according to ASCE 41 (see Table 4-1). Unlike group A and group B specimens, specimens JC-1 exhibited a comparable behaviour in both loading directions. This can be attributed to the use of 90 hooks for both the bottom and the top beam bars. The maximum recorded load in the positive direction is 50kN and took place at 2.0% drift level; whereas the maximum recorded load in the negative loading direction is 47.2 kN and took place at a drift level equal to 1.5%. Degradation in both stiffness and strength is more pronounced after the 1.5% drift level in both directions (see Figure 4.26). Similar to all the

previous specimens, no reinforcement yielding was found and hence, the exhibited mode of failure is *J-Type* failure.

4.4.6 SPECIMEN JC-2

4.4.6.1 Description of Damage

Specimen JC-2 was subjected to the same displacement history as specimens in group A and B. Similarly to JA-3 and JB-2, the column of JC-2 was subjected to an axial compressive force equal to 250 kN. Figure 4.39 shows the developed cracks of specimen JC-2 between 0.25% and 2.0% drift levels. Arrows denote the direction of positive loading.

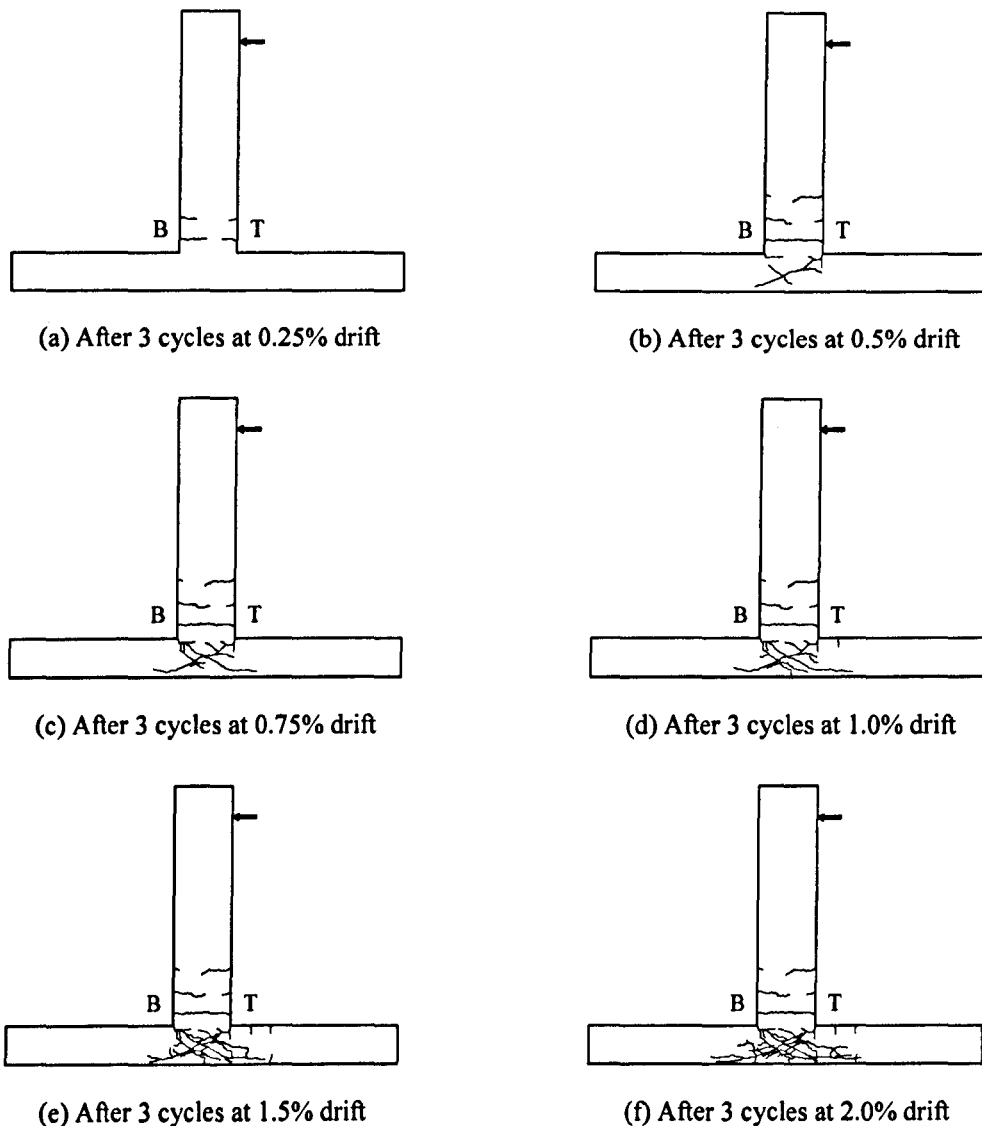


Figure 4.39: Progression of cracking for specimen JC-2

The damage observed during 0.1% drift cycles was limited to hairline cracks of width less than 0.1 mm. Apart from these cracks, no further damage was observed. Figure 4.40 shows the cyclic load-drift response of specimen JC-2 and the overall envelope. Key changes to the response envelope are marked and denoted.

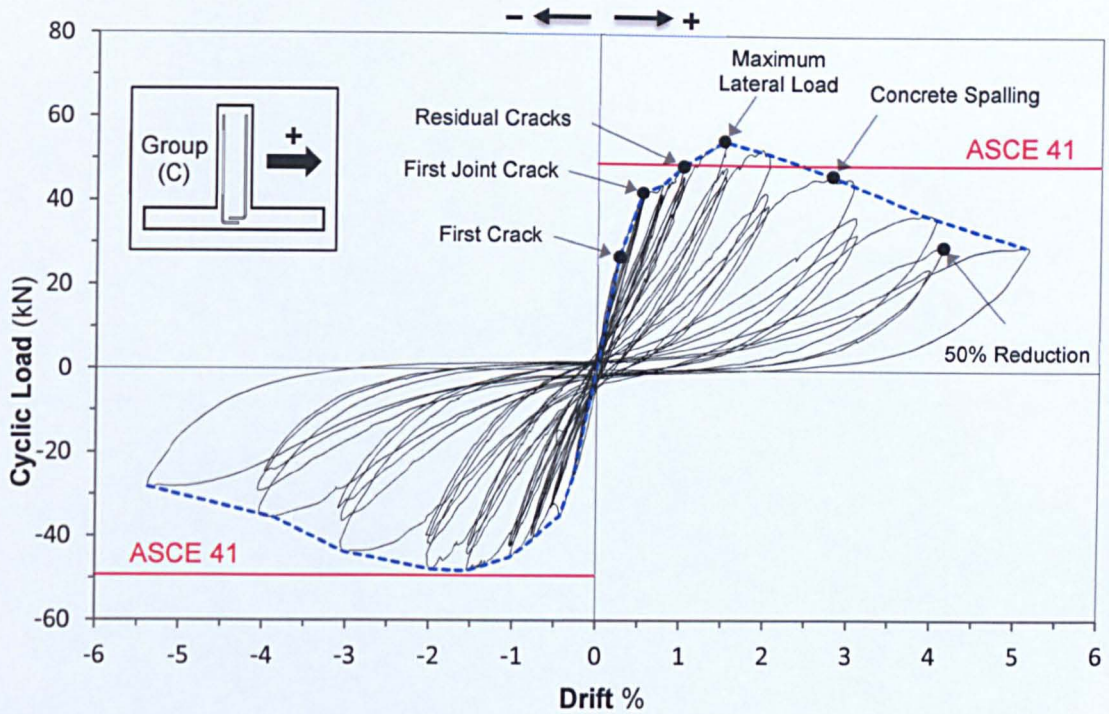


Figure 4.40 Lateral load-drift response for specimen JC-2

In general, the exhibited crack pattern and the progression of damage of specimen JC-2 during the test is very similar to that of specimen JC-1. Table 4-5 describes the progress of damage of specimen JC-2 at each drift level. The detailed description of the observed crack pattern and progress of damage of specimen JC-2 is given in Appendix B.

Table 4-5 Description of observed damage of specimen JC-2

Drift %	Damage description	Crack width (mm)
0.1	Hairline cracks	<0.1
0.25	Beam cracks of limited length – at 1 st & 2 nd shear links	<0.5
0.5	Extended beam cracks - First diagonal shear crack	<1
0.75	x-shaped diagonal cracks extending to columns – new cracks parallel to diagonals	1
1.0	More diagonal cracks – further extension to columns - visible residual cracks	1.5-2
1.5	Further cracking in the joint – peak maximum strength	2-3
2.0	Concrete flaking - increased width and length of cracks – cracks along the column outer bars	6-8
3.0	Concrete spalling – sever damage to the joint at the centre – extra damage to the top column	10-12

During the 4.0% drift cycles, specimen JC-2 suffered further severe damage accompanied by continuous loss in both strength and stiffness. The total loss by the third cycle was 50% of the maximum lateral load capacity, as can be seen in Figure 4.40. At the end of the third cycle, the specimen was severely damaged and suffering from extensive expansion in the core area.

The test was continued by displacing the joint to the 5% drift level. Similarly to the previous drift level, the joint suffered further damage leaving the bottom concrete triangle barely hanging from the bottom longitudinal reinforcement. After completing one full cycle, the specimen was near the point of total collapse. Therefore, for safety purposes, the test was stopped and concluded. Figure 4.41 shows specimen JC-2 after completing one full cycle at 5.0% drift.

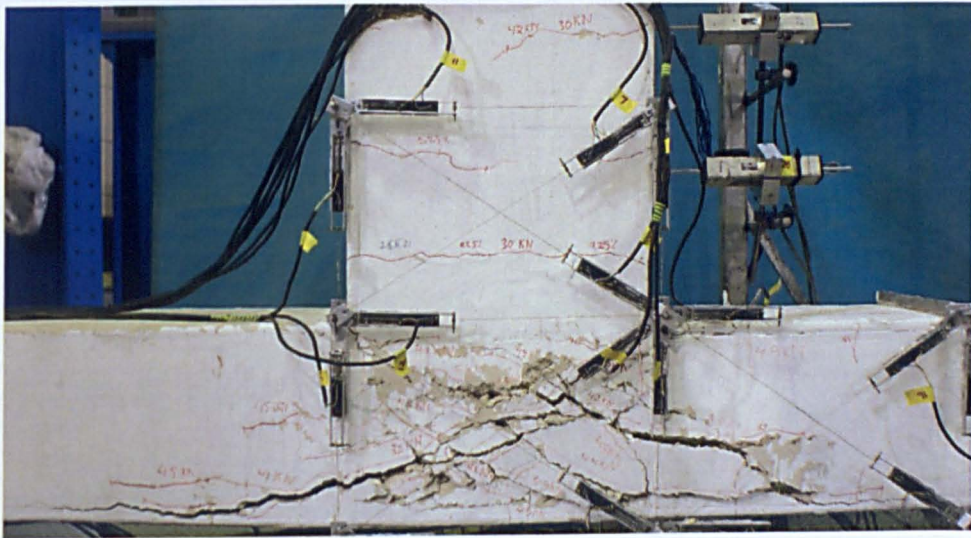


Figure 4.41: Specimen JC-2 after one cycle at 5.0% drift

4.4.6.2 Load Drift Response

Figure 4.40 shows the applied lateral load-drift hysteretic response of joint specimen JC-2 and the equivalent beam shear calculated according to ASCE 41 (see Table 4-1). Specimens JC-2, like JC-1, exhibited a comparable behaviour in both loading directions due to the use of 90 hooks for both the bottom and the top beam bars. The maximum recorded load in the positive direction is 55kN and took place at 1.5% drift level, whereas the maximum recorded load in the negative loading direction is 48kN and also at 1.5% drift. The degradation in both stiffness and strength is more pronounced after the peak in both directions (see Figure 4.40). Similar to JC-1, no reinforcement yielding was found and, hence, the exhibited mode of failure is *J-Type* failure.

4.5 PERFORMANCE INDICATORS

4.5.1 AXIAL LOAD CAPACITY

The applied axial load history to the top column of each specimen was monitored in order to investigate if any of the tested specimens failed due to the loss of axial load capacity.

Figure 4.42 shows the history of the applied axial load to the column of specimen of JA-2. As mentioned before in Chapter 3, the initial axial load on the top column at the beginning of the test was set to 150kN (corresponding to $0.07f_c A_g$). As can be seen, the axial load increased during the first half cycle at 0.1% drift level to reach a maximum value of 159.2 kN (106%). Soon after, however, the axial load started decreasing during the following cycles until it reached a steady level of 135 kN \pm 5kN. All tests were displacement controlled; therefore this slight reduction (6%) is acceptable and can be attributed to the initial rigid body movement of the specimen. In addition, it can be concluded that the observed failure did not occur due to the loss of the specimen's axial load capacity. The same applies to the other tested specimens. Plots of the applied axial load history of all the other specimens are given in Appendix B.

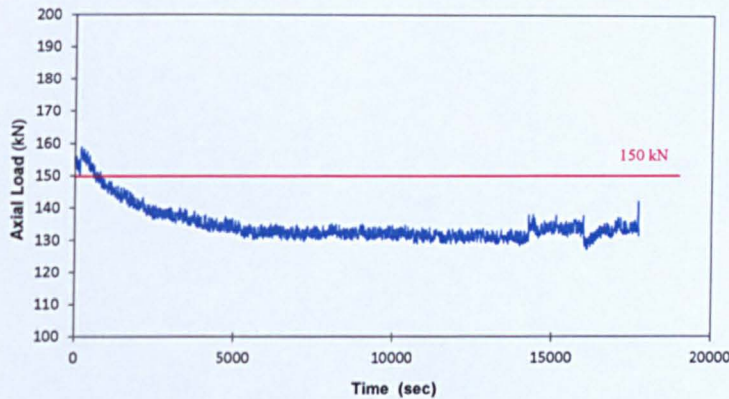


Figure 4.42 Applied axial load history of specimen JA-2

4.5.2 STIFFNESS DEGRADATION

Figure 4.43 and Figure 4.44 show the peak-to-peak stiffness degradation, as well as, the positive and negative half-cycle secant stiffness degradation of specimen JA-2 and specimen JA-3, respectively, (as defined in Chapter 2). The numbers in Figure 4.43 and Figure 4.44 denote the peak-to-peak stiffness (K_p) and the secant stiffness (K_{sec}) of the first cycle for each drift increment. The peak-to-peak stiffness of specimen JA-2 at 0.25% drift level is 6.5kN/mm, whereas the positive and negative half-cycle secant stiffness is 6.3kN/mm and 5.7kN/mm, respectively. It's evident from Figure 4.43 that stiffness degradation continued throughout the test, however, most of the degradation occurred during the initial cycles up to 1.0% drift level. Furthermore, the specimen in the negative loading direction exhibited less stiffness. This can be expected due to the straight bar anchorage and the cracks that develop in the joint panel during the preceding positive half cycle. By the end of the test, and at 2% drift, 80% of specimen JA-2 peak-to-peak stiffness at 0.25% drift was lost. As can be seen in Figure 4.44, specimen JA-3 exhibited similar behaviour to specimen JA-2. However, at 5.0% drift, 96% of specimen JA-3 peak-to-peak stiffness at 0.25% drift was lost.

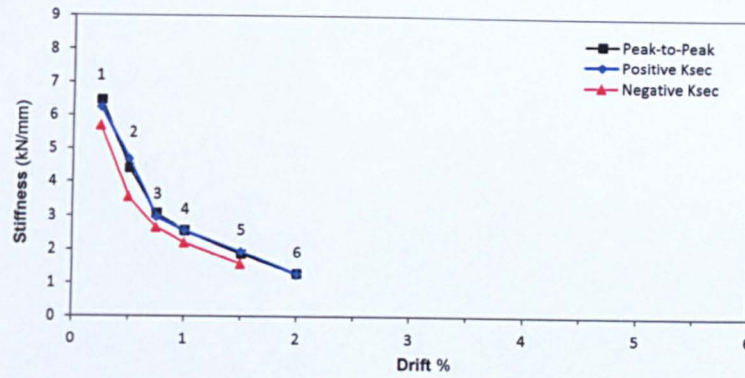


Figure 4.43 Peak-to-peak and half-cycle secant stiffness degradation of specimen JA-2

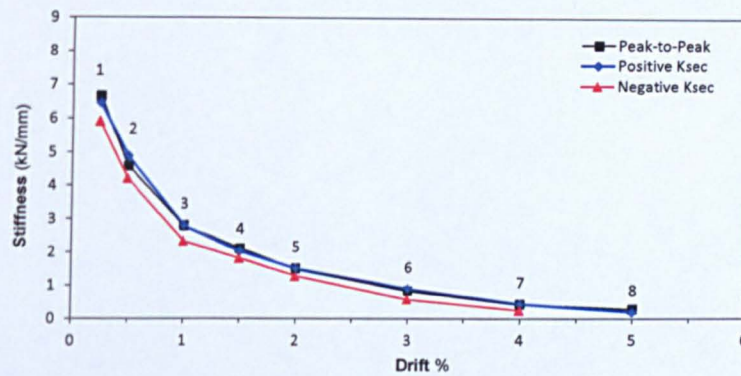


Figure 4.44 Peak-to-peak and half-cycle secant stiffness degradation of specimen JA-3

Despite the different anchorage detailing, group B and group C specimens exhibited similar behaviour to group A. Plots of the peak-to-peak stiffness degradation and the half-cycle secant stiffness degradation of the remaining specimens are given in Appendix B.

4.5.3 SHEAR STRESS-STRAIN RESPONSE CURVE

The joint shear stress τ_j (normalised by $\sqrt{f_c}$) vs. the joint shear strain γ_j of specimen JA-2 and specimen JA-3 are shown in Figure 4.45 and Figure 4.46, respectively. For specimen JA-2, the maximum joint shear stress is 2.9 MPa, which in terms of the joint shear strength coefficient γ , is equal to 0.53 ($\sqrt{\text{MPa}}$). This maximum shear stress occurred during positive loading at 1.5% drift level. The corresponding joint shear strain (γ_j) to the maximum shear stress in the positive loading direction is 6540 $\mu\epsilon$ (0.00654 Rad). Moreover, the maximum joint shear stress in the negative loading direction is 2.7 MPa or $\gamma = 0.49$ ($\sqrt{\text{MPa}}$), and it also occurred at 1.5% drift level. The corresponding joint shear strain (γ_j) to the maximum shear stress in the negative loading direction is 6480 $\mu\epsilon$ (0.00648 Rad).

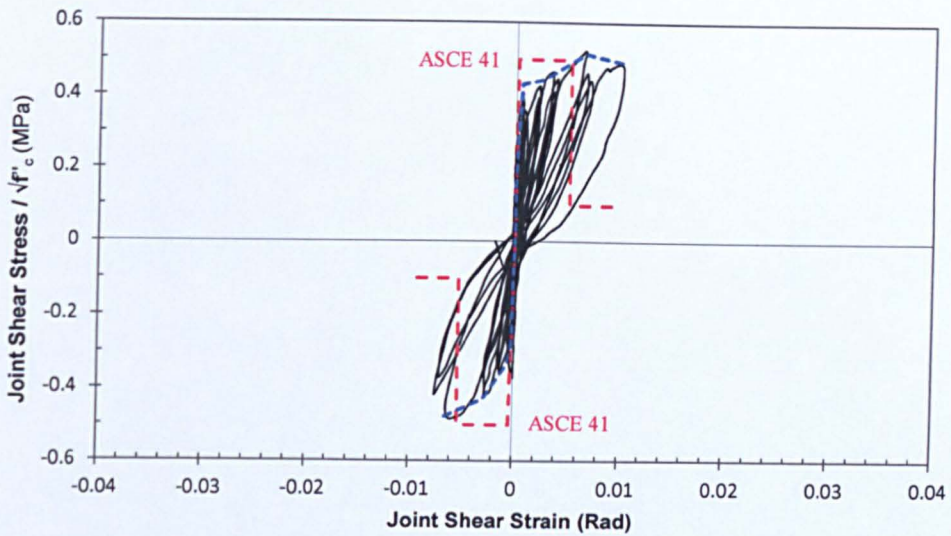


Figure 4.45 Joint shear stress-shear strain of specimen JA-2

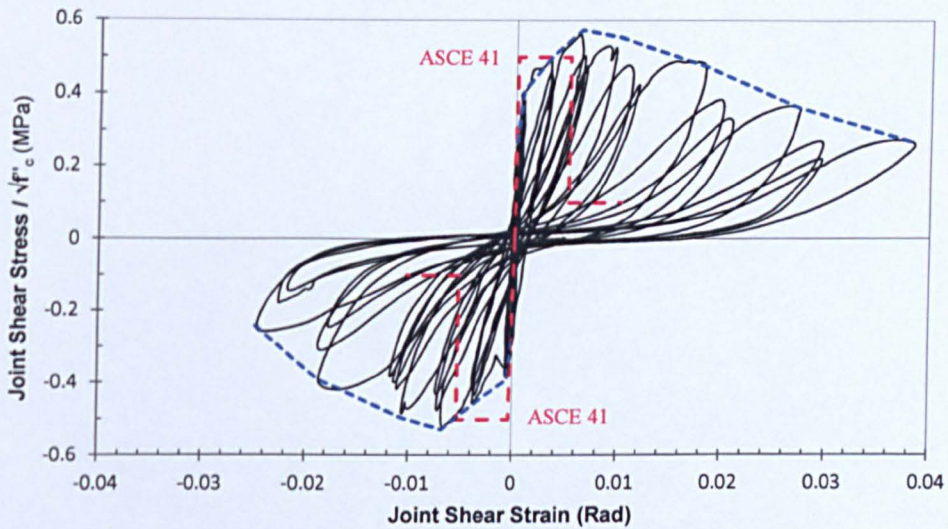


Figure 4.46 Joint shear stress-shear strain of specimen JA-3

The overall shear stress-strain response curve of specimen JA-3 is very similar to that of specimen JA-2, as can be seen in Figure 4.46. Table 4-6 shows the maximum joint shear stress and the corresponding shear strain of specimen JA-3 in both loading directions.

Table 4-6 Maximum joint shear stress-strain of specimen JA-3

Specimen No.	Loading direction	Drift %	Shear stress (MPa)	γ ($\sqrt{\text{MPa}}$)	shear strain (Rad)	ASCE 41 ($\sqrt{\text{MPa}}$)
JA-3	+	1.5	3.3	0.57	0.0063	0.50
	-	-1.5	-3.0	-0.53	-0.0067	-0.50

It is evident from Figure 4.45 that the shear provisions of ASCE 41 (2006) predicted with fairly good accuracy ($\pm 4\%$) the joint shear strength of specimen JA-2 in both positive and negative

loading directions. The same can be said about the prediction of the initial stiffness in both directions. However, the overall shape of the predicted envelope, the point at which joint shear strength is achieved, and strength degradation do not match that of the experiment, especially that the test ended at an early stage, as can be seen in Figure 4.45. Moreover, in the case of specimen JA-3, and as can be seen in Figure 4.46, ASCE 41 (2006) was less successful in predicting the envelope of the measured shear stress-strain response.

Furthermore, Figure 4.47 and Figure 4.48 show the peak-to-peak normalised shear modulus degradation of specimen JA-2 and specimen JA-3, respectively. As before, numbers denote the peak-to-peak shear modulus of the first cycle for each drift increment. The initial peak-to-peak shear stiffness at 0.25% drift is 9.2GPa for specimen JA-2 and 10.3GPa for specimen JA-3, whereas the shear modulus calculated from concrete sample cylinders is 10.9GPa and 11.2GPa for JA-2 and JA-3, respectively. It's evident from Figure 4.52 and Figure 4.53 that the shear modulus degradation was rather steep during the initial cycles up to 1% drift level. By the end of the first cycle at 2% drift, around 97% of the initial stiffness was lost in both specimens.

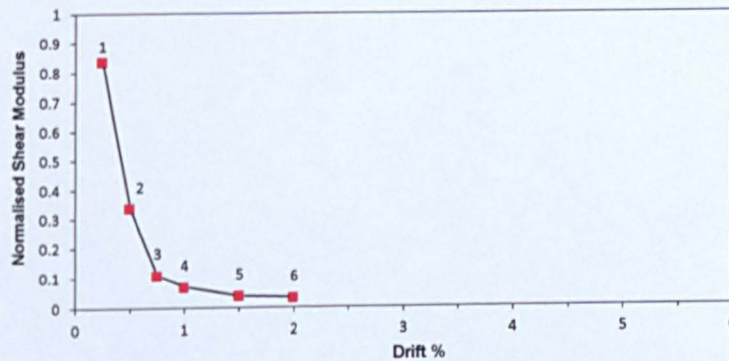


Figure 4.47 Peak-to-peak Shear Modulus Degradation of specimen JA-2

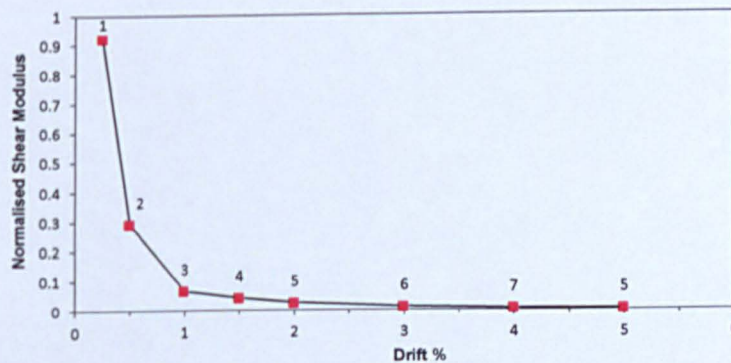


Figure 4.48 Peak-to-peak Shear Modulus Degradation of specimen JA-3

The same behaviour was found in the other specimens. Plots of the shear stress-shear strain response of all the remaining specimens with comparison to ASCE 41 and the peak-to-peak normalised shear modulus degradation are given in Appendix B.

4.5.4 JOINT SHEAR DEFORMATION

Figure 4.49 through Figure 4.51 show the contribution of joint shear deformation (Δ_j) to the total drift (i.e. beam tip displacement Δ_b) of group A, B & C specimens, respectively. The contribution of joint shear deformation, Δ_j is calculated based on the joint geometry and the average joint shear strain determined following the proposed method in Chapter 3. As can be seen in Figure 4.49 through Figure 4.51, the ratio of joint shear deformation to the overall beam tip displacement, Δ_j/Δ_b kept increasing throughout the test, even beyond the point of peak shear strength. This confirms the shear failure of the joint (i.e. *J-Type* failure).

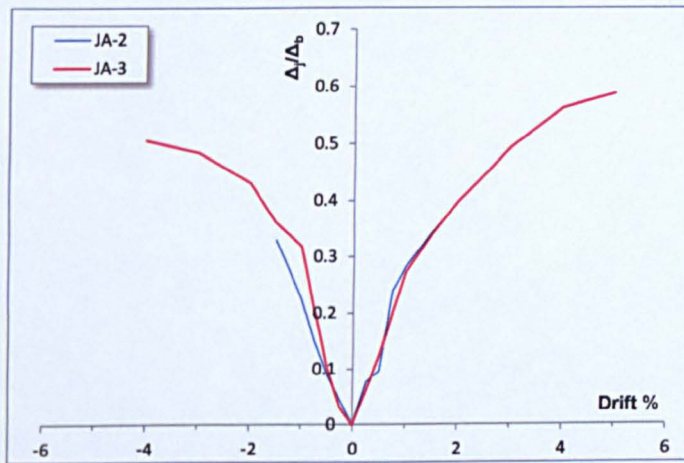


Figure 4.49 Contribution of joint shear deformation of group A specimens to total drift

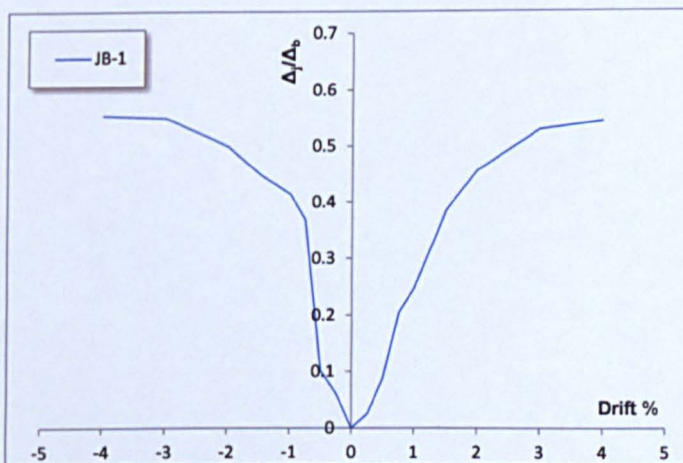


Figure 4.50 Contribution of joint shear deformation of group B specimens to total drift

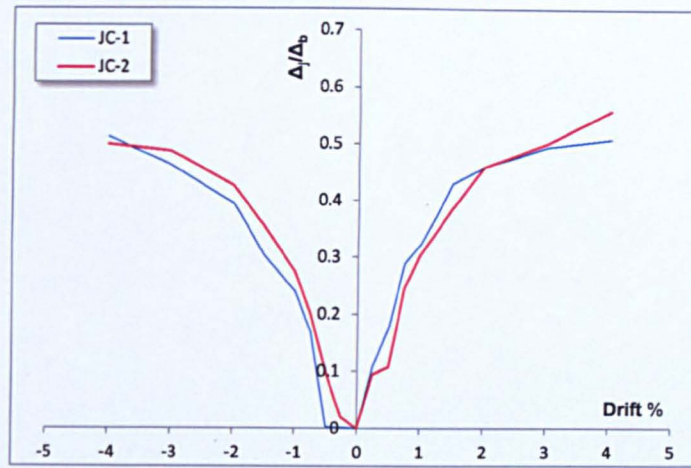


Figure 4.51 Contribution of joint shear deformation of group C specimens to total drift

Despite the difference in the joint detailing, a similar trend, with small variances, can be observed in these three groups. For specimens JA-2 and JA-3, at 0.5% drift level, the contribution of joint shear deformation to the total beam tip displacement is on average 10% in both the negative and positive directions. At 1.5% drift level, the contribution of joint shear deformation increases to an average of 34% in both directions, whereas at 2% drift the ratio becomes 40% for both specimens in the positive direction and 43% in the negative direction for JA-3 only. Moreover, when specimen JA-3 loses 50% of its maximum strength at 4% drift level, the contribution of joint shear strain to beam displacement becomes 56%. This confirms the flexible/deformable nature of joint panels of deficient joints. It also indicates that a dedicated joint panel element capable of representing the joint nonlinear shear deformations is required for RC frame analysis of older buildings.

The same findings with comparable results can be observed in the other specimens (JB-1; JC-1; JC-2), as can be seen in Figure 4.50 and Figure 4.51.

4.5.5 DISSIPATED ENERGY

The cumulative energy dissipation of specimen JA-2 and specimens JA-3 are shown in Figure 4.52. The numbers in Figure 4.52 denote the last cycle of each drift increment. However, number 7 in specimen JA-2 denotes only the first half cycle at 2% drift, as at this stage the test was stopped. In addition, each small circle denotes one complete cycle.

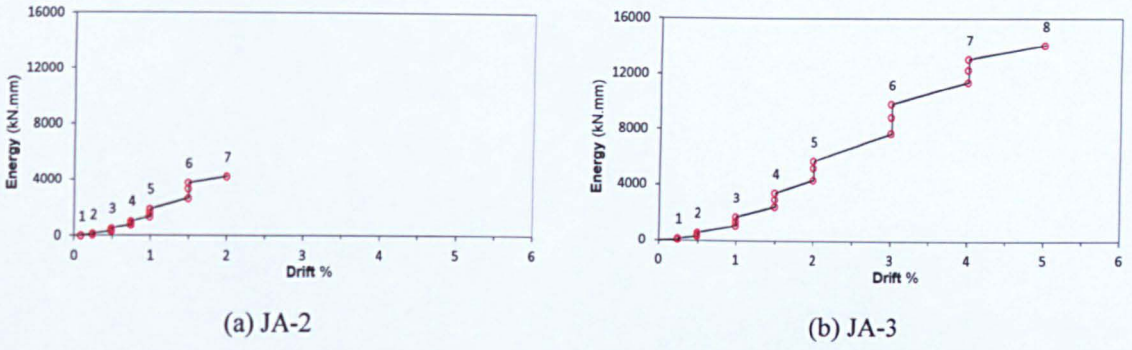


Figure 4.52 Cumulative energy dissipation of specimen JA-2 and specimen JA-3

Figure 4.53 shows the dissipated energy per cycle of specimen JA-2 and specimen JA-3. It is evident from Figure 4.53 that the dissipated energy increased with each drift increment. However, for each drift increment, the dissipated energy of the first cycle is always the highest. At 1.5% drift level, at which the maximum lateral load was recorded in both the positive and the negative loading directions in both specimens, the dissipated energy in the first cycle for specimen JA-2 and specimen JA-3 is 756 kN.mm and 745kN.mm, respectively.

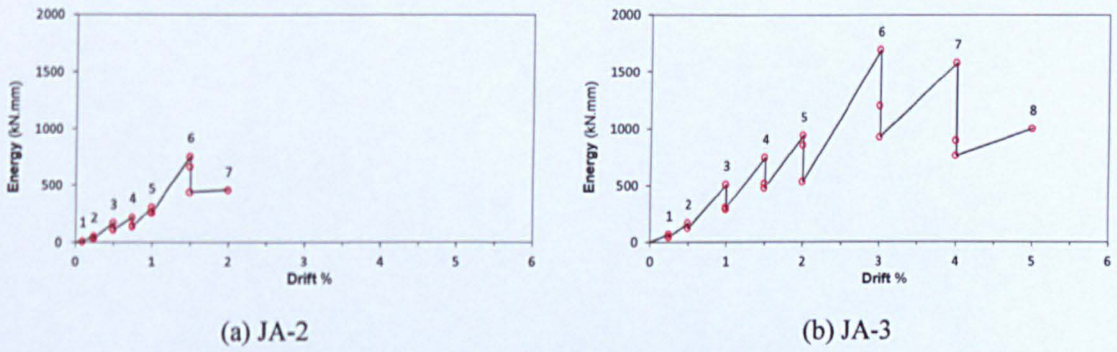


Figure 4.53 Dissipated energy per cycle for specimen JA-2 and specimen JA-3

Similar findings were found for the other specimens. Plots of the cumulative energy dissipation and energy dissipation per cycle of all the remaining test specimens are given in Appendix B.

4.5.6 BEAM BAR STRAINS

Strain distribution of the beam top and bottom bars was monitored, throughout the test, using strain gauges. Figure 4.54 shows the strain gauge configuration for the beam bars of specimens JA-2 and JA-3.

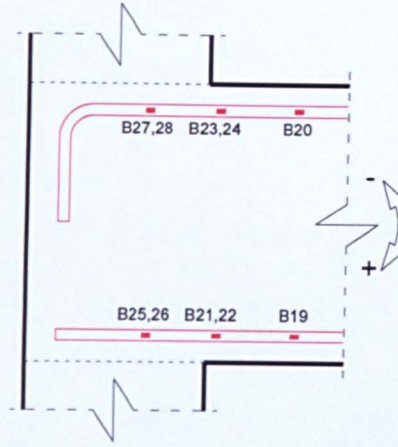


Figure 4.54 Investigated strain gauges of beam top and bottom bars

Figure 4.55 and Figure 4.56 show the strain distribution of the top and bottom reinforcement bars around the joint-beam interface of specimens JA-2 and JA-3. The measured strains of the top and bottom bars of each specimen showed comparable results outside the joint. However, inside the joint, measured strains of bottom bars generally decreased after the 1.0% drift level (i.e. after the onset of diagonal joint cracking).

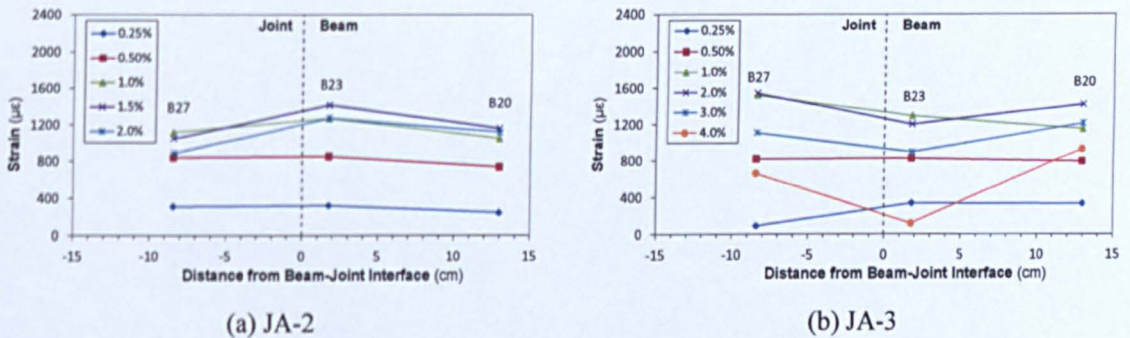


Figure 4.55 Strain distribution of top beam bar at first positive peak of each drift level

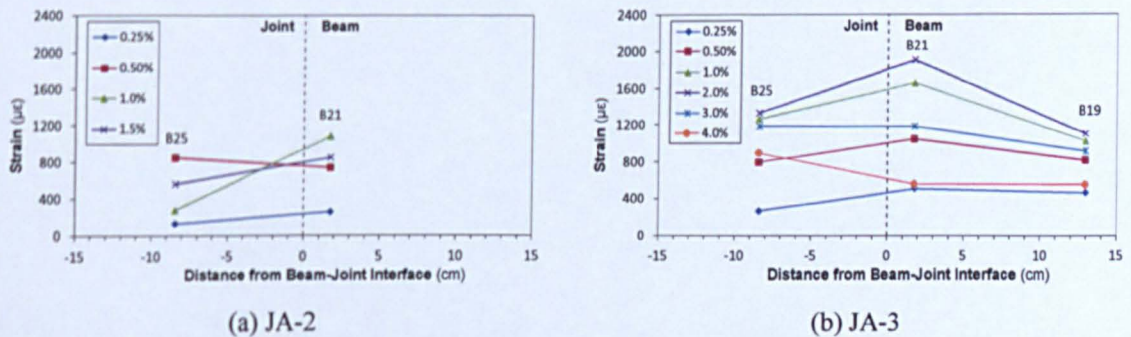


Figure 4.56 Strain distribution of bottom beam bar at first negative peak of each drift level

The strain profiles of beam top and bottom bars, shown in Figure 4.55 and Figure 4.56, indicate that the beam remained within the elastic range (i.e. no yielding) during the test. This is also confirmed in Figure 4.57, as it shows the agreement between measured strains of the top bar of

specimen JA-2 and calculated strains from section analysis based on the applied force at each drift level. This shows that the beam's contribution to the total drift is limited to beam elastic deformations (of a cracked section). It also shows that the bottom bar did not pull-out (as was expected), which indicates that the observed joint deterioration is a result of only shear deformation within the joint panel.

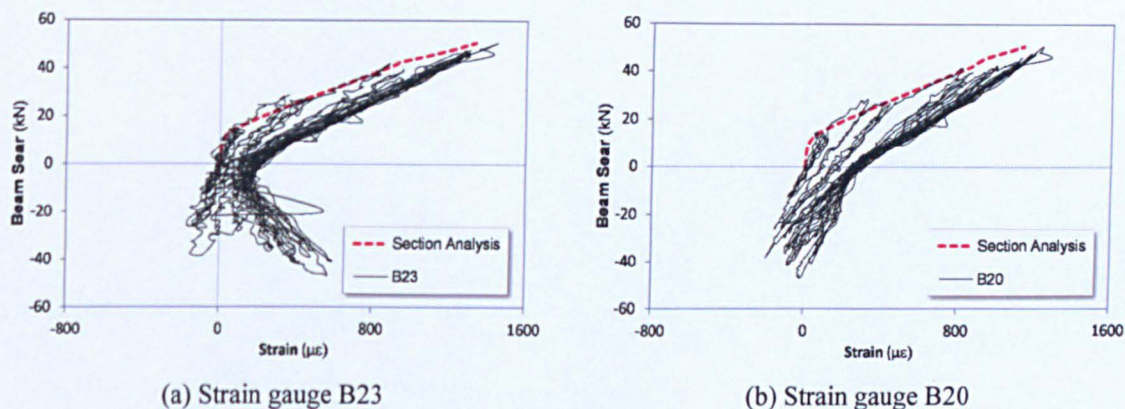


Figure 4.57 Top bar measured strains of specimen JA-2 in comparison to section analysis prediction

The same findings apply to the other specimens. Full details of all the measured strains of beam and column bars are given in Appendix B. Similar results were attained from the column strains.

4.6 EVALUATION OF TEST VARIABLES

4.6.1 EFFECT OF AXIAL LOAD LEVEL

The effect of axial load level on the nonlinear behaviour of deficient exterior beam-column joints was investigated in this research. This was accomplished by applying two levels of axial loads 150kN ($\approx 0.07f'_c A_g$) and 250kN ($\approx 0.12f'_c A_g$) to the top column of the first and second specimens, respectively, of each group, as shown in Table 4-7.

Table 4-7 Applied axial load level

Specimen No.	N nominal (kN)	N Actual (kN)	$\frac{N}{f'_c A_g}$	f'_c (Mpa)
JA-1	150	152	0.09	24.3
JA-2	150	136	0.07	31.0
JA-3	250	248	0.11	32.4
JB-1	150	148	0.07	31.1
JB-2	250	246	0.12	30.8
JC-1	150	144	0.08	27.2
JC-2	250	239	0.11	32.6

As can be seen in Table 4-7, the differences in the axial load level between the specimens of each group are quite small. This is due to the unintentional increase in the concrete compressive strength of the test specimens. As previously discussed in Chapter 3, the initial design called for concrete compressive strength, f'_c equal to 16 MPa, whereas the measured values (on the day of testing) were almost double, as shown in Table 4-7.

In the following section, the effect of axial load variation on the joint performance of the tested specimens is discussed and quantified.

4.6.1.1 Joint Shear Strength and Load-Drift Response

Table 4-8 shows beam shear and joint shear strength of all the tested specimens. All test specimens experienced joint shear failure with no prior reinforcement yielding (*J-Type* failure). Figure 4.58 through Figure 4.60 show the normalised load-drift response curves of group A, B & C specimens, respectively.

Table 4-8 Joint shear strength of the test specimens

Specimen No.	**	N (kN) ¹	Drift % [*]	V_b (kN) ¹	$V_b/\sqrt{f'_c}$ ²	γ ³	Shear strain (Rad) [*]
JA-2	+	150	1.55	50.6	9.1	0.52	0.0065
	-		-1.59	-47.1	-8.5	-0.48	-0.0065
JA-3	+	250	1.51	56.6	9.9	0.57	0.0063
	-		-1.53	-52.3	-9.2	-0.53	-0.0067
JB-1	+	150	1.59	50.8	9.1	0.52	0.0069
	-		-1.48	-37.9	-6.8	-0.39	-0.0077
JB-2	+	250	1.40	58.0	10.4	0.61	-
	-		-1.45	-43.3	-7.8	-0.45	-
JC-1	+	150	1.98	50.2	9.6	0.56	0.0111
	-		-1.39	-47.2	-9.0	-0.52	-0.0051
JC-2	+	250	1.49	55.0	9.6	0.56	0.0070
	-		-1.55	-48.0	-8.4	-0.49	-0.0067

* This table lists the joint shear strains and drift levels that occurred at peak loads (in both loading directions).

** (+/-) refers to the loading direction.

¹ N is the column axial load (kN), and V_b is the corresponding beam shear (applied cyclic load) at peak load.

² here V_b is taken as (kN) and f'_c is taken as (MPa)

³ γ is denoted here as the "joint shear strength coefficient" ($\sqrt{\text{MPa}}$), as defined in section 2.4.2.

Comparing the response curves of group A specimens show that both specimens exhibit the same response curve up to 0.5% drift, after which the effect of the axial load level is evident (see Figure 4.58). The average increase ratio in both directions, due to the increase in the axial load level, is 11.1% (see Table 4-8). Similarly, the same trend is found between group B

specimens, however, the average enhancement ratio in both directions is 14.8%, (see Figure 4.59).

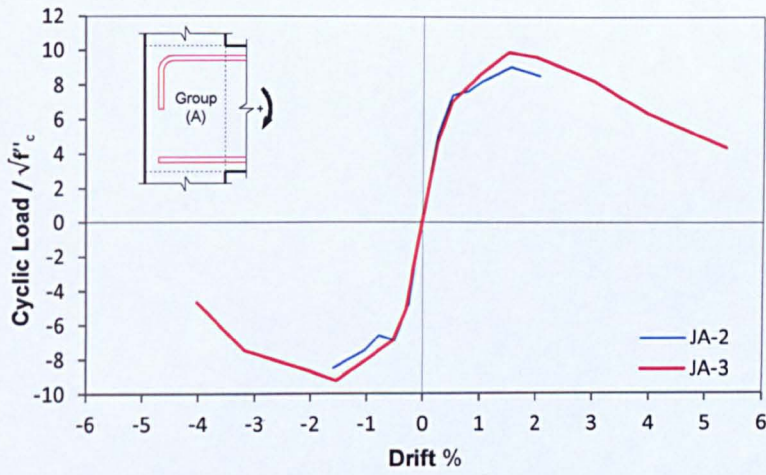


Figure 4.58 Normalised load-drift envelope curves of group A specimens

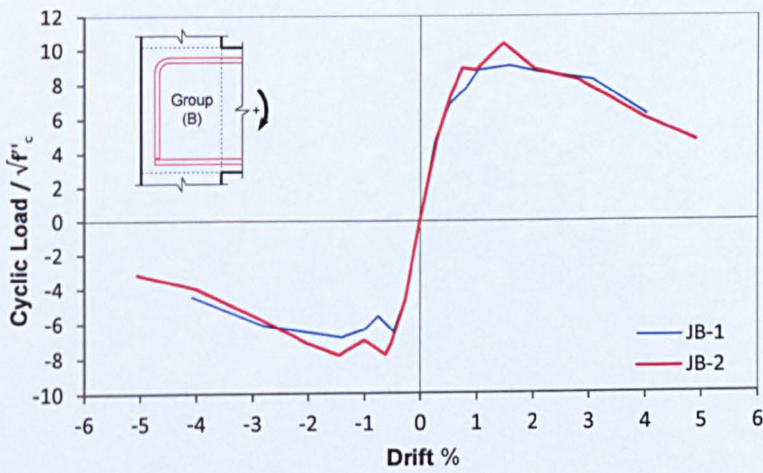


Figure 4.59 Normalised load-drift envelope curves of group B specimens

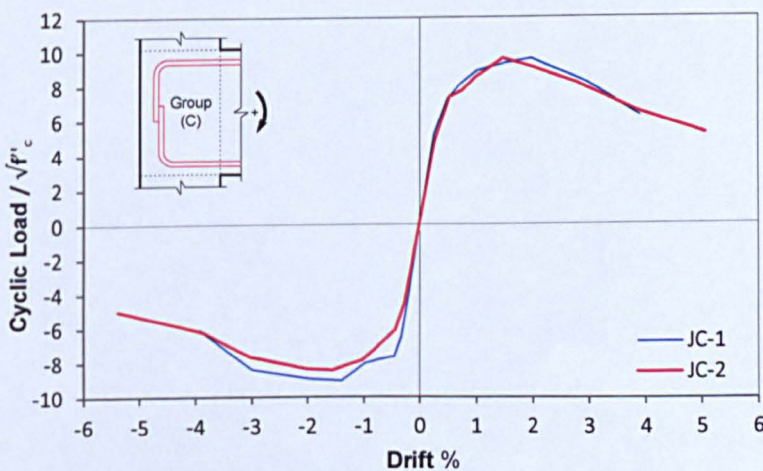


Figure 4.60 Normalised load-drift envelope curves of group C specimens

As for group C, both specimens show almost identical response in the negative loading direction, whereas JC-2 achieves 9.5% higher strength than JC-1 in the positive loading direction. When taking into account the normalised beam shear, results show a slight discrepancy as the strength of JC-1 in the negative loading direction becomes 7% higher than JC-2, while in the other direction JC-2 stays slightly higher than JC-1 (see Figure 4.60). This discrepancy is due to the differences in the displacement history of both specimens. Specimen JC-1 completed only 2.5 cycles at 1% drift level, as at the last half cycle the specimens was displaced by mistake to 1.5% drift level in the negative direction. This caused the main diagonal shear crack to appear in this direction and, as a result, reduced the shear capacity in the positive direction. This is also reflected in the positive to negative direction strength ratios, as can be seen in Table 4-9.

Table 4-9 Positive to negative direction strength ratios of the test specimens

Strength ratio	JA-2	JA-3	JB-1	JB-2	JC-1	JC-2
(+/-) %	7.6	8.2	34	34	6.4	14.4

Based on these notes, the comparison presented here regarding the negative loading direction is not enough to establish a solid conclusion about group C specimens. Therefore, only the results of the positive direction are considered for further analysis.

As previously discussed in Chapter 2 the effect of axial load level on joint shear strength is a matter of debate, especially for unconfined joints. However, for the current tests, it can be concluded that for exterior joints with Type A and B anchorages and *J-Type* failure, a higher axial load level, (within the range of 0 to $0.2f'_c A_g$) can enhance the overall joint strength up to an average of 14%. On the other hand, for Group C joints (two 90° hooks), the axial load level has to be increased more than 3% of the column axial strength ($f'_c A_g$) to see a clear effect on the joint shear strength (the axial load increased from $0.08f'_c A_g$ for JC-1 to $0.11f'_c A_g$ for JC-2, see Table 4-7). This is contrary to what was reported in the literature that the influence of column axial load levels smaller than $0.2f'_c A_g$ is small or insignificant on the joint shear strength (see Chapter 2).

This enhancement to the joint strength, due to the increase of the column axial load level, becomes much clearer when comparing the load-drift response curves (i.e. without normalisation) of each group specimens, especially for Group C. Figure 4.61 through Figure 4.63 show the load-drift response curves of group A, B & C specimens, respectively.

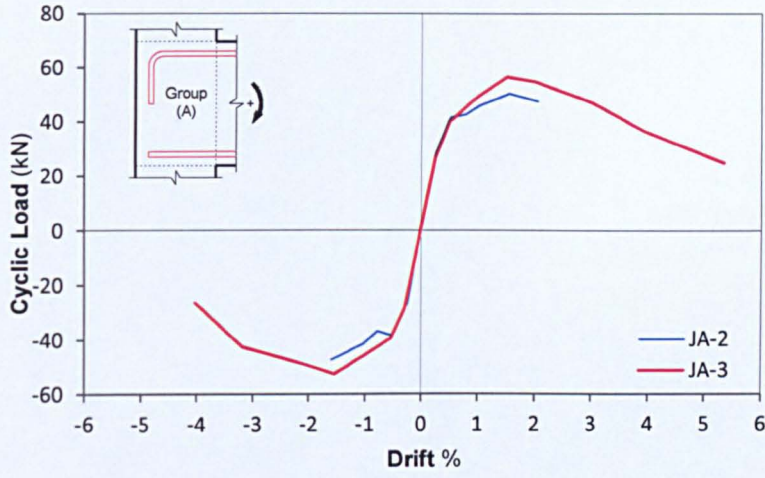


Figure 4.61 Load-drift envelope curves of group A specimens

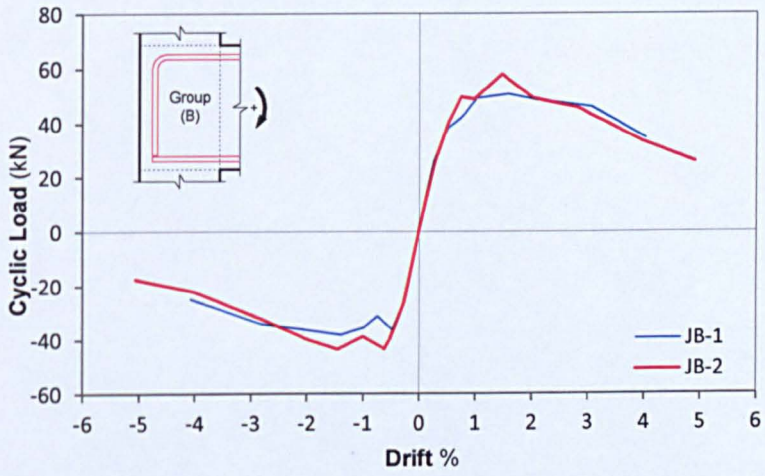


Figure 4.62 Load-drift envelope curves of group B specimens

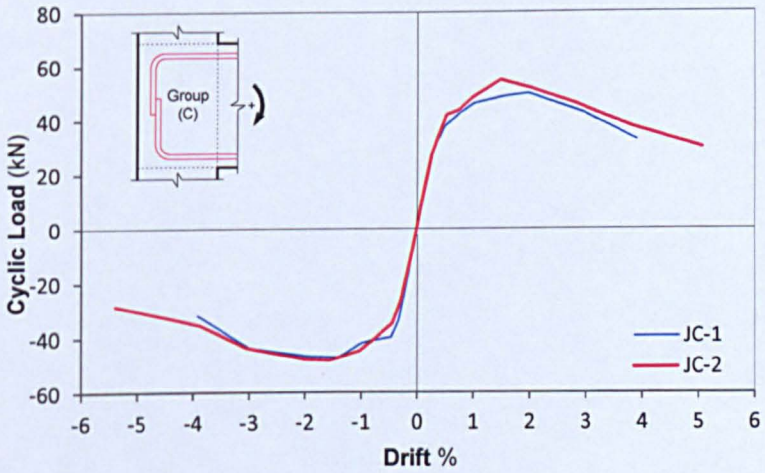


Figure 4.63 Load-drift envelope curves of group C specimens

4.6.1.2 Stiffness Degradation

Figure 4.64 through Figure 4.66 show the normalised peak-to-peak stiffness degradation of group A, B & C specimens, respectively. Despite the differences in the beam anchorage reinforcement, a similar trend can be observed in the three figures. At 0.25 % and 0.5% drift levels all specimens show similar stiffness values. Between 0.75% and 1.5% drift the specimens with higher axial load exhibit higher strength, whereas after 1.5% drift the specimens with lower axial load show higher stiffness values.

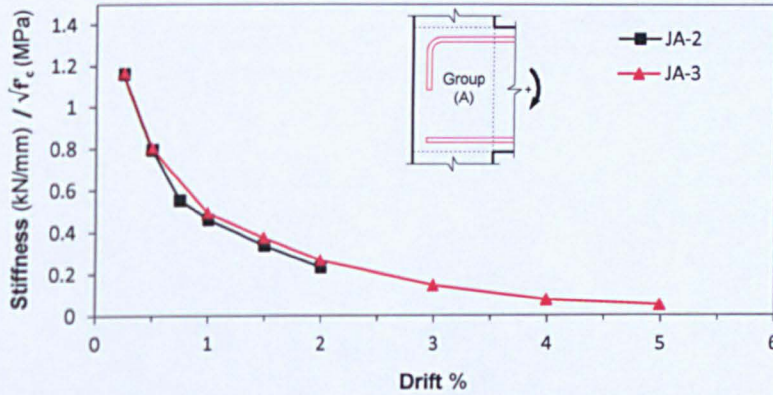


Figure 4.64 Normalised Peak-to-Peak stiffness degradation of group A specimens

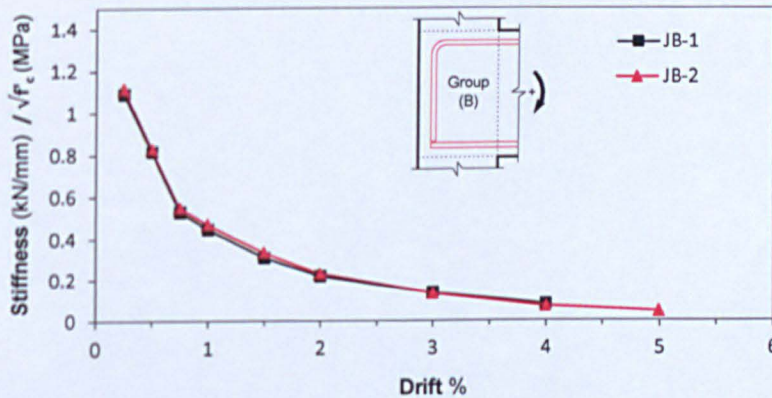


Figure 4.65 Normalised Peak-to-Peak stiffness degradation of group B specimens

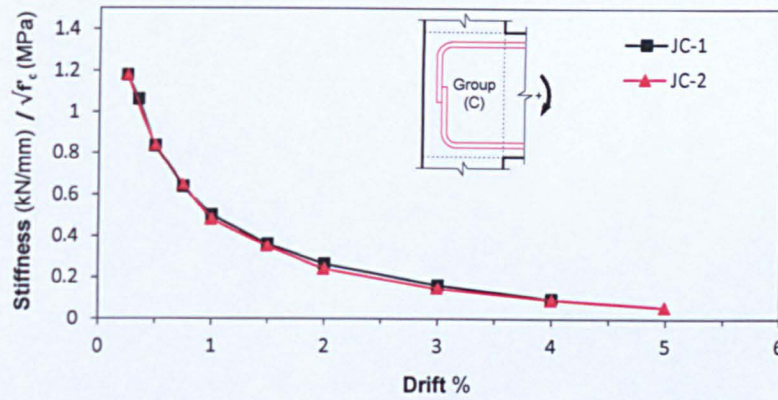


Figure 4.66 Normalised Peak-to-Peak stiffness degradation of group C specimens

Based on these observations, it can be concluded that for exterior joints with similar geometry (Type A, B or C anchorage) and *J-Type* failure, a higher axial load increases the stiffness in the pre-peak range, whereas the effect on the post-peak stiffness is reversed. Similar trend can be observed when comparing the half-cycle secant stiffness ($\pm K_{sec}$) for each group. Figure 4.67 through Figure 4.69 show the positive and negative half-cycle secant stiffness degradation of group A, B & C specimens, respectively.

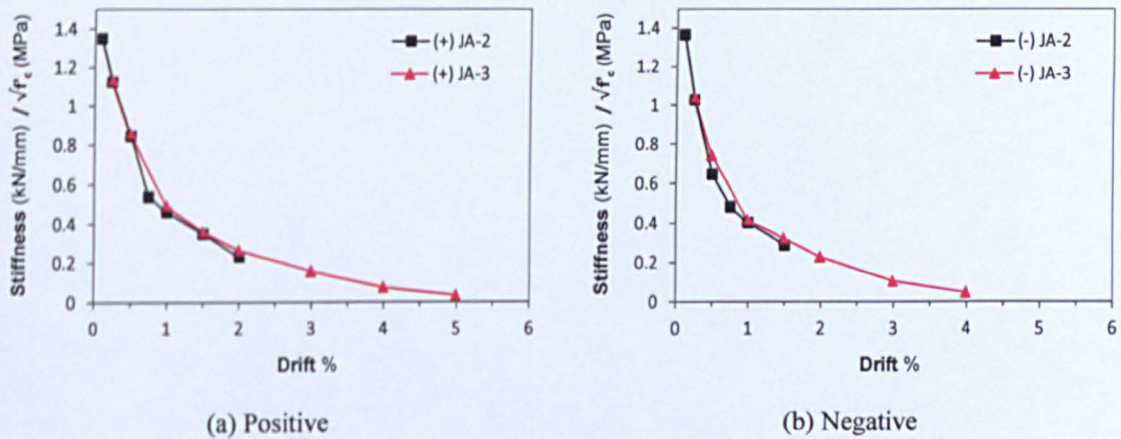


Figure 4.67 Half-cycle secant stiffness degradation of group A specimens

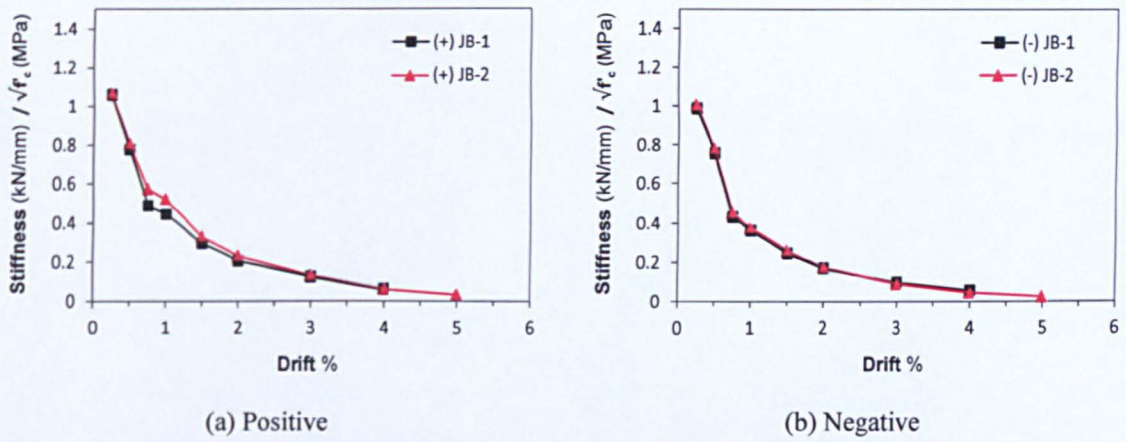


Figure 4.68 Half-cycle secant stiffness degradation of group B specimens

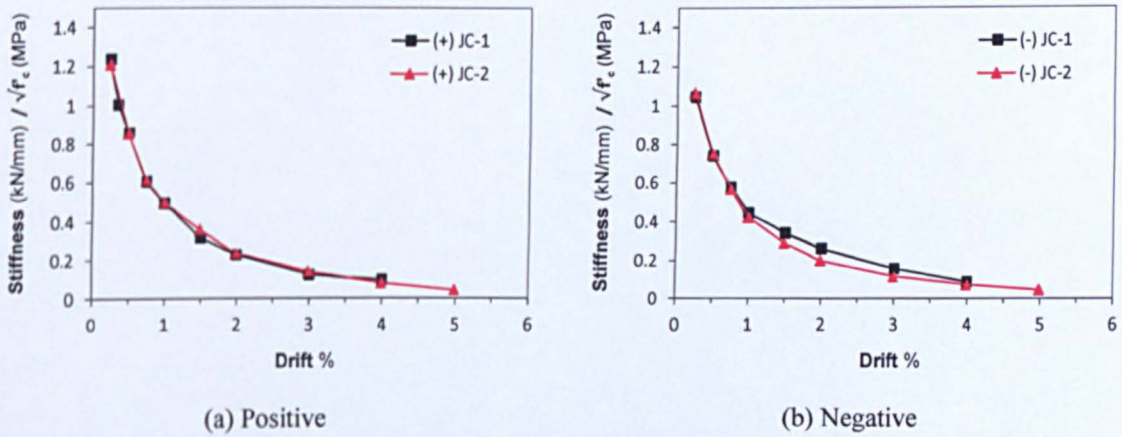


Figure 4.69 Half-cycle secant stiffness degradation of group C specimens

4.6.2 ANCHORAGE TYPE

One of the main aims of this research is to investigate the effect of different anchorage details on the nonlinear behaviour of deficient exterior beam column joint. This was achieved by dividing the test specimens into three groups (A, B & C), where each group utilised a different type of beam longitudinal reinforcement, as described in Chapter 3.

In the following section, the effect of different anchorage types on the joint performance of the tested specimens is discussed and quantified. For comparison purposes, test specimens are divided into two groups based on their axial load level. Group I consists of JA-2, JB-1 and JC-1, whereas Group II consists of JA-3, JB-2 and JC-2.

4.6.2.1 GROUP I

Figure 4.70 shows the normalised load-drift envelope curves of Group I specimens. As previously mentioned, all three specimens were subjected to an axial load level equal to 150 kN and experienced joint shear failure with no prior reinforcement yielding (*J-Type Failure*).

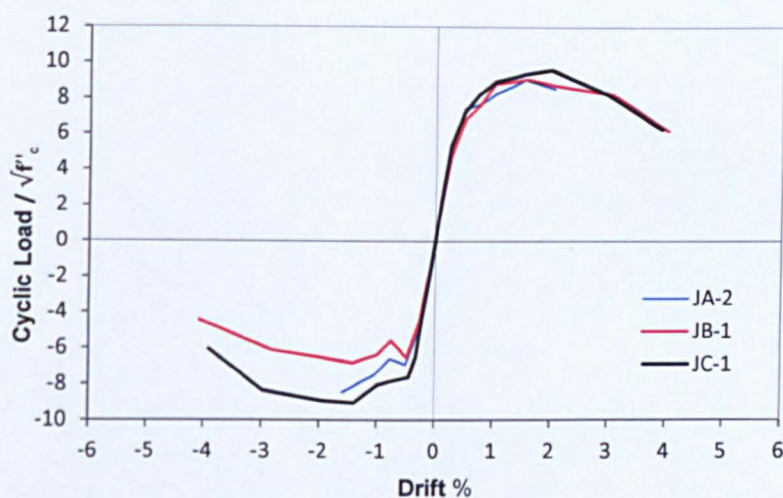


Figure 4.70 Normalised load-drift envelope curves of group I specimens

All specimens showed almost the same response curve in the positive loading direction up to 0.5% drift. Specimen JC-1 achieved the highest strength, whereas JB-1 barely topped JA-2, as shown in Table 4-8. In the negative loading direction, differences in the performance due to the use of straight bar anchorage are much more pronounced. However, despite specimen JB-1 having a technically better anchorage (longer hook) than JA-2, the former achieved the lowest strength. The maximum normalised beam shear force of specimen JC-1 is 5% higher than both specimen JA-2 and JB-1 in the positive loading direction, whereas in the negative direction it is 7% higher than JA-2 and 33.2% higher than JB-1.

Based on the outcome of this comparison, it is clear in the positive loading direction that changing the length of the vertical part of the top hook within the joint had practically no significant effect on the overall joint shear strength for the specimens with anchorage Type A&B. This is probably because bending on the beam was not enough to cause anchorage failure of the hook.

On the other hand, in the negative loading direction or when the bottom straight bar anchorage side is in tension, JC-1 attained the highest strength, whereas JA-2 is higher than JB-1. The extra strength achieved by JC-1 means that the presence of a bottom hook enhances the capacity of the diagonal compressive strut which in turn leads to a higher strength. However, the fact that JA-2 achieved a higher strength than JB-1 was not expected, especially since the latter has a longer hook. This only indicates that the extra length of JB-1's hook has no effect on improving the performance of the bottom straight bar, but rather a negative effect. The only explanation for

this negative effect is that when the hooked bar is compressed, the end of the hook pushes the cover out. This weakens the concrete compressive strut. This is evident when comparing the damage pictures of both JA-2 and JB-1 (see section 4.4), as they clearly show how the longer hook, in the latter, caused more damage to the core at the same drift level.

Therefore, it can be concluded that, in general, exterior joints with Type C anchorage can achieve higher shear strength than both Type A and Type B joints, when the bottom beam bars are in tension. This can be attributed to the extra confinement offered by the bottom hooks to the concrete core, in comparison to the other two types. However, more tests are needed to quantify further the effect of type B anchorage and to establish more solid conclusions.

The same findings, for both the negative and the positive side, can be observed when comparing the load-drift envelope curves and the normalised shear stress-strain envelope curves of Group I specimens, as can be seen in Figure 4.71 and Figure 4.72.

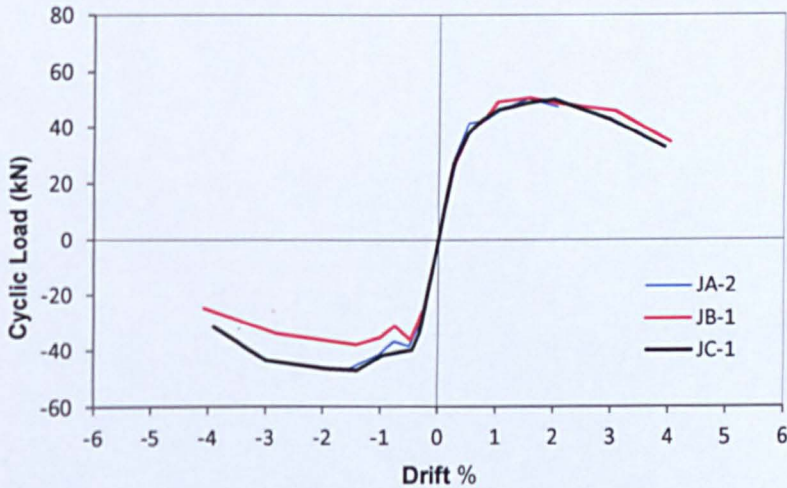


Figure 4.71 Load-drift envelope curves of Group I specimens

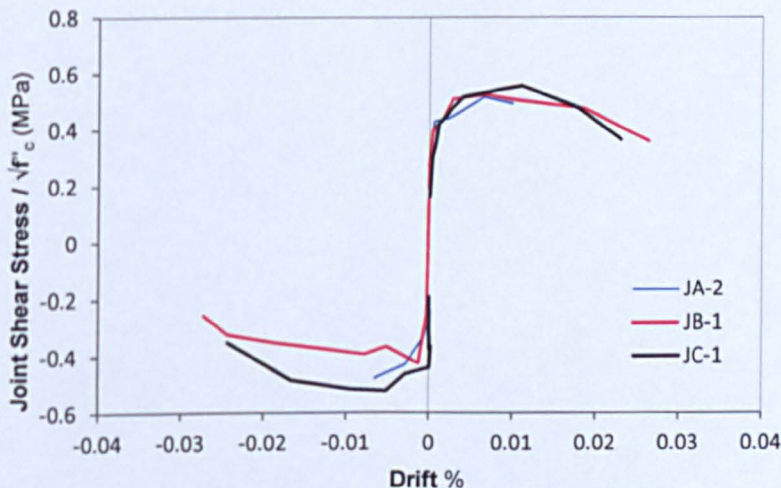


Figure 4.72 Normalised shear stress-strain envelope curves of Group I specimens

4.6.2.2 GROUP II

All Group II specimens were subjected to an axial load level equal to 250 kN and experienced joint shear failure with no prior reinforcement yielding. Figure 4.73 shows the normalised load-drift envelope curves of Group II specimens (*J-Type Failure*).

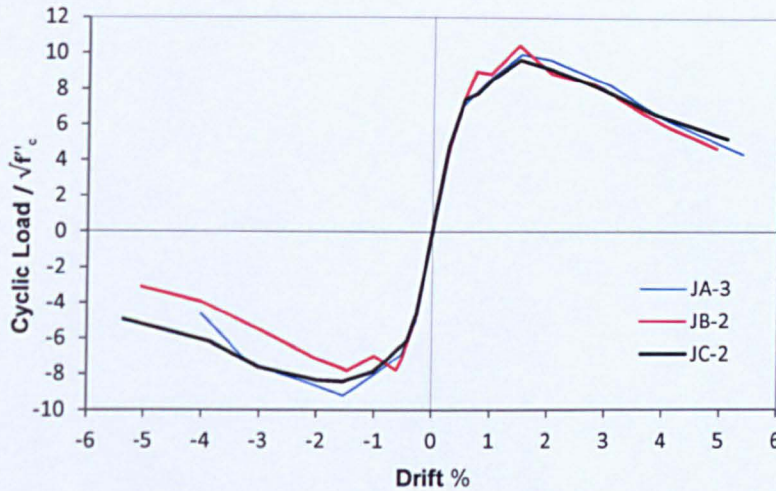


Figure 4.73 Normalised load-drift envelope curves of Group II specimens

In the positive direction, there is not much difference in the measured response, which can be attributed to the same reasons stated above. In the negative loading direction, specimen JA-3, and unlike the case of specimen JA-2, managed to achieve a slightly higher normalised strength than JC-2 (around 7%). However, the post-peak stiffness and strength for specimen JA-3 was lost at higher rate than specimen JC-2, as can be seen in Figure 4.73. On the other hand, JB-2 exhibited a comparable behaviour to specimen JB-1, as specimen JB-2 reached the peak maximum negative strength at drift level equal to 0.61%, after which the specimen experienced a sudden drop in strength followed by an increase to the same peak value, as previously explained in section 4.4.4.

The same can be observed, for both the negative and the positive side, when comparing the load-drift envelope curves and the normalised shear stress-strain envelope curves of Group II specimens. Figure 4.74 and Figure 4.75 show the load-drift and the normalised shear stress-strain envelope curves of Group II specimens, respectively.

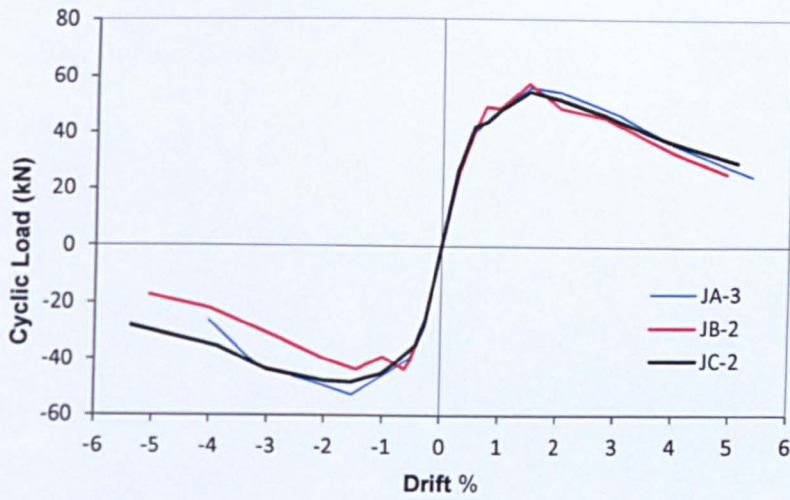


Figure 4.74 Load-drift envelope curves of Group II specimens

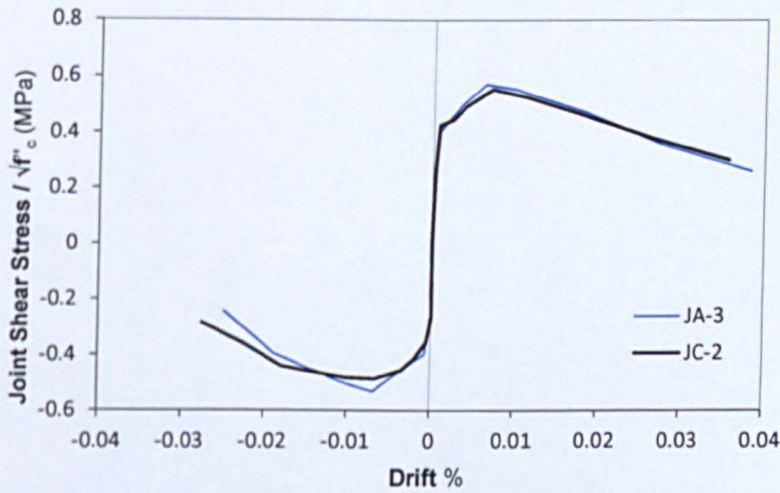


Figure 4.75 Normalised shear stress-strain envelope curves of Group II specimens

Based on these observations, it can be concluded that for exterior joint with *J-Type* failure, the overall joint shear strength is dependent on the combination between the anchorage detail and the axial load level. However, more tests with a wider range of axial load are required to quantify the effect of each different anchorage detail.

4.7 RECAP AND CONCLUSIONS

Seven full-scale isolated exterior beam-column joints were tested under quasi-static cyclic loading for the purpose of studying the effects of using different types of beam anchorages and low column axial loads on the seismic shear performance of exterior joints with no shear reinforcement. Three types of beam bar anchorages were used. Type A and type B had straight anchorage for beam bottom bars and 90° hooks for the top bars, whereas 90° hooks was used for both top and bottom bars in Type C.

Based on the observed damage and hysteretic behaviour of the tested specimens of the current research, presented in this chapter, the following conclusions can be drawn:

- 1- All seven specimens, and despite the differences in reinforcement details within the joint, exhibited shear failure with no prior reinforcement yielding (*J-Type failure*). This was confirmed by strain measurements on beam and column bars.
- 2- In joints of type A, the maximum sustained strength when the hooks are in tension (denoted positive loading in this research) is approximately 8% higher than the other loading direction (i.e. beam bottom bars are in tension). The strength ratio between the two loading directions is 34% for Joints type B, and 14% for joints type C.
- 3- In terms of stiffness degradation, all specimens exhibited similar behaviour. Stiffness degradation continued throughout the test, however, most of the degradation occurred during the initial cycles up to 1.0% drift level. By the end of the 2% drift cycles, approximately 80% of the peak-to-peak stiffness at 0.25% drift was lost.
- 4- The ASCE 41 (2006) shear provisions predicted the shear strength of one specimen (JA-2) with fairly good accuracy ($\pm 4\%$), whereas overestimated by up to 15% and underestimated by up to 21% the rest of the specimens. This is because the joint shear strength coefficient proposed in ASCE 41 for isolated exterior joints or exterior joints with one stub beam is the same value [$0.5 \sqrt{\text{MPa}}$], regardless of the beam reinforcement ratio, the type of beam reinforcement anchorage and column axial load ratio
- 5- The proposed ASCE 41 shear stress-strain envelope for non-linear modelling was found to be unrealistic and does not represent the measured shear behaviour (i.e. shear envelope) of the tested specimen, especially in terms of initial stiffness, peak strength, and strength degradation.
- 6- The peak-to-peak normalised shear modulus degradation, for all specimens, was rather steep during the first cycles up to 1% drift level. By the end of the first cycle at 2% drift, approximately 98% of the initial stiffness was lost.
- 7- The ratio of joint shear deformation to the overall beam tip displacement, Δ_j/Δ_b , kept increasing throughout the test, even beyond the point of peak shear strength. All specimens exhibited similar behaviour; the ratio was around 34% at joint shear strength and around 56% at 50% of the maximum strength. Strain measurements of beam bars confirmed that joint deterioration was due to shear deformations of the panel zone, as no bar pull-out occurred.

- 8- The relationship between low column axial load levels (lower than $0.2f'_cA_g$) and joint strength was found to be beneficial, for deficient exterior joints exhibiting *J-Type* failure. Increasing the column axial load from 0.07 to $0.12f'_cA_g$, enhances the strength of group type A, B and C specimens by 11%, 15%, and 10%, respectively.
- 9- For deficient exterior joints with similar geometry but different detailing (Type A, B or C anchorage) and exhibiting *J-Type* failure, increasing the column axial load slightly increases the stiffness in the pre-peak range, whereas the effect on the post-peak stiffness is reversed (rapid deterioration). This is for column axial load levels within the tested ratios (i.e. lower than $0.15f'_cA_g$).
- 10- The achieved joint strength was found to be affected by the type of beam reinforcement details within the joint.
- 11- For a column axial load level of $0.07f'_cA_g$ (150 kN), joints of type C achieved 5% higher strength than joints of type A and type B, when the hook was in tension. On the other hand, for a column axial load level of $0.12f'_cA_g$ (250 kN), type A, B, and C joints achieved similar shear strengths.
- 12- For a column axial load level of $0.07f'_cA_g$ (150 kN), the joint strength of type C joints was 7% higher than type A and 33% higher type B, when beam bottom bars were in tension. On the other hand, for a column axial load level of $0.12f'_cA_g$ (250 kN), the joint strength of type A joints was 9% higher than type C and 18% higher type B.
- 13- For deficient exterior beam-column joints exhibiting *J-Type* failure, when the hook is in tension, changing the length of the vertical part of the hook within the joint has practically no significant effect on the overall joint strength. This is because the imposed demand on the hook from the adjacent beam is not enough to cause anchorage failure of the hook.
- 14- Using 90° hooks for beam bottom bars can lead to enhancing the shear strength for the case of deficient exterior beam-column joints exhibiting *J-Type* failure, when beam bottom bars are in tension. This means that the presence of a bottom hook can enhance the capacity of the diagonal compressive strut due to the better anchoring of beam bars which in turn leads to a higher strength.
- 15- Elongated hooks when used with straight anchorage for beam bottom bars can have a detrimental effect on the joint shear strength. This is true for the case of deficient exterior beam-column joints exhibiting *J-Type* failure, when beam bottom bars are in tension. The only explanation for this negative effect is that when the hooked bar is

compressed, the end of the hook pushes the cover out which weakens the concrete compressive strut and in turn the joint strength.

- 16- The overall joint shear strength of deficient exterior joint with *J-Type* failure is dependent on the combination between the anchorage detail and the axial load level. However, more tests with a broader range of axial load levels are required to quantify the effect of each different anchorage detail.

CHAPTER 5

JOINT SHEAR STRENGTH MODEL

5.1 INTRODUCTION

The majority of the existing joint strength models found in the literature were developed for well-confined beam-column joints. However, much of the recent research focuses on the prediction of shear strength of beam-column joints with no shear links. In this chapter, an evaluation of the most recent joint shear strength models that were reviewed in Chapter 2 is presented. In addition, an analytical model that predicts the shear strength of exterior deficient beam-column joints in both loading directions is developed. The model predicts the maximum shear strength taking into account the effect of the beam longitudinal anchorage and the column axial load level. Finally, the accuracy and the applicability of the model are verified against a database of 24 exterior beam-column joint tests.

5.2 JOINT DATABASE

A database of 24 exterior beam-column joints was used to assess the existing joint shear models reported in Chapter 2. The database includes, in addition to the data from the current research, data from 17 other specimens collected from previous experimental work reported in the literature, as shown in Table 5-1. The included tests in the database are isolated specimens without transverse beams or slab. In addition, all specimens are without transverse reinforcement in the joint area and with anchorage details similar to the ones used in the current research. Thus, specimens with 180° hooks or very short embedment length were excluded from the database.

Table 5-1 Database of exterior deficient beam-column joints

Researcher	Specimen	h_c (mm)	b_c (mm)	h_b (mm)	b_b (mm)	f'_c ² (MPa)	$N/A_g f'_c$ ²	γ_{test} ³	γ_{model} ³	$\gamma_{test}/\gamma_{model}$
Jemaa (current research)	JA-1	260	260	400	260	24.3	0.09	0.54	0.54	1.00
	JA-1 (-)	260	260	400	260	24.3	0.09	0.52	0.51	1.02
	JA-2	260	260	400	260	31.0	0.07	0.52	0.53	0.97
	JA-2 (-)	260	260	400	260	31.0	0.07	0.48	0.49	0.98
	JA-3	260	260	400	260	32.4	0.11	0.57	0.59	0.96
	JA-3 (-)	260	260	400	260	32.4	0.11	0.53	0.52	1.01
	JB-1	260	260	400	260	31.1	0.07	0.52	0.52	1.01
	JB-1 (-)	260	260	400	260	31.1	0.07	0.42	0.41	0.96
	JB-2	260	260	400	260	30.8	0.12	0.61	0.60	1.02
	JB-2 (-)	260	260	400	260	30.8	0.12	0.45	0.47	0.97
	JC-1	260	260	400	260	27.2	0.08	0.56	0.54	1.02
	JC-1 (-)	260	260	400	260	27.2	0.08	0.52	0.50	1.05
	JC-2	260	260	400	260	32.6	0.11	0.56	0.57	0.97
JC-2 (-)	260	260	400	260	32.6	0.11	0.49	0.53	0.91	
Clyde et al. (2000)	#2	457	305	406	305	46.2	0.11	1.00	1.00	1.00
	#6	457	305	406	305	40.1	0.11	1.05	0.98	1.08
	#4	457	305	406	305	41.0	0.24	1.11	1.14	0.97
	#5	457	305	406	305	37.0	0.28	1.11	1.13	0.98
Ghobarah & Said (2001)	T1	400	250	400	250	30.8	0.19	0.95	0.97	0.98
	T1 (-)	400	250	400	250	30.8	0.19	0.83	0.91	0.92
	T2	400	250	400	250	30.8	0.10	0.89	0.84	1.07
	T2 (-)	400	250	400	250	30.8	0.10	0.81	0.82	0.99
Antonopoulos & Triantafillou (2003)	C1	200	200	300	200	19.4	0.06	0.62	0.55	1.12
	C1 (-)	200	200	300	200	19.4	0.06	0.53	0.55	0.97
	C2	200	200	300	200	23.7	0.05	0.55	0.56	0.99
	C2 (-)	200	200	300	200	23.7	0.05	0.55	0.56	0.99
Karayannis et al. (2008)	A0	200	200	300	200	31.6	0.05	0.37	0.41	0.91
	A0 (-)	200	200	300	200	31.6	0.05	0.36	0.41	0.89
	B0	300	200	300	200	31.6	0.05	0.61	0.62	0.99
	B0 (-)	300	200	300	200	31.6	0.05	0.60	0.62	0.97
	C0	300	200	300	200	31.6	0.05	0.65	0.62	1.06
	C0 (-)	300	200	300	200	31.6	0.05	0.63	0.62	1.02
Wong (2005)	BS-L	300	300	450	260	30.9	0.15	0.68	0.68	1.00
	BS-LL	300	300	450	260	42.1	0.15	0.73	0.73	1.00
	BS-U	300	300	450	260	31.0	0.15	0.73	0.68	1.08
	BS-L-LS	300	300	450	260	31.6	0.15	0.73	0.68	1.08
	BS-L-V2T10	300	300	450	260	32.6	0.15	0.83	0.68	1.22
	BS-L-600	300	300	600	260	36.4	0.15	0.56	0.60	0.94
mean=									1.01	
COV=									0.06	

¹ h_c , b_c are the column depth and width (mm), respectively; and h_b , b_b are the beam depth and width (mm), respectively.

² N is the column axial load (N); A_g is the gross area of column cross section (mm^2); and f'_c is the concrete compressive (cylinder) strength MPa (N/mm^2).

³ γ is denoted here as the "joint shear strength coefficient" ($\sqrt{\text{MPa}}$), as defined in section 2.4.2.

5.3 ASSESSMENT OF PREVIOUS JOINT STRENGTH MODELS

5.3.1 Hwang and Lee Model

The “Softened Strut-and-Tie Model (SST)” by Hwang and Lee (1999) was developed to predict the shear strength of exterior beam-column joints, as described in Chapter 2. The model was developed with emphasis on confined exterior joints, in which joint hoops and intermediate longitudinal reinforcement are present. According to the SST model, the joint shear force is resisted by three basic mechanisms: diagonal, vertical, and horizontal. The joint shear strength is calculated using an iterative solver that satisfies stress equilibrium, strain compatibility and constitutive laws of reinforced concrete. In order to apply the model to unconfined exterior joints, the authors ignored the contribution of the horizontal tie and considered the column reinforcement to be yielding. The authors tested the model against a database of 63 exterior beam-column joints. However, only two of the included joints were for unconfined joints. The model showed good agreement with the reported experimental results for confined joints, whereas the shear strength of the two unconfined joints was underestimated by 26% and 52%, (see Figure 5.1).

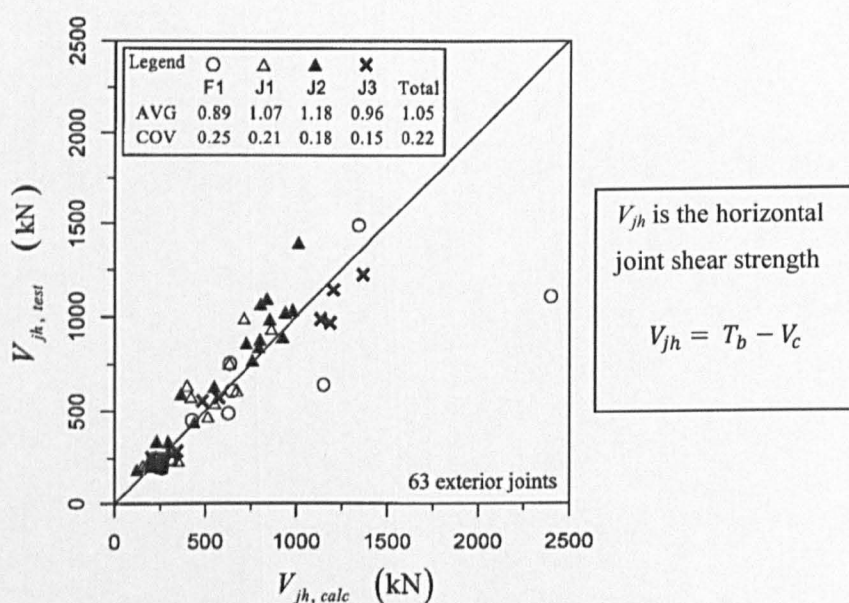


Figure 5.1 Verification of SST Model (Hwang & Lee, 1999)

In order to assess the applicability of Hwang and Lee (SST) model to unconfined joints, the model was applied to the 24 joints included in the aforementioned database. Figure 5.2 compares experimental and predicted joint shear strengths of all the joints in the database using the SST model.

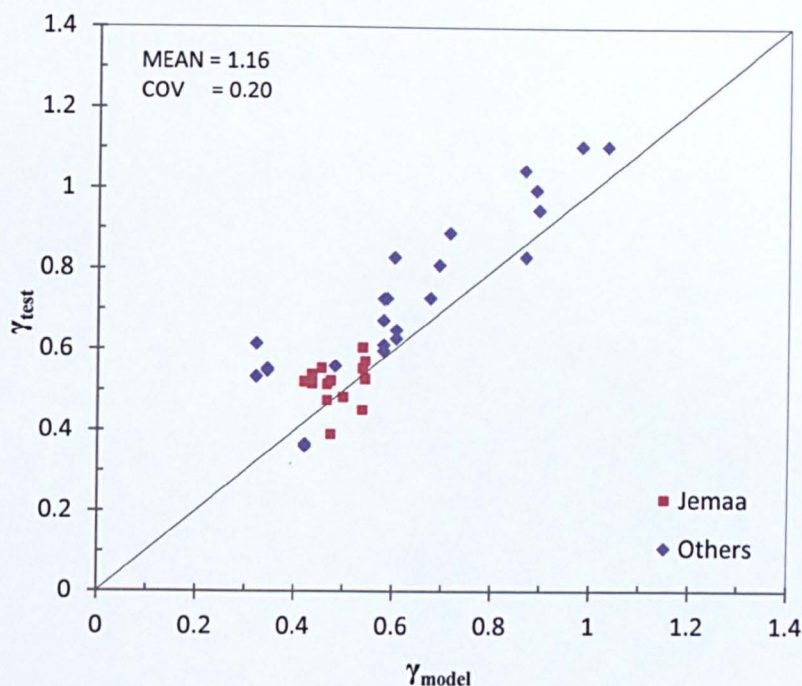


Figure 5.2 Assessment of Hwang and Lee (1999) model for unconfined exterior joints

The model, in general, underestimates the shear strength of unconfined exterior beam-column joints. Similar observations were reported by Park & Mosalam (2009) and Hassan (2011). As for the current research specimens, the model showed inconsistency in the predicted joint shear strengths, as can be seen in Figure 5.2. The overall mean of the $\gamma_{test}/\gamma_{model}$ ratio is (1.16) and the coefficient of variation for the same ratio is $COV=0.20\%$.

The model's poor ability to predict the shear strength of unconfined joints in comparison to confined ones is attributed to the omission of the beam contribution to the diagonal strut width. The authors explicitly mentioned that the model can be applied for joints, in which the beam is expected to develop a plastic hinge. Another reason is the proposed initial condition that the intermediate column reinforcement has yielded. It was observed that for unconfined joints this condition causes overestimation when calculating the concrete softening coefficient ξ , which in turn leads to underestimation of the joint shear strength. Moreover, the model neglects the effect of different types of beam anchorages. Therefore, the model predicted the same strength for both positive and negative loading directions.

5.3.2 Vollum and Newman Model

Vollum (Vollum & Newman, 1999) developed a Strut-and-Tie model to predict the shear capacity of RC exterior beam-column joints with and without transverse reinforcement, as presented in Chapter 2. The proposed model managed to predict the joint shear strength of previous monotonic exterior joint tests with good accuracy. However, Vollum and Newman (1999) concluded that a simple strut-and-tie model does not offer a realistic representation of the complex behaviour of beam-column joints. This is due to the high complexity and difficulty of

determining the nodal zones and the strut width which requires establishing the forces and concrete compression zones at the joint boundaries. For these reasons, Vollum and Newman (1999) further simplified their SAT model and proposed a simple empirical model that takes into account the effects of beam anchorage detail and joint aspect ratio. The model is capable of predicting the shear strength of exterior beam-column joints with and without transverse reinforcement, as described in Chapter 2.

The applicability of the model to shear-critical unconfined exterior joints was assessed using the joints included in the database. Figure 5.3 compares experimental and calculated joint shear strengths using the Vollum and Newman model.

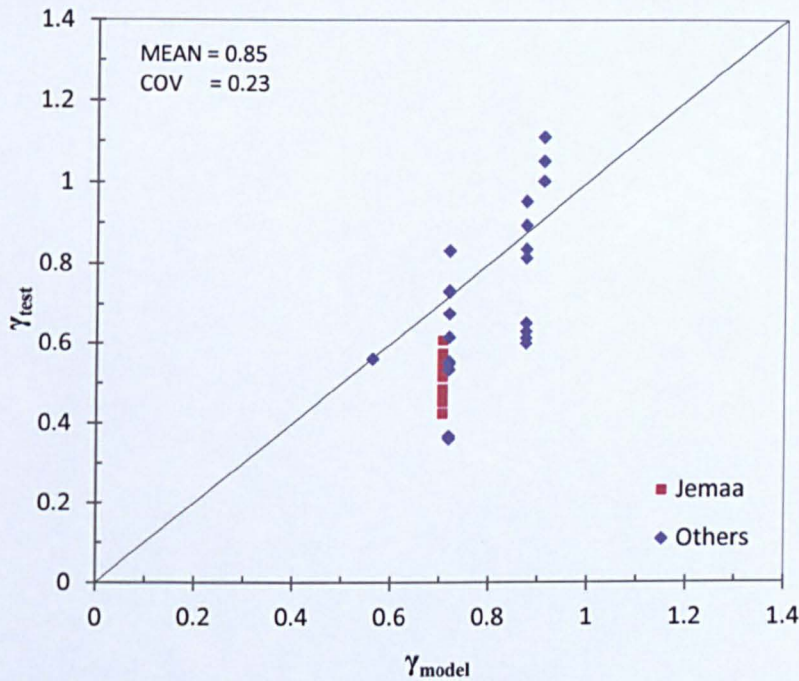


Figure 5.3 Assessment of Vollum and Newman (1999) model for unconfined exterior joints

The model generally overestimates the joint shear strength of the unconfined exterior joints included in this research database, as shown in Figure 5.3. This is contrary to what Park and Mosalam (2009) reported about *J-Type* failure joints (see Chapter 2). After analysing the results, shown in Figure 5.3, it can be observed that the model predicts the same joint shear strength for joints with different anchorage details, but with the same concrete compressive strength and joint aspect ratio. This can be attributed to the limitations of the factor β which does not seem to properly address the effects of beam reinforcement ratio [as pointed out by Park and Mosalam (2009)] and the beam anchorage details. The calculated mean and coefficient of variation for the $\gamma_{test}/\gamma_{model}$ ratio are, MEAN = 0.85 and COV = 0.23%.

5.3.3 Tsonos Model

Tsonos (2007) proposed a model based on the Strut-and-Tie mechanism. The model predicts the ultimate shear strength of exterior beam-column joints by solving a fifth-order polynomial equation of the concrete biaxial strength curve. The model was developed for confined joints but can be applied to unconfined joints by ignoring the confining contribution of the transverse reinforcement in the factor K , as described in Chapter 2.

The applicability of the model to unconfined joints was assessed using the joints included in the database. Figure 5.4 compares experimental and calculated joint shear strengths using the Tsonos model.

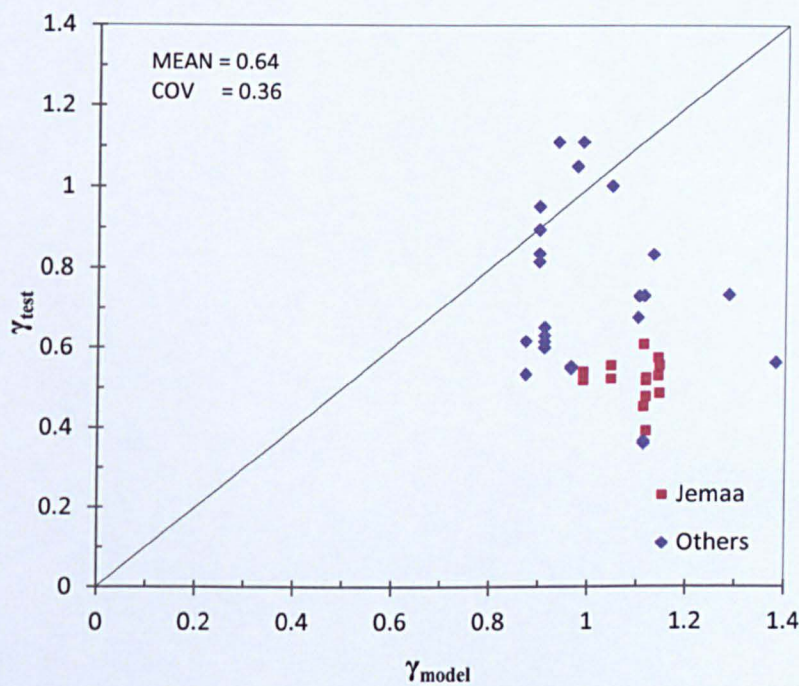


Figure 5.4 Assessment of Tsonos (2007) model for unconfined exterior joints

The model generally overestimates the joint shear strength of unconfined exterior joints, as shown in Figure 5.4. Similar observations were reported by Park & Mosalam (2009) and Hassan (2011). This can be attributed to the concrete confining factor K , which enhances the concrete compressive strength due to the contribution of joint shear links. Whereas, in the case of unconfined joints, the concrete compressive strength f_c is taken without introducing any reduction factor to account for the lack of shear links. The calculated mean and coefficient of variation for the $\gamma_{test}/\gamma_{model}$ ratio are, MEAN = 0.64 and COV = 0.36%.

5.3.4 Park and Mosalam Model

Park & Mosalam (2009; 2012a) proposed an analytical model to predict the shear strength of unconfined exterior beam-column joints based on a new Strut-and-Tie approach. As described in Chapter 2, the model assumes the horizontal joint shear to be resisted by two inclined

compressive struts working in a parallel manner. The model avoids estimating the diagonal strut area and addresses the variation of joint shear strengths based on the joint aspect ratio and the beam reinforcement ratio. Using an iterative solver, the joint shear strength can be calculated from global geometry after knowing the beam tension force at the column face.

The model was applied to the 24 joints in the database to assess the model's ability to predict the shear strength of unconfined exterior joints with different top and bottom anchorages in both loading directions, such as the current research specimens. Figure 5.5 compares experimental and predicted joint shear strengths of all the joints in the database using Park & Mosalam model.

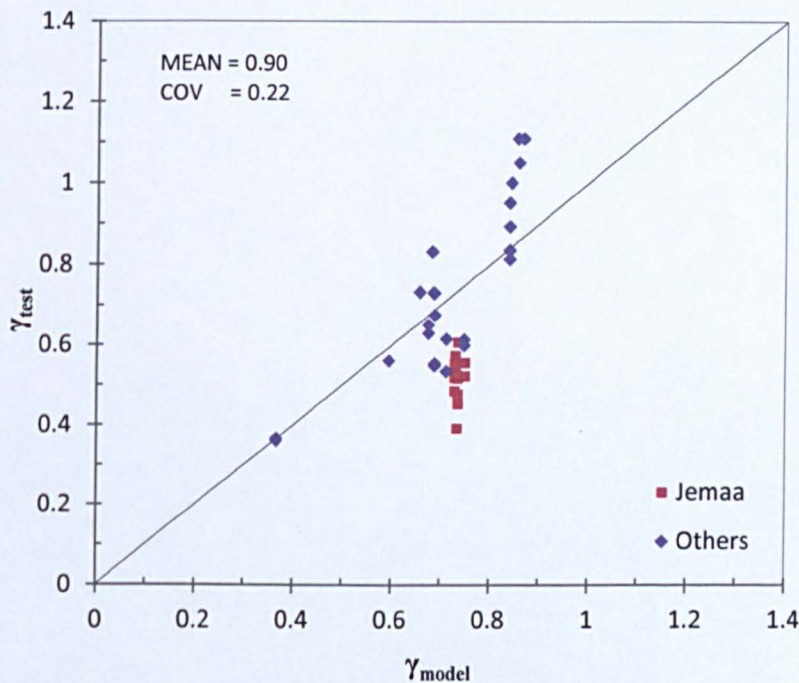


Figure 5.5 Assessment of Park & Mosalam (2009) model for unconfined exterior joints

The mean and coefficient of variation for the $\gamma_{test}/\gamma_{model}$ ratio are, MEAN =0.90 and COV=0.22%. Therefore, the model generally overestimates the joint shear strength of unconfined exterior joints, as can be seen in Figure 5.5. This can be attributed to the proposed fixed width of the second strut of $0.65h_c$ regardless of the calculated column compression zone. This approximation, in addition to fixing the beam internal moment lever arm, can cause the model to overestimate the stress in the beam longitudinal reinforcement.

5.3.5 Hassan Model

Hassan (2011) proposed an analytical model to predict the shear strength of unconfined joints with *J-Type* failure. The model formulation is based on the Strut-and-Tie model of the ACI 318-08 (2008), as described in Chapter 2. In addition, the author included extra provisions for

estimating the joint shear strength for joints with yielding beams and for joints with very short straight anchorages.

The accuracy of the model to predict the shear strength of the current research specimens in both loading directions, in addition to the remaining joints in the database, was assessed. Figure 5.6 compares experimental and calculated joint shear strengths using Hassan model.

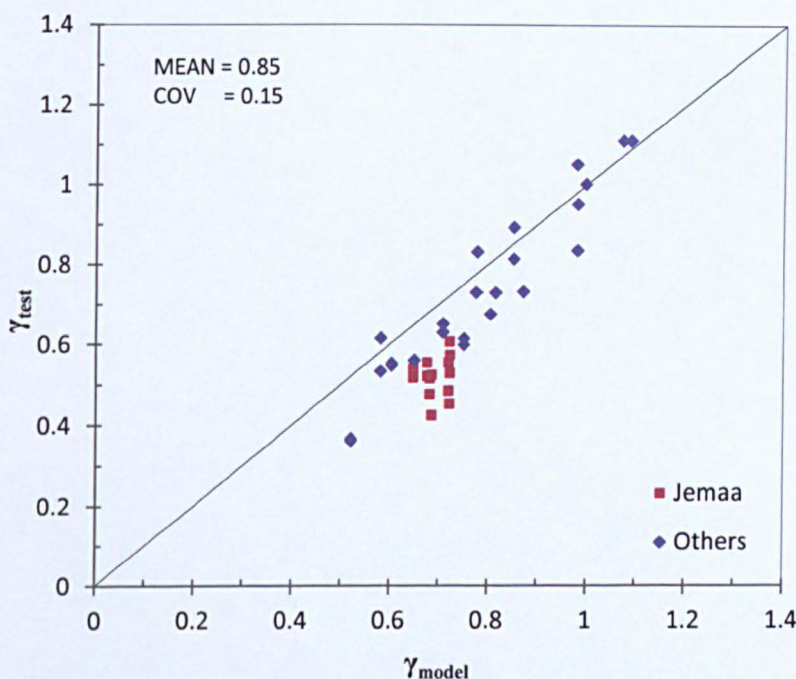


Figure 5.6 Assessment of Hassan (2011) model for unconfined exterior joints

As can be seen from Figure 5.6, the model in general overestimates the joint shear strength of unconfined exterior joints. Hassan (2011), as reported in Chapter 2, assumed that in all *J-Type* failure joints, the beam remains within the elastic range. As a result, the beam compression zone is calculated from the transformed cracked linear section. This leads to the overestimation of the diagonal strut width especially for cases where beams are close to yielding, such as the current work. The mean and coefficient of variation for the $\gamma_{test}/\gamma_{model}$ ratio are, MEAN =0.85 and COV=0.15%.

5.4 PROPOSED STRENGTH MODEL

5.4.1 Model Development and Background

The experimental programme of the current research and the research conducted by others, such as Wong (2005), showed that geometrically identical beam-column joints with different reinforcement ratios and anchorage types can exhibit different shear strengths. After reviewing previous joint shear strength models in section (5.3), it was found that existing models lack the feature to explicitly predict the joint shear strength based on the anchorage type of the beam

longitudinal reinforcement. Thus, a model that includes such feature and can still be practical enough to be used by structural engineers and not just researchers was sought after.

The ACI 318-08 (2008) strut-and-tie approach was chosen as the basis for this model. Hassan (2011), as previously mentioned in Chapter 2, adopted a similar approach, and while his model seems simple enough, it over-predicts the cases where joints fail by *J-Type* failure just before yielding of the beam reinforcement (i.e. very close to yielding), such as the current experiments. For these cases, calculating the beam compression zone depth a_b using the transformed cracked linear beam section is no longer valid, due to the non-linearity of the concrete stress.

The proposed model, predicts the joint shear strength based on the strength of a single compression strut. Compression struts are normally formed between at least two nodal zones (ACI 318-08, 2008). In the case of exterior beam-column joints, the idealised compression strut takes a tapered shape due to the presence of the beam compression zone at only one end of the compression strut, as shown in Figure 5.7. Due to the width difference between the inner and the outer nodal zone and the nature of both nodes, the strut failure is expected to initiate at the weaker node, which in this case is the outer nodal zone. The same assumption, based on experimental observations, was also adopted by several researchers such as Vollum (1998), Vollum and Newman (1999) and Park and Mosalam (2009).

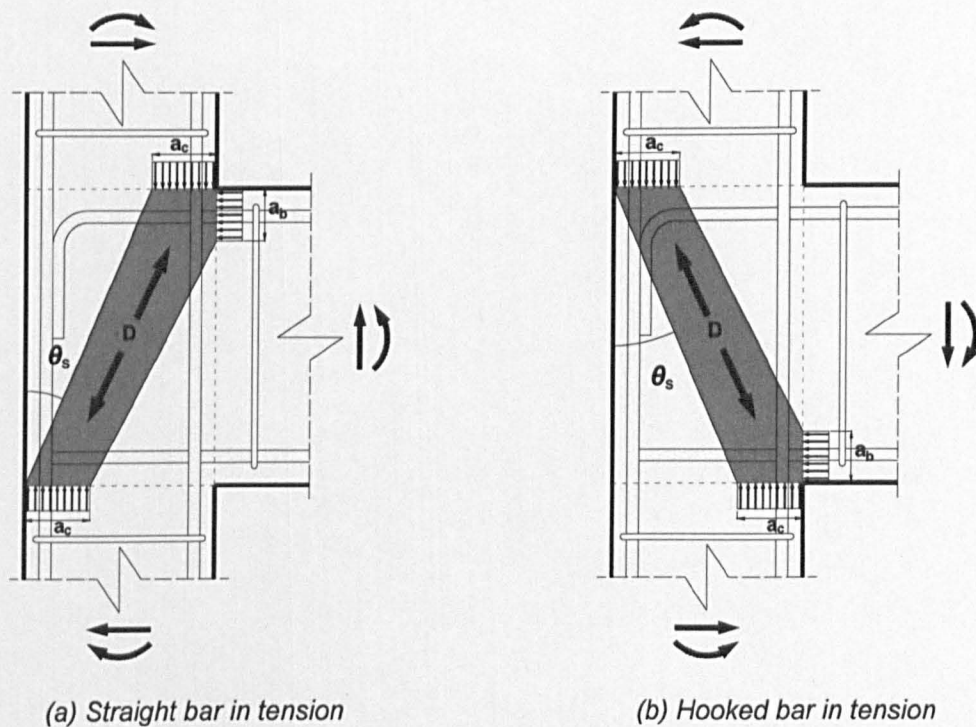


Figure 5.7: Idealised compression strut in exterior beam-column joints

In practice, however, such as the tests shown by this research, shear cracks can develop even beyond the assumed diagonal strut area (see Figure 5.8). These observations which were also reported by Park & Mosalam (2009), suggest an extended width for the compression strut due to forces that develop over the beam longitudinal bars.



Figure 5.8: Crack pattern of JA-2 showing an extended compression strut

According to the new Strut-and-Tie model proposed by Park & Mosalam (2009; 2012a), as described in Chapter 2, the horizontal joint shear is assumed to be resisted by two inclined compressive struts working in a parallel manner. The first strut ST1 is developed by the 90° hook at the end of the anchored beam bar, whereas the second strut ST2 is developed by the bond induced forces surrounding the straight portion of the beam bars within the joint, as shown in Figure 5.9.

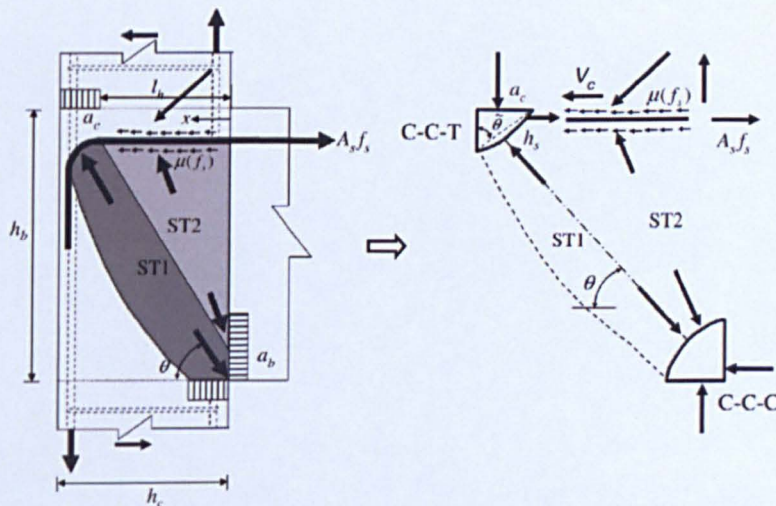


Figure 5.9: Proposed Strut and Tie joint shear model (Park & Mosalam, 2012a)

By applying this model's assumptions to exterior joints with beam straight bars, such as the one shown in Figure 5.7.a (i.e. beam straight bars in tension), the only way for the first strut ST1 to be developed is through bond induced forces along the bar, as shown in Figure 5.10. However, without a hook, this raises the question about the developed tie force within the nodal zone of the first strut.

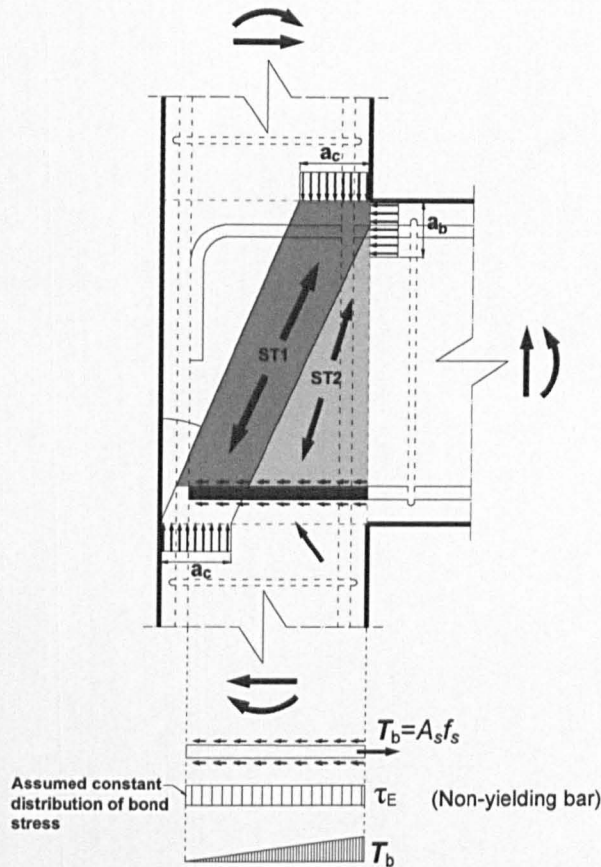


Figure 5.10: Strut and Tie in a joint with straight bars according to the model by Park & Mosalam (2009; 2012a)

Park & Mosalam (2009; 2012a) developed their strut and tie model for hooked bars only, which means the model cannot be applied to exterior joints with straight bars (in tension). As a result, the representation shown Figure 5.10 in is not entirely correct. After further examining the progression of cracking shown in Figure 5.8 and similar joint tests by Wong (2005), it can be observed that the developed shear cracks up to the point of peak joint strength are concentrated in the assumed location of the first strut and the area directly adjacent to it. (i.e. the first part of the assumed fan-shaped second strut ST2).

Based on these observations, it can be concluded that the compressive stress distribution within the joint core is not uniform and that the compressive stress is highest (i.e. reaches the concrete capacity first) in the strut corresponding to the column compression zone width a_c and the lowest at the far end of the fan-shaped strut (i.e. near the beam). Therefore, it can be assumed

that the area of the joint core most effective in resisting the horizontal shear is the area related to the column compression zone width a_c and the narrow area next to it.

5.4.2 Assumptions and Equilibrium

The model is developed based on the case of beam straight bars in tension, as this case is the critical case of anchorage in comparison to the case of 90° hooks. The model is then extended to include other types of beam reinforcement anchorages, such as 90° hooks. Joint shear failure is assumed to occur before yielding of reinforcement (i.e. *J-Type* Failure). In the case of straight bars, the estimated joint strength should be compared to the bar strength (i.e. bond strength of the anchored bar) in order to determine the type of failure mechanism, whether it is due to shear failure within the joint or simply due to bar pull-out of beam bars. In the latter case, the predicted strength using the model is higher than the bar strength. Moreover, based on the experimental results of the current research, it was observed that achieving the peak strength in one direction might lead to a slight reduction in the peak strength of the other direction. However, as this is based on the result of one joint specimen (see Chapter 4), the model neglects any strength reduction that might be caused by the loading history (i.e. previous loading in the other direction), as further investigation is required.

In the proposed model, the horizontal joint shear, V_{jh} is resisted by the horizontal component of a single but extended diagonal compressive strut, as shown in Figure 5.11. The strut strength is estimated based on the total strut width, a_s and by assuming the strut effective compressive strength, f_{ce} to be uniformly distributed over the entire strut width, as shown in Figure 5.11. This proposed extension to the original strut width at the base a_c is assumed to be attributed to the force that develops in the bottom beam bars due to the effect of the diagonal compressive strut. The magnitude of this force varies with the column axial force and the length and type of anchorage of the beam longitudinal bars.

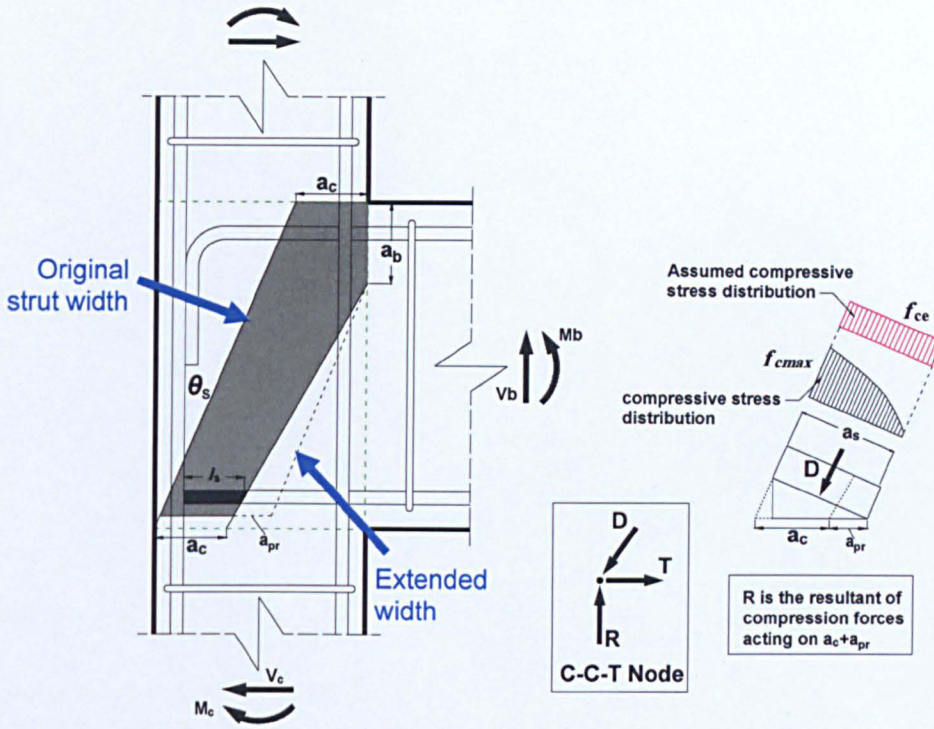


Figure 5.11: Extension and stress distribution of the assumed diagonal compressive strut

In order to estimate the extended width, a_{pr} of the original strut, the ACI 318-08 concept of an anchored tie force in a nodal zone is revisited. According to the ACI 318-08, in the strut-and-tie model, the presence of a tension force, provided by an anchored tie, usually extends the nodal zone area which in turn increases the strut width at that end. The anchorage for this tension force is usually provided by a certain bar development length, l_{anc} within the nodal zone and can be represented by a bearing plate, its width being equivalent to the effective tie width, w_t , as shown in Figure 5.12.

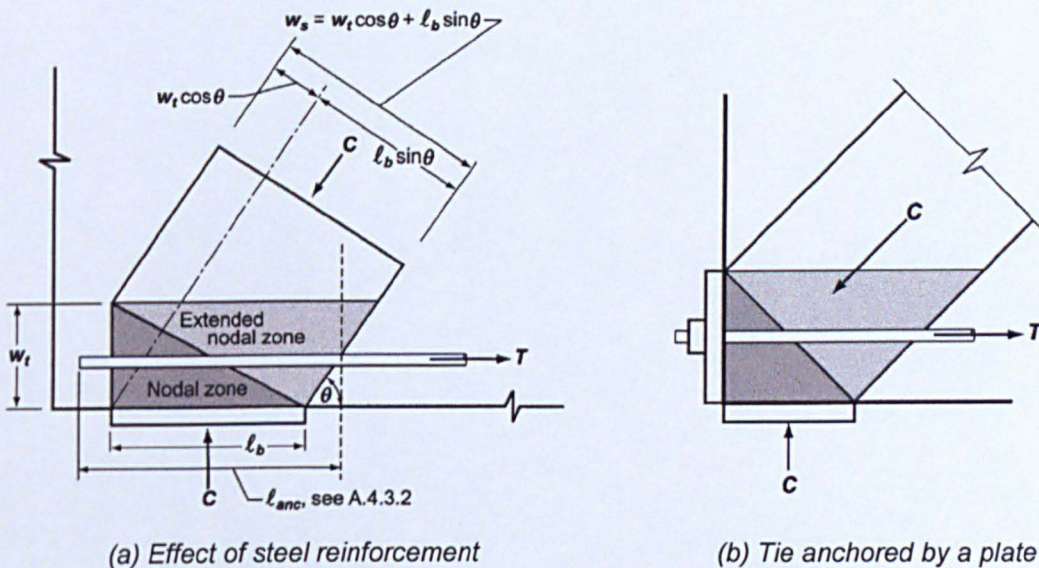


Figure 5.12: Extended nodal zone due to the presence of a tension force (ACI 318-08, 2008)

By applying this definition to an exterior joint with an extended beam where the required anchored length, l_{anc} is provided, the assumed anchored tie extends the nodal zone as shown in Figure 5.13.

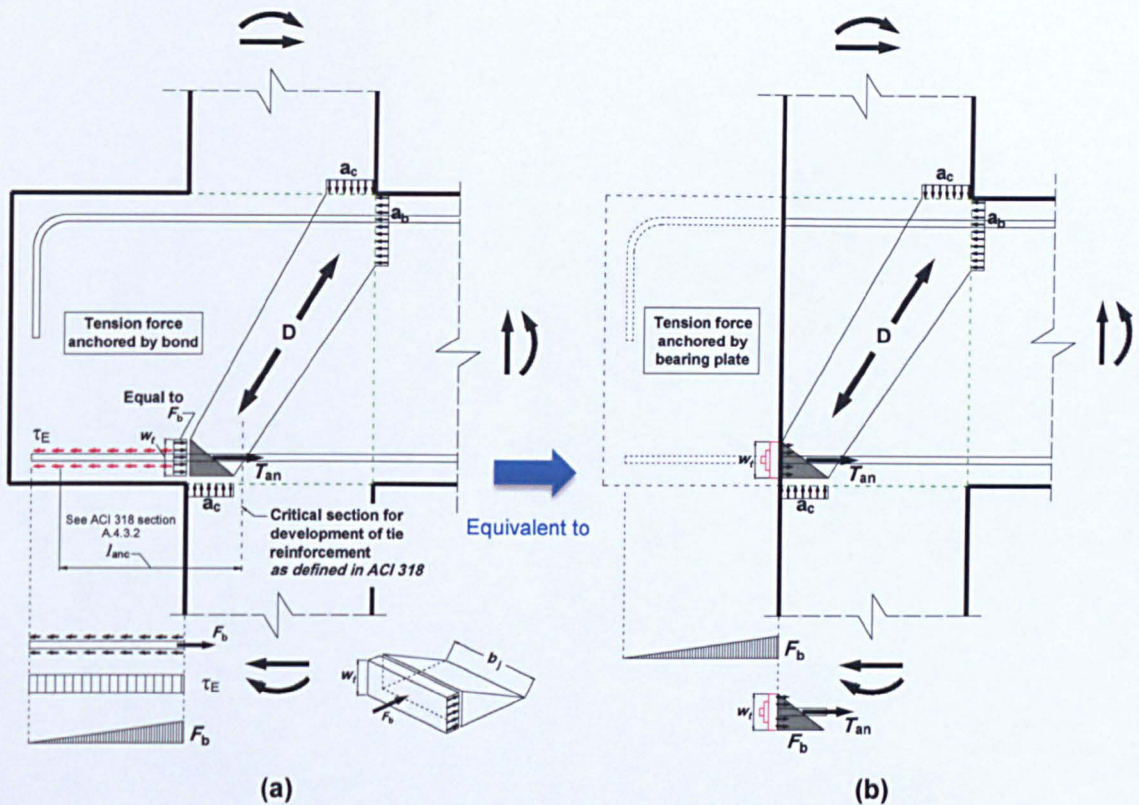


Figure 5.13: Types of anchored ties as defined in ACI 318-08 (2008)

In the case of deficient exterior beam column joints, where a straight bar anchorage is part of the outer nodal zone, a similar anchored tie at the beginning of the nodal zone (i.e. at the end of the straight bar), as shown in Figure 5.12.a, cannot be developed due to the lack of the required development length, l_{anc} . Instead, anchoring of the bar is assumed to develop by the end of the original strut width, assisted by the transverse pressure from the diagonal compressive strut (see Figure 5.14 & Figure 5.15).

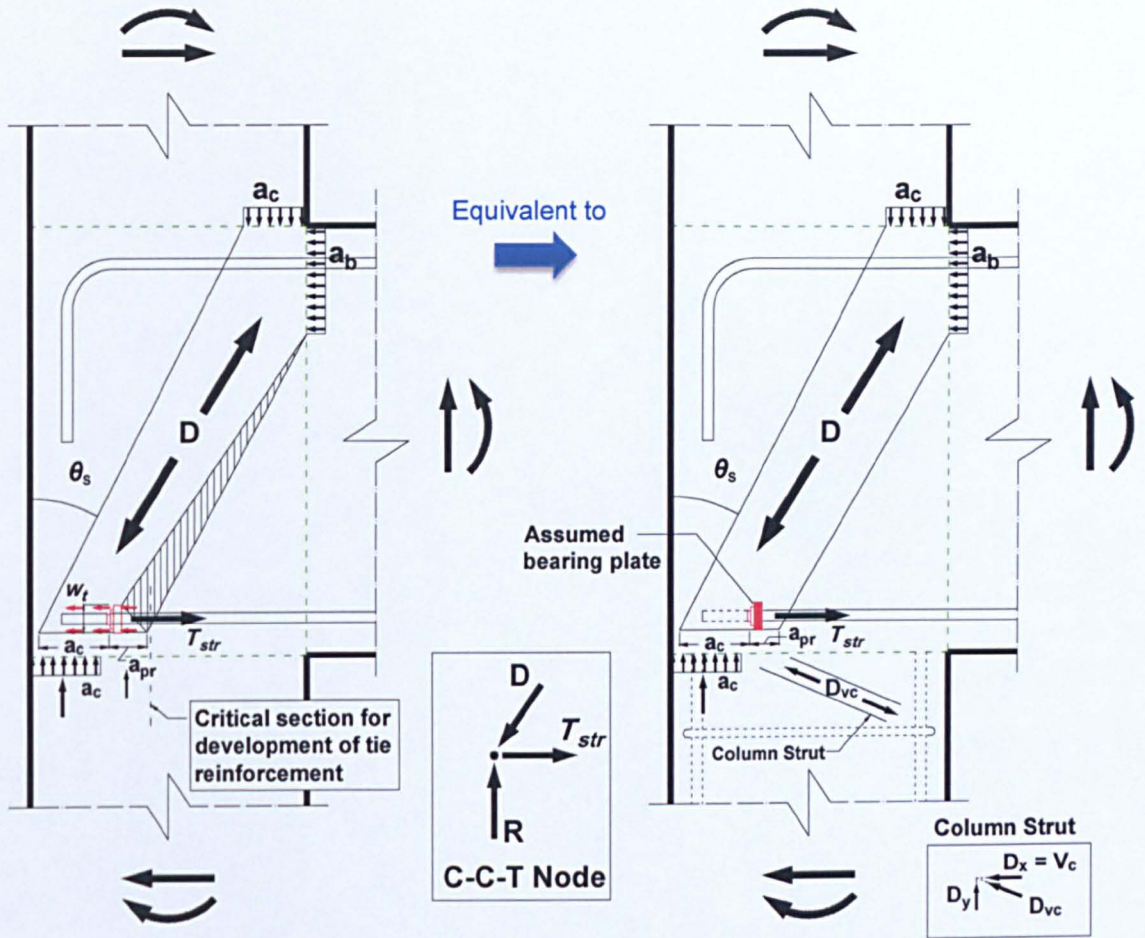


Figure 5.14: Assumed anchored tie in deficient exterior joints

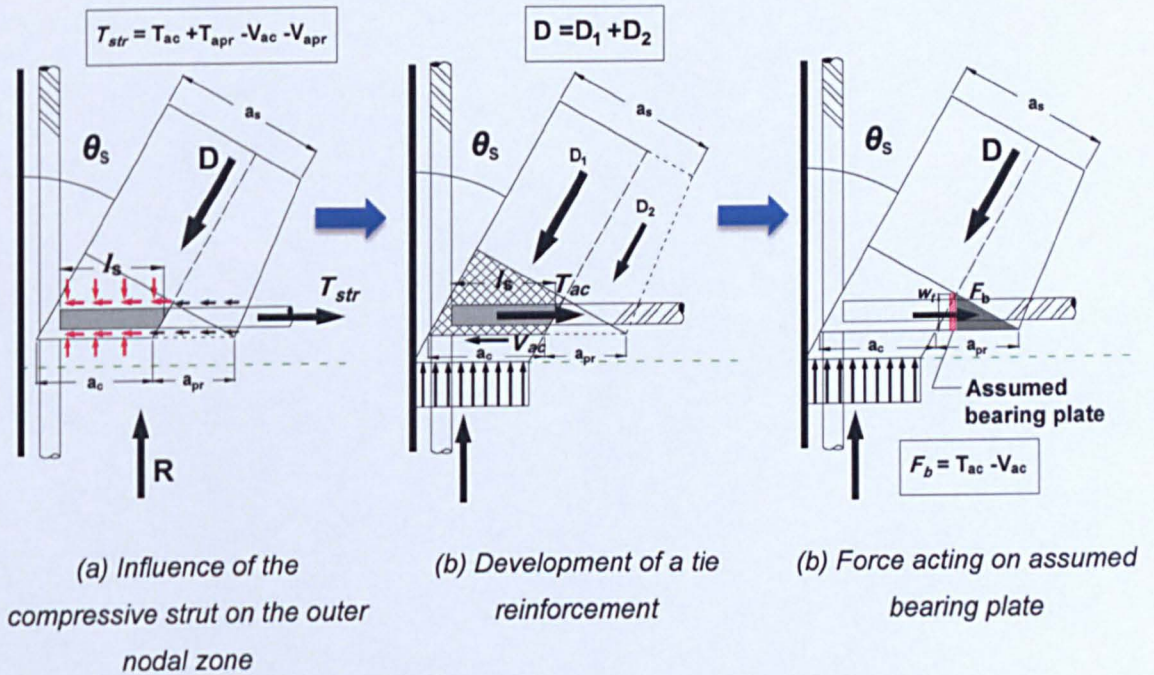


Figure 5.15: The outer nodal zone in the assumed strut

The effective tie width, w_t , which represents the portion of concrete that surrounds the bar, is assumed to be given, at point of failure, by the following equation:

$$w_t = \frac{F_b}{0.85f'_c b_j} ; F_b = T_{ac} - V_{ac} \quad (5.1)$$

where T_{ac} is the tension force that develops in the beam reinforcement within the width of the original strut (i.e. over the length l_s), b_j is the joint effective width, as defined in ACI 318-08 (ACI 318-08, 2008), and V_{ac} is the column shear contribution along the original strut width, a_c and can be calculated as follows:

$$V_{ac} = \frac{a_c V_c}{h_c} \quad (5.2)$$

where V_c is the column shear force and h_c is the column depth.

The horizontal projection of the extended strut width, a_{pr} can be calculated from geometry after determining the strut angle, θ_s and estimating the effective tie width, w_t as follows:

$$a_{pr} = \frac{2w_t}{\sin(2\theta_s)} \quad (5.3)$$

For exterior beam column joints, the concrete compressive strut applies a transverse pressure at the end of beam longitudinal bars. According to *fib* Bulletin 55: Model Code 2010, when the pulled bar is under transverse pressure, the bond stress over a limited length should be modified by the factor $\Omega_{p,tr}$, as shown in Figure 5.16.a. The transverse pressure factor, $\Omega_{p,tr}$ can be calculated according to Eq (5.4).

$$\Omega_{p,tr} = 1 - \tanh \left[0.2 \left(\frac{\sigma_{pr}}{0.1 f_c} \right) \right] \text{ for } \sigma_{pr} \leq 0 \quad (5.4)$$

where:

- σ_{pr} is the mean compressive stress averaged over a cylindrical volume of a 3ϕ around the bar (N/mm^2).
- f_c is the mean concrete compressive strength (N/mm^2).

The increase in bond forces due to the transverse pressure compensates for the lack of development length and can lead to the development of a significant force, see Figure 5.15. Since shear failure of a joint is directly related to reaching the capacity of the compressive strut,

the applied transverse pressure at the load of strut failure is considered to be the strut effective compressive strength, f_{ce} .

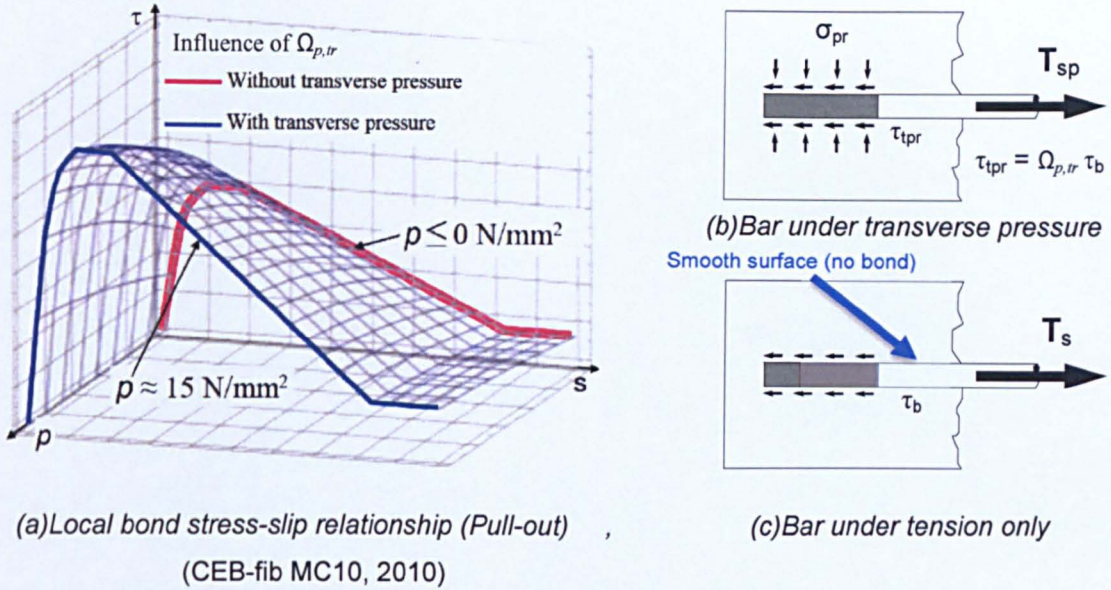


Figure 5.16: Influence of transverse pressure on bond stress

Therefore, by taking into account the effect of the original compressive strut, the force, T_{ac} for straight bars in tension and under transverse pressure can be calculated as follows:

$$T_{ac} = n\pi\phi_b l_s \Omega_{p,tr} \tau_b \quad (5.5)$$

where:

- n is number of beam longitudinal bars in tension.
- ϕ_b is the beam bar diameter.
- l_s is the anchored part of the bar under transverse pressure, see Figure 5.15.a.
- τ_b is the average bond stress over the anchored length without transverse pressure (N/mm^2), see Figure 5.16.c.

According to Model Code 2010 (CEB-fib MC10, 2010), for beam longitudinal bars ending with straight short anchorage lengths, the average bond stress, τ_b that develops over the limited anchored length can be calculated using a semi-empirical expression that was accurately calibrated using the results of more than 800 tests as follows:

$$\tau_b = 13.5\eta_2 \frac{\phi_b}{l_b} \left(\frac{f_c}{20}\right)^{0.25} \left(\frac{20}{\phi_b}\right)^{0.2} \left(\frac{l_b}{\phi_b}\right)^{0.55} \left(\frac{c_{min}}{\phi_b}\right)^{0.33} \left(\frac{c_{max}}{c_{min}}\right)^{0.1} \quad (5.6)$$

where:

- η_2 is the casting position coefficient and is taken as 1 for good bond conditions and 0.7 for all other bond conditions.
- l_b is the horizontal projection of the embedment length measured from the joint interface to the end of the bar, as shown in Figure 5.17.b.
- c_{min} is $\min\{c_x, c_y, c_s\}$, as defined in Figure 5.17.a.
- c_{max} is $\max\{c_x, c_s\}$.

The previous expression is only valid if:

$$0.5 < c_{min}/\phi_b < 3; 1 < c_{max}/c_{min} < 5; c_y > \phi_b; c_s > 3\phi_b$$

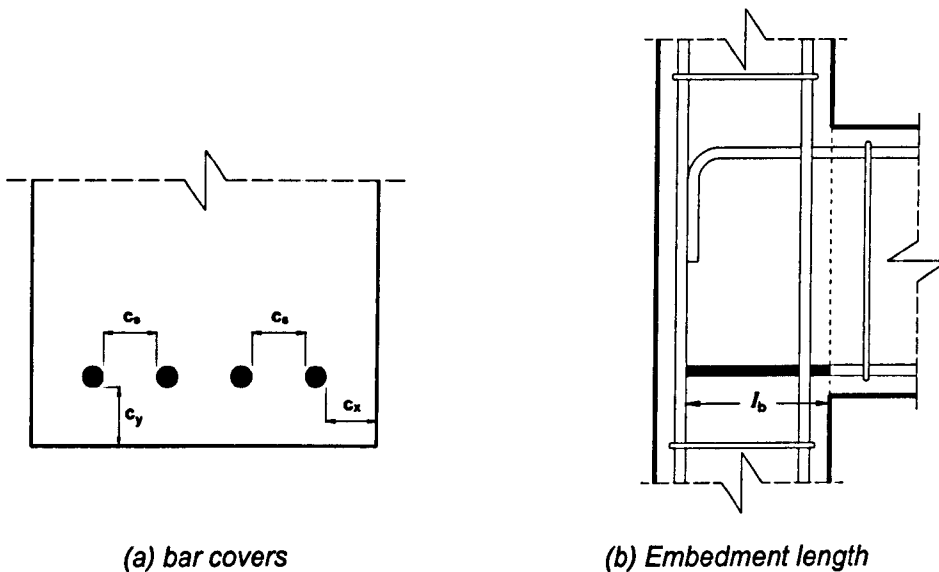


Figure 5.17: Definition of anchorage length and bar covers

Figure 5.18 shows the geometry and applied forces on a typical exterior beam-column joint specimen. From global equilibrium, the column shear force, V_c can be calculated as follows:

$$V_c = V_b \frac{L + \frac{h_c}{2}}{H} \quad (5.7)$$

where:

- V_b, V_c are the applied cyclic load or beam shear and the reaction on the column or the column shear force, respectively.
- H, L, h_c are the column height, the beam length and the column depth, respectively.

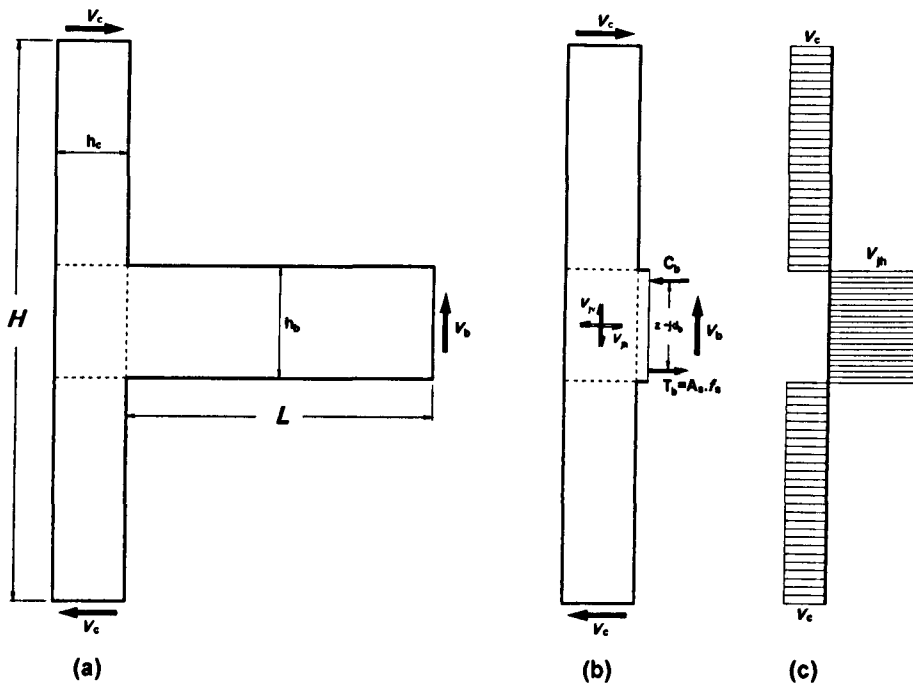


Figure 5.18 a) Free body diagram, b) global equilibrium, c) shear force distribution of a typical test specimen

Similarly, from global equilibrium of the joint panel, shown in Figure 5.18.b, the beam moment at the column face can be calculated as follows:

$$M_b = V_b \times L = T_b \times jd_b = A_s f_s \times jd_b \quad (5.8)$$

where:

- T_b is the tension force in beam reinforcement at the column face.
- A_s, f_s are the area and the stress of the beam reinforcement in tension at the column face.
- jd_b is the beam moment lever arm and j is taken as 0.875 of the beam effective depth, d_b for *J-type* failures and 0.9 for *BJ-Type* failures.

In the proposed model, the column shear force, V_c is required for the estimation of the extended width, a_{pr} . This, in turn, requires the estimation of M_b or the beam tension force at the column face, T_b . One option for estimating T_b is by assuming the stress in the bar, f_s or the bond stress distribution along the bar. Taking into account that the compressive stress distribution within the joint core is not uniform and that it is the highest within the original strut width and the lowest next to the beam, it can be concluded that bond stress distribution along the bar is not uniform as well. This can be attributed to the factor $\Omega_{p,tr}$ which varies according to the compressive stress distribution. Based on this, the factor $\Omega_{p,tr}$ can be taken as the full value (i.e. maximum value) within the original strut width; and a much lesser value within the width a_{pr}

and equal to 1 (i.e. no factor is considered) within the length ($h_c - a_c - a_{pr}$). Conservatively, it can be assumed that the factor $\Omega_{p,tr}$ is only effective within the original strut width and equal to 1 over the remainder of the bar length.

By adopting the previous assumptions, the maximum possible force, T_{bmax} that can be developed at the joint face in the beam reinforcement is approximated as follows:

$$T_{bmax} = n\pi\phi_b\Omega_{p,tr}\tau_b l_s + n\pi\phi_b\tau_b(l_b - l_s) \quad (5.9)$$

The previous force (i.e. T_{bmax}) can only be reached if pull-out failure occurred before reaching f_{ce} within the inclined compressive strut. Therefore, if the predicted joint shear strength using the proposed model yielded $T_{b-predicted} > T_{bmax}$ then the expected failure mechanism is pull-out failure.

The horizontal projection of the original strut is considered here to be the column compression zone width, a_c . Thus, the column shear force, V_{ac} acting along the column compression zone can be approximated by taking ($T_b = T_{bmax}$) as follows:

$$V_{ac} = \frac{a_c T_b j d_b}{h_c L} \left[\frac{L + \frac{h_c}{2}}{H} \right] \quad (5.10)$$

The column compression zone, a_c can be estimated according to Paulay & Priestley (1992) and limited by Vollum (1998) as follows:

$$a_c = \left(0.25 + 0.85 \frac{N}{f'_c h_c b_c} \right) h_c \leq 0.4 h_c \quad (5.11)$$

where:

- N is the column axial force.
- h_c and b_c are the column depth and width, respectively.

The upper bound in Eq (5.11) was proposed by Vollum (1998) who found through many experimental observations that unless a hinge forms in the upper column, the joint shear strength remains independent of column axial load (Vollum & Newman, 1999). Moreover, the angle θ_s can be calculated from geometry and the concrete compression zone as follows:

$$\theta_s = \tan^{-1} \left(\frac{h_c - a_c}{h_b} \right) \quad (5.12)$$

Determining the length, l_s at the end of beam reinforcement bars depends on the estimated column compression zone, a_c and the reinforcement layout within each different joint. For instance, in the case where the beam bottom straight bars end at the exterior layer of the column reinforcement bars, as shown in Figure 5.17.b, the length, l_s can be estimated as follows:

$$l_s = d'_b \tan \theta_s + a_c - d'_c - \frac{\phi_c}{2} \quad (5.13)$$

where:

- d'_b and d'_c are the concrete covers measured to the centre of the beam and column longitudinal reinforcement, respectively, as shown in Figure 5.19.
- ϕ_c is the column bar diameter.

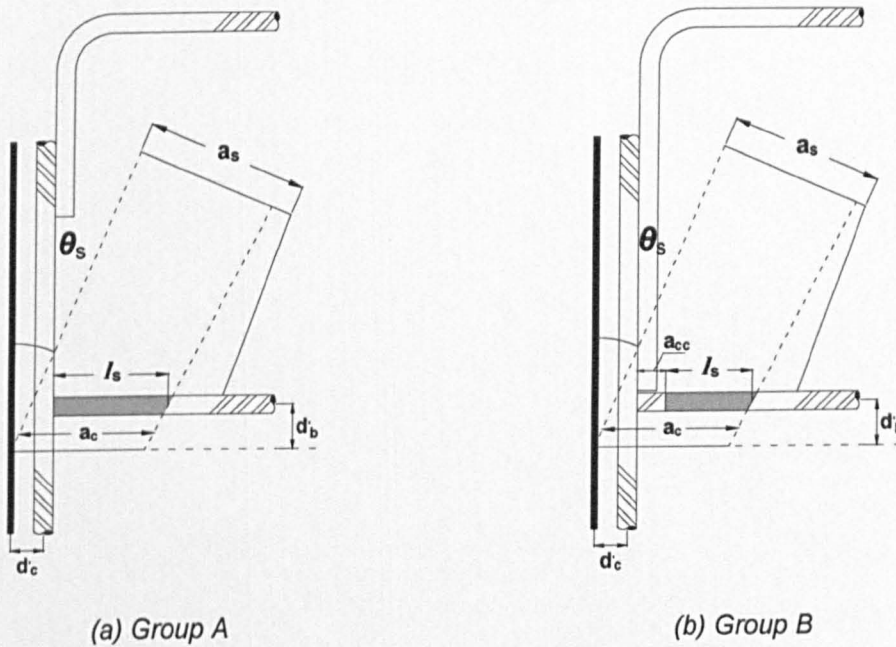


Figure 5.19: Definition of l_s for beam straight bars

The previous expression given in Eq (5.13) can be used for group A specimens of the current research, as shown in Figure 5.19.a. However, for group B specimens where the beam top hooks extend all the way down to the beam bottom bars, the final value of l_s should be reduced by a_{cc} , as shown in Figure 5.19.b. The reason behind this reduction is due to the forces imposed by the vertical part of the top hooks on the outer nodal zone of the compression strut. These forces work opposite to the developed bond forces and try to push the concrete cover outward, and eventually cause spalling. This leads to the reduced strength observed in the negative direction for Group B specimens in comparison to Group A specimens. Based on these experimental observations, the anchored length, l_s was reduced by $a_{cc} = 1.5\phi_c$. It should be noted, however, that this value of a_{cc} is valid only for joints that hold the same aspect ratio and with the same reinforcement layout, in which the top hook touches the bottom straight bar.

Moreover, the force that develops at the end of a beam reinforcement bar due to the effect of the diagonal strut varies depending on the shape and length of the end anchorage. Therefore, for exterior beam-column joints where beam longitudinal bars end with 90° hooks, the extension in the strut width will be larger. This can be attributed to the contribution of the bend and vertical part of the hook to the transfer of the beam bar forces, (CEB-fib MC10, 2010). Thus, in this model, an additional force develops over the vertical portion, l_v of the hook affected by the compression strut, as shown in Figure 5.20.b. This force, denoted as F_v , is equal to the force required to crush the area of concrete occupied by this vertical portion and can be calculated as follows:

$$F_v = 0.5n_v\phi_b l_v f_{ce} \quad (5.14)$$

where:

- n_v is number of beam hook in tension.
- l_v is the vertical projection of the hook affected by the compression strut, as shown in Figure 5.20.b.

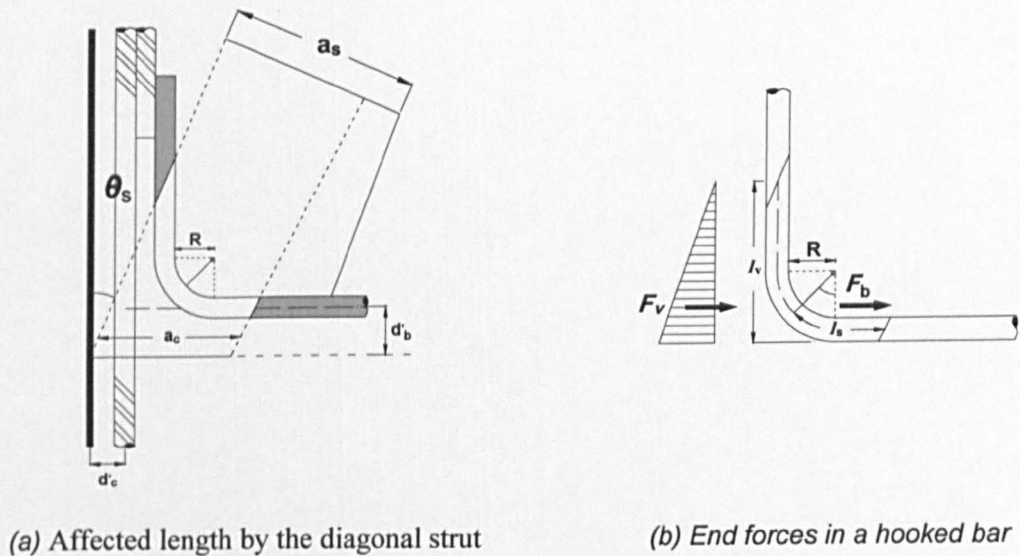


Figure 5.20: Definition of hook contribution to the tie reinforcement

Similarly to straight bars, determining the anchoring length for hooks is also dependant on reinforcement layout within the joint and the column compression zone. For example, Figure 5.20.a shows the affected portion of the beam bottom hooks in group C specimens. While calculating l_v is similar in all hook cases, the length l_s for hooks can be divided into two cases.

The first case is for exterior joints where beam bars remain within the elastic range. It was found by Shima & Fukuju (2008) that when a bar is still in the elastic range the stresses that develop within the bent part are almost negligible after the 45° bent, as can be seen in Figure 5.21.

Therefore, for the calculation of T_{ac} in hooks, the length, l_s , should be limited to the end of the 45° bent, as shown in Figure 5.20.b.

The previous limitation, however, is valid only for exterior joints in which the horizontal projection of the hook l_b is at least 40% of the recommended embedment length value, l_{dh} by section R12.5, ACI 318-08 (2008).

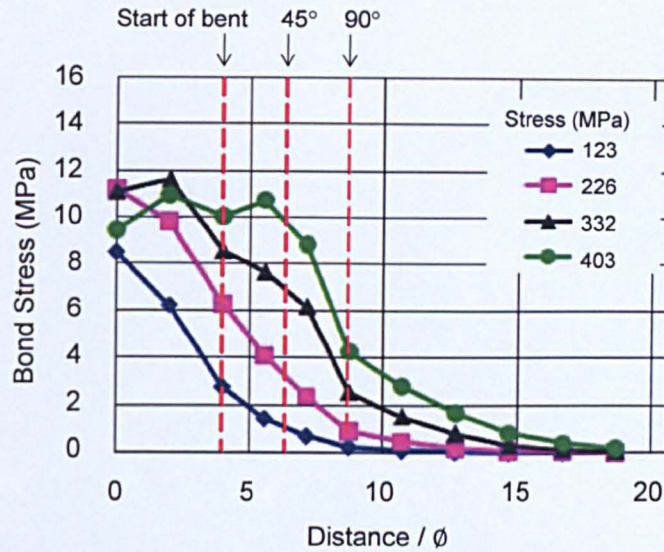


Figure 5.21: Local bond stress of 90° hook bar (Shima & Fukuju, 2008)

The second case is for exterior joints in which beam bars reach yielding. In this case, the anchored length, l_s can be taken up to the end of the 90° bent.

Furthermore, in case of 90° hooks, pull-out failures are more difficult to occur in exterior joints. Therefore, and rather than using Eq (5.6), a more general expression that calculates the local bond stress, τ_b over a limited length, l_s regardless of the type of failure is more accurate. According to Model code 2010, the average local bond stress over a limited short length can be estimated as follows:

$$\tau_b = 6.54\eta_2 \left(\frac{f_{ck}}{20}\right)^{0.25} \left(\frac{20}{\phi_b}\right)^{0.2} \left(\frac{c_{min}}{\phi_b}\right)^{0.33} \left(\frac{c_{max}}{c_{min}}\right)^{0.1} \quad (5.15)$$

where f_{ck} is the characteristic cylinder concrete compressive strength (N/mm²) and with the same limitations as Eq (5.6).

5.4.3 Joint Shear Capacity

In the strut-and-tie model approach, the horizontal joint shear force, V_{jh} is considered to be the horizontal component of the compressive strut capacity, D . From equilibrium of forces on the outer nodal zone, as shown in Figure 5.15, the joint shear force can be calculated according to Eq (5.16).

$$V_{jh} = D \sin \theta_s \quad (5.16)$$

The compressive strut capacity, D is the contribution of both the original, D_1 strut and the extended strut D_2 and can be calculated according to ACI 318-08 as follows:

$$D = f_{ce} A_{st} \quad (5.17)$$

$$f_{ce} = 0.85 \beta_s f'_c \quad (5.18)$$

$$A_{st} = b_j a_s \quad (5.19)$$

where:

- A_{st} is the area of the compressive strut.
- β_s is the concrete softening coefficient. For exterior joints with no shear links, the compression strut is considered to start and end with different widths (bottle-shaped strut). Therefore, the softening coefficient, β_s can be taken equal to 0.6, see section A.3.2, (ACI 318-08, 2008).

The strut effective width, a_s at the outer nodal zone can be calculated from geometry as follows:

$$a_s = (a_c + a_{pr}) \cos \theta_s \quad (5.20)$$

The width, a_{pr} given in Eq (5.3) is for straight bars, whereas for hooked bars a_{pr} can be calculated from the effective tie width after substituting F_b in Eq (5.1) with $F_b + F_v$.

5.5 VERIFICATION OF THE PROPOSED MODEL

The applicability and the accuracy of the proposed shear strength model are verified against the 24 unconfined exterior beam-column joints given in Table 5-1. Figure 5.22 compares experimental and predicted joint shear strengths of all the joints in the database using the proposed model. The model predicted with good accuracy the strength of group A specimens in both loading directions. However, it should be noted that the test results of Group A of this research did not demonstrate a great reduction in strength due to the absence of hooks in the negative loading directions. Moreover, the model's good prediction of the strengths of JB-1 and JB-2 in the negative loading direction, as mentioned before, is based on the proposed reduction of the length, l_s at the end of the straight bar (reduced by $a_{cc} = 1.5\phi_c$), which was calibrated based on the tests results of these two tests. Therefore, further verification of the proposed model on tests similar to Group A/B specimens is required. In the case of hooks and extended hooks, the model does not account for the extended length as long as the hook having shorter length is covered by the assumed original strut.

In general, the model showed good agreement with the reported experimental results, as the average test to predicted shear strength ratio, $\gamma_{test}/\gamma_{model}$ is 1.01 and the coefficient of variation for the same ratio is 0.06%. The detailed results are given in Table 5-1.

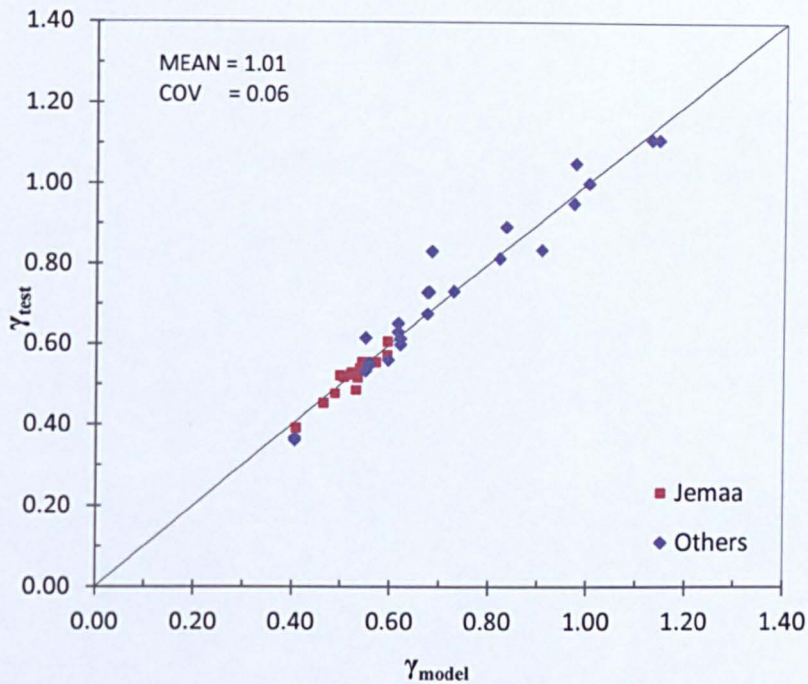


Figure 5.22 Verification of the proposed Strut-and-Tie joint shear strength model

5.6 MODEL LIMITATIONS

The proposed model was verified against a limited database of 24 isolated exterior unconfined beam-column joints. Therefore, the following should be noted:

- 1- The database included specimens with beam anchorages similar to Type A, B and C that were investigated in the current research. Thus, the applicability of the model to specimens with 180 hooks is uncertain.
- 2- The proposed value of $l_b/l_{ch} \leq 0.40$ to define the included length of the bent part of the hook in l_s was calibrated based on the specimens included in the database.
- 3- The applicability of the model to specimens with joint aspect ratio higher than 2 is uncertain.

5.7 RECAP AND CONCLUSIONS

The work presented in this chapter included evaluating some of the joint strength models, presented in Chapter 2, which can be applicable or specifically developed for deficient exterior joints. This was achieved using a database of 24 deficient exterior beam-column joints. In addition, this chapter included the development of a new exterior joint shear strength model.

The following summarises the work and the key findings of this chapter:

- 1- The joint strength model by Hwang and Lee (1999) is not suitable for the strength prediction of deficient exterior beam-column joints. The model's poor ability to predict the shear strength of joints with no shear reinforcement in comparison to confined ones is attributed to the omission of the beam contribution to the diagonal strut width. Another reason is the proposed initial condition that both the intermediate column reinforcement and beam bars have yielded when the joint reaches its maximum strength. Using the joint database of this research the overall mean of the $\gamma_{test}/\gamma_{model}$ ratio is 1.16 and the coefficient of variation for the same ratio is COV=0.20%.
- 2- The simplified joint strength model by Vollum and Newman (1999) was developed for estimating the joint shear strength of both confined and unconfined exterior joints taking into account the effects of beam anchorage detail and joint aspect ratio. The model was evaluated by using the joints included in the database of this research. The overall mean of the $\gamma_{test}/\gamma_{model}$ ratio is 0.85 and the coefficient of variation for the same ratio is COV=0.23%. The model generally overestimates the joint shear strength of unconfined exterior joints included in this research database. This can be attributed to the limitations of the beam anchorage factor β , and the exclusion of the effect of column axial load for the case of unconfined joints (see Chapter 2&5).
- 3- The joint strength model by Tsonos (2007) does not produce reliable results when used for deficient exterior beam-column joints. This is because the lack of shear links is not accounted for in the model formulations. Based on the deficient exterior joint database of this research, the calculated mean and coefficient of variation for the $\gamma_{test}/\gamma_{model}$ ratio are, MEAN =0.64 and COV=0.36%.
- 4- The joint strength model by Hassan (2011) was developed for estimating the joint shear strength of unconfined exterior joints but with standard hooks. Using the model on the joint database of this research, the mean and coefficient of variation for the $\gamma_{test}/\gamma_{model}$ ratio are, MEAN =0.85 and COV=0.15%. The model in general is overestimating. This is because the model assumes that in all *J-Type* failure joints, the beam remains within the elastic range. This leads to the overestimation of the diagonal strut width especially for cases where beams are close to yielding.
- 5- The strength model proposed by Park & Mosalam (2012a) was developed for estimating the joint shear strength of unconfined exterior joints with at least one hook. Based on the deficient exterior joint database of this research, the calculated mean and coefficient of variation for the $\gamma_{test}/\gamma_{model}$ ratio are, MEAN =0.90 and COV=0.22%. The model generally overestimated the joint shear strength of the included deficient exterior joints.

This can be attributed to the proposed fixed width of the second strut of $0.65h_c$ regardless of the calculated column compression zone. This approximation, in addition to fixing the beam internal moment lever arm, can cause the model to overestimate the stress in the beam longitudinal reinforcement.

- 6- An analytical model that predicts the shear strength of exterior deficient beam-column joints in both loading directions is developed. The model predicts the maximum shear strength using a modified version of the ACI strut-and-tie model approach.
- 7- In the proposed model, the tie and in turn the strut is highly influenced by the shape and length of the beam longitudinal anchorage and the column axial load level. The model was validated using the available shear data acquired from this research and results of similar joint tests reported by others. The model predicted the experimental peak strength values of the available specimens with good accuracy. The average test to predicted shear strength ratio, $\gamma_{test}/\gamma_{model}$ is 1.01 and the coefficient of variation for the same ratio is 0.06%.

CHAPTER 6

RC JOINT MODEL FOR FE FRAME ANALYSIS

6.1 INTRODUCTION

This chapter will present the development of an exterior beam-column joint model for finite element frame analysis of deficient RC structures. A nonlinear structural analysis software, which offers nonlinear beam elements and zero-length rotational springs with pinching and degradation capabilities, is used to represent the connection model. The joint shear strength model, presented in Chapter 5, is used to develop a quad-linear shear stress-strain constitutive envelope for the joint panel zone. The experimental results of the current research and results from others (presented in Table 5-1) are used to calibrate the constitutive model. The joint model is validated by comparing the predicted cyclic response with experimental data.

6.2 CONSTITUTIVE SHEAR MODEL

6.2.1 Development of Shear Envelope Model

After reviewing the experimental shear stress-strain response results presented in Chapter 3, four distinctive stages of behaviour were identified, as shown in Figure 6.1.

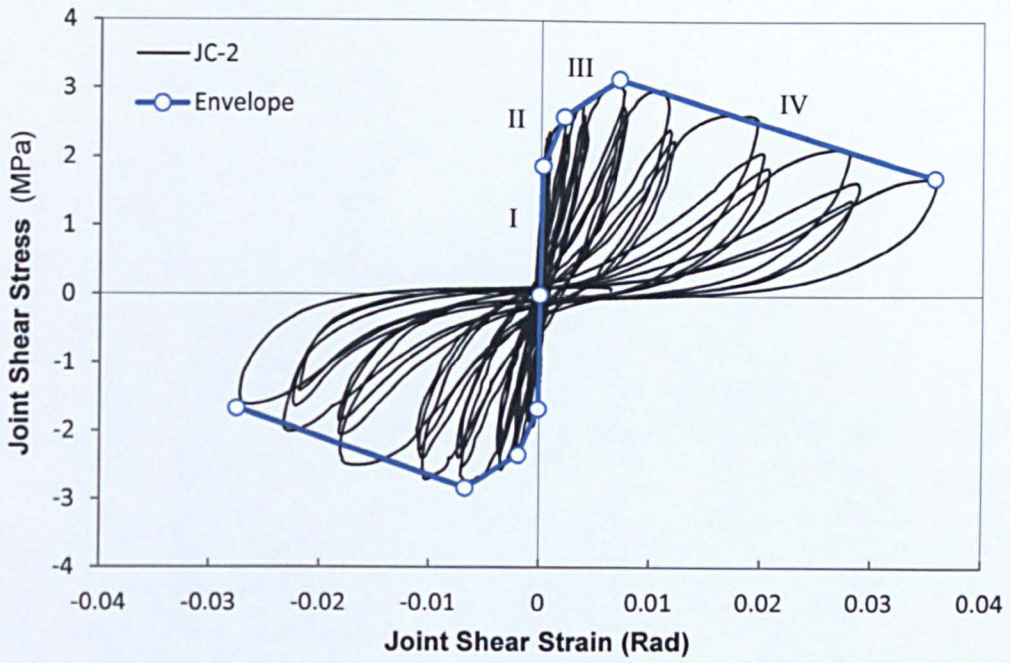


Figure 6.1 Shear stress-strain of specimen JC-2 and proposed envelope

Each stage ends with a significant event that causes a change in the joint shear stiffness. Figure 6.2, shows the proposed shear stress-strain envelope curve for unconfined exterior beam-column joints. In order to simplify the model implementation in spring based joint models, each point on the envelope is represented by the tangent shear modulus of that stage. In the following section, the procedure to determine each point is detailed.

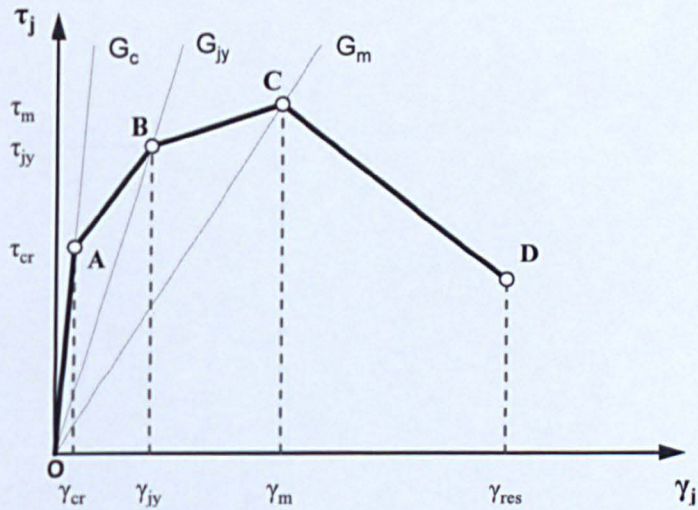


Figure 6.2 Proposed exterior joint shear stress-strain envelope curve

6.2.2 Proposed Shear Stress-Strain Envelope

6.2.2.1 Hairline Cracking Shear Strength (Point A)

Point A of the shear stress-shear strain envelope curve represents the joint stress state at the end of the elastic range where initial hairline cracking occurs. One way to determine point A is by finding the cracking shear strain. Based on the experimental results of the current research, the observed cracking shear strain ranged from 0.0001 to 0.00013. Similar results were reported by Clyde et al. (2000), as their test specimens experienced hairline cracking at a shear strain ranging between 0.00009 and 0.00011. Pantelides et al. (2002) also reported a cracking shear strain of 0.00013 in three of the tested specimens, whereas the fourth specimen developed hairline cracks at a higher strain of 0.00034. Moreover, Celik & Ellingwood (2008), after collecting experimental data from several unconfined interior and exterior beam-column joints, found that shear strain when hairline cracking occurs ranges from 0.0001 to 0.00013 regardless of the axial load level.

Based on these findings, for simplicity, the cracking shear strain for exterior unconfined beam-column joints, in this model, can be taken as 0.00012 at Point A. This value corresponds to the value also proposed by Vecchio & Collins (1986).

The cracking shear stress τ_{cr} at point (A) of the shear stress-shear strain envelope curve can be defined based on the cracking strain γ_{cr} and the initial stiffness of the first segment, G_0 as follows:

$$\tau_{cr} = \gamma_{cr} G_0 \quad (6.1)$$

Hassan (2011) and Anderson et al. (2008), based on the experimental results of unconfined interior and exterior joints, proposed the initial stiffness, G_0 to be taken as half the theoretical elastic shear modulus, G_c . Hassan (2011) argued that this reduced stiffness might result due to joint micro cracking. However, the experimental results of the current research in addition to results from several other exterior joint tests, such as Clyde et al. (2000) and Pantelides et al. (2002), show that G_0 is closer to the theoretical elastic shear modulus, G_c .

Therefore, in the proposed model, for exterior unconfined beam-column joints the initial stiffness, G_0 is taken as the full theoretical elastic shear modulus, G_c , which can be calculated by:

$$G_c = \frac{E_c}{2(1 + \nu)} \quad (6.2)$$

where E_c is the concrete modulus of elasticity and ν is the concrete Poisson's ratio and can be taken as 0.2 for normal concrete.

6.2.2.2 Pre-Peak Strength (Point B)

Point B of the shear stress-strain envelope curve represents the joint stress state when significant change in the cracked stiffness occurs. This change usually marks the development of the main diagonal shear cracks for *J-Type* failure joints, whereas for joints with *BJ-Type* failure it reflects yielding of beam reinforcement (In this case point B is very close to point C).

The shear strain, γ_{jy} at point B varied depending on the type of beam anchorage. Based on the limited experimental results of the current research and results from others, such as Clyde et al. (2000) and Pantelides et al. (2002), it was found that γ_{jy} can be taken as 0.002 for hooks. For straight bars the shear strain, γ_{jy} can be taken as 0.0015 for joints Type A and 0.001 for joints Type B.

Hassan (2011) proposed that the joint shear stress τ_{jy} at point B does not exceed 90% of the peak joint shear stress, τ_m . Anderson et al. (2008), on the other hand, proposed τ_{jy} to be 95% of the calculated joint shear stress when the stress in the beam bars reaches 1.25 times the yield stress. However, based on the tests results of the current research and results from others, such as Clyde et al. (2000) and Pantelides et al. (2002), it was found that the average observed shear stress at the pre-peak point, τ_{jy} can be taken as $0.85\tau_m$, and the secant stiffness, G_{jy} is equal to $0.12G_c$ when the beam bar in tension is a 90° hook. These values are consistent with the value proposed by Hassan (2011). On the other hand, for straight beam bars in tension, τ_{jy} can be taken as $0.80\tau_m$ for joints Type A and $0.95\tau_m$ for joints Type B. The corresponding secant stiffness, G_{jy} for these two cases is $0.14G_c$ and $0.2G_c$, respectively.

Based on the peak shear stress, τ_m and the secant stiffness, G_{jy} the shear strain at the point B can be given as follows:

$$\gamma_{jy} = \frac{c_j \tau_m}{G_{jy}} \quad (6.3)$$

where c_j is the ratio of the peak shear stress corresponding to the beam anchorage detail (hook 0.85, straight Type-A 0.8, and straight Type-B 0.95).

6.2.2.3 Peak Shear Strength (Point C)

The peak joint shear strain, γ_m can be estimated based on the calculated joint shear strength using the proposed shear strength model presented in section 5.4 as follows:

$$\gamma_m = \frac{\tau_m}{G_m} \quad (6.4)$$

Based on the experimental results by Clyde et al. (2000), it was found that the joint shear strain at maximum nominal shear stress ranged between 0.003 and 0.0048. Similar findings were reported by Pantelides et al. (2002). On the other hand, based on the experimental results of the current research, the average shear strain at the peak shear stress in both directions was found to be 0.0065. Hassan (2011) estimated the peak shear secant stiffness based on the joint aspect ratio and the type of joint failure. However, his predictions did not compare well with the measured strains from this study.

In this research, for the calculation of joint secant stiffness G_m at the peak shear stress, τ_m the following equation is proposed:

$$G_m = 0.19 \left(1 - 0.5 \frac{h_b}{h_c} \right) G_c ; 0.8 \leq \frac{h_b}{h_c} \leq 1.6 \quad (6.5)$$

Eq (6.5) is calibrated using the shear stress-strain results of the current research and results from Clyde et al. (2000). The proposed equation shows good correlations between the measured and the predicted peak joint shear strain, as can be seen in Figure 6.3. Moreover, it was found that the same value for γ_m can be used for both loading directions. Therefore, γ_m can be obtained for both directions by substituting the maximum value of τ_m in Eq (6.4).

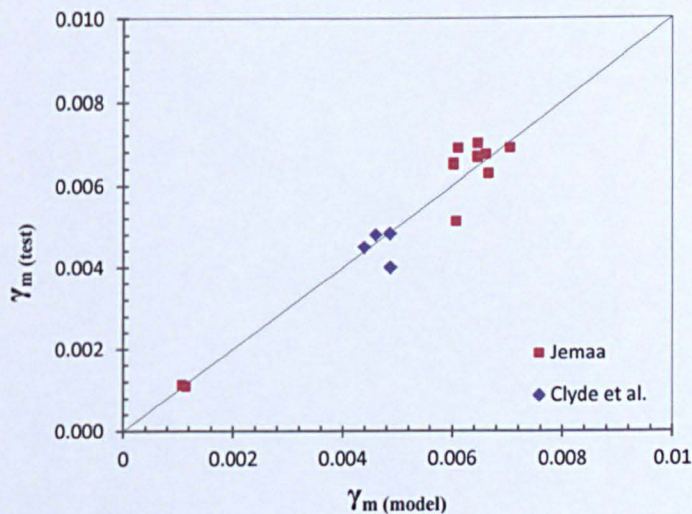


Figure 6.3 Comparison of measured and predicted strain at the peak joint shear stress

6.2.2.4 Residual Strength/Degrading Branch (Point D)

Point D of the shear stress-strain envelope curve is defined as when the joint shear stress drops to 50% of the peak shear stress, τ_m . Based on the measured residual shear strains of the current

research tests and results from others, such as Clyde et al. (2000) and Pantelides et al. (2002), it was found that the average slope of the degrading branch (C-D) is 10% of the peak secant stiffness, G_m for beam hooks in tension. On the other hand, for straight beam bars in tension, the slope is $0.18G_m$ and $0.1G_m$ for Type A and B, respectively. Accordingly, the joint shear strain at point D can be calculated as follows:

$$\gamma_{res} = \gamma_m + \frac{0.5\tau_m}{c_n G_m} \quad (6.6)$$

where c_n is the ratio of the peak secant stiffness corresponding to the beam anchorage detail, as presented above (hook 10%, straight Type-A 18%, and straight Type-B 10%).

6.2.3 Predicted Shear Envelope

Figure 6.4 to Figure 6.6 show a comparison between the measured response and the predicted envelope of the current research specimens. The envelope of each loading direction should be determined separately based on the corresponding anchorage detail and by following the appropriate procedure and proposed values in section 6.2.2. It should be noted that for the predicted envelopes, the calculated shear strength values presented in Table 5-1 are used.

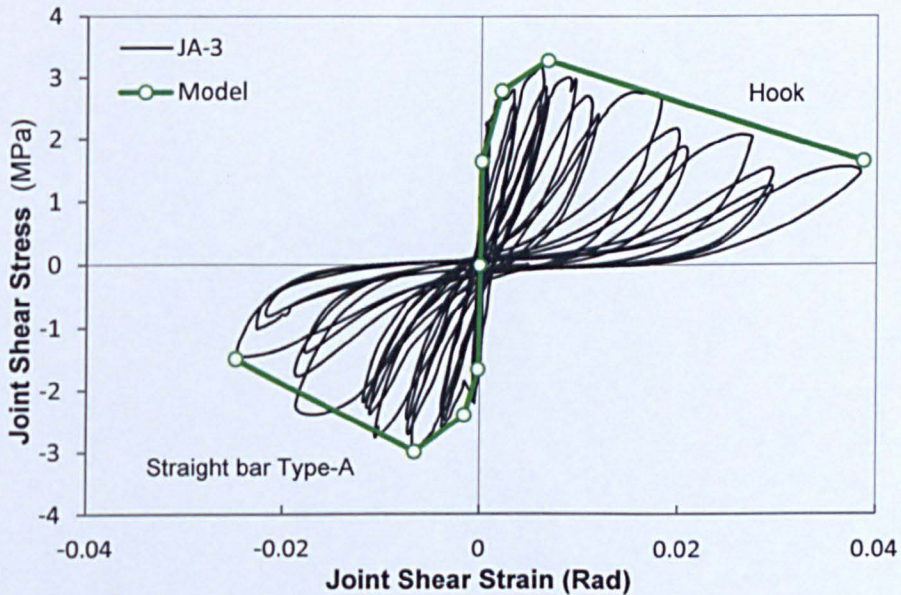


Figure 6.4 Shear stress-strain of specimen JA-3 and predicted envelope

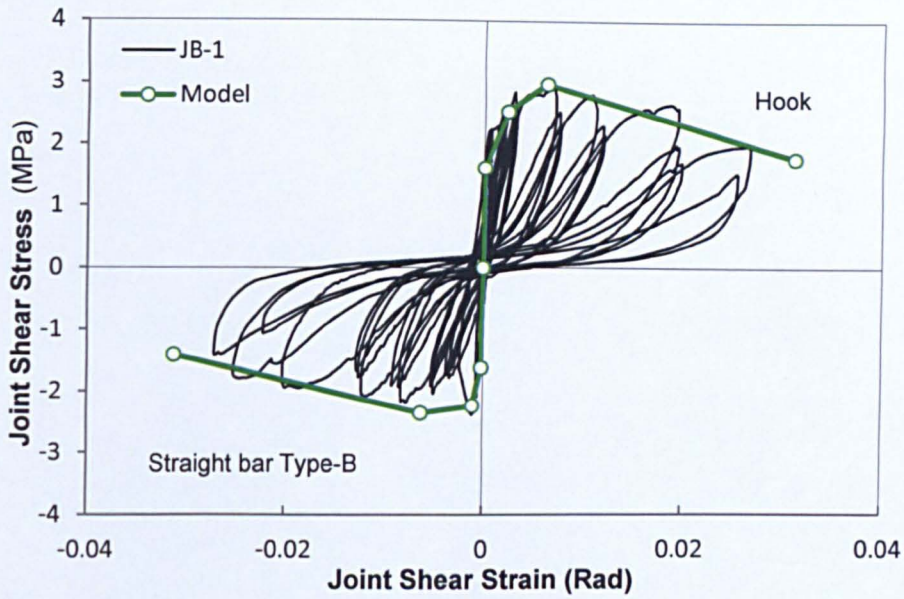


Figure 6.5 Shear stress-strain of specimen JB-1 and predicted envelope

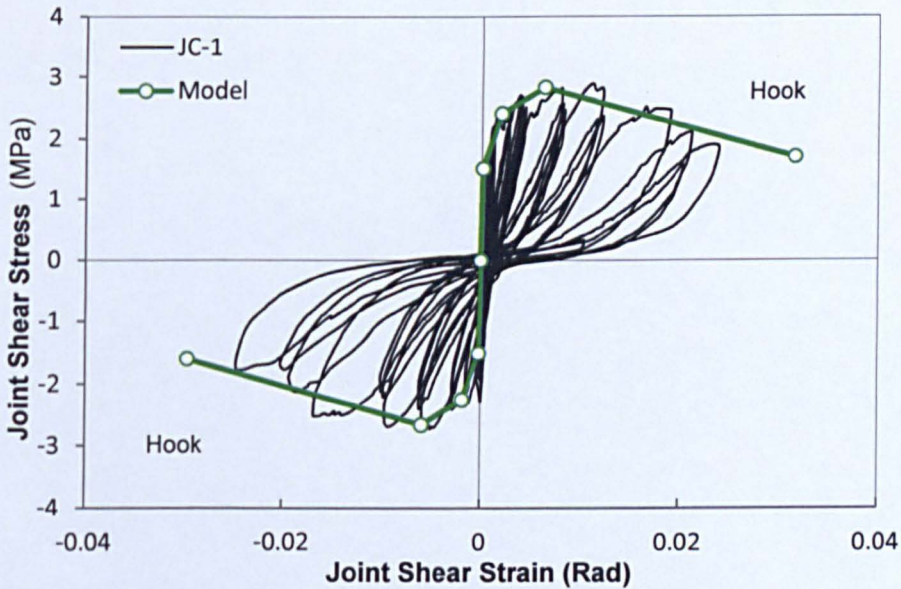


Figure 6.6 Shear stress-strain of specimen JC-1 and predicted envelope

6.3 SELECTION OF THE ANALYTICAL TOOL

A nonlinear structural analysis software, which offers nonlinear elements and rotational hinges with pinching and degradation capabilities, is required to represent the joint panel zone connection model. Finite Element software, mainly developed for seismic analysis, such as OpenSees (McKenna & Fenves, 2012) and DRAIN-2DX (Prakash et al., 1993), are well suited for this task. Both OpenSees and DRAIN-2DX have a rich library of elements which allow the user to perform highly sophisticated static and dynamic analysis. In addition, both tools are

capable of representing strength degradation, stiffness degradation, pinching, and other hysteresis properties with great accuracy.

OpenSees and DRAIN-2DX were successfully utilized by several researchers to perform linear and nonlinear dynamic analysis, such as Shin & LaFave (2004), Jemaa (2007), Kyriakides (2008), Park & Mosalam (2009), Hassan (2011), and Ahmad (2011).

For this study, both OpenSees and DRAIN-2DX can be used to represent the joint model. However, DRAIN-2DX is simpler to use when compared to OpenSees, which requires previous knowledge in C++. Based on the comprehensive previous personal knowledge and the highly praised capabilities, DRAIN-2DX was chosen to represent the exterior beam-column joint connection model of this research.

6.4 NONLINEAR JOINT MODELLING

6.4.1 Background and Previous Models

In moment resisting frame analysis, beam-column joints are often modelled as rigid connections. While this might be acceptable for well confined joints, Celik & Ellingwood (2008) found that using the same representation to model unconfined beam-column joints can yield wrong results in terms of joint drift and stiffness.

Many past researchers, as described in chapter 2, realized this issue and therefore tried to simulate the nonlinear load-drift response of beam-column joints by proposing different component-based joint models. In some of these models the joint nonlinear deformation is limited to plastic hinge zones at the end of beam elements, whereas in others, explicit panel zone elements are used to represent the nonlinear contribution of joints.

One, widely used, panel zone representation is the joint scissors model (Krawinkler & Mohasseb, 1987). In this model the joint is represented by two rigid links connected by a single rotational spring, as shown in Figure 6.7.a. Due to its simplicity, this model was used by many researchers for confined and unconfined beam-column joint analysis, as discussed in Chapter 2.

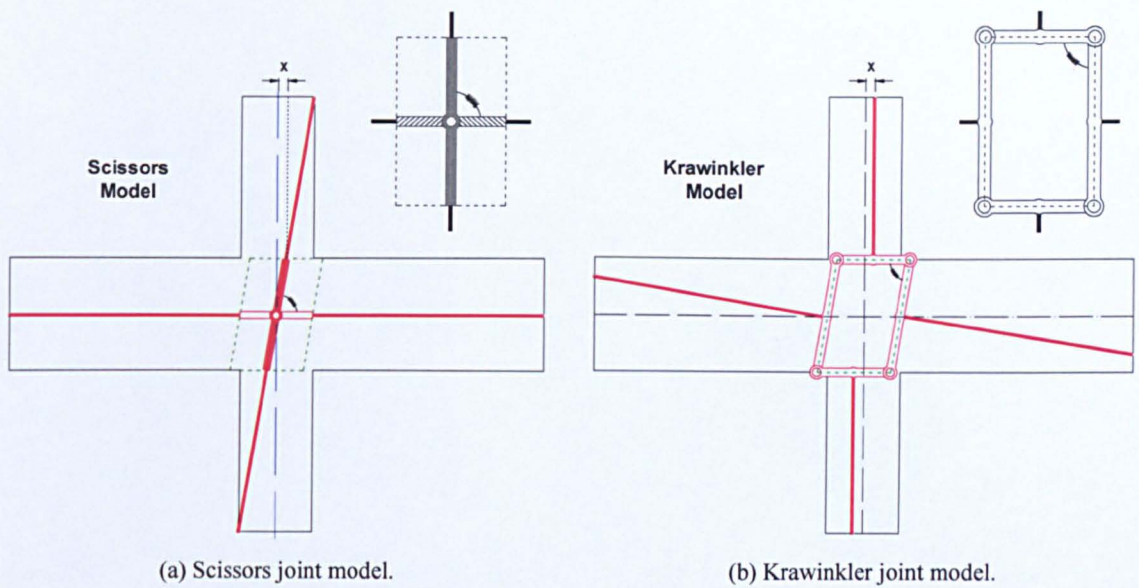


Figure 6.7 Panel zone joint model

Another, commonly used joint panel zone representation is the model by Krawinkler (2001) which is an improved version of the scissors model. The Krawinkler model, similarly to the scissors model, was used by many past researchers. However, this model requires more elements and hinges to be defined, which in turn requires extra computational effort especially when used for multi-storey buildings. Moreover, the main advantage of this model, in comparison to the scissors model, is that when it represents the deformation of the joint panel zone, it also allows a relative displacement between the top and bottom columns, as can be seen in Figure 6.7.b. Another way to achieve this is by introducing extra translational shear hinges to the scissors model at the top and bottom column-joint interfaces to account for the missing relative displacement between the top and bottom columns, as shown in Figure 6.8. With this addition, the joint response from both models is identical. On the other hand, it was found based on an extensive testing using DRAIN-2DX, that the difference between the two models has no significant impact on the overall structural response (BSSC, 2012). As a result, both panel zone idealizations can be considered valid for exterior beam-column joint modelling.

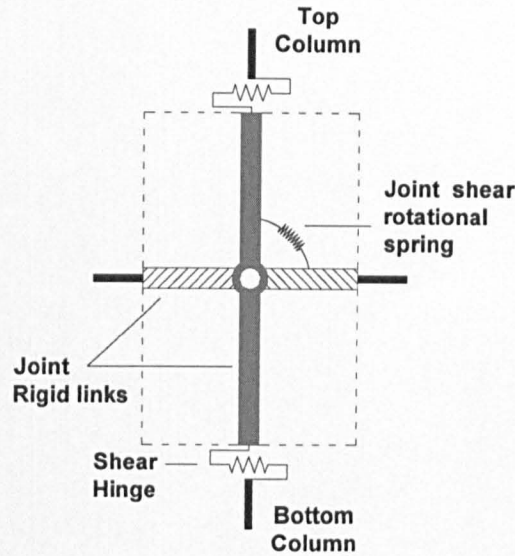


Figure 6.8 Modified Scissors joint model with translational shear hinges

In the following section a new panel zone joint model is proposed. The chosen model is based on the Krawinkler joint model and is implemented in DRAIN-2DX Program (Prakash et al., 1993). The selected elements and material models are detailed in the following section.

6.4.2 Proposed Joint Panel Zone Model

The proposed joint panel zone model consists of four rigid link elements, in which the central axis of each rigid link is located at the joint interface and connected to the adjacent rigid link through a hinge connection, as shown in Figure 6.9. The hysteretic joint shear behaviour is represented by a shear rotational hinge located at the top right hinge of the panel zone, whereas fixed-end rotation due to slip of anchored beam longitudinal bars are represented by an extra rotational hinge located at the joint-beam interface, as shown in both Figure 6.9 and Figure 6.10.

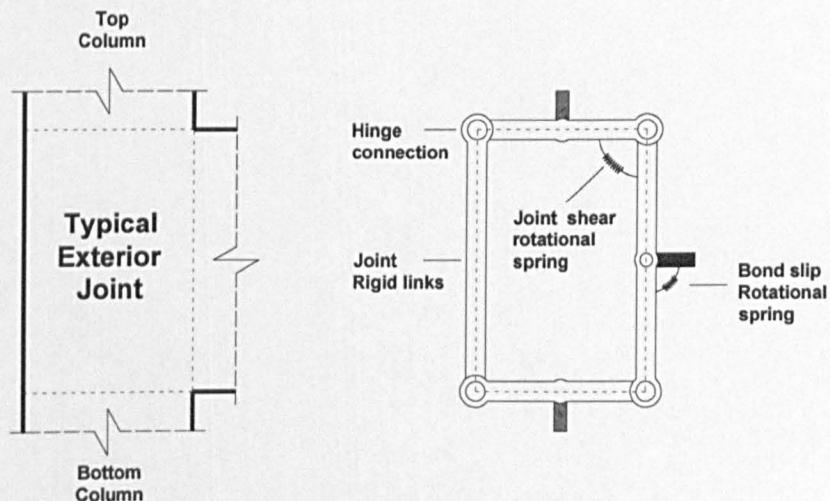


Figure 6.9 Proposed Krawinkler-type panel zone joint model

Figure 6.10 illustrates the layout and the element selection of a DRAIN-2DX computer-based model for a typical unconfined exterior beam-column joint under imposed lateral loading. DRAIN-2DX Element 02 (Powell, 1993), which is a simple inelastic element, is used with very stiff properties to model the rigid links of the joint panel zone. Each rigid element requires two nodes to be defined. The starting node of one rigid link has the same coordinates of the ending node of the adjacent rigid element, (see Figure 6.10). Moreover, a hinge connection that allows free rotation between these rigid elements is achieved by restraining the relative translation in the X and Y direction between every set of two nodes with identical coordinates.

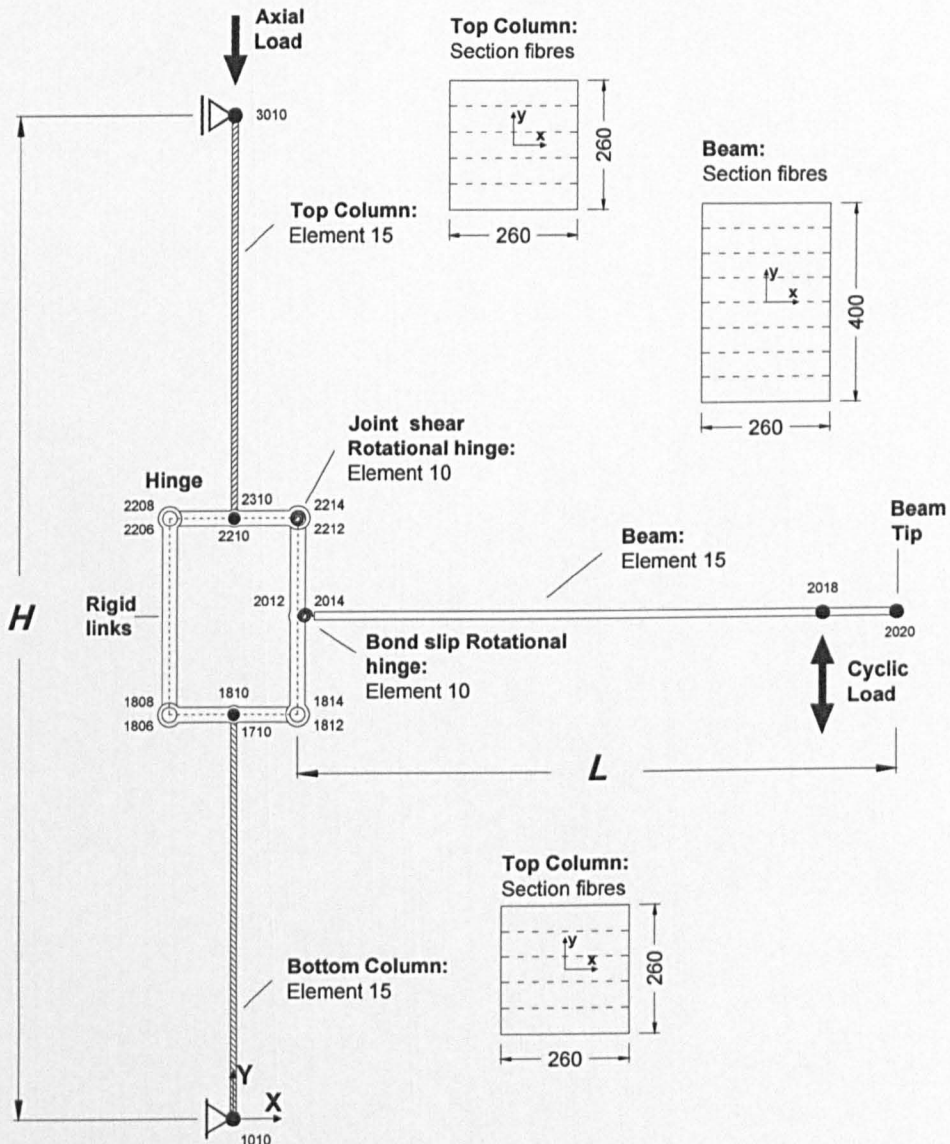


Figure 6.10 DRAIN-2DX exterior beam-column joint model: Geometry and Elements

For the nonlinear rotational hinges of the joint panel zone, DRAIN-2DX Element 10 is used. This element, which was developed by Foutch et al. (2003), is an improved version of DRAIN-2DX Element 04 and can be used as a zero length rotational spring or translational spring, as shown in Figure 6.11. Besides to the original features of Element 04, the new Element 10

includes new hysteretic models that allows for strength degradation, stiffness degradation, and pinching. One of the included hysteretic models is for concrete connections, (see Figure 6.12). Each Element 10 spring requires certain input parameters to be defined, such as: initial stiffness $[k_1]$, strain hardening ratio $[k_2/k_1]$, positive and negative yield moments $[M_y^+, M_y^-]$, strength degradation factor, and positive and negative pinching moments $[M_g^+, M_g^-]$, as shown in Figure 6.12.

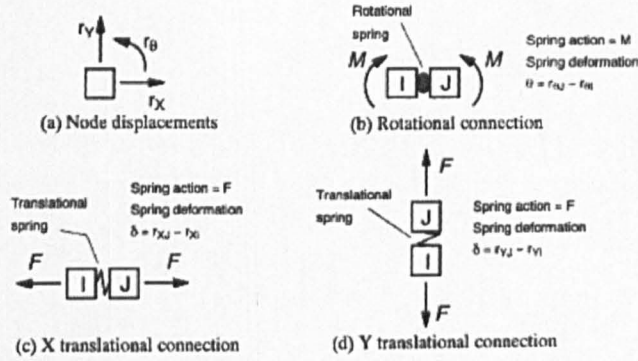


Figure 6.11 DRAIN-2DX Element 10: connection types, after Foutch et al. (2003)

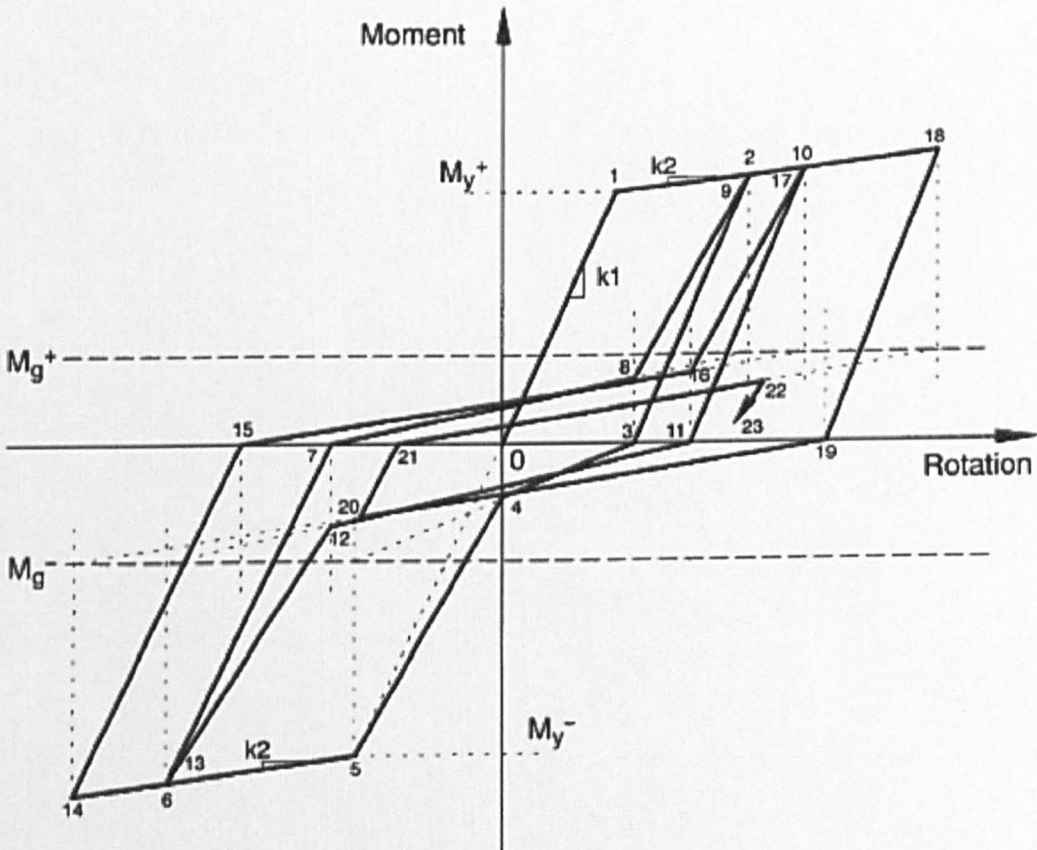


Figure 6.12 DRAIN-2DX Element 10: concrete connection hysteresis model, after Foutch et al. (2003)

The hysteric shear moment M_j shear rotation θ_{sh} properties of the joint rotational shear hinge can be determined based on the shear stress-strain (τ_j - γ_j) quad-linear envelope previously proposed in section 6.2. While θ_{sh} can be taken as γ_j , the joint shear moment M_j can be calculated as follows:

$$M_j = L_b V_b = \tau_j h_c b_j \frac{L_b}{\frac{L_b}{jd_b} - \frac{L_b + h_c/2}{H}} \quad (6.7)$$

Each Element 10 spring can only express a bi-linear moment-rotation envelope. Thus, in this research, six Element 10 rotational springs are connected in parallel at the top right hinge of the panel zone to represent the joint shear quad-linear envelope, (see Figure 6.10). To determine the component of each spring, the original quad-linear envelope is first decomposed into three main bi-linear components. Afterwards, each resulting component is divided and assigned to two of the springs, as shown in Figure 6.13.

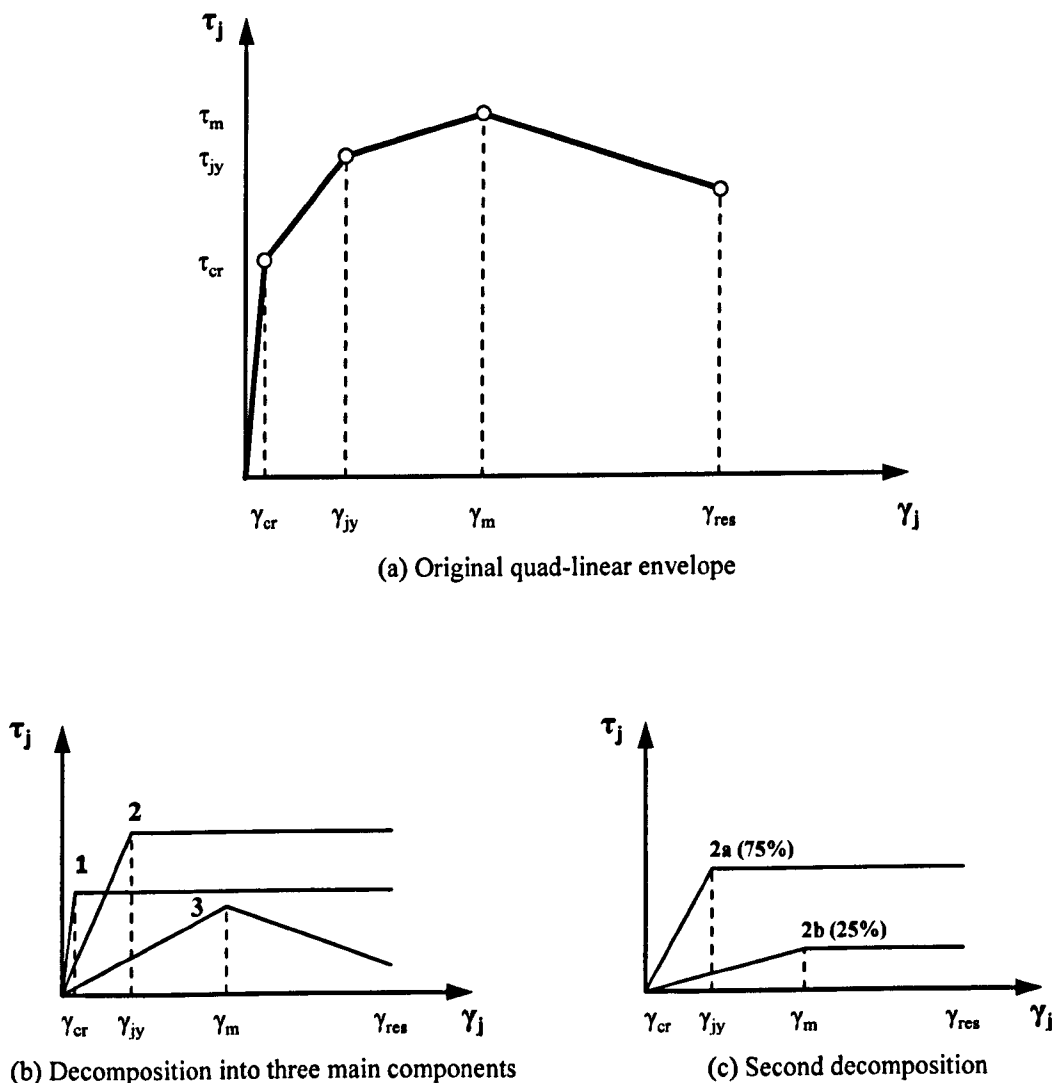


Figure 6.13 Decomposition of shear hinge quad-linear envelope

This decomposition was devised due to the restrictions of the strain hardening ratio $[k_2/k_1]$ of Element 10, which only accepts positive values. Therefore, the negative slope of the original envelope is achieved by applying the strength degradation factor after further decomposing each bi-linear component into two extra bi-linear components. It should be noted, however, that the second decomposition ratio should be chosen so that the joint initial stiffness remains unaffected.

Furthermore, an additional Element 10 nonlinear rotational spring is located at the joint-beam interface. As can be seen in Figure 6.9 & Figure 6.10, the rotational spring represents the additional rotation at the joint-beam interface caused by slip due to bond deterioration and yielding of the beam longitudinal bars embedded in the joint.

Outside the joint panel zone, beam and columns are modelled using feature-rich DRAIN-2DX Element 15 (Powell, 1993). According to DRAIN-2DX element description manual, Element 15 is a fibre inelastic element that can be used for modelling beams and columns. In addition, it can include both elastic and inelastic parts, where inelastic parts can be divided into several segments with different section properties, as shown in Figure 6.14. The section of each segment can be divided into multiple fibres, in which fibres can have different steel and concrete properties. Modelling sections with fibres also accounts for the interaction between axial force and bending moment (P-M). The main advantage of this element, however, is that it uses the distributed plasticity concept which allows the inelastic deformations to be spread over the cross section and along the member's deformable length (Powell, 1993). This distributed plasticity with the use of multiple segments and fibres allows for accurate predictions of the member's flexural stiffness.

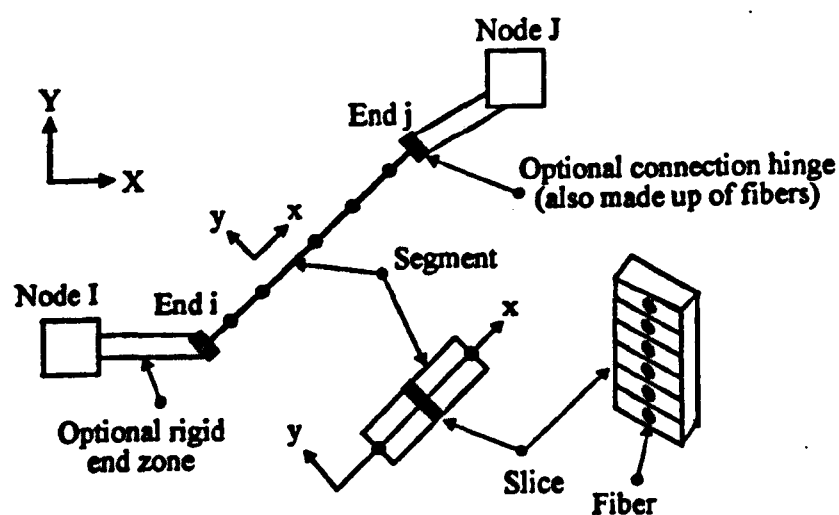


Figure 6.14 DRAIN-2DX Element 15 description, after Powell (1993)

The geometry and the boundary conditions of the proposed DRAIN-2DX model, as shown in Figure 6.10, represent those of the actual tests. The general layout of the model is similar to the model proposed by Shin & LaFave (2004). However, the model by Shin and LaFave was developed for well-confined interior beam column joints, as discussed in Chapter 2.

6.4.3 Beam Anchorage Slip Modelling

There are different approaches for representing the additional rotation caused by bond slip of the beam embedded anchorage at the beam-joint interface. In this research, and as mentioned in the previous section, a dedicated Element 10 rotational slip located at the joint-beam interface is used to represent the fixed-end bond-slip rotation, as shown in Figure 6.9 & Figure 6.10. Another acceptable approach is the one proposed by Park & Mosalam (2009) and Hassan (2011), among others, for the purpose of simplifying the joint model calculations. In this approach, the slip induced deformations and the joint shear deformations are combined in one single spring. Hassan (2011), however, investigated both the first and the second approaches and found no significant difference between the two. Alternatively, slip deformations can be indirectly accounted for by reducing the flexural stiffness of beam and columns which allows for achieving higher drifts, as recommended by ASCE/SEI 41 (2006).

Many researchers, such as Sezen (2000), proposed calculating the slip rotation based on the assumption that the beam cross-section rotates about the neutral axis, (see Figure 6.15). Consequently, the slip induced rotation θ_{sp} , according to Eq (6.8), can be calculated by dividing the total slip of the beam bars at the joint interface by the beam effective depth, d_b minus the compression zone depth, c .

$$\theta_{sp} = \frac{slip}{d_b - c} \quad (6.8)$$

where c can be estimated from beam section analysis.

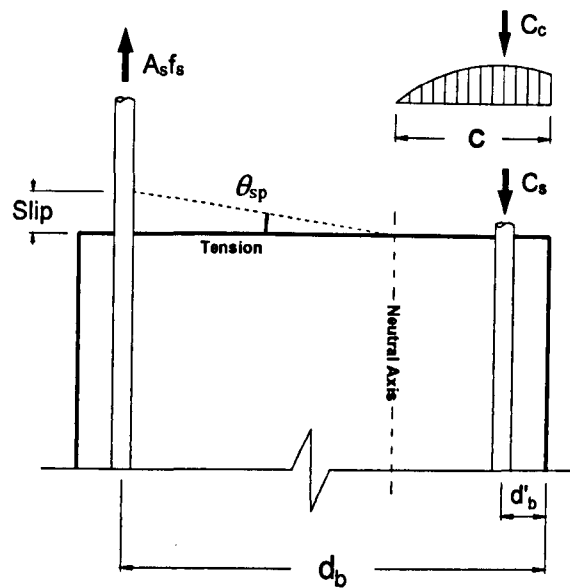


Figure 6.15 Calculations of slip induced rotation at a cross-section

Previous computer-based joint models utilised different bond-slip model to calculate slip of beam bars at the joint interface. The bond-slip models proposed by Lehman & Moehle (1998) and the model proposed by Sezen (2000) were widely used and showed good correlations with experimental results. Both models adopt comparable bond stress values and propose similar formulations.

In this research, slip is calculated using the bond-slip model formulations of Sezen (2000). According to the model, slip can be calculated by integrating the bar strains from where bar bond-slip initiates to the joint-beam interface. In addition, the model assumes a uniform distribution of bond stress within the joint

The moment-rotation envelope of the slip spring is taken as a bi-linear curve, in which the moment value at the end of the first segment is calculated as the beam yielding moment, unless the moment is less due to lack of anchorage. Figure 6.16 shows an application of the adopted bond-slip model on an exterior beam-column joint for slip calculation in the proposed DRAIN-2DX model. As can be seen from the figure, in this case the required bar length, l_s to develop the demand stress f_s is less than the available anchorage length, l_{am} .

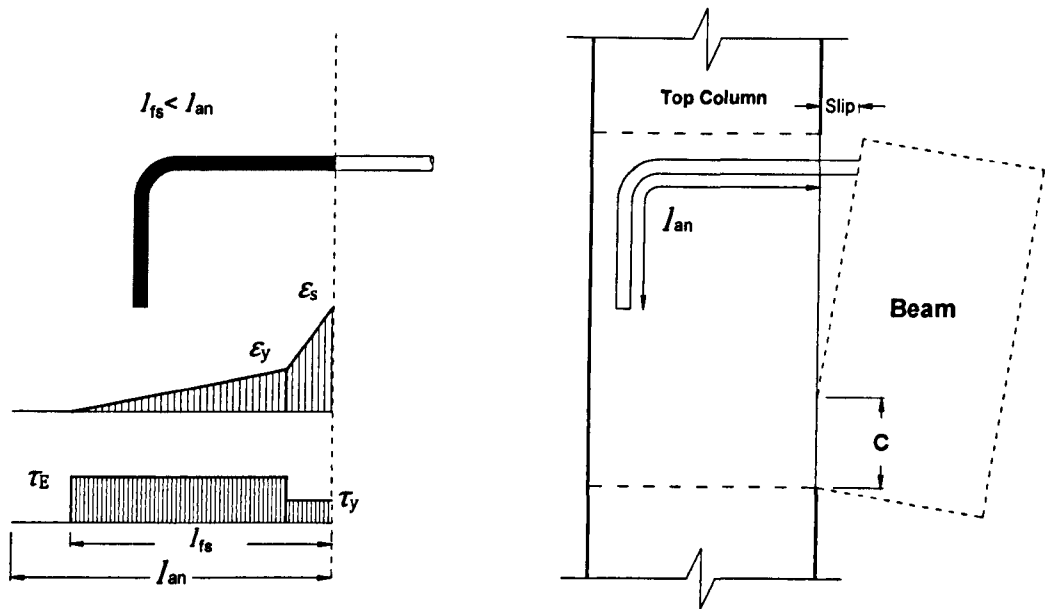


Figure 6.16 Application of the adopted Sezen model on exterior joints

6.4.4 Simulation Results and Comparisons

In this section, the accuracy and the validity of the proposed DRAIN-2DX joint model is demonstrated by applying the joint model to a number of the exterior joints included in Table 5-1. The model input values for each specimen were calculated based on the actual material properties and geometry of the tested specimen. Cyclic analysis was performed using a quasi-static displacement history similar to the actual displacement history used during the test.

6.4.4.1 Rigid Joint Model

Cyclic analysis using the conventional centreline rigid joint idealization was performed on joint specimens JC-1 and JC-2. This is a widely used idealisation in structural modelling. Figure 6.17 and Figure 6.18 show the analytical results of specimens JC-1 and JC-2 with no joint model (rigid joint) in comparison to the actual measured response. It is evident, from these two figures, that assuming a rigid connection between beam and columns produces rather unrealistic results. As detailed in Chapter 4, specimens JC-1 and JC-2 suffered *J-Type* failure without any reinforcement yielding, whereas the analytical response, with the rigid connection assumption, clearly overestimates the initial stiffness and the joint maximum strength. In general, it can be concluded that the overall predicted response is dominated by beam flexural capacity.

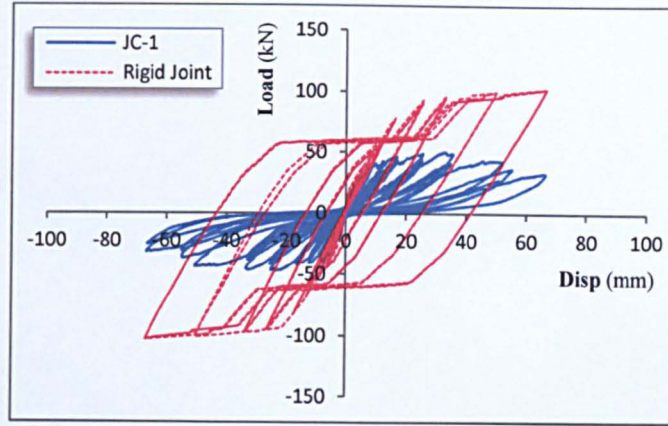


Figure 6.17 Comparison of rigid joint model response with measured response of specimen JC-1

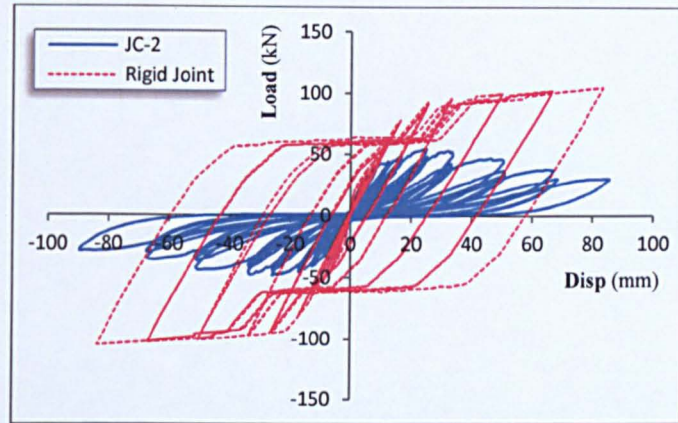


Figure 6.18 Comparison of rigid joint model response with measured response of specimen JC-2

6.4.4.2 Proposed Joint Model

6.4.4.2.1 Current Research Specimens

Figure 6.19 through Figure 6.24 show comparisons between the experimental load-displacement responses and the analytical responses of Group A, B, and C specimens using the proposed panel zone joint model. It is evident that the model predicted with good accuracy the joint strength capacity and the initial stiffness in both directions. In some cases, such as JA-3 and JC-2 the maximum joint strength in the positive loading direction is slightly higher than the measured values. This can be attributed to the shear stress-strain envelope used as input values for the joint shear hinge. These values, which were predicted using the procedure outlined in section 6.2, were higher than the actual values in both directions. Moreover, the model managed to represent the overall stiffness and strength degradation with good accuracy, except at 5% drift where the predicted response is slightly higher. This can be attributed to the limitation of the strength degradation factor of DRAIN-2DX Element 10, as using small values cause convergence problems.

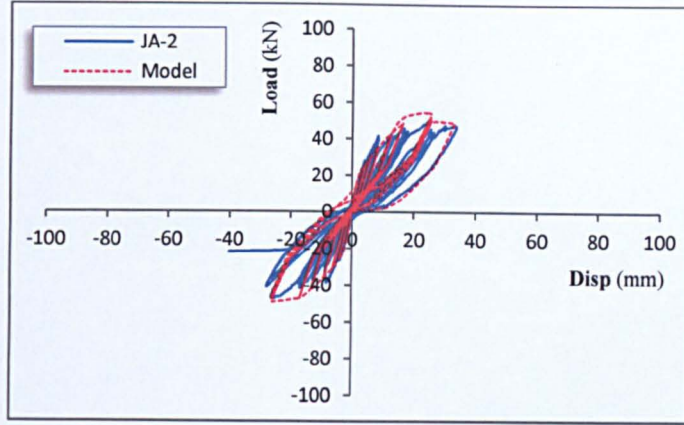


Figure 6.19 Simulation results of Joint specimen JA-2

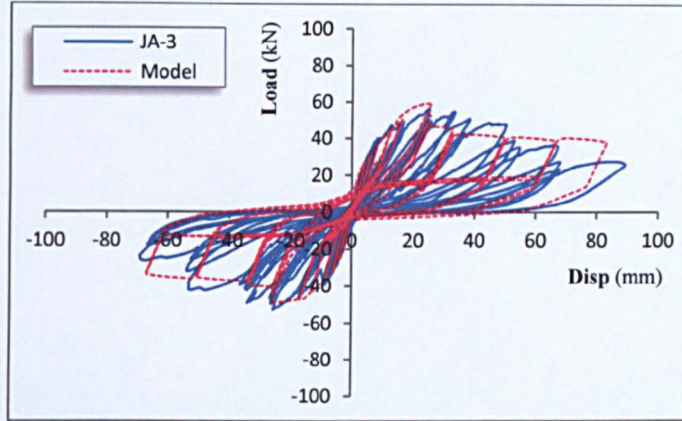


Figure 6.20 Simulation results of Joint specimen JA-3

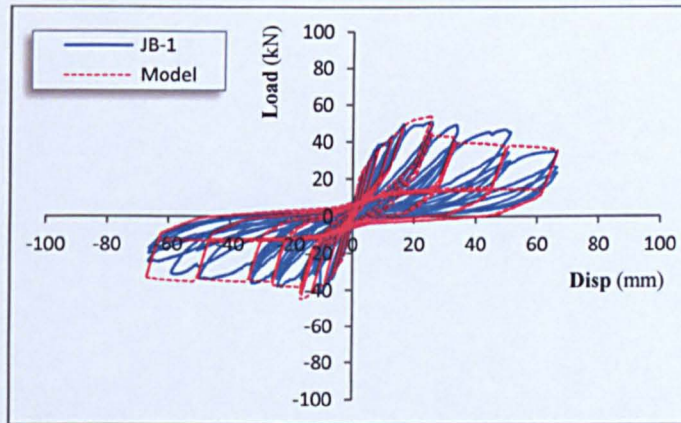


Figure 6.21 Simulation results of Joint specimen JB-1

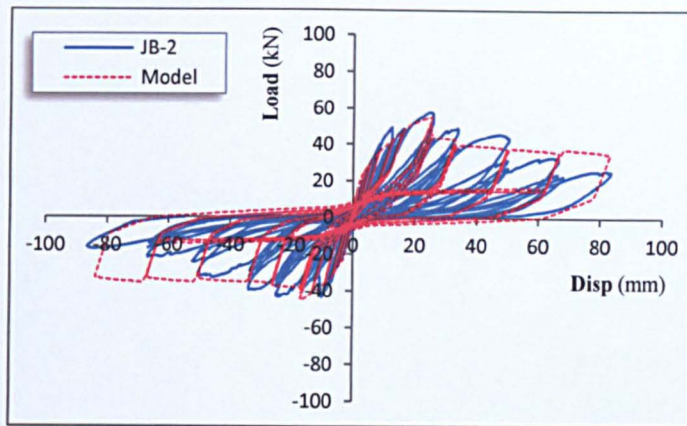


Figure 6.22 Simulation results of Joint specimen JB-2

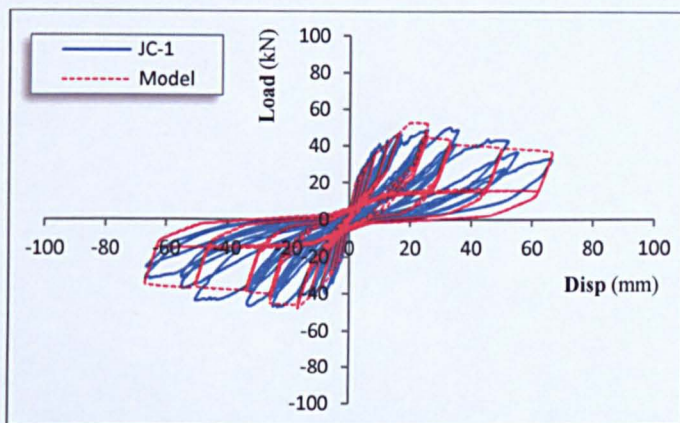


Figure 6.23 Simulation results of Joint specimen JC-1

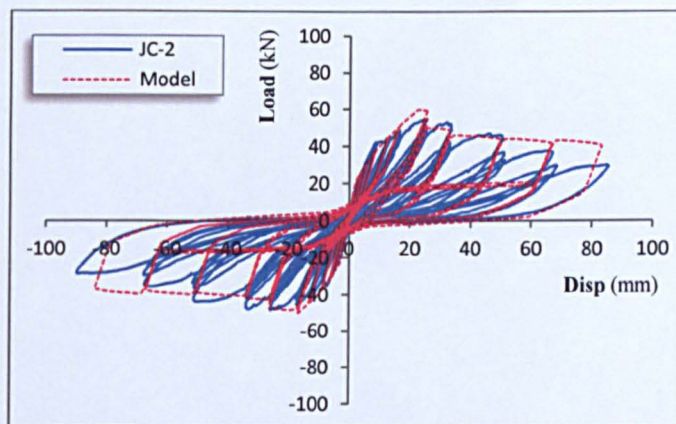


Figure 6.24 Simulation results of Joint specimen JC-2

6.4.4.2.2 Other Specimens

To further validate the model and explore its accuracy, simulations of four other specimens were performed using the proposed model. Figure 6.25 and Figure 6.26 show comparisons between the experimental and the analytical responses of specimens BS-U and BS-L by Wong (2005). As can be seen from the figures, the model predicted with good accuracy the joint strength capacity and the initial stiffness in both directions. Additionally, the model managed to represent the overall stiffness and strength degradation with good accuracy. In general, it can be

concluded that the analytical response agrees rather well with the overall measured response and type of failure.

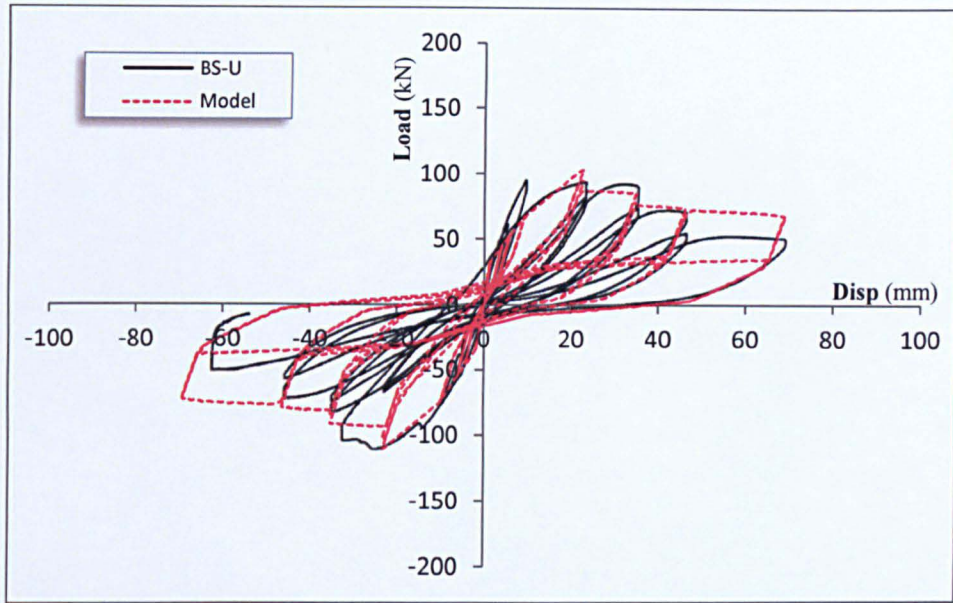


Figure 6.25 Prediction of Wong (2005) specimen BS-U

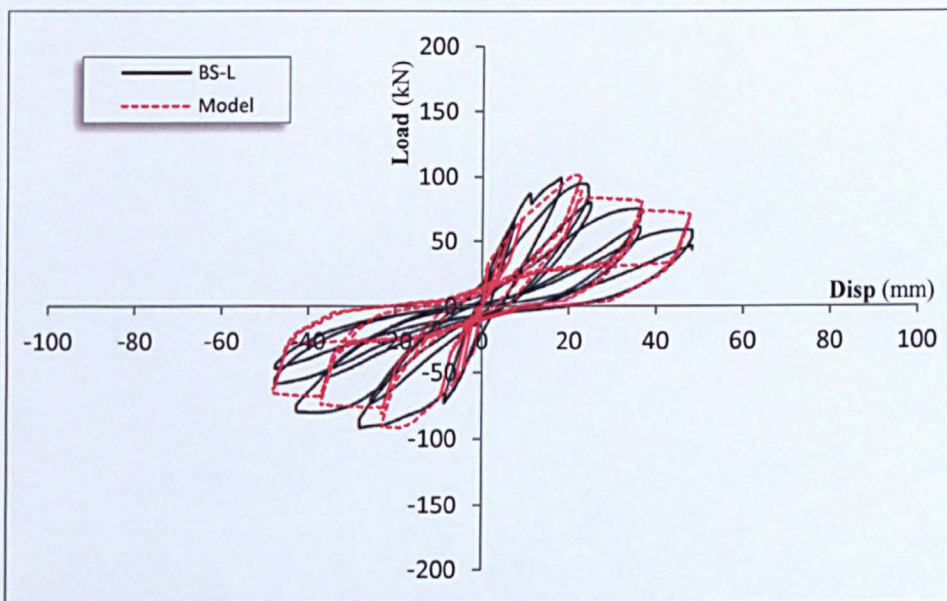


Figure 6.26 Prediction of Wong (2005) specimen BS-L

Figure 6.27 and Figure 6.28 show comparisons between the experimental and the analytical responses of specimens #2 and #4 by Clyde et al. (2000). It is evident from the figures that the model predicted with good accuracy the joint strength capacity in both directions. Additionally, the predicted initial stiffness agrees well in the positive direction but slightly softer in the other. Moreover, the model managed to represent the overall stiffness and strength degradation with reasonable accuracy.

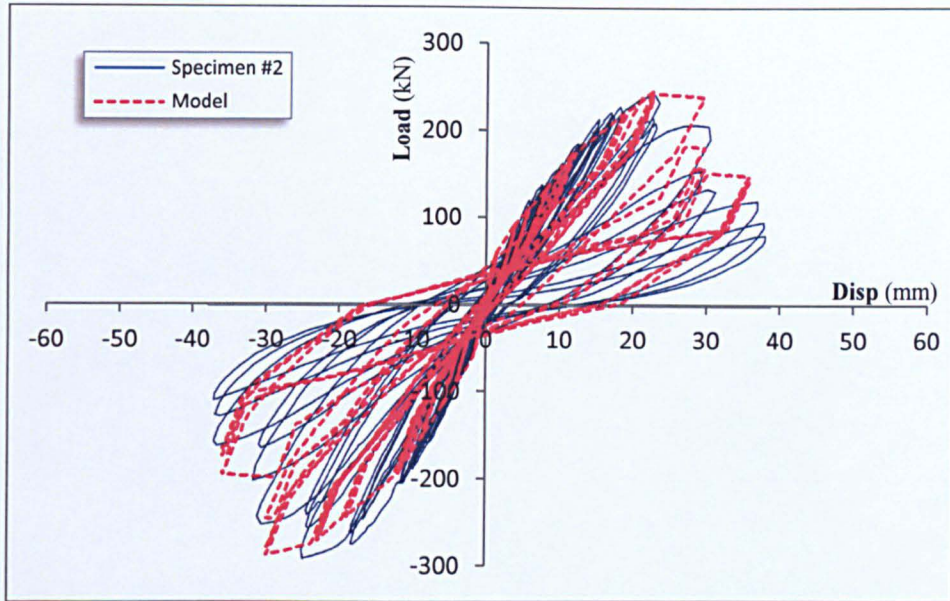


Figure 6.27 Prediction of Clyde et al. (2000) specimen #2

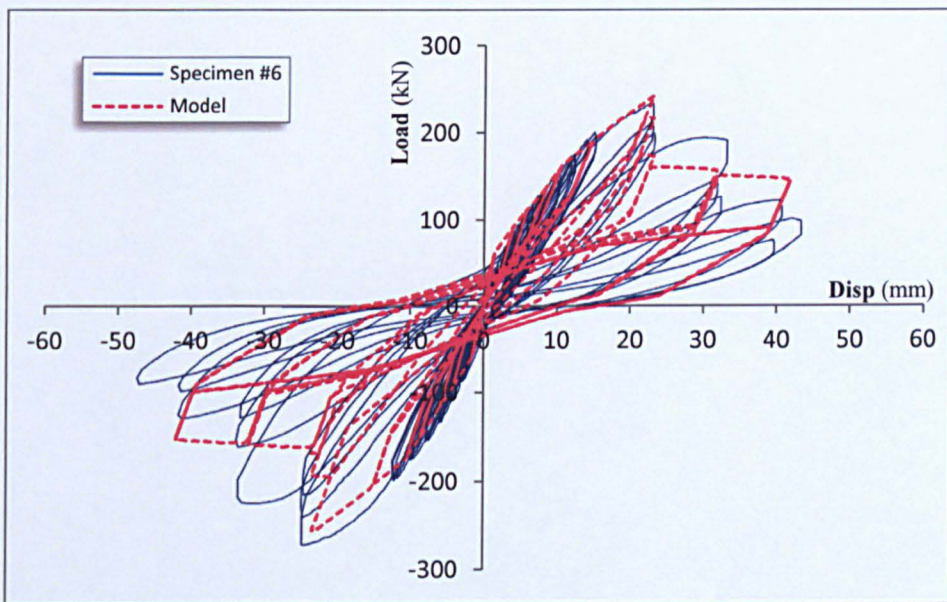


Figure 6.28 Prediction of Clyde et al. (2000) specimen #6

6.5 RECAP AND CONCLUSIONS

The following summarises the work and the key findings of this chapter:

- 1- The Krawinkler (2001) joint panel zone representation has been used in many proposed models. The main advantage of this model, in comparison to the scissors model, is that it represents the deformation of the joint panel and allows for relative displacement between the top and bottom columns.

- 2- After extensive testing using DRAIN-2DX, it was found that the difference between the Krawinkler joint panel representation and the scissors model has no significant impact on the overall structural response (BSSC, 2012).
- 3- Based on the shear behaviour of unconfined exterior beam-column joints exhibiting *J-Type* and *BJ-Type* failures, a quad-linear shear stress-strain envelope curve was proposed. The model is intended for nonlinear simulations of Frame structures. The peak shear stress is defined based on the proposed joint strength model, presented in Chapter 5. The model was calibrated using the results of the current research in addition to results reported by other researchers.
- 4- A new panel-zone joint model for representing the nonlinear behaviour of deficient exterior beam-column joint is proposed. The model is based on the Krawinkler panel zone joint model, in which the joint panel is represented by four rigid links and a rotational spring. The model is implemented in DRAIN-2DX software. The model demonstrated the weakness of utilizing the conventional centreline rigid joint modelling concept in cyclic analysis.
- 5- The proposed joint model showed good correlations between the measured and the predicted joint response, in terms of initial stiffness, peak joint shear strength, and stiffness degradation.

CHAPTER 7

CONCLUSIONS AND FUTURE RECOMMENDATIONS

The following presents a summary and the concluding remarks of each section of the work conducted for this research.

7.1 LITERATURE REVIEW AND CURRENT KNOWLEDGE

Based on the reviewed literature on the seismic performance of deficient exterior RC beam-column joints presented in chapter 2 the following conclusions can be drawn:

- 1- Buildings constructed prior to 1980 especially in developing countries are highly vulnerable to joint shear failure under seismic excitations. Failure of joints can lead to partial or total building collapse. The seismically deficient reinforcement details of exterior beam-column joints of older existing building vary based on the adopted design guidelines, but the most common type of deficiency found in the majority of these joints is the lack of shear reinforcement within the joint area.
- 2- The current seismic and retrofitting codes are mostly over-conservative and lack the transparency required to allow the designer to fully understand and control the evaluation process. There is an urgent need to develop rational yet transparent procedures that are capable of accurately simulating the real behaviour of deficient beam-column joints and their effect on the global response during seismic events.
- 3- It is assumed in deficient exterior joints and due to the lack of shear reinforcement that the only effective shear resisting mechanism is the diagonal compressive strut that forms within the core between the beam and column compression zones. The strut concrete strength and in turn the joint shear strength is a function of the stress and strain state within the joint panel. Concrete compressive strength within the joint panel is reduced due to the effect of the principal tensile strains that cause tensile cracks parallel to the axis of compressive loading. In addition, cyclic loading causes extra detrimental

reduction to the concrete strength due to the continuous opening and closing of joint shear cracks.

- 4- Several types of failure mechanisms can be defined for deficient joints typical of older RC buildings: i) joint shear failure without reinforcement yielding (*J-Type*) ii) shear failure shortly after reinforcement yielding (*BJ-Type*) iii) failure due to bar pull-out (*P-Type*). Other failure types are identified but are less common.
- 5- The most influential parameters that affect the seismic behaviour of deficient exterior beam-column joints include: concrete compressive strength, joint panel geometry, beam reinforcement ratio, and column axial load. Key parameter in terms of joint shear stress and strain is the concrete strength and the square root of the concrete compressive strength is found to be proportional to the joint shear stress.
- 6- Higher joint aspect ratio (h_b/h_c), reduces strength. The adverse effect is slightly clearer for *J-Type* failure exterior deficient joints in comparison to *BJ-Type* failure joints. This relationship is dependent on other parameters such as axial load and beam reinforcement.
- 7- Joint shear strength is also dependent on the amount of beam reinforcement and increases linearly with beam reinforcement ratio, for deficient exterior joints of joint aspect ratio between 0.89 and 1.33.
- 8- The relationship between the column axial load and the joint shear strength of deficient exterior joints is mostly unclear. For joints where the column axial load is less than $0.2f'_cA_g$, the influence is believed to be insignificant. Whereas, the effect is assumed to be mostly beneficial up to the point of joint shear strength, in terms of strength and stiffness, and detrimental afterwards for joints with a column axial load level higher than $0.2f'_cA_g$.
- 9- Many past experimental studies focused on improving the behaviour and deformability of well-confined beam-column joints under seismic excitations. On the other hand, only a limited number of these studies focused on the behaviour of deficient exterior joints, mostly focusing on developing strengthening techniques.

7.2 EXPERIMENTAL PROGRAMME

Seven full-scale isolated exterior beam-column joints were tested under quasi-static cyclic loading for the purpose of studying the effects of different types of beam anchorages and low column axial loads on the seismic shear performance of exterior joints with no shear reinforcement. Three types of beam bar anchorages were used. Type A and type B had straight

anchorage for beam bottom bars and 90° hooks for the top bars, whereas 90° hooks was used for both top and bottom bars in Type C.

Based on the observed damage and hysteretic behaviour of the tested specimens of the current research presented in Chapter 4 the following conclusions can be drawn:

- 1- All seven specimens, and despite the differences in reinforcement details within the joint, exhibited shear failure with no prior reinforcement yielding (*J-Type failure*). This was confirmed by strain measurements.
- 2- In joints of type A, the maximum sustained strength when the hooks are in tension (denoted positive loading in this research) is approximately 8% higher than the other loading direction (i.e. beam bottom bars are in tension). The strength ratio between the two loading directions is 34% for Joints type B, and 14% for joints type C.
- 3- In terms of stiffness degradation, all specimens exhibited similar behaviour. Stiffness degradation continued throughout the test, however, most of the degradation occurred during the initial cycles up to 1.0% drift level. By the end of the 2% drift cycles, approximately 80% of the peak-to-peak stiffness at 0.25% drift was lost.
- 4- The ASCE 41 (2006) shear provisions (code) managed to predict the shear strength of one specimen (JA-2) with good accuracy ($\pm 4\%$). On the other hand, ASCE 41 overestimated by up to 15% and underestimated by up to 21% the rest of the specimens. This is because the joint shear strength coefficient proposed in ASCE 41 for isolated exterior joints or exterior joints with one transverse beam is the same value [$0.5 \sqrt{MPa}$], regardless of the beam reinforcement ratio, the type of beam reinforcement anchorage and column axial load ratio
- 5- The proposed ASCE 41 shear stress-strain envelope for non-linear modelling was found to be unrealistic and does not represent the measured shear behaviour (i.e. shear envelope) of the tested specimen, especially in terms of initial stiffness, peak strength, and strength degradation.
- 6- The peak-to-peak normalised shear modulus degradation, for all specimens, was rather steep during the first cycles up to 1% drift level. By the end of the first cycle at 2% drift, approximately 98% of the initial shear stiffness was lost.
- 7- The ratio of joint shear deformation to the overall beam tip displacement, Δ_j/Δ_b , kept increasing throughout the test, even beyond the point of peak shear strength. All specimens exhibited similar behaviour; the ratio was around 34% at joint shear strength and around 56% at 50% of the maximum strength. Strain measurements of beam bars

- confirmed that joint deterioration was due to shear deformation of the panel zone, as no bar pull-out occurred.
- 8- The relationship between low column axial load levels (lower than $0.2f'_cA_g$) and joint strength was found to be beneficial, for deficient exterior joints exhibiting *J-Type* failure. Increasing the column axial load from 0.07 to $0.12f'_cA_g$, enhanced the strength of group type A, B and C specimens by 11%, 15%, and 10%, respectively.
 - 9- For deficient exterior joints with similar geometry but different detailing (Type A, B or C anchorage) and exhibiting *J-Type* failure, increasing the column axial load slightly increases the stiffness in the pre-peak range, whereas the effect on the post-peak stiffness is reversed (rapid deterioration). This is for column axial load levels within the tested ratios (i.e. lower than $0.15f'_cA_g$).
 - 10- The achieved joint strength was found to be affected by the type of beam reinforcement details within the joint. The enhancement due to the type of anchorage details can be up to 34%, provided that the joint panel geometry and the column axial load are kept unchanged.
 - 11- For deficient exterior beam-column joints exhibiting *J-Type* failure, when the hook is in tension, changing the length of the vertical part of the hook within the joint has practically no significant effect on the overall joint strength. This is because the imposed demand on the hook from the adjacent beam is not enough to cause anchorage failure of the hook.
 - 12- Using 90° hooks for beam bottom bars can lead to enhancing the shear strength for the case of deficient exterior beam-column joints exhibiting *J-Type* failure, when beam bottom bars are in tension. This means that the presence of a bottom hook can enhance the capacity of the diagonal compressive strut due to the better anchoring of beam bars which in turn leads to a higher strength.
 - 13- Elongated hooks when used with straight anchorage for beam bottom bars can have a detrimental effect on the joint shear strength. This is true for the case of deficient exterior beam-column joints exhibiting *J-Type* failure, when beam bottom bars are in tension. The only explanation for this negative effect is that when the hooked bar is compressed, the end of the hook pushes the cover out which weakens the concrete compressive strut and in turn the joint strength.
 - 14- The overall joint shear strength of deficient exterior joint with *J-Type* failure is dependent on the combination between the anchorage detail and the axial load level.

However, more tests with a broader range of axial load levels are required to quantify the effect of each different anchorage detail.

7.3 SHEAR STRENGTH MODELS FOR DEFICIENT EXTERIOR JOINTS

Based on the reviewed literature on exterior joint shear strength models presented in Chapter 2, and based on the evaluation, presented in Chapter 5, of some of these models that can be applied to deficient exterior joints against a database of 24 exterior beam-column joints the following conclusions can be drawn:

- 1- Until recently, there were only joint shear strength models for well-confined exterior and interior, but mostly interior, beam column joints. The common problem found is that the shear strength and failure mechanisms are predicted based on constitutive models developed specifically for well-confined joints such as the MCFT.
- 2- The few, recently proposed, joint strength models for deficient exterior joints assume proper beam reinforcement embedment length within the joint area (i.e. standard hook). The cases between very short anchorage and full standard hook have not been explored yet.
- 3- The joint strength model by Hwang and Lee (1999) is not suitable for the strength prediction of deficient exterior beam-column joints. The model's poor ability to predict the shear strength of joints with no shear reinforcement in comparison to confined ones is attributed to the omission of the beam contribution to the diagonal strut width. Another reason is the proposed initial condition that both the intermediate column reinforcement and beam bars have yielded when the joint reaches its maximum strength. Using the joint database of this research the overall mean of the $\gamma_{test}/\gamma_{model}$ ratio is (1.16) and the coefficient of variation for the same ratio is COV=0.20%.
- 4- The simplified joint strength model by Vollum and Newman (1999) was developed for estimating the joint shear strength of both confined and unconfined exterior joints taking into account the effects of beam anchorage detail and joint aspect ratio. The model was evaluated by using the joints included in the database of this research. The overall mean of the $\gamma_{test}/\gamma_{model}$ ratio is (0.85) and the coefficient of variation for the same ratio is COV=0.23%. The model generally overestimates the joint shear strength of unconfined exterior joints included in this research database. This can be attributed to the limitations of the beam anchorage factor β , and the exclusion of the effect of column axial load for the case of unconfined joints (see Chapter 2&5).
- 5- The joint strength model by Tsonos (2007) does not produce reliable results when used for deficient exterior beam-column joints. This is because the lack of shear links is not

accounted for in the model formulations. Based on the deficient exterior joint database of this research, the calculated mean and coefficient of variation for the $\gamma_{\text{test}}/\gamma_{\text{model}}$ ratio are, MEAN =0.64 and COV=0.36%.

- 6- The strength model proposed by Park & Mosalam (2009; 2012a) was developed for estimating the joint shear strength of unconfined exterior joints with at least one hook. Based on the deficient exterior joint database of this research, the calculated mean and coefficient of variation for the $\gamma_{\text{test}}/\gamma_{\text{model}}$ ratio are, MEAN =0.90 and COV=0.22%. The model generally overestimated the joint shear strength of the included deficient exterior joints. This can be attributed to the proposed fixed width of the second strut of $0.65h_c$ regardless of the calculated column compression zone. This approximation, in addition to fixing the beam internal moment lever arm, can cause the model to overestimate the stress in the beam longitudinal reinforcement.
- 7- The joint strength model by Hassan (2011) was developed for estimating the joint shear strength of unconfined exterior joints but with standard hooks. Using the model on the joint database of this research, the mean and coefficient of variation for the $\gamma_{\text{test}}/\gamma_{\text{model}}$ ratio are, MEAN =0.85 and COV=0.15%. The model in general is unconservative. This is because the model assumes that in all *J-Type* failure joints, the beam remains within the elastic range. This leads to the overestimation of the diagonal strut width especially for cases where beams are close to yielding.
- 8- An analytical model that predicts the shear strength of exterior deficient beam-column joints in both loading directions is developed. The model predicts the maximum shear strength using a modified version of the ACI strut-and-tie model approach. In the proposed model, the horizontal joint shear, V_{jh} is resisted by an extended diagonal compressive strut. The developed tie and in turn the extended strut, in the proposed model, are highly influenced by the shape and length of the beam longitudinal anchorage and the column axial load level. The model predicted with good accuracy the shear strength of the deficient exterior beam-column joints included in the research joint database. The average test to predicted shear strength ratio, $\gamma_{\text{test}}/\gamma_{\text{model}}$ is 1.01 and the coefficient of variation for the same ratio is 0.06%.

7.4 JOINT MODELS FOR FE FRAME ANALYSIS

Based on the reviewed literature, presented in Chapter 2, on computer based joint models for FE frame simulations which might be applicable for shear-critical deficient exterior joints, and the proposed panel zone spring-based exterior joint model the following conclusions can be drawn:

- 1- Accurate simulations of RC frames under lateral load excitations have always posed a great challenge for structural engineers due to the complex behaviour of beam-column joints. Many attempts were made to account for joint shear deformations and beam bar-slip induced rotation in RC FE frame simulations using simple spring elements. These attempts ranged in their complexity from one spring element to models consisting of several springs with rigid links
- 2- Based on an analytical study by Celik & Ellingwood (2008), it was found that modelling the panel zone as a rigid zone yields inaccurate results in terms of strength and stiffness. They also concluded that, when adopting an accurately calibrated shear stress-strain constitutive model, a simple representation for the joint panel zone using scissors type rigid links and a rotational spring can produce sufficiently accurate results in comparison to the predictions of a more sophisticated model (i.e. super-element panel zone joint mode).
- 3- The Krawinkler (2001) joint panel zone representation has been used in many proposed models. The main advantage of this model, in comparison to the scissors model, is that it represents the deformation of the joint panel and allows for relative displacement between the top and bottom columns. After extensive testing using DRAIN-2DX, it was found that the difference between the Krawinkler joint panel representation and the scissors model has no significant impact on the overall structural response (BSSC, 2012).
- 4- Based on the shear behaviour of unconfined exterior beam-column joints exhibiting *J-Type* and *BJ-Type* failures, a quad-linear shear stress-strain envelope curve is proposed. The model is intended for nonlinear simulations of frame structures. The peak shear stress point of the shear constitutive model is defined based on the proposed joint strength model. The remaining points of the constitutive model are defined based on a calibration procedure that involves the results of the current research in addition to results reported by other researchers.
- 5- A new panel-zone joint model for representing the nonlinear behaviour of deficient exterior beam-column joint is proposed. The model is based on the Krawinkler panel zone joint model, in which the joint panel is represented by four rigid links and a rotational spring. The model is implemented in DRAIN-2DX software. The model demonstrated the weakness of utilizing the conventional centreline rigid joint modelling concept in cyclic analysis. The proposed joint model showed good correlations between the measured and the predicted joint response, in terms of initial stiffness, peak joint shear strength, and stiffness degradation.

7.5 RECOMMENDATIONS FOR FUTURE WORK

Based on the work conducted in this research the following can be recommended for future work:

- 1- Investigate and better quantify the effect of low column axial load levels on the shear performance of deficient exterior beam-column joints by testing several levels lower than $0.2f_c A_g$ and different beam detailing.
- 2- Experimentally investigate and quantify the effect of intermediate column reinforcement on the shear performance of deficient exterior beam-column joints by testing several specimens with different ratios of this reinforcement.
- 3- Investigate the effect of low strength concrete typical of developing countries on the seismic behaviour and shear deformations of deficient exterior beam-column joints.
- 4- Study and confirm the negative effect of the elongated hook in joints type B through testing several joints with different aspect ratios and axial load levels
- 5- Extend the joint shear strength model to other types of beam anchorages such as exterior joints with 180 hooks.
- 6- The developed shear strength model is mainly for exterior joints exhibiting *J-Type* failure. Therefore, include more test results of exterior beam-column joints failing in shear after beam reinforcement yielding (*BJ-Type failure*).
- 7- Extend the shear strength model proposed in this research to deficient interior and knee beam-column joints.
- 8- Improve and further validate the proposed joint shear strength model by addressing/completing the following tasks:
 - a. Evaluate experimentally the available bond-slip model (or develop a new one) for the representation of beam hooks and straight bars within the joint.
 - b. Investigate experimentally the proposed limit for the column compression zone depth and variation with column axial load.
 - c. Investigate adjusting the angle of inclination by taking into account the extended strut width.
 - d. Evaluate experimentally the proposed method for calculating the contribution of the bend and the vertical part of hooks.

-
- e. Evaluate the adopted softening factor as opposed to other concrete softening models.
 - 9- Use the proposed joint panel zone model to simulate the seismic response of an older multi -storey frame building.
 - 10- Simulate the seismic response of deficient buildings tested on a shaking table using the proposed joint panel zone model.
 - 11- Implement the panel zone joint model in DRAIN-2DX software and develop a rotational spring element with a degrading hysteresis rule.
 - 12- Compare the simulated response using the proposed joint shear strength model and the panel zone joint model with the simulated response of commercial software and point out the drawbacks and the advantages to each in order to achieve better and simple analytical solutions.

REFERENCES

- ACI 318-02, 2002. *Building Code Requirements for Structural Concrete (ACI 318-02) and Commentary(318R-02)*. Farmington Hills, Mich: American Concrete Institute.
- ACI 318-08, 2008. *Building Code Requirements for Structural Concrete (ACI 318M-08)*. Framington Hills (MI): American Concrete Institute.
- ACI 318-11, 2011. *Building Code Requirements for Structural Concrete (ACI 318-11) and Commentary*. Framington Hills (MI): American Concrete Institute.
- ACI 318-95, 1995. *Building Code Requirements for Structural Concrete (ACI 318-1995) and Commentary(318R-95)*. Farmington Hills, Mich: American Concrete Institute.
- ACI 352R-02, 2002. *Recommendations for Design of Beam-Column Connections in Monolithic Reinforced Concrete Structures (ACI 352R-02)*. Framington Hills (MI): American Concrete Institute.
- ACI 369R, 2011. *Guide for Seismic Rehabilitation of Existing Concrete Frame Buildings and Commentary*. Framington Hills (MI): American Concrete Institute.
- Ahmad, S., 2011. *Seismic Vulnerability of Non-Ductile Reinforced Concrete Structures in Developing Countries*. PhD Thesis. Sheffield, UK: The University of Sheffield.
- Alath, S. & Kunnath, S., 1995. Modeling inelastic shear deformation in RC beam-column joints. In *Proc. Tenth conference on Engineering Mechanics*. Boulder, Colorado, 1995. University of Colorado at Boulder, pp. 822-825.
- Alire, D.A., 2002. *Seismic Evaluation of Existing Unconfined RC Beam-Column Joints*. MSc Thesis. University of Washington.
- Anderson, M., Lehman, D. & Stanton, J., 2008. A cyclic shear stress-strain model for joints without transverse reinforcement. *Engineering Structures*, 30(4), p.941-954.
- Anderson, J. & Townsend, W.H., 1977. Models for RC frames with degrading stiffness. *Journal of the Structural Division, ASCE*, 103(ST12), p.2361-2376.
- Antonopoulos, C.P. & Triantafillou, T.C., 2003. Experimental Investigation of FRP Strengthened RC Beam-Column Joints. *ACSE Journal of Composites for Construction*, 7(1), pp.39-49.
- ASCE/SEI 41, 2006. *Seismic Rehabilitation of Existing Buildings*. Design Code. Reston, Virginia: American Society of Civil Engineers.

- Bakir, P.G. & Boduroğlu, H.M., 2002. A new design equation for predicting the joint shear strength of monotonically loaded exterior beam-column joints. *Engineering Structures*, 24, pp.1105-17.
- Barnes, M., Jiogural, S., Park, S. & Moehle, J.P., 2008. *Evaluation of Exterior Non-Ductile Reinforced Concrete Building Joints Experiencing Early Column Failure*. PEER/NEES-REU Research Report, August 2008. Berkeley, California: Pacific Earthquake Engineering Research Center University of California, Berkeley.
- Bedirhanoglu, I., Ilki, A., Pujol, S. & Kumbasar, N., 2010. Behavior of Deficient Joints with Plain Bars and Low-Strength Concrete. *ACI STRUCTURAL JOURNAL*, May-June 2010, pp.300-10.
- Belarbi, A. & Hsu, T.C., 1995. Constitutive laws of softened concrete in biaxial tension-compression. *ACI Structural Journal*, 92(S54), p.562-573.
- Beres, A., White, R.N. & Gergely, P., 1992. *Seismic Performance of Interior and Exterior Beam-to-Column Joints Related to Lightly RC Frame Buildings: Detailed Experimental Results*. Structural Engineering Report 92-7, November 1992. Ithaca, New York: School of Civil and Environmental Engineering, Cornell University.
- Biddah, A. & Ghobarah, A., 1999. Modelling of shear deformation and bond. *Journal of Structural Engineering and Mechanics*, 7(4), pp.413-32.
- BS EN 12390-3, 2009. *Testing hardened concrete - Part3: compressive strength of test specimens*. British Standard.
- BS EN 12390-6, 2000. *Testing hardened concrete - Part 6: Tensile splitting strength of test specimens*. BRITISH STANDARD.
- BSI EC2, 1992. *Eurocode 2: Design of concrete structures - Part 1-1: General rules and rules for buildings (BS EN 1992-1-1)*. Design code. London: Milton Keynes British Standards institution.
- BSI EC2, 2004. *Eurocode 2: Design of concrete structures - Part 1-1: General rules and rules for buildings (BS EN 1992-1-1)*. Design code. London: British Standards institution.
- BSI EC8, 2004. *Eurocode 8: Design of structures for earthquake resistance — Part 1: General rules, seismic actions and rules for buildings (BS EN 1998-1)*. Design Code. London: British Standards institution.
- BSSC, 2012. *FEMA 451B Topic 15-5a Notes, Advanced Analysis: Instructional Material Complementing FEMA 451, Design Examples*. [Online] Available at:

<http://bssc.nibs.org/client/assets/files/bssc/Topic15-5a-AdvancedAnalysisPart1Notes.pdf>

[Accessed 20 December 2012].

CEB-fib MC10, 2010. *fib Bulletin 55: Model Code 2010, First complete draft: Volume 1*. Lausanne, Switzerland: The International Federation for Structural Concrete (fib).

CEB-fip BN 231, 1996. *fib Bulletin No. 231: RC Frames under Earthquake Loading- state of the art report*. Lausanne, Switzerland: (printed revised hardbound edition of Bulletin 220), Thomas Telford, London, Chapter3, pp. 138-165. The International Federation for Structural Concrete (fib).

Celik, O.C. & Ellingwood, B.R., 2008. Modeling Beam-Column Joints in Fragility Assessment of Gravity Load Designed Reinforced Concrete Frames. *Journal of Earthquake Engineering*, 12(3), pp.357-81.

Chaudat, T. et al., 2005. *Seismic Tests on a Reinforced Concrete Bare Frame with FRP retrofitting-Tests Report*. Ecoleleader project No 2.

Chung, Y.S., Meyer, C. & Shinozuka, M., 1987. *Seismic damage assessment of reinforced concrete members*. Technical Report NCEER-87-0022, State University of New-York at Buffalo.

Clyde, C., Pantelides, C.P. & Reaveley, L.D., 2000. *Performance-based evaluation of exterior reinforced concrete building joints for seismic excitation*. PEER Report July 2000. Pacific Earthquake Engineering Research Center.

Collins, M.P. & Mitchell, D., 1991. *Prestressed Concrete Structures*. Prentice-Hall, Englewood Cliffs.

D'Ayala, D. & Charleson, A., 2002. Review of seismic strengthening guidelines for RC Buildings in developing countries. In *12th European Conference on Earthquake Engineering*, 2002.

EERI, 1999a. *EERI Special Earthquake Report – September 1999. The Tehuacan, Mexico, Earthquake of June 15, 1999*. [Online] Available at: <http://www.eeri.org/earthquakes/earthquakes.html>.

EERI, 1999b. *EERI Special Earthquake Report – November 1999. The Athens, Greece Earthquake of September 7, 1999*. [Online] Available at: <http://www.eeri.org/earthquakes/earthquakes.html>.

- EERI, 1999c. *EERI Special Earthquake Report – December 1999. The Chi-Chi, Taiwan Earthquake of September 21, 1999.* [Online] Available at: <http://www.eeri.org/earthquakes/earthquakes.html>.
- Eligenhausen, R., Popov, E.P. & Bertero, V.V., 1983. *Local bond stress-slip relationships of deformed bars under generalized excitations.* Rep. No. 83/23. California: Earthquake Engineering Research Council (EERC) University of California, Berkeley.
- El-Metwally, S.E. & Chen, W.F., 1988. Moment-rotation modeling of reinforced concrete beam-column connections. *ACI Structural Journal*, 85(S36), pp.384-94.
- Engindeniz, M., 2008. *REPAIR AND STRENGTHENING OF PRE-1970 REINFORCED CONCRETE CORNER BEAM-COLUMN JOINTS USING CFRP COMPOSITES.* PhD Thesis. Atlanta: Georgia Institute of Technology.
- Favvata, M.J., Izzuddin, B.A. & Karayannis, C.G., 2008. Modelling exterior beam-column joints for seismic analysis of RC frame structures. *Earthquake Engineering and Structural Dynamics*, 37(13), pp.1527-48.
- FEMA 273, 1997. *NEHRP Guidelines for seismic rehabilitation of buildings.* Design Code. Washington, D.C: Federal Emergency Management Agency Building Seismic Safety Council.
- FEMA 313, 1998. *NEHRP: Promoting the Adoption and Enforcement of Seismic Building Codes: A Guidebook for State Earthquake and Mitigation Managers.* Washington, D.C.: Federal Emergency Management Agency.
- Foutch, D.A., Shi, S. & Yun, S.-Y., 2003. *Element 10: A stiffness and strength degrading element developed.* [Online] Available from <http://nisee.berkeley.edu/elibrary/Software/DRAIN2DXZIP>: Distributed with DRAIN-2DX by the National Information Service for Earthquake Engineering (NISEE) Available at: <http://nisee.berkeley.edu/elibrary/Software/DRAIN2DXZIP>.
- Ghobarah, A. & Said, A., 2001. Seismic rehabilitation of beam-column joints using FRP laminates. *Journal of Earthquake Engineering*, 5(1), pp.113-29.
- Ghobarah, A. & Youssef, M., 1999. Modeling of reinforced concrete structural walls. *Engineering Structures*, 21(10), p.912–923.
- Giberson, M.F., 1967. *The Response of Nonlinear Multi-Story Structures Subjected to Earthquake Excitation.* PhD Thesis. Pasadena, California: California Institute of Technology.
- Hanson, N.W. & Connor, H.W., 1967. Seismic Resistance of Reinforced Concrete Beam-Column Joints. *Journal of the Structural Division, ASCE*, 95(5), pp.533-60.

- Hassan, W.M., 2011. *Analytical and Experimental Assessment of Seismic Vulnerability of Beam-Column Joints without Transverse Reinforcement in Concrete Buildings*. PhD Thesis. California: UNIVERSITY OF CALIFORNIA, BERKELEY.
- Hsu, T.C., 1998. Softened truss model theory for shear and torsion. *ACI Structural Journal*, 85(6), pp.624-35.
- Hwang, S.-J. & Lee, H.-J., 1999. Analytical Model for Predicting Shear Strengths of Exterior Reinforced Concrete Beam-Column Joints for Seismic Resistance. *ACI Structural Journal*, 96(5), pp.846-58.
- Izzuddin, B.A., 1991. *Nonlinear dynamic analysis of framed structures*. Department of Civil Engineering, Imperial College, University of London.
- Jemaa, Y., 2007. *Seismic design and analysis of reinforced concrete structures*. MSc Thesis. The University of Sheffield.
- Karayannis, C.G., Chalioris, C.E. & Sirkelis, G., 2008. Local Retrofit of Exterior RC Beam-Column Joints Using Thin RC Jackets: An Experimental Study. *Earthquake Engineering and Structural Dynamics*, 37, pp.727-46.
- Khan, S., 2011. *An earthquake risk assessment framework for developing countries: Pakistan case study*. PhD Thesis. Sheffield, UK: The University of Sheffield.
- Kim, J. & LaFave, J.M., 2007. Key influence parameters for the joint shear behaviour of reinforced concrete (RC) beam-column connections. *Journal of Engineering Structures*, 29(10), pp.2523-39.
- Koru, B.Z., 2002. *Seismic Vulnerability Assessment of Low-Rise Reinforced Concrete Buildings*. PhD Thesis. West Lafayette, IN: Purdue University.
- Krawinkler, H., 2001. *State of the art report on systems performance of steel moment frames subjected to earthquake ground shaking*. FEMA-355C. Washington, DC: Federal Emergency Management Agency.
- Krawinkler, H. & Mohasseb, S., 1987. Effects of panel zone deformation on seismic response. *Journal of Construction Steel Research*, 8, pp.233-50.
- Kyriakides, N., 2008. *Seismic Vulnerability Assessment of Reinforced Concrete Structures*. PhD Thesis. Sheffield, UK: The University of Sheffield.
- Kythreoti, S., 2007. *Earthquake Risk Assessment and Management. Case study: Cyprus*. PhD Thesis. Sheffield, UK: The University of Sheffield.

- Lehman, & Moehle, J., 1998. *Seismic Performance of Well-Confined Concrete Bridge Columns*. PEER Report 1998/01.
- Lowes, L.N. & Altoontash, A., 2003. Modeling reinforced-concrete beam-column joints subjected to cyclic loading. *Journal Of Structural Engineering (ASCE)*, 129(12), pp.1686-96.
- Lowes, L.N., Mitra, N. & Altoontash, A., 2003. *A beam-column joint model for simulating the earthquake response of reinforced concrete frames*. Peer Report 2003/10. California: Pacific Earthquake Engineering Research Center College of Engineering, Uni. of California, Berkeley.
- Lowes, L.N. & Moehle, J.P., 1999. Evaluation and retrofit of beam-column T-joints in older reinforced concrete bridge structures. *ACI Structural Journal*, 96(4), p.519–532.
- Mazzoni, S., McKenna, F., Scott, M.H. & Fenves, G.L., 2006. *OpenSees user command language manual*. [Online] (1.7.3) Available at: <http://opensees.berkeley.edu/OpenSees/manuals/ExamplesManual/HTML/>.
- McKenna, F. & Fenves, G., 2012. *OpenSees: Open System for Earthquake Engineering Simulation*. [Online] PEER, University of California, Berkeley. (2.4.0) Available at: <http://opensees.berkeley.edu/> [Accessed Dec 2012].
- Mitra, N., 2007. *An analytical study of reinforced concrete beam-column joint behavior under seismic loading*. PhD Thesis. University of Washington.
- Mitra, N. & Lowes, L.N., 2007. Evaluation, calibration, and verification of a reinforced concrete beam-column joint model. *Journal of Structural Engineering (ASCE)*, 133(1), pp.105-20.
- Moehle, J.P., 2000. State of research on seismic retrofit of concrete building structures in the US. In *US-Japan Symposium and Workshop on Seismic Retrofit of Concrete Structures - State of Research and Practice*, 2000.
- Moehle, J.P., 2008. *Beam-Column Connections*. PowerPoint Presentation, NEES GC Project: Mitigation of Collapse Risk of Older Concrete Buildings. Pacific Earthquake Engineering Website.
- Morita, S. & Kaku, T., 1984. Slippage of reinforcement in beam-column joint of reinforced concrete frame. In *Eighth World Conf. on Earthquake Engineering, San Francisco, CA*, 1984.
- Mosier, G., 2000. *Seismic Assessment of Reinforced Concrete Beam-Column Joints*. MSc thesis. University of Washington, Seattle.
- Naeim, F., 2001. *The Seismic Design Handbook*. Second Edition ed. Norwell, MA: Kluwer Academic Press, Chapter 10, pp. 472-519.

- NISEE, 2012. *National Information Service for Earthquake Engineering (NISEE), Pacific Earthquake Engineering Center, University of California, Berkeley*. [Online] Available at: <http://nisee.berkeley.edu/elibrary/>.
- Novák, B., Karusala, R., Roehm, C. & Sasmal, S., 2008. Comparison of Seismic Performance of D-Region of Existing RC Structures Designed with Different Recommendations. *Journal of Structural Engineering*, 35(1), pp.46-51.
- Otani, S., 1974. Inelastic analysis of RC frame structures. *Journal of Structural Division (ASCE)*, 100(ST7), pp.1433-49.
- Pampanin, S., Magenes, G. & Carr, A.J., 2003. Modelling of shear hinge mechanism in poorly detailed RC beam-column joints. In *fib 2003 Symposium "Concrete Structures in Seismic Regions", May 2003. Paper n.171*. Athens, Greece, 2003. University of Canterbury. Civil Engineering.
- Pantelides, C.P., Hansen, J., Nadauld, J. & Reaveley, L.D., 2002. *Assessment of reinforced concrete building exterior joints with substandard details*. PEER Report May 2002. Pacific Earthquake Engineering Research Center.
- Park, S. & Mosalam, K., 2009. *Shear Strength Models of Exterior Beam-Column Joints without Transverse Reinforcement*. PEER Report 2009/106, November 2009. Pacific Earthquake Engineering Research Center.
- Park, S. & Mosalam, K.M., 2012a. Analytical Model for Predicting Shear Strength of Unreinforced Exterior Beam-Column Joints. *ACI STRUCTURAL JOURNAL*, March-April, 109(2), pp.149-60.
- Park, S. & Mosalam, K.M., 2012b. *Experimental and Analytical Studies on Reinforced Concrete Buildings with Seismically Vulnerable Beam-Column Joints*. PEER Report 2012/03, OCTOBER 2012. PACIFIC EARTHQUAKE ENGINEERING RESEARCH CENTER.
- Paulay, T., Park, R. & Priestley, M.J.N., 1978. Reinforced Concrete Beam-column Joints Under Seismic Actions. *ACI Structural Journal*, 75(60), pp.585-93.
- Paulay, T. & Priestley, M.J.N., 1992. *Seismic Design of Reinforced Concrete and Masonry Buildings*. John Wiley and Sons.
- Paulay, T. & Scarpas, A., 1981. *The Behaviour of Exterior Beam-Column Joints*. Bulletin of the New Zealand National Society for Earthquake Engineering, Vol.14, No.3, Sept.1981, pp.131-144.

- Pgni, C. & Lowes, L., 2003. *Predicting Earthquake Damage in Older Reinforced Concrete Beam-Column Joints*. PEER Report 2003/17. College of Engineering, University of California, Berkeley.
- Powell, G.H., 1993. *DRAIN-2DX Element Description and Used Guide For Element TYPE01, TYPE02, TYPE04, TYPE09, and TYPE01: Version 1.10*. California: University of California Berkeley.
- Prakash, V., Powell, G.H. & Campbell, S., 1993. *DRAIN-2DX base program description and user guide*. University of California, Berkeley, California.
- Priestley, M.J.N., 1997. Displacement based seismic assessment of reinforced concrete buildings. *Journal of Earthquake Engineering*, 1(1), pp.157-92.
- Reyes de Ortiz, I., 1993. *Strut and Tie Modelling of Reinforced Concrete Short Beams and Beam-Column Joints*. PhD thesis. London: University of Westminster.
- Sezen, H., 2000. *Seismic Behavior and Modeling of Reinforced Concrete Building Columns*. PhD. CALIFORNIA: UNIVERSITY OF CALIFORNIA, BERKELEY.
- Sezen, H. et al., 2000. *Structural engineering reconnaissance of the August 17, 1999 earthquake: Kocaeli (Izmit), Turkey*. PEER-2000/09, Berkeley. Pacific Earthquake Engineering Research Center, University of California, Dec.
- Sharma, , Eligehausen, R. & Reddy, G.R., 2011. A new model to simulate joint shear behavior of poorly detailed beam-column connections in RC structures under seismic loads, Part I: Exterior joints. *Engineering Structures*, 33, pp.1034-51.
- Sheikh, S.A. & Uzumeri, S.M., 1982. Analytical model for concrete confinement in tied columns. *Journal of the Structural Division, ASCE*, 108, p.2703-2722.
- Shima, H. & Fukuju, S., 2008. BOND STRESS DISTRIBUTION ALONG BAR AXIS IN HOOK ANCHORAGE OF DEFORMED REINFORCING BAR. In Uomoto, T. & Van Nga, T., eds. *The 3rd ACF International Conference- ACF/VCA 2008*. Ho Chi Minh, Vietnam, 2008. Vietnam Institute for Building Materials.
- Shin, M. & LaFave, J.M., 2004. Modeling of cyclic joint shear deformation contributions in RC beam-column connections to overall frame behavior. *Journal of Structural Engineering and Mechanics*, 18(5), pp.645-69.
- Soyluk, A. & Harmankaya, Z.Y., 2012. The History of Development in Turkish Seismic Design Codes. *International Journal of Civil & Environmental Engineering IJCEE-IJENS*, 12(01), pp.25-29.

- Stevens, N.J., Uzumeri, S.M. & Collins, M.P., 1991. Reinforced-Concrete Subjected to Reverse-Cyclic Shear – Experiment and Constitutive Model. *ACI Structural Journal*, 88(2), p.135–146.
- Taciroglu, E. & Khalili-Tehrani, P., 2008. *M7.8 Southern San Andreas Fault Earthquake Scenario: Non-ductile Reinforced Concrete Building Stock*. The ShakeOut Scenario Supplemental Study: Prepared for United States Geological Survey (USGS) and California Geological Survey (CGS).
- Takeda, T., Sozen, M.A. & Nielsen, N.N., 1970. Reinforced concrete response to simulated earthquakes. *Journal of the Structural Division, ASCE*, 96(ST12), p.2557–2573.
- Tsonos, A.G., 1999. Lateral Load Response of Strengthened Reinforced Concrete Beam-to-Column Joints. *ACI Structural Journal*, 96(1), pp.46-56.
- Tsonos, A.G., 2007. Cyclic Load Behavior of Reinforced Concrete Beam-Column Subassemblages of Modern Structures. *ACI Structural Journal*, 104(4), pp.468-78.
- Tsonos, A.G., 2008. Effectiveness of CFRP-jackets and RC-jackets in post-earthquake and pre-earthquake retrofitting of beam–column subassemblages. *Engineering Structures*, 30, p.777–793.
- Uma, S.R. & Parsad, A.M., 2004. *Seismic Behavior of Beam Column Joints in Reinforced Concrete Moment Resisting Frame*. [Online] Available at: <http://www.iitk.ac.in/nicee/IITK-GSDMA/EQ31.pdf>.
- Uma, S.R. & Prasad, A.M., 1996. Analytical modeling of RC beam-column connections under cyclic load. In *Proc. Eleventh World Conference on Earthquake Engineering*. Acapulco, Mexico, number 1869, 1996.
- Umemura, H. & Aoyama, H., 1969. Evaluation of inelastic seismic deflection of RC frames based. In *Proc. Fourth World Conference on Earthquake Engineering*. Chile, 1969.
- Uzumeri, S.M., 1977. Strength and Ductility of Cast-in-Place Beam Column. *Reinforced Concrete Structures in Seismic Zones*, Publication SP 53–12, American Concrete Institute, pp.293-350.
- Vecchio, F.J. & Collins, M.P., 1986. The Modified Compression-Filed Theory for Reinforced Concrete Elements Subjected to Shear. *ACI Structural journal*, 83(22), pp.219-31.
- Verderame, G.M., Iervolino, I. & Ricci, P., 2009. *Report on the damages on buildings following the seismic event of 6th of April 2009, VI.10*. [Online] Available at: <http://www.reluis.it/>.

- Viwathanatepa, S., Popov, E.P. & Bertero, V.V., 1979. *Effects of generalized loadings on bond of reinforcing bars embedded in confined concrete blocks*. Technical Report UCB/EERC 79/22. California: Earthquake Engineering Research Center University of California, Berkeley.
- Vollum, R.L., 1998. *Design and Analysis of Exterior Beam Column Connections*. PhD Thesis. London: Imperial College of Science Technology and Medicine-University of London.
- Vollum, L. & Newman, J.B., 1999. Strut and tie models for analysis/design of external beam-column joints. *Magazine of Concrete Research*, Vol. 51, No. 6, pp.415-25.
- Walker, S.G., 2001. *Seismic Performance of Existing RC Beam-Column Joints*. MSc Thesis. University of Washington.
- Walraven, J.C., 1981. Fundamental analysis of aggregate interlock. *Journal of Structural Division (ASCE)*, 107(11), p.2245–2270.
- Walraven, J.C., 1994. Rough cracks subjected to earthquake loading. *Journal of Structural Division*, 120(5), p.1510–1524.
- Wong, H.F., 2005. *Shear Strength and Seismic Performance of Non-Seismically Designed Reinforced Concrete Beam-Column Joints*. PhD Thesis. Hong Kong: The Hong Kong University of Science and Technology.
- Youssef, M. & Ghobarah, A., 2001. Modeling of RC beam-column joints and structural walls. *Journal of Earthquake Engineering*, 5(1), pp.93-111.

APPENDIX A

MATERIAL PROPERTIES AND INITIAL DESIGN

A.1 INITIAL DESIGN OF SPECIMENS

A.1.1 FEMA273 Joint Shear Strength

Initial joint shear strength was estimated based on FEMA 273, Table (6-9) (FEMA 273, 1997). FEMA 273 provides a formula to predict the nominal joint shear strength taking into account the joint type and the joint shear reinforcement ratio. The nominal joint shear strength, V_n , is defined according to FEMA 273 as follows:

$$V_n = \lambda \gamma \sqrt{f'_c} A_j \text{ psi} \quad (\text{A.1})$$

where λ is taken as 1 for normal weight aggregate concrete, γ (as defined in Table 6-9 in FEMA 273) is the joint shear strength coefficient and can be calculated by normalising the joint shear stress v_j as follows:

$$\gamma = \frac{v_j}{\sqrt{f'_c}} \quad (\text{A.2})$$

The effective joint area A_j , is defined according to ACI 318-02 (2002) as follows:

$$A_j = b_{je} h_j \quad (\text{A.3})$$

where h_j is the joint depth which is equal to the column depth h_c and b_{je} is the joint effective width as defined by ACI 318-02 (2002).

According to FEMA 273 Table 6-9, the joint shear strength coefficient γ is 6 ($\sqrt{\text{psi}}$) or 0.5 ($\sqrt{\text{MPa}}$) for exterior joints without transverse beams and with a volumetric ratio of transverse reinforcement within the joint area of less than 0.3%. This value of $\gamma = 0.5$ ($\sqrt{\text{MPa}}$) was used in to calculate the nominal joint shear strength of the pilot test specimen, as the selected specimen has no out-of-plane (transverse) beams and no shear links within the joint core. In addition, since both the beam and the column have the same width (260mm), the joint effective width b_{je} is taken as the column width b_c . By assuming the concrete compressive strength, f'_c equal to 18MPa, the joint depth $h_j = 260\text{mm}$, $\gamma = 0.5$, and $b_{je} = 260\text{mm}$, the resulting estimated joint shear strength, is V_n equal to 143.4 kN.

A.1.2 Equivalent Beam Shear

The beam shear V_b (i.e. the applied lateral load) can be related to the nominal joint shear strength, V_n , from geometry and moment equilibrium using the following equations:

$$V_n = T_b - V_c \quad (\text{A.4})$$

where V_c is the column shear force and T_b is the tension force in the beam at the joint interface. T_b is related to the beam moment at the joint interface M_b as follows:

$$T_b = \frac{M_b}{jd_b} \quad (\text{A.5})$$

where d_b is the effective beam depth and j is the beam moment lever arm reduction factor. j can be taken as the average negative and positive beam moment arms from section analysis. However, to simplify the procedure, a common approximation of 0.875 is used. The beam moment at the joint interface is calculated as follows:

$$M_b = V_b L_b \quad (\text{A.6})$$

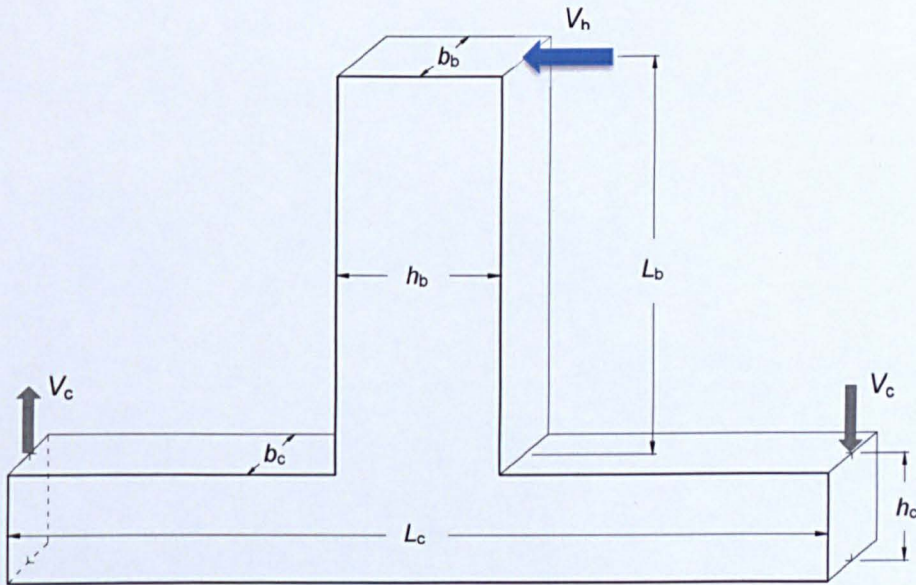


Figure A.1 Applied forces and geometry of a typical test specimen

From global equilibrium the column shear force V_c is calculated as follows:

$$V_c = V_b \frac{L_b + \frac{h_c}{2}}{L_c} = V_b Q_1 \quad (\text{A.7})$$

where L_b , L_c and h_c are as defined in Figure A.1. By substituting M_b from Eq (A.5) in Eq (A.6), T_b becomes:

$$T_b = V_b \frac{L_b}{jd_b} = V_b Q_2 \quad (\text{A.8})$$

By substituting Eq (A.7) and Eq (A.10) in Eq (A.4), the beam shear can be calculated as follows

$$V_b = \frac{V_n}{Q_2 - Q_1} \quad (\text{A.9})$$

Using the calculated joint shear strength (V_n equal to 143kN), $L_b = 1445\text{mm}$, and $L_c = 2370\text{mm}$, the equivalent beam shear V_b is equal to 36.8kN. This corresponds to $M_b = 53\text{kN.m}$ and $V_c = 24.5\text{kN}$.

The reinforcement detailing of both beam and column was adopted from the first-storey corner joint of the Ecoleader no.2 frame structure, as described in Chapter 2. The only difference is replacing the T14 bars with T16. The flexural capacity of both beam and column (with either 150kN or 250kN axial load) are almost twice higher than those corresponding to the estimated joint shear strength. Shear links of both beam and column were increased from T8 to T10 for the pilot specimen only due to unavailability, as discussed in Chapter 2.

A.2 Material Properties

The following sub-sections provide full details of concrete and steel reinforcement materials used in the construction of the beam-column joint specimens.

A.3 Concrete

This section describes the concrete mix properties, the target and the final compressive strength, the testing procedure and results of the performed tests.

A.3.1 Concrete mix properties and target strength

The specimens were designed for a maximum concrete compressive strength of 18Mpa. A special concrete mix was developed at the University of Sheffield to replicate the low strength concrete usually found in older buildings, especially in developing countries. However, due to the small capacity of the available concrete mixer, three full batches of concrete were needed to complete one specimen and that on its own is a major obstacle as it leads to inconsistent concrete throughout the specimen. Eventually, decision was made for concrete to be ordered from a ready mix concrete company.

The concrete mix of the first and the second batch which included the pilot test JA-1 for the first and JC-1, JB-1, JB-2 for the second had the following properties:

- Concrete grade C16/20
- Target slump S3
- Maximum aggregate size 10mm

The restrictions on the available resources, such as strength of aggregates and cement grades, prevented the goal strength to be achieved. Therefore, the third batch of concrete which included joints JA-2, JA-3 and JC-2 was of a lower grade than the previous two batches. The concrete mix properties were as follows:

- Concrete grade C12/16
- Target slump S3
- Maximum aggregate size 10mm

Despite ordering the lowest concrete grade available at the time, the resulted concrete strength was even higher than the maximum concrete strength attained in batch No. 2 and 3, as shown in A.3.4.

A.3.2 Casting and sample preparation

All specimens were cast, cured, prepared and tested according to BS EN 12390-3:2009. The first specimen was cast separately as a pilot test to examine and monitor the concrete mix. Several sample cubes and cylinders were cast with each concrete batch. Initial tests of sample cubes and cylinders of the first batch after 3, 7 and 14 days, showed the concrete compressive strength to be within the acceptable range. However, due to many problems faced during assembling the loading apparatus, the tests were delayed many times resulting in a much higher strength, as shown later in A.3.4.

A.3.3 Testing procedure

Sample cubes and cylinders underwent two types of tests to determine the concrete compressive and tensile strength.

Uniaxial compressive strength

Sample cubes and cylinders were tested according to BS EN 12390-3:2009 in a compression testing machine until failure. The maximum recorded load by the machine was used to calculate the concrete compressive strength. Further information about the testing machine and the procedure can be found in BS EN 12390-3:2009.

Tensile splitting strength

Sample cylinders were tested according to BS EN 12390-6:2000 to determine their tensile strength. In this test a cylinder is subjected to a compressive force along its length until the specimens fails in tension. Full description of the testing machine, procedure and calculations can be found in BS EN 12390-6:2000.

Modulus of Elasticity

Concrete modulus of Elasticity for this research was determined from uniaxial compressive tests according to BS EN 1992-1-1 and results were verified according to ACI 318-08. Sample cylinders which were subjected to uniaxial compression tests were equipped with three LVDTs mounted parallel to their length. This setup was utilized for concrete batch No. 2 and 3 only. Figure A.2 shows the concrete compressive stress-strain relationship of two sample cylinders BN2 and BN3 from batch No. 2 and batch No. 3, respectively, which were subjected to the uniaxial compression test.

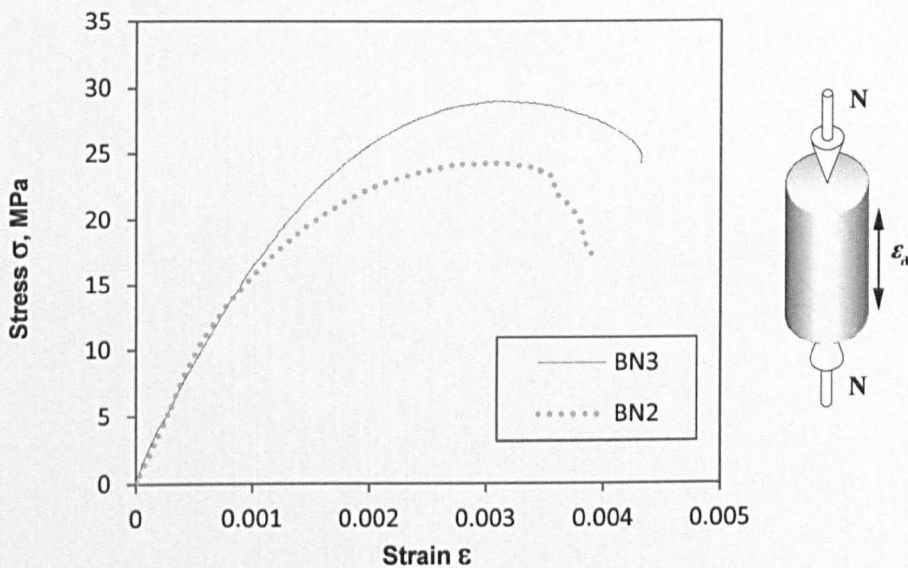


Figure A.2 Concrete stress-strain relationship of batch No. 2&3

According to Eurocode 2, the static modulus of elasticity E_c can be approximated as the secant value between the origin and a stress value of $0.4f_{cm}$, however this value is highly dependent on the aggregate modulus of elasticity. Additional reductions must be applied when using different than quartzite aggregates (BSI EC2, 2004). The experimental values of E_{cm} calculated based on the secant value concept were compared with the general equations of ACI 318 and Eurocode 2 as follows:

- Eurocode 2:

$$E_{cm} = 22[f'_{cm}/10]^{0.3} \text{ GPa} \quad (\text{A.10})$$

- ACI 318:

$$E_c = 4700\sqrt{f'_c} \text{ MPa} \quad (\text{A.11})$$

After comparing the results, it was noted that values calculated using Eurocode 2 were slightly higher than values calculated according to ACI 318. A total reduction of 13% was needed to match the experimental results. This was attributed to the types of aggregates used in the concrete mixes. The experimental values of the modulus of elasticity are detailed in A.3.4.

A.3.4 Concrete Test Results

Table A-1 and Table A-2 show the concrete compressive test results of concrete batch No. 2 and batch No. 3, respectively. The mean compressive strength was calculated by averaging the results of three 150x300 mm cylinders for each specimen.

Table A-1 Concrete compressive strength of batch No. 2 specimens on the day of test

Concrete Batch № 2 cast on 23 September 2010								
Specimen	Cylinder №	Testing date	Weight (kg)	Height (mm)	Diam (mm)	Crushing Force (kN)	f'_c (Mpa)	f'_c average (Mpa)
JC-1	1	02-Nov-10	12.371	305	152	507.4	27.96	27.18
	2		12.375	305	153	483	26.27	
	3		12.451	304	153	502	27.30	
JB-1	1	29-Mar-11	12.103	304	151	570.4	31.85	31.05
	2		12.117	304	152	586.2	32.30	
	3		12.156	305	152	525.9	28.98	
JB-2	1	14-Apr-11	12.130	303.5	152.5	557.8	30.54	30.78
	2		12.147	305	152	568.7	31.34	
	3		11.639	300	150	538.2	30.46	

Table A-2 Concrete compressive strength of batch No. 3 specimens on the day of test

Concrete Batch № 3 cast on 15 October 2010								
Specimen	Cylinder №	Testing date	Weight (kg)	Height (mm)	Diam (mm)	Crushing Force (kN)	f'_c (Mpa)	f'_c average (Mpa)
JA-2	1	08-Dec-10	12.385	301	152	569.1	31.36	31.03
	2		12.386	302	152	556.6	30.67	
	3		11.849	295	150	548.9	31.06	
JA-3	1	25-Jan-11	12.340	302	153	581.2	31.61	32.41
	2		12.341	304	152	596.7	32.88	
	3		11.684	296.5	149.5	574.4	32.72	
JC-2	1	21-Feb-11	12.235	302	152	595.1	32.80	32.57
	2		11.730	295	150	563.4	31.88	
	3		12.274	303	153	607.5	33.04	

Table A-3 and Table A-4 show the concrete tensile splitting strength of concrete batch No. 2 and batch No. 3, respectively. The test was carried out on 100x200 mm cylinders.

Table A-3 Concrete splitting strength of batch No. 2

Concrete Batch № 2 cast on 23 September 2010						
Cylinder №	Testing date	Height (mm)	Diam (mm)	Maximum Load (kN)	<i>Splitting Strength</i>	Average Strength (Mpa)
1	18-Jan-11	204	101	80	2.47	2.43
2		201	100	79.7	2.52	
3		202	100	76.3	2.40	
4		200	100	69.7	2.22	
5		200	100	69.1	2.20	
6		200	100	90	2.86	
7	12-May-11	200	100	76.2	2.43	
8		205	102	85.8	2.61	
9		206	102	72.2	2.19	

Table A-4 Concrete splitting strength of batch No. 3

Concrete Batch № 3 cast on 15 October 2010						
Cylinder №	Testing date	Height (mm)	Diam (mm)	Maximum Load (kN)	<i>Splitting Strength</i>	Average Strength (Mpa)
1	18-Jan-11	203	102	80.2	2.47	2.44
2		200	100	74	2.36	
3		200	100	72.2	2.30	
4	22-Mar-11	202	101	69.3	2.16	
5		203	102	79.4	2.44	
6		200	100	76.5	2.44	
7		201	100	80.5	2.55	
8		203	101	80.6	2.50	
9		200	100	86.1	2.74	

Furthermore, Table A-5 and Table A-6 show the concrete tensile splitting strength of concrete batch No. 2 and batch No. 3, respectively. The test was carried out on 100x200 mm cylinders.

Table A-5 Modulus of elasticity of batch No. 2

Specimen №	$\frac{N}{f'_c A_g}$	f'_c average (Mpa)	E_c (GPa)
JC-1	0.10	27.18	24.50
JB-1	0.10	31.05	26.19
JB-2	0.25	30.78	26.08

Table A-6 Modulus of elasticity of batch No. 3

Specimen №	$\frac{N}{f'_c A_g}$	f'_c average (Mpa)	E_c (GPa)
JA-2	0.10	31.03	26.18
JA-3	0.25	32.41	26.76
JC-2	0.25	32.57	26.82

A.4 Reinforcement A.3

Two different sizes of steel rebar were used in the test specimens. Two different batches of T16 rebar were used as the longitudinal reinforcement for both columns and beams, whereas T8 was used for the shear links. Sample bars of each different batch/size underwent standard tensile tests.

The yield strength (f_y) and the ultimate strength (f_u) of the main longitudinal reinforcement are shown in Table A-7, in which (A) denotes the reinforcement of the pilot specimen while (B) refers to the main reinforcement of the remaining six specimens. Figure A.3 shows the typical stress-strain relationship of the main longitudinal reinforcement.

Table A-7 Main reinforcement properties

Bar size (mm)	f_y (MPa)	ϵ_y	ϵ_{sh}	ϵ_u	f_u (MPa)	E_s (GPa)
16A	478	0.0024	0.023	0.09	616	198
16B	554	0.0024	0.020	0.10	756	230

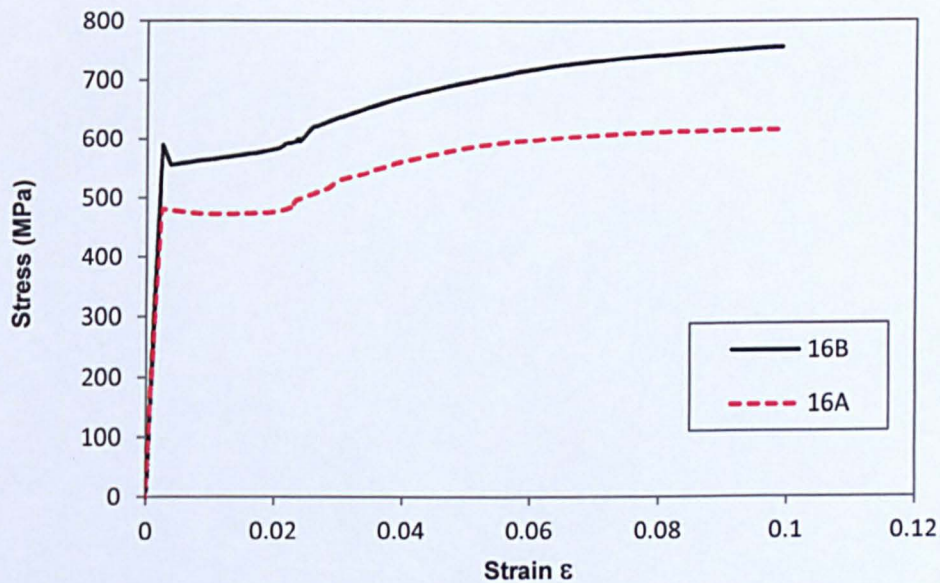
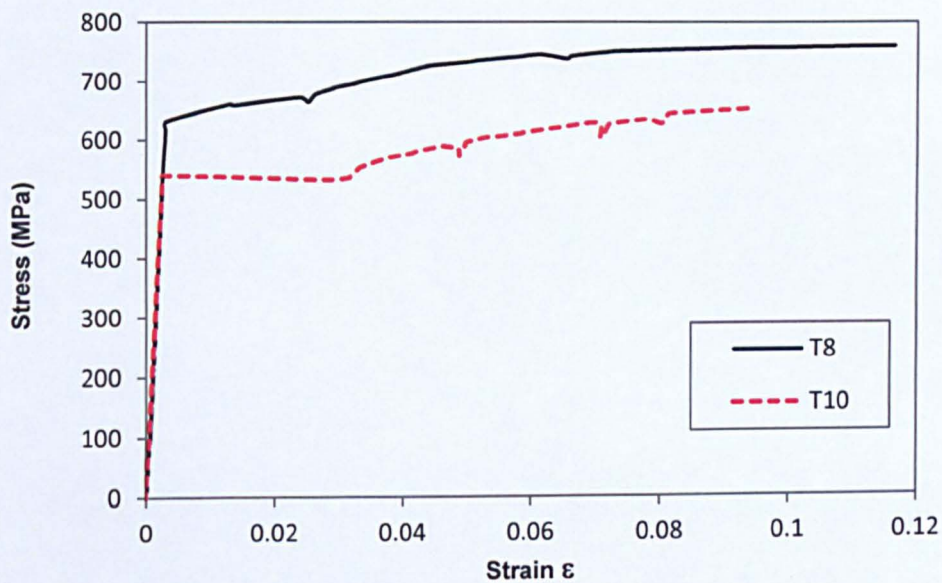


Figure A.3 Stress-strain relationship for the main reinforcement

Table A-8 shows the yield (f_y) and the ultimate (f_u) strengths of the shear reinforcement used in the six remaining specimens. Figure A.4 shows the typical stress-strain relationship of the specimen's shear reinforcement.

Table A-8 Transverse reinforcement properties

Bar size (mm)	f_y (MPa)	ϵ_y	ϵ_u	f_u (MPa)	E_s (GPa)
8	616	0.0028	0.11	758	220
10	533	0.0027	0.09	654	197

**Figure A.4 Stress-strain relationship for the transverse reinforcement**

APPENDIX B

EXPERIMENTAL RESULTS

B.1 SPECIMEN JA-3: Description of Damage

Test specimen JA-3 was subjected to the same displacement history as specimen JA-2. However, the applied axial compressive force on the column was 250kN instead of 150kN as in JA-2. Figure B.1 shows the crack development for specimen JA-3 during the test between 0.25% and 3.0% drift levels. After 3% drift, the damage was difficult to track; therefore, cracks were no longer marked. The cyclic load-drift response of specimen JA-3 and the overall envelope are shown in Figure B.2. Key changes to the response envelope are marked and denoted.

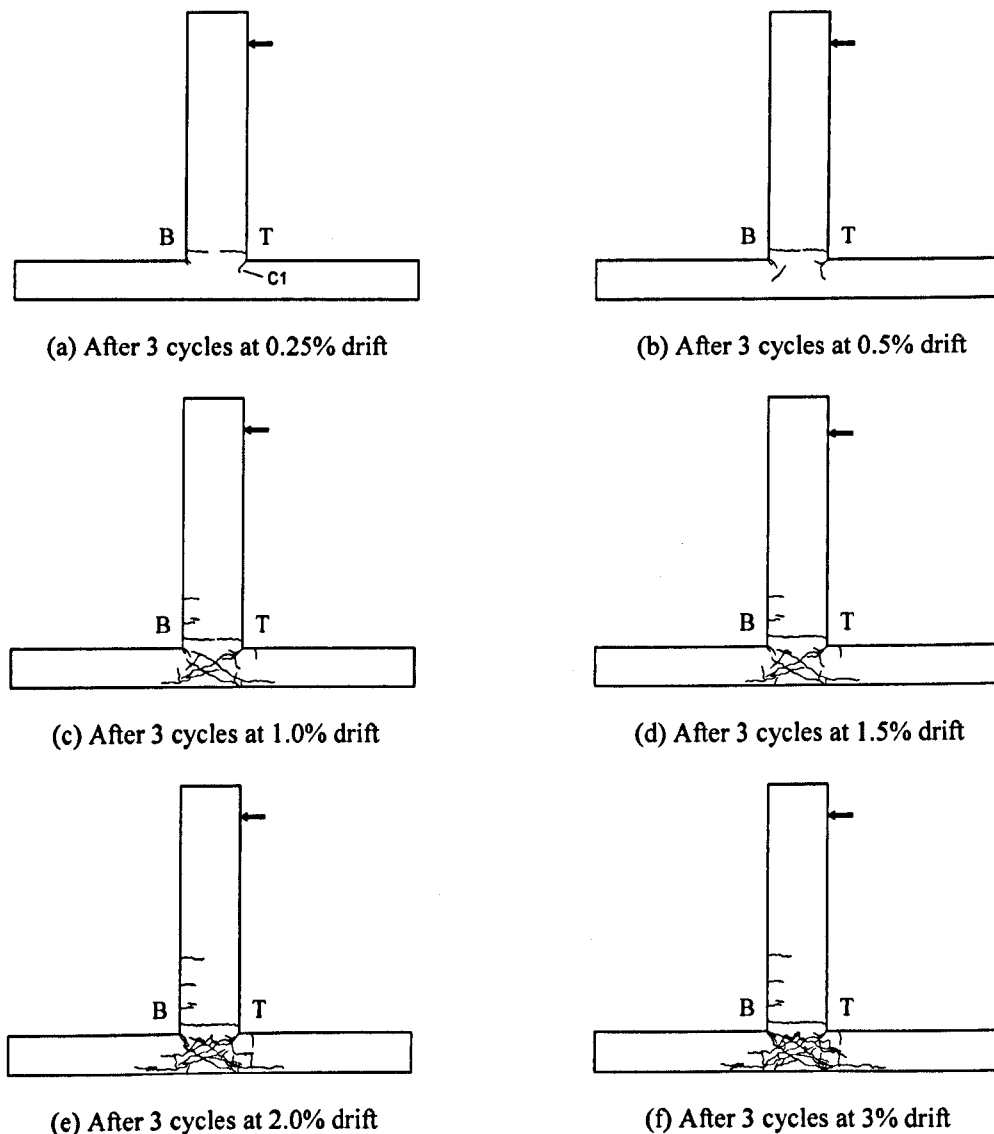


Figure B.1 Progression of cracking for specimen JA-3

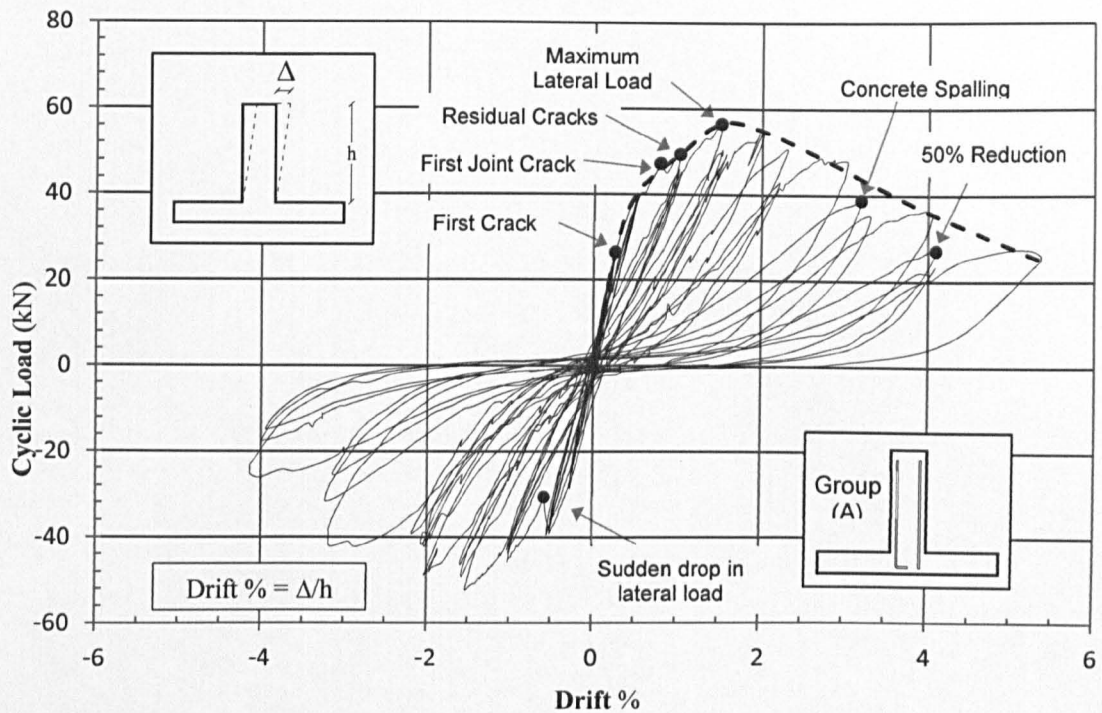


Figure B.2 Lateral load-drift response for specimen JA-3

Hairline cracks of widths less than 0.1 mm appeared when displacing the specimen to 0.1% drift level and disappeared once the specimen was brought to the starting point. Apart from these cracks, no significant damage was observed throughout the first three cycles.

In general, the observed crack pattern and the progression of damage up to 2.0% drift level of specimen JA-3 was similar to that of specimen JA-2. However, the intensity of damage at each drift level was always slightly less in JA-3 in comparison to JA-2. For instance, in JA-2, the first diagonal shear crack developed during 0.5% drift cycles, whereas JA-3 developed similar crack at a drift level equal to 0.78%. The slight difference between the two specimens in terms of the damage level can be attributed to the effect of using two different axial load levels.

The damage developed during the three cycles at 0.25% drift level was not as significant as the damage observed in test specimen JA-2. The first observed crack was developed during the first positive loading to 0.25% drift at the location of the first beam shear link. This was accompanied by an inclined crack, denoted as C1, at the top column-beam corner. The width of both cracks was less than 0.5mm. Similarly, the second half of the same cycle showed almost identical crack pattern. No further damage was observed during the remaining two cycles. Figure B.1.a shows the developed cracks of specimen JA-3 after three cycles at 0.25% drift.

During the first positive peak at 0.5% drift level, the beam horizontal cracks joined together and extended over the entire width of the beam. In addition, the inclined corner crack (C1) split into two branches and extended further into the joint following the paths of both the beam and column longitudinal reinforcement, as can be seen in Figure B.3.

The crack pattern during the second half of the first cycle was slightly different. Unlike the first positive half, the two corner cracks extended further following the joint diagonal. As negative loading continued, another inclined crack perpendicular to the previous two cracks, denoted as C2, suddenly appeared, as can be seen in Figure B.3. All cracks were of widths less than 1mm. No further damage was observed during the remaining 0.5% drift cycles. Figure B.1.b shows the crack pattern of specimen JA-3 after completing three cycles at 0.5% drift. A quick comparison between JA-2 and JA-3 in terms of the achieved damage shows how the different levels of axial loads affected the behaviour of these two specimens.

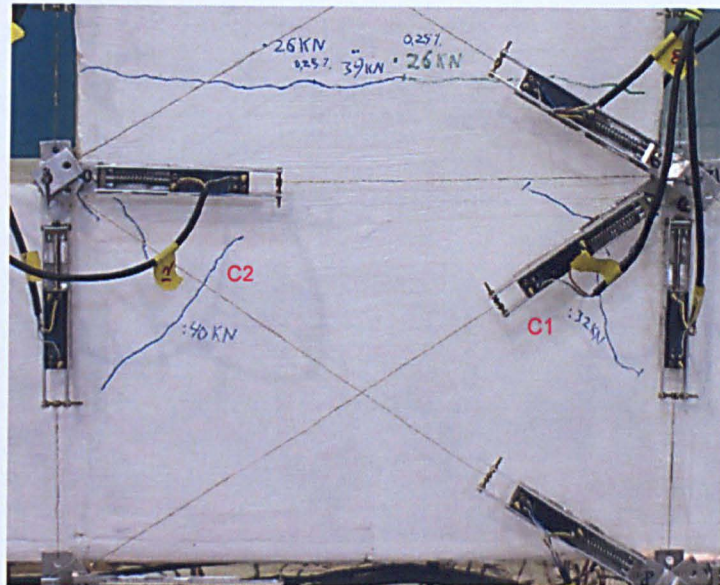


Figure B.3 Specimen JA-3 after one cycle at 0.5% drift

The 0.75% drift level was skipped to the next displacement increment for this test. During the first half cycle at 1% drift, a fairly long diagonal shear crack (denoted as C3) suddenly formed across the monitored joint face. This happened when the specimen reached a drift level equal to 0.78%. The formed crack (C3) caused a sudden drop in the applied lateral load, as can be seen in Figure B.2.

As the test continued, the previous shear crack (C3) extended further penetrating the top column and following the path of the column longitudinal reinforcement. In addition, another diagonal shear crack (denoted as C4) formed parallel to the previous crack and over the whole joint face, as shown in Figure B.4.a. The damage attained during this half cycle caused a significant impact to the stiffness of the cyclic load-drift response, as shown in Figure B.2. Moreover, when bringing the specimen to 0% drift level, residual cracks as wide as 0.8mm were observed.

The second half of the same cycle exhibited relatively the same level of damage but with a different crack pattern. As the negative loading increased, a much extended diagonal shear crack started to form. However, unlike during positive loading, the formed crack was in the shape of multiple diagonal cracks (C5; C6; C7) rather than a single crack extending over the whole joint

height. The crack surpassed the joint limits extending further into the bottom column, as can be seen in Figure B.4.b. Similarly to the first positive loading, the attained damage caused a significant stiffness reduction in the lateral load-drift response. Though, the sudden drop in the applied lateral load is more evident, as shown Figure B.2.

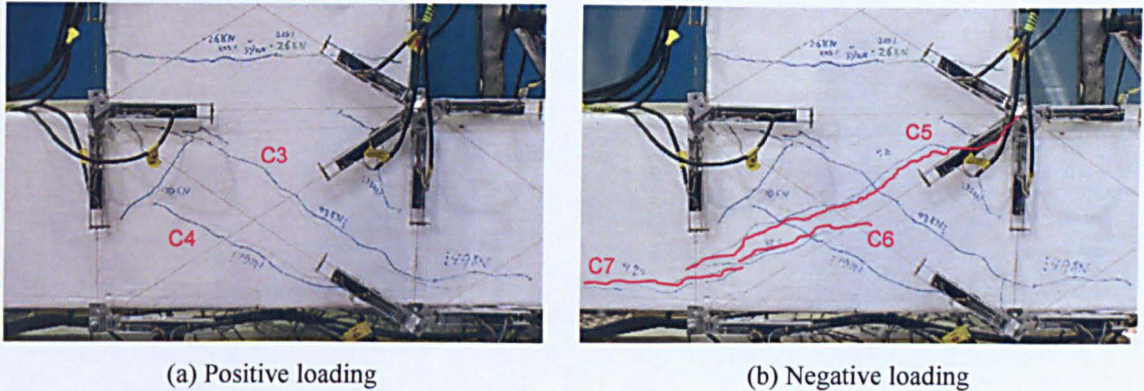


Figure B.4 Specimen JA-3 after one cycle at 1.0% drift

No further significant change in damage was recorded during the second and the third cycles at 1.0% drift. However, a couple of small vertical cracks formed around the joint interfaces, as shown in Figure B.5. The measured residual cracks at the end of the third cycle were around 1 to 1.5 mm. Figure B.1.c shows the crack pattern of specimen JA-3 at the end of the 1.0% drift cycles.

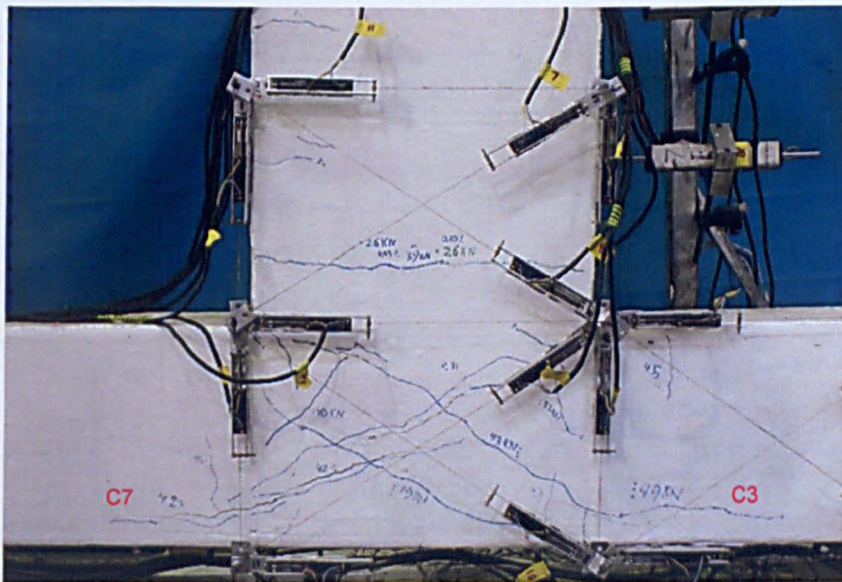


Figure B.5 Specimen JA-3 after three cycles at 1.0% drift

Figure B.1.d shows the crack pattern of specimen JA-3 after the 1.5% drift level. Displacing the specimen to 1.5% drift caused the existing joint cracks to increase in both width and length. Figure B.6 shows specimen JA-4 after reaching the positive and negative peaks of the first cycle at 1.5% drift. Small cracks appeared surround the existing cracks, while the diagonal cracks extended further into the top and bottom columns. The most notable event during this cycle was

reaching the maximum load carrying capacity of the specimen. No reinforcement yielding or any sign of concrete spalling were yet observed at this stage. Diagonal cracks measured as wide as 3mm.

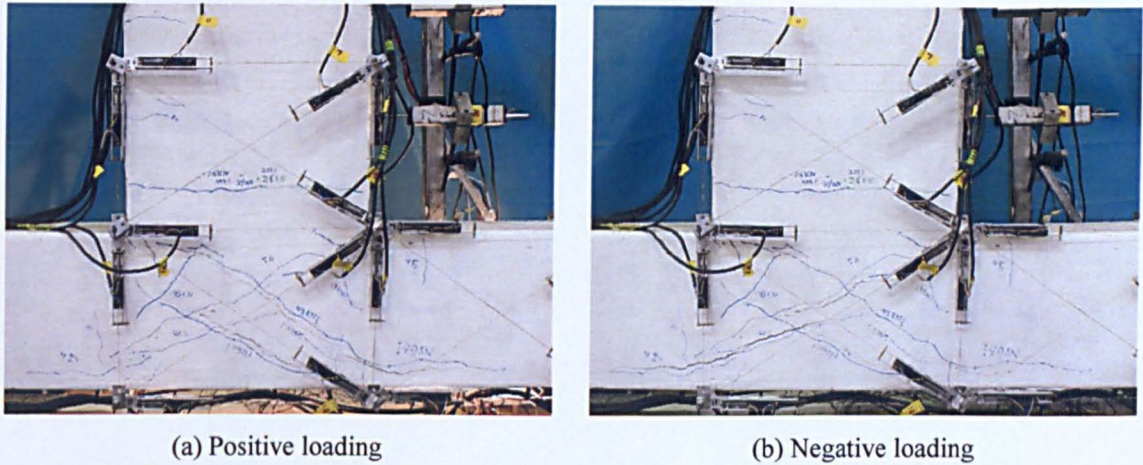


Figure B.6 Specimen JA-3 after one cycle at 1.5% drift

As the test continued no further damage was recorded during the second and the third cycle. However, a rapid decrease in joint stiffness was evident during these remaining cycles, as shown in Figure B.2. Figure B.7 shows the final state of JA-3 at the end of 1.5% drift.

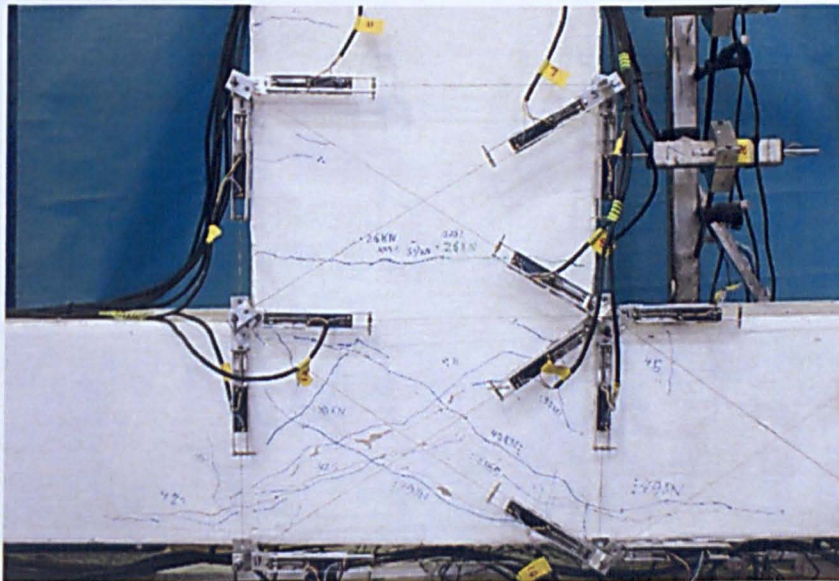


Figure B.7 Specimen JA-3 after three cycles at 1.5% drift

The overall crack pattern of specimen JA-3 showed a barely noticeable change during the first cycle at 2.0% drift level. However, as the test continued to the second and third cycle, cracks were widened rapidly leading to concrete flaking around the joint diagonal cracks. In addition, all diagonal cracks including the short ones extended further into the top and bottom columns. Figure B.1.e shows the crack pattern of specimen JA-3 at the end of the third cycle at 2.0% drift.

The observed cracks ranged in width between 3 to 6 mm. The damage level increased with each cycle causing loss in both strength and stiffness, as can be seen in Figure B.2. However, the straight anchorage side of the beam exhibited far greater loss. By the end of the three cycles, concrete flaking was observed in the joint close to the beam-column interface. Figure B.8 demonstrates the damage reached in specimen JA-2 at the end of the 2.0% drift level.

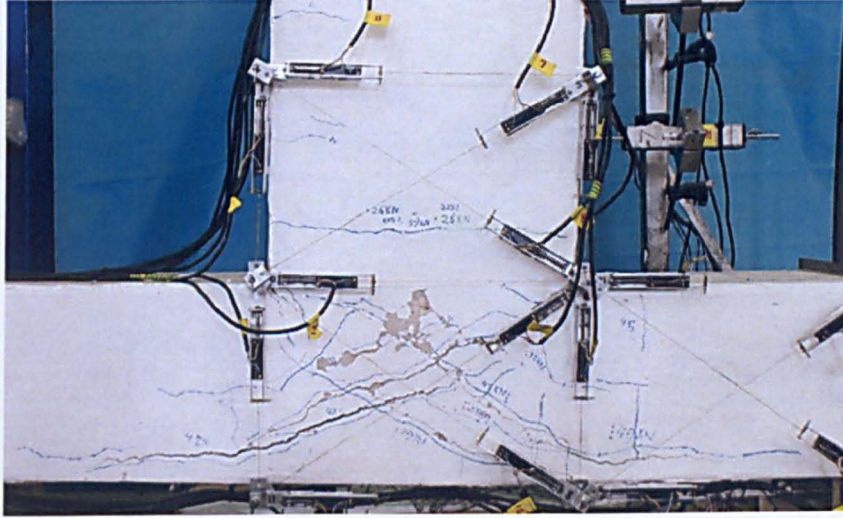


Figure B.8 Specimen JA-3 after three cycles at 2.0% drift

No more diagonal cracks were developed during the three cycles at 3.0% drift level. However, in addition to the increasing width, diagonal cracks extended further into the top and bottom columns. The penetrated length into the columns was almost equal to the joint height. The observed diagonal cracks measured 8 to 10 mm. Eventually, this extensive damage caused significant spalling of the joint concrete cover. Figure B.9 shows the extent of damage attained by specimen JA-3 after completing three cycles at 3.0% drift.

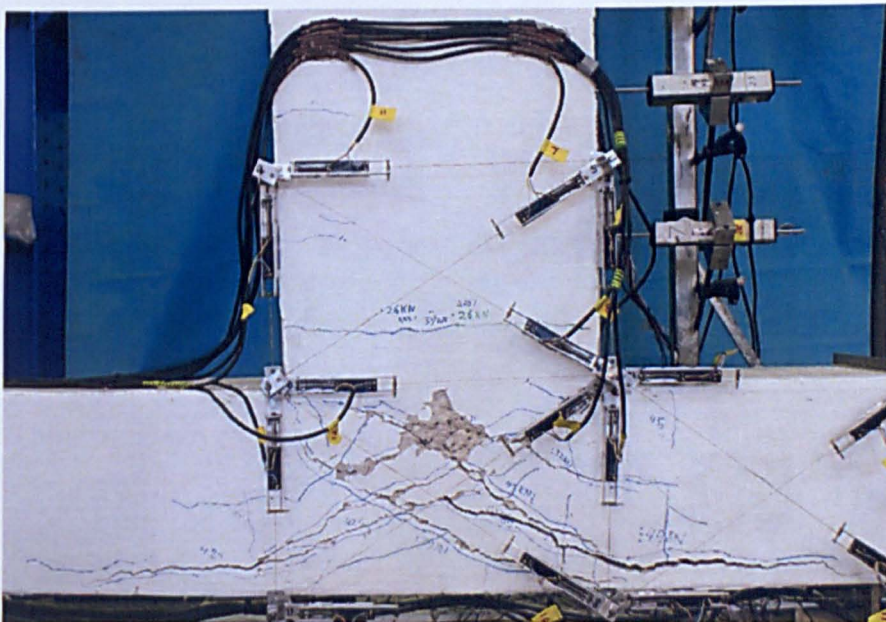


Figure B.9 Specimen JA-3 after three cycles at 3.0% drift

The specimen continued to become softer with each cycle, which in turn led to continuous loss in both strength and stiffness. However, the most notable change during these cycles was the drastic drop in both strength and stiffness between the first and the second cycle, as can be seen in Figure B.2. Figure B.1.f shows the final crack pattern of specimen JA-3 at the end of the third cycle at 3.0% drift.

Specimen JA-3 suffered substantial damage during the 4.0% drift cycles. Figure B.10 shows the level of damage attained by specimen JA-3 after completing three cycles at 4.0% drift.

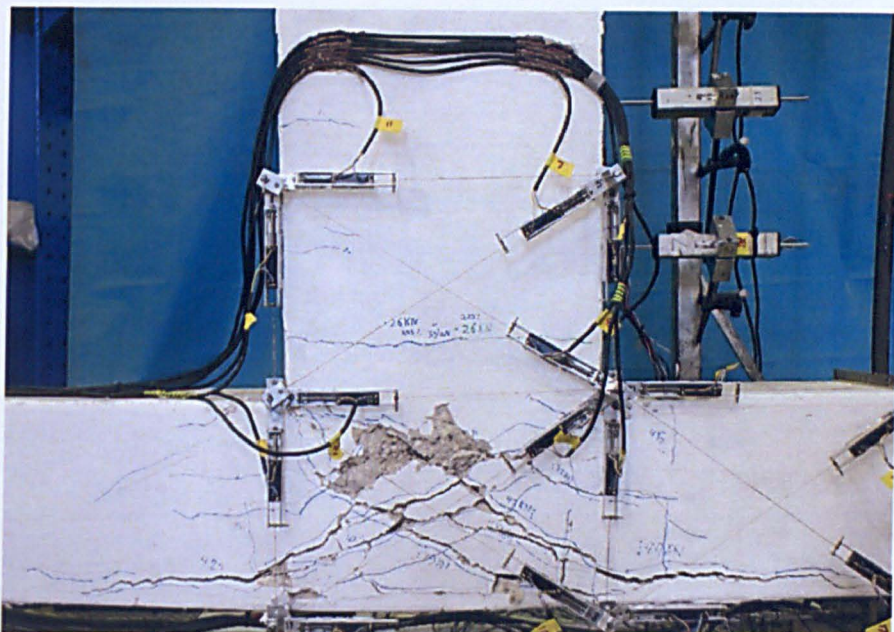


Figure B.10 Specimen JA-3 after three cycles at 4.0% drift

Similarly to the previous drift level, the specimen kept losing its strength and stiffness with each cycle. When the specimen reached the positive peak of the second cycle, the specimen had lost 50% of its maximum strength, as shown in Figure B.2. This point was considered to be joint failure. However, to explore the damage pattern even further, the test was continued

As the test continued, existing cracks became greater in width and length with every new cycle. In addition, a new horizontal crack was developed at the bottom of the joint following the path of the columns longitudinal reinforcement. The new crack made the bottom joint cover to be barely attached to the longitudinal reinforcement. At the end of the three cycles the damage was so severe that pieces of the centre concrete cover had fallen out, as shown in Figure B.10.

The test was continued by displacing the joint to 5% drift level. However, the specimen was deemed to be unstable, and hence only half a cycle was performed. Figure B.11 shows the damage achieved at the first positive peak to 5.0% drift.

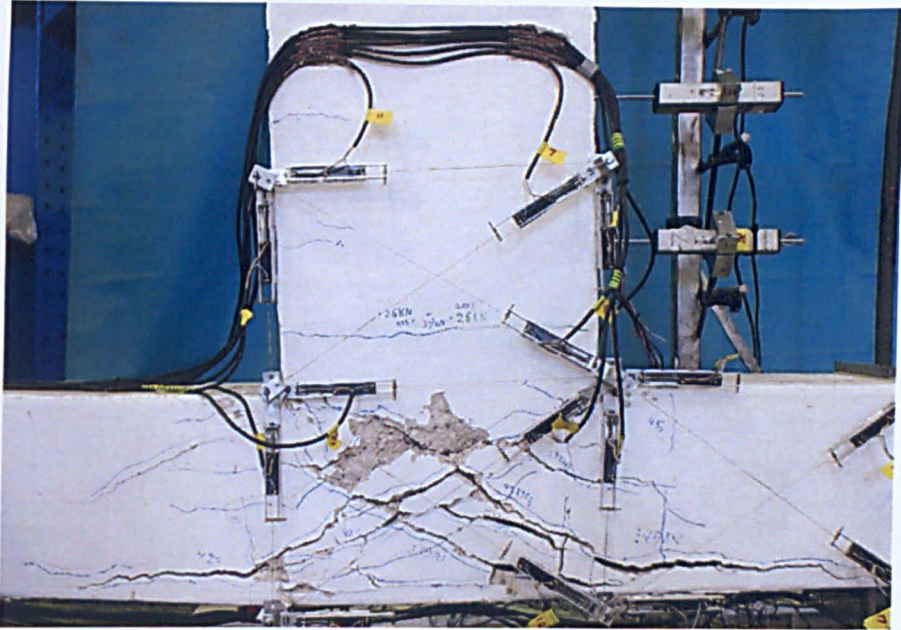


Figure B.11 Specimen JA-3 at the first positive peak to 4.0% drift

B.2 SPECIMEN JB-2: Description of Damage

Specimen JB-2 was subjected to the same displacement history as JB-1. However, the column's axial compression force was increased from 150 to 250kN. Figure B.12 shows how cracks were developed between 0.25% and 2.0% drift levels. Arrows denote the direction of positive loading and the top side of the beam.

Figure B.13 shows the cyclic load-drift response of specimen JB-2 and the overall envelope. In addition, key changes to the response envelope are marked and denoted.

The damage observed during the first cycle at 0.1% drift was limited to hairline cracks which were of width less than 0.1 mm. Except for these cracks, no further damage was observed throughout the first three cycles.

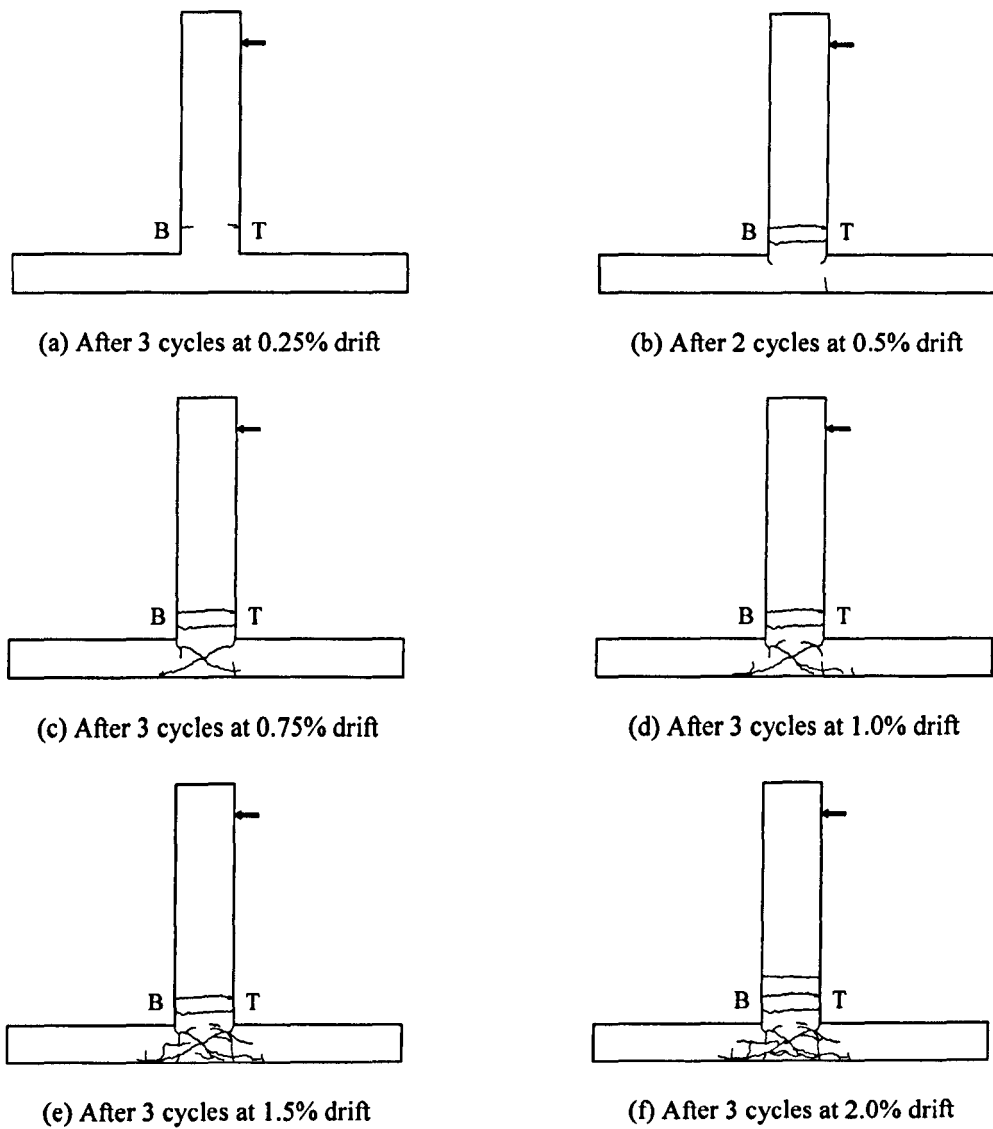


Figure B.12 Progression of cracking for specimen JB-2

A limited level of damage was achieved by specimen JB-2 during the 0.25% drift cycles. During the first positive loading, a crack was formed at the location of the second beam shear link. A similar crack was observed during the second half of the same cycle. All observed cracks were of width less than 0.5 mm.

As the test continued, no further damage was observed during the remaining two cycles. Figure B.12.a shows the crack pattern of specimen JB-1 after three cycles at 0.25% drift.

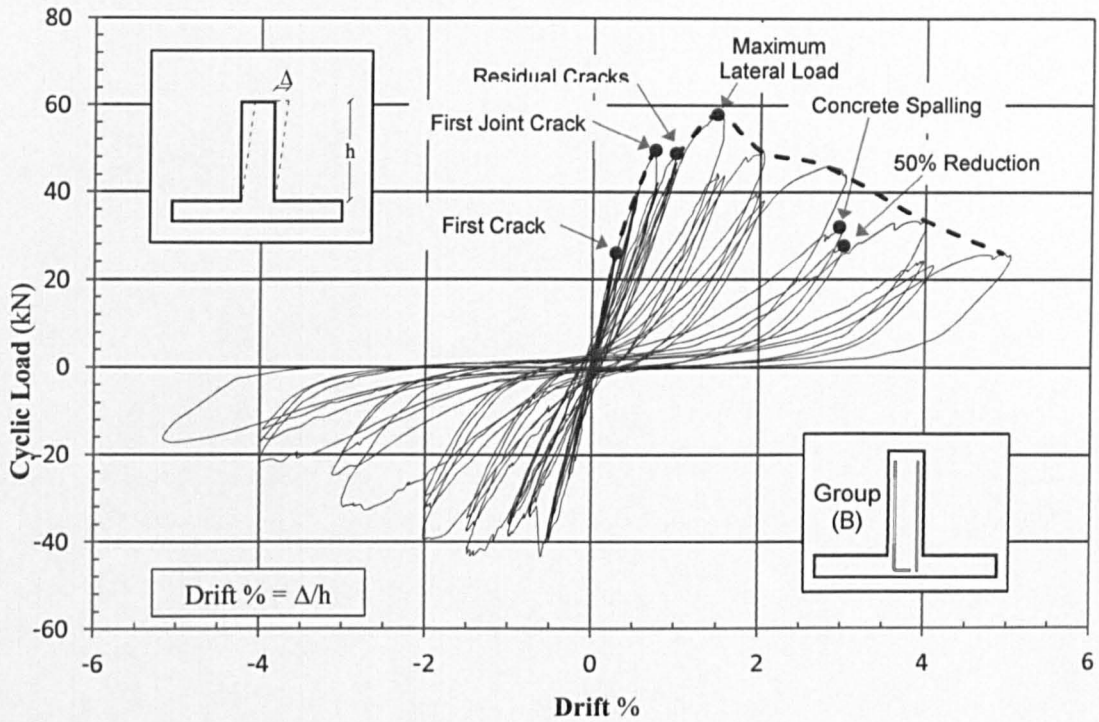


Figure B.13 Lateral load-drift response for specimen JB-2

During the first positive loading to 0.5% drift level, several new cracks formed in the beam. The existing crack at the location of the second shear link extended further as the test progressed and connected with the opposite crack. At the same time, a new crack appeared across the beam height and at the location of the first beam shear link. These cracks were accompanied by an inclined crack at the top column-beam corner, denoted as C1 in Figure B.14.a. The width of all formed cracks was less than 1mm.

Similarly, the second half of the same cycle showed almost identical crack pattern. However, in addition to the crack at the bottom column-beam corner (denoted here as C2), a new crack, denoted as C3, formed exactly at the top column-joint interface and extended till the mid height of the column, as shown in Figure B.14.b.

The remaining two cycles at 0.5% drift level exhibited no further damage. Figure B.12.b. shows the exhibited crack pattern for specimen JB-2 after three cycles at 0.5% drift.

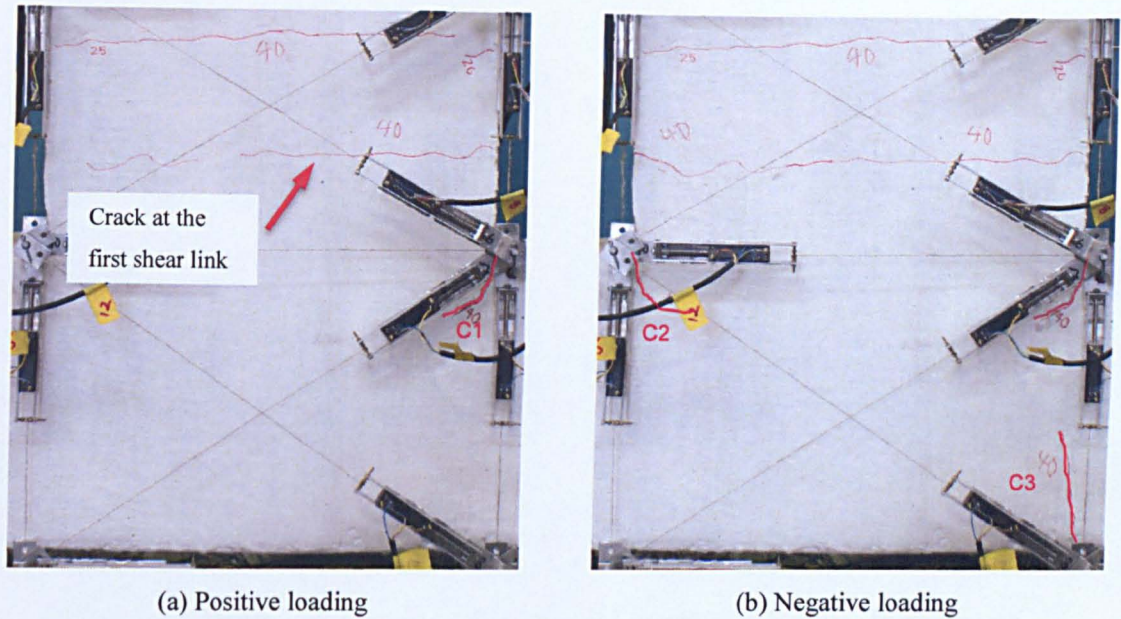


Figure B.14 Specimen JB-2 after one cycle at 0.5% drift

Specimen JB-2 exhibited a significant level of damage during the 0.75% drift level. During the first positive loading and exactly at a drift level equal to 0.61%, an inclined shear crack suddenly appeared across the joint. The crack connected to the bottom column-beam corner C2 and extended along the joint diagonal into the top column, as shown in Figure B.15.a. The formed diagonal crack C2 caused a sudden drop in the applied lateral load (see Figure B.13).

Similar damage was observed during the second half of the first cycle. However, the formed diagonal shear crack C1, in this case, extended further into the bottom column, as shown in Figure B.15.b.

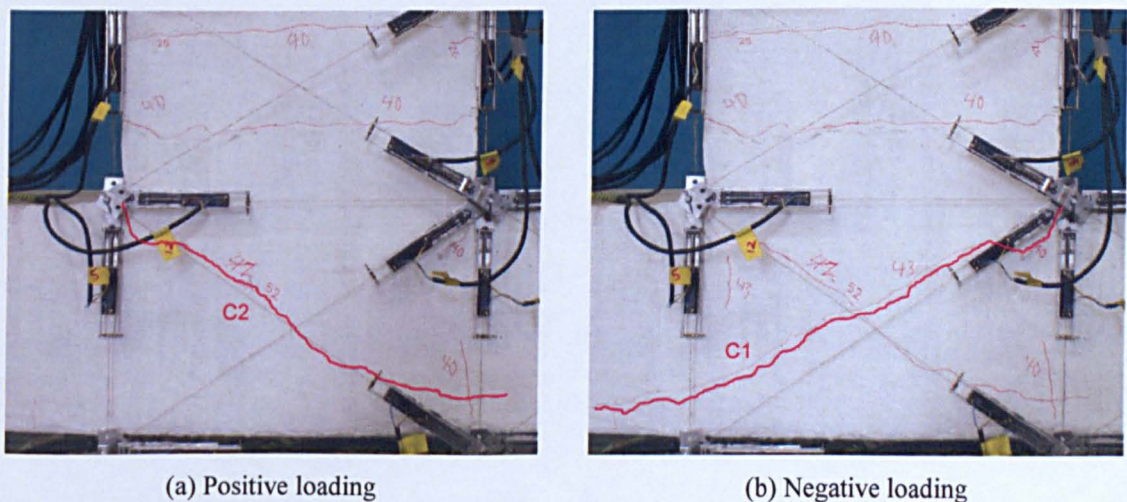


Figure B.15 Specimen JB-2 after one cycle at 0.75% drift

As the tests progressed to the second cycle, a significant stiffness and strength reduction was evident, (see Figure B.13). However, no further damage was observed during the second and

third cycles. Figure B.12.c shows the exhibited crack pattern of specimen JB-2 at the end of the third cycle at 0.75% drift.

No new cracks were observed during positive and negative loading of the first cycle at 1.0% drift. However, the two diagonal shear cracks C1 and C2 extended further into the top and bottom columns. In addition, the width of all cracks was increased, especially cracks in the joint. Cracks as wide as 2 mm were observed at both the positive and negative peak drift value.

No further damage was observed during the remaining 2 cycles of 1.0% drift, as can be seen in Figure B.16. However, when the specimen was brought to zero drift, by the end of the third cycle, residual cracks as wide as 1 mm were observed. Figure B.12.d shows the crack pattern of specimen JB-2 after three cycles at 1.0% drift.

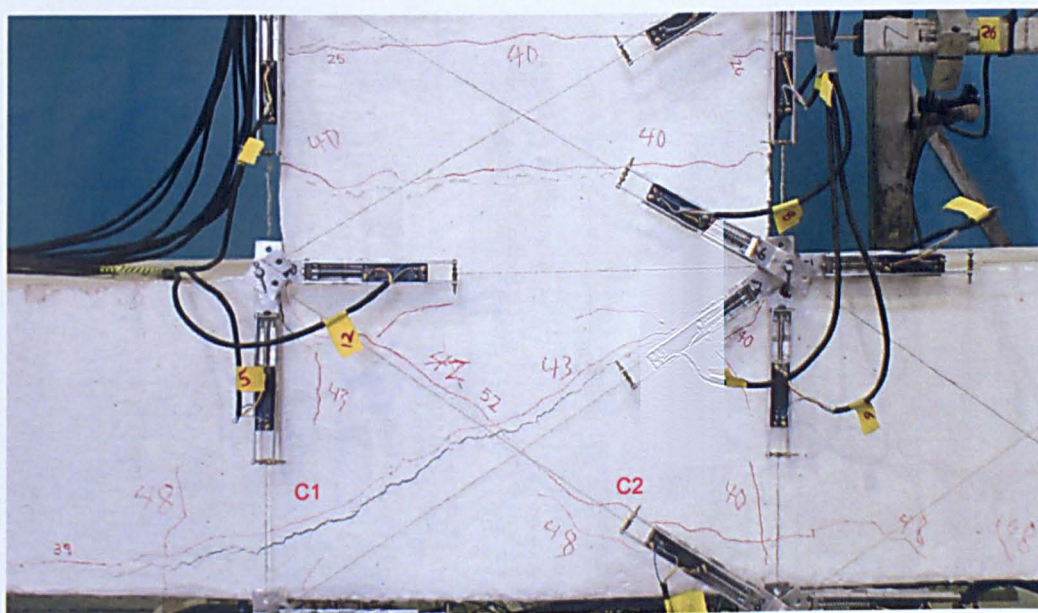


Figure B.16 Specimen JB-2 after three cycles at 1.0% drift

Specimen JB-2 suffered significant damage during the first cycle at 1.5% drift. Existing cracks became bigger in both length and width. In addition, some new cracks formed in the joint. Diagonal shear cracks due to negative loading measured 4mm wide while only 2mm for positive loading. Figure B.17 shows specimen JB-2 at both the positive and negative peak drift values of the first cycle at 1.5% drift.

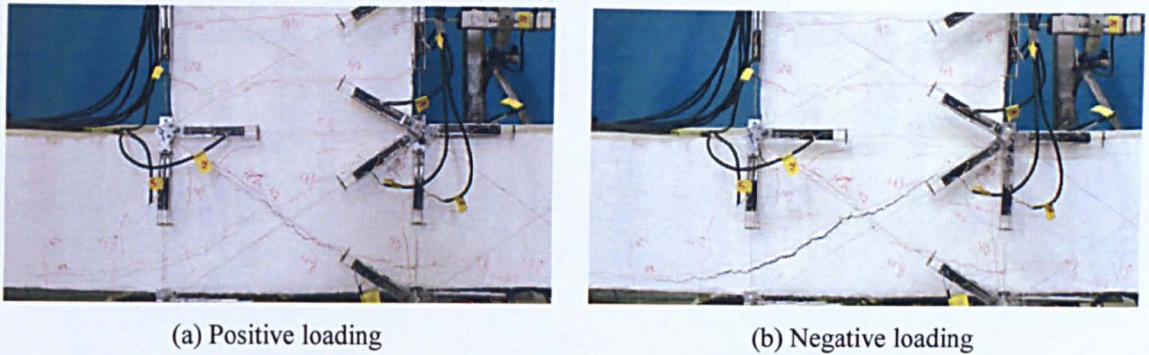


Figure B.17 Specimen JB-2 after one cycle at 1.5% drift

At this drift level, and during the first half cycle, the maximum load carrying capacity was achieved, as shown in Figure B.13. However, no reinforcement yielding or concrete spalling was observed.

No further damage was observed during the remaining two cycles, as shown in Figure B.18. However, as the test progressed, the specimen kept becoming softer which caused a massive 23% strength reduction between the first and the second cycle, (see Figure B.13). Figure B.12.e shows the crack pattern of specimen JB-2 after three cycles at 1.5% drift.

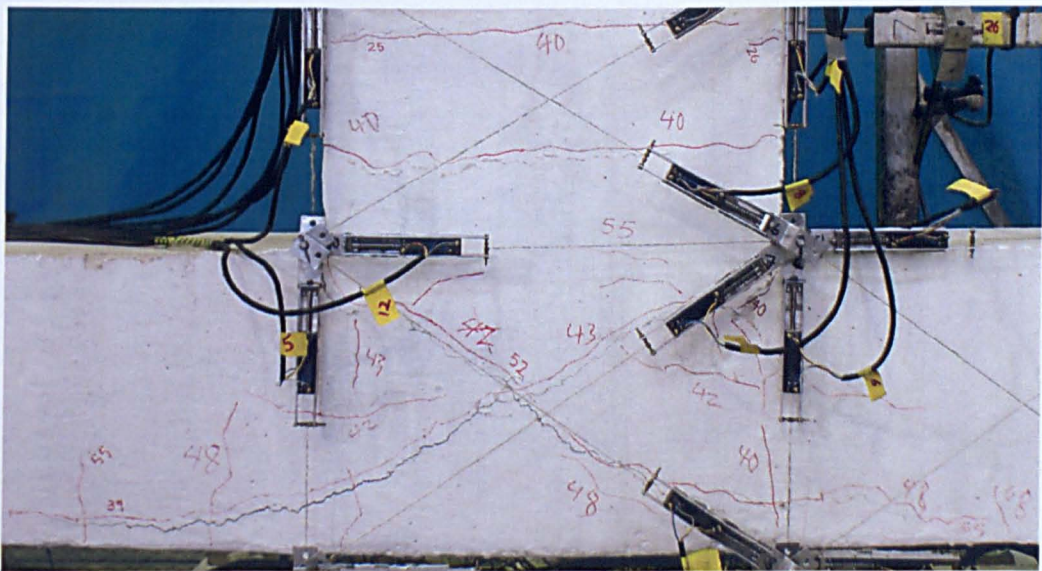


Figure B.18 Specimen JB-1 after three cycles at 1.5% drift

Specimen JB-2 was heavily damaged during the 2.0% drift cycles. The diagonal cracks C1 and C2 extended further into the top and bottom columns following the path of the column longitudinal reinforcement. In addition, many new cracks formed, especially in the joint area.

The extensive damage caused concrete flaking around the intersected diagonal cracks at the centre of the joint, as shown in Figure B.19. As the test continued, the observed damage increased with each cycle causing a 19% loss in strength between the first and the second cycle, (see Figure B.13). Cracks at both peak drift values ranged between 3 to 6 mm. Figure B.12.f

shows the final observed crack pattern of specimen JB-2 after completing three cycles at 2.0% drift.

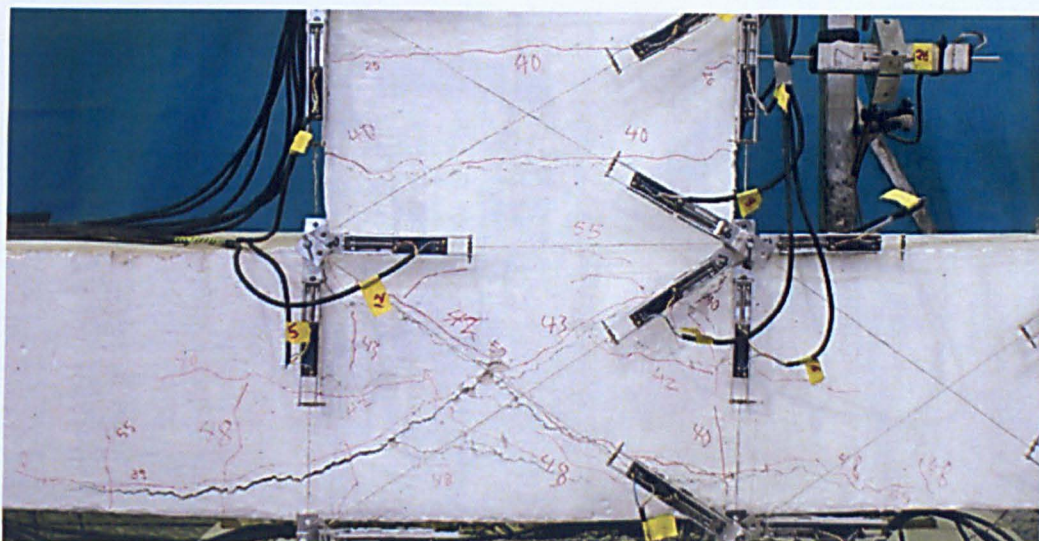


Figure B.19 Specimen JB-2 after three cycles at 2.0% drift

The specimen was severely damaged during the first cycle of the 3.0% drift level. As the specimen was displaced to the first positive peak, several diagonal cracks appeared and connected to the already existing ones.

During negative loading of the first cycle, the two central diagonal cracks extending into the columns opened widely leaving the bottom concrete cover barely hanging. The observed diagonal cracks at peaks measured around 10 to 15 mm. Figure B.20 shows specimen JB-2 after completing one cycle at 3.0% drift.

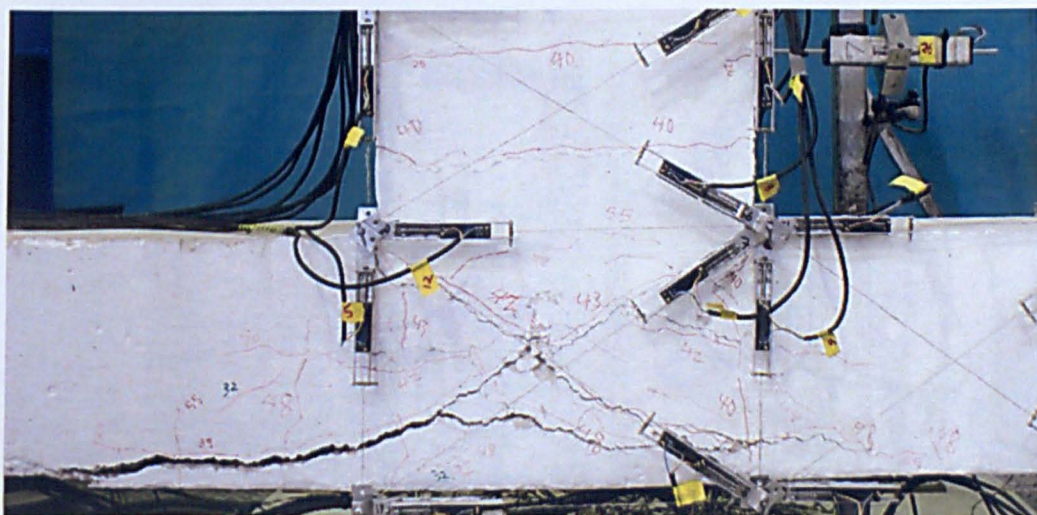


Figure B.20 Specimen JB-2 after one cycle at 3.0% drift

As the test continued, the specimen kept becoming weaker with each cycle leading to further loss in both strength and stiffness. The strength reduction was approximately 31% between the

The test was continued by displacing the joint to 5% drift level. However, the specimen was near the point of total collapse, and therefore only one cycle was performed. Figure B.23 shows specimen JB-1 after completing one cycle at 5.0% drift.

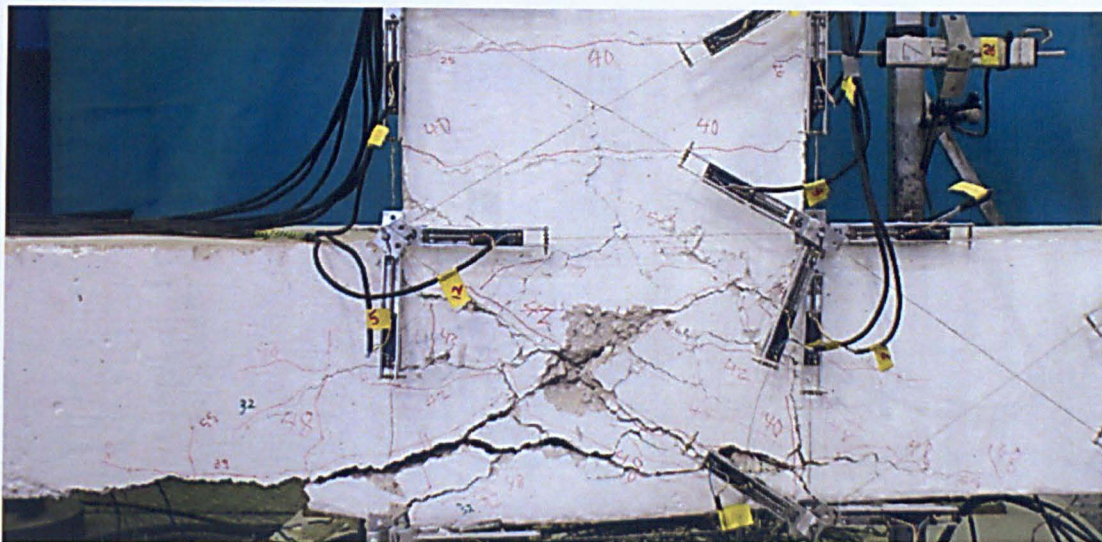


Figure B.23 Specimen JB-2 after one cycle at 5.0% drift

B.3 SPECIMEN JC-2: Description of Damage

Specimen JC-2 was subjected to the same displacement history as specimens in group A and B. Similarly to JA-3 and JB-2, the column of JC-2 was subjected to an axial compressive force equal to 250 kN. Figure B.24 shows how cracks developed between 0.25% and 2.0% drift levels. Arrows denote the direction of positive loading.

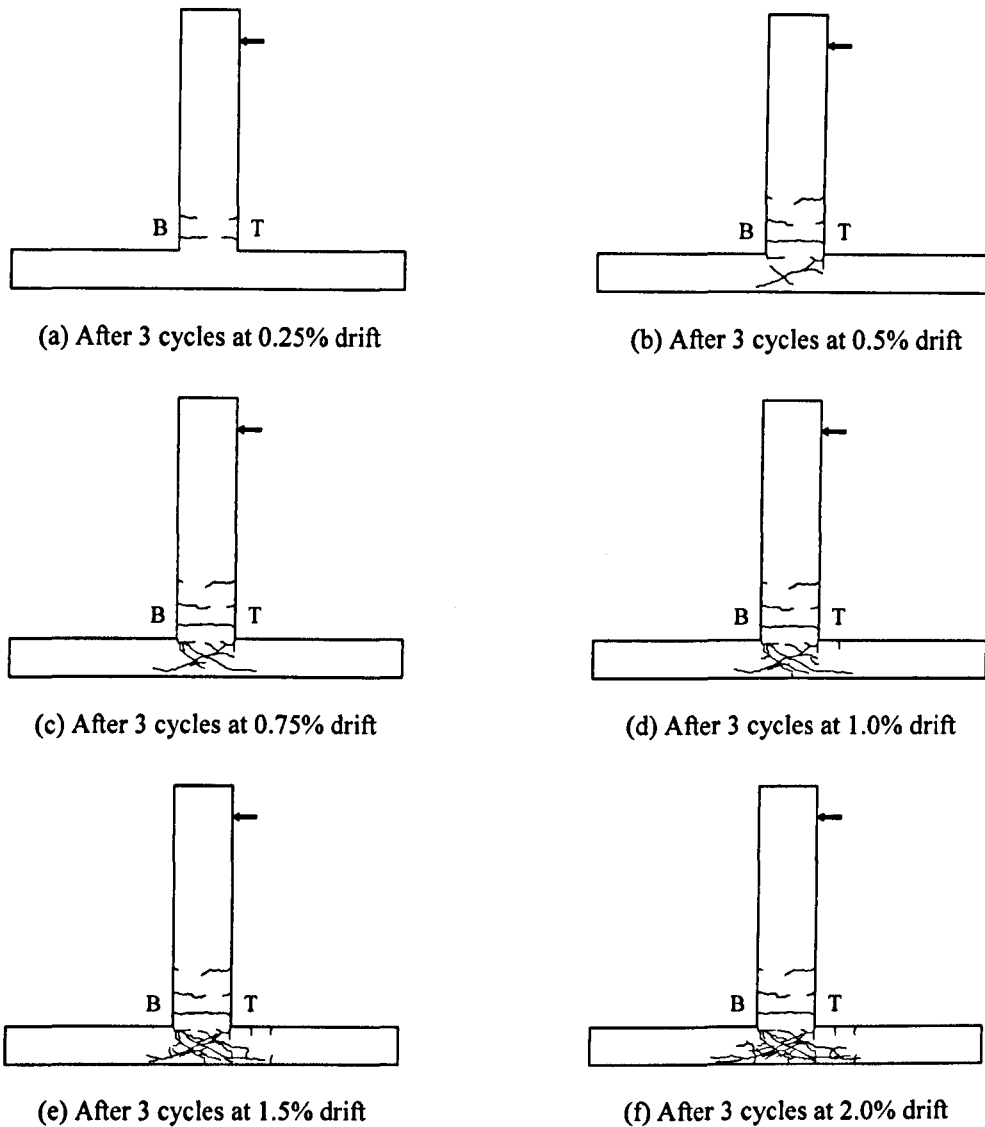


Figure B.24 Progression of cracking for specimen JC-2

Figure B.25 shows the cyclic load-drift response of specimen JC-2 and the overall envelope. Key changes to the response envelope are marked and denoted. The damage observed during the first cycle at 0.1% drift was limited to hairline cracks which were of width less than 0.1 mm. Apart from these cracks, no further damage was observed throughout the remaining cycles at 0.1% drift level.

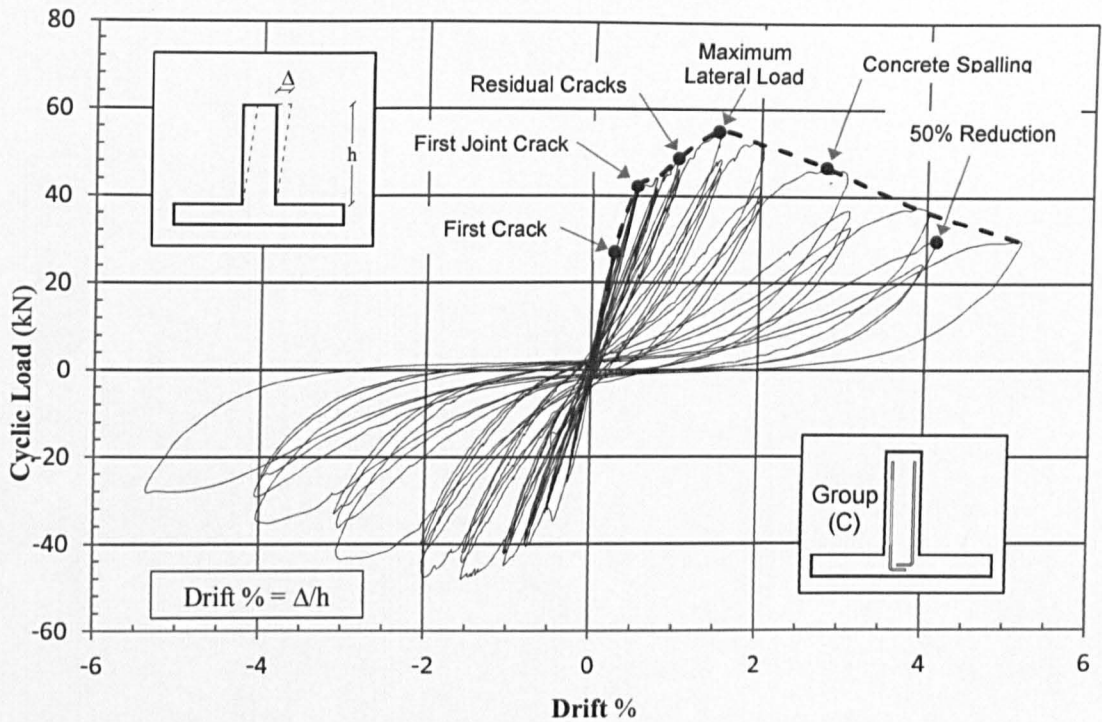
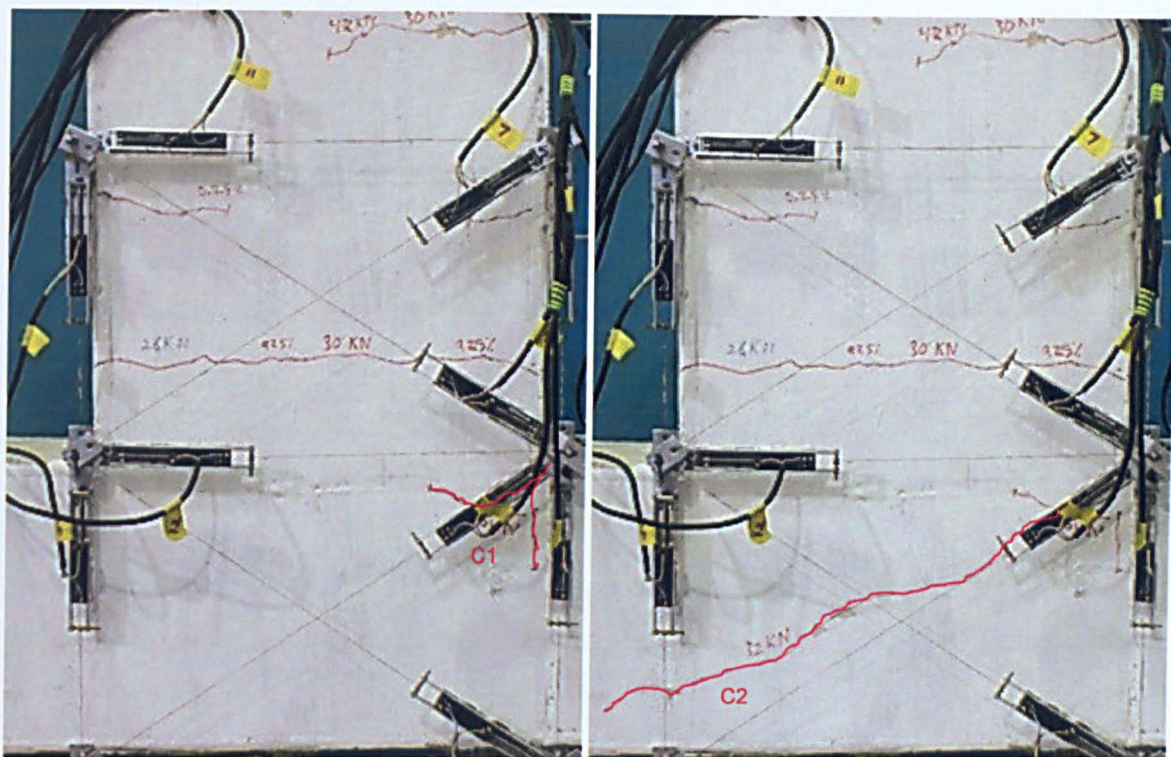


Figure B.25 Lateral load-drift response for specimen JC-2

Specimen JC-2 suffered a limited level of damage during the 0.25% drift cycles. On the way to the first positive peak, two horizontal cracks were observed around the location of the first and second beam shear links. A similar crack pattern on the opposite side of the beam was observed during the second half of the same cycle.

As the test continued, no further damage was observed during the remaining two cycles. All observed cracks were of width less than 1mm. Figure B.24.a shows the crack pattern of specimen JC-2 after three cycles at 0.25% drift.

During the first positive loading at 0.5% drift level, existing beam cracks increased in both width and length. When the specimen reached a drift level equal to 0.32%, a new crack appeared around the location of the third shear link from the beam-column interface. In addition, the first horizontal crack extended over the entire width of the beam. Moreover, as positive loading continued, a new inclined crack, denoted as C1 in Figure B.26.a, was formed at the top column-beam corner and extended (in the shape of two branches) into the joint core. The width of all observed cracks was less than 1mm.



(a) Positive loading

(b) Negative loading

Figure B.26 Specimen JC-2 after one cycle at 0.5% drift

During the second half of the same cycle; and as negative loading continued, a long diagonal crack suddenly appeared and caused a steep drop in the applied lateral load, (see Figure B.25). The formed crack, denoted as C2 in Figure B.26.b, started from the top column-beam corner and extended along the joint diagonal all the way to the bottom, as shown in Figure B.26.b.

During the first half of the second cycle, a new crack, denoted as C3, appeared around the beam-column interface. In addition, two new cracks (denoted as C4 and C5) formed around the diagonal crack C2, as shown in Figure B.27. The remaining cycle at 0.5% drift level exhibited no further damage. Figure B.24.b. shows the exhibited crack pattern for specimen JB-2 after three cycles at 0.5% drift.

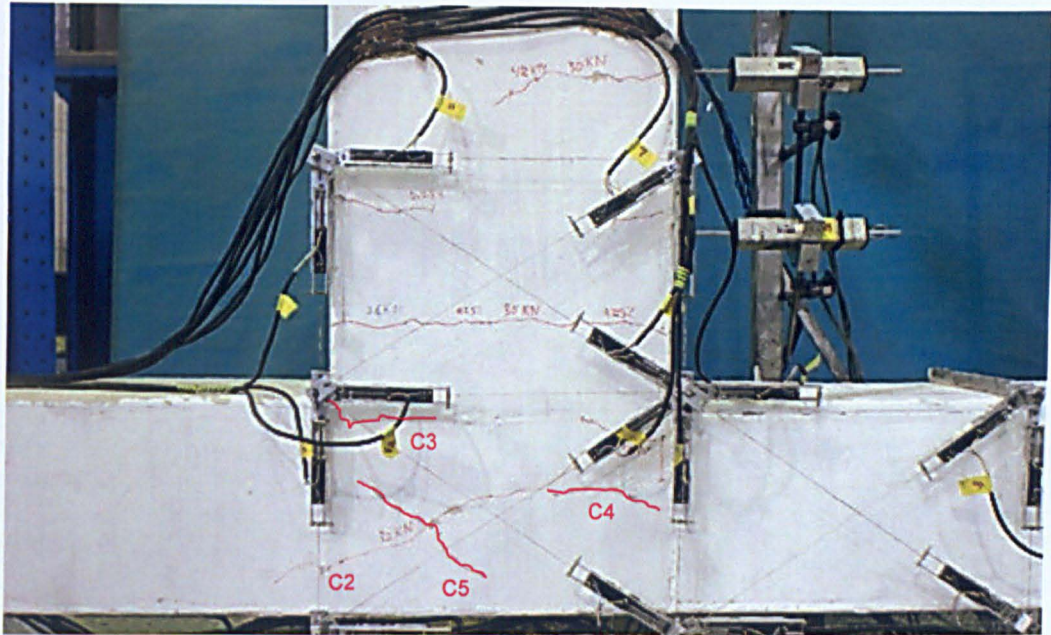
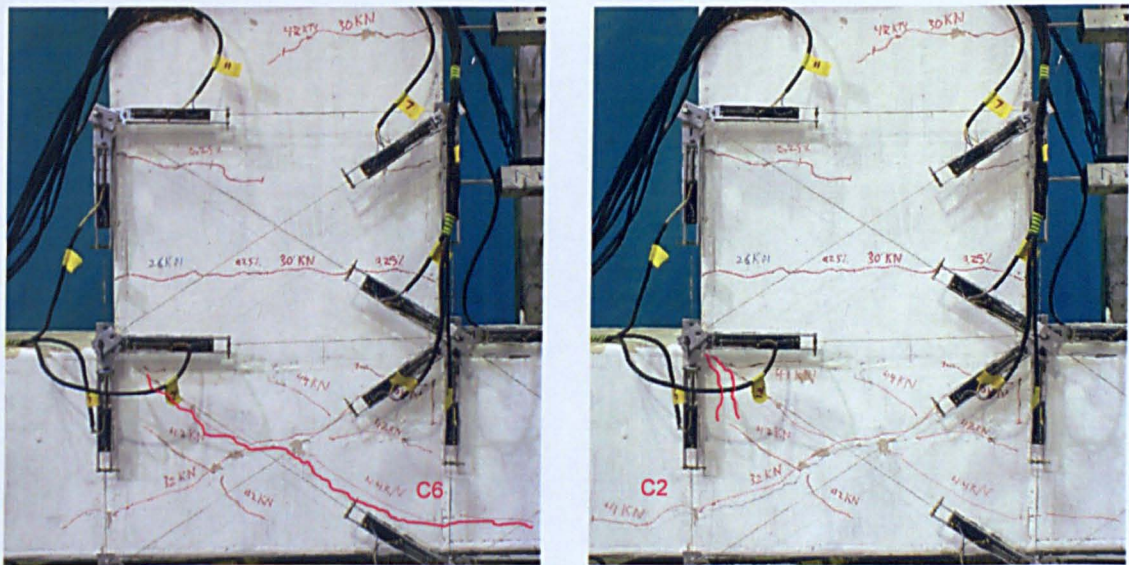


Figure B.27 Specimen JC-2 after two cycles at 0.5% drift

Specimen JC-2 exhibited a significant level of damage during the 0.75% drift level. During the first positive loading and exactly at the peak drift value, an inclined shear crack, denoted as C6, suddenly appeared across the joint. The crack C6 started from the bottom column-beam corner and extended along the joint diagonal into the top column, as shown in Figure B.28.a.



(a) Positive loading

(b) Negative loading

Figure B.28 Specimen JC-2 after one cycle at 0.75% drift

During negative loading of the same cycle, the diagonal joint crack C2 extended further into the bottom column, whereas several new cracks formed around the bottom column-beam corner, as shown in Figure B.28.b. Cracks as wide as 1 mm were observed at both the positive and negative peaks.

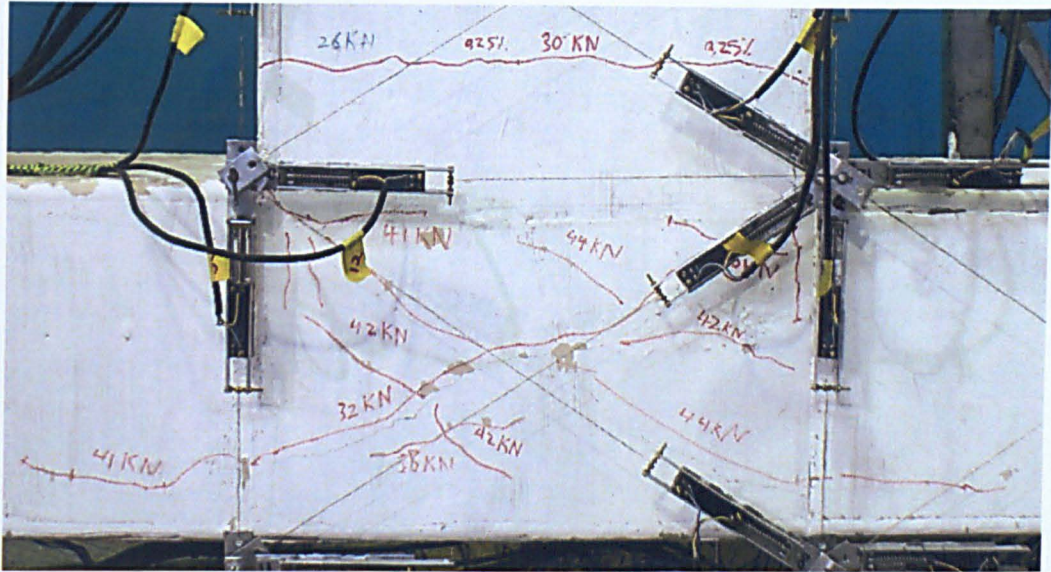
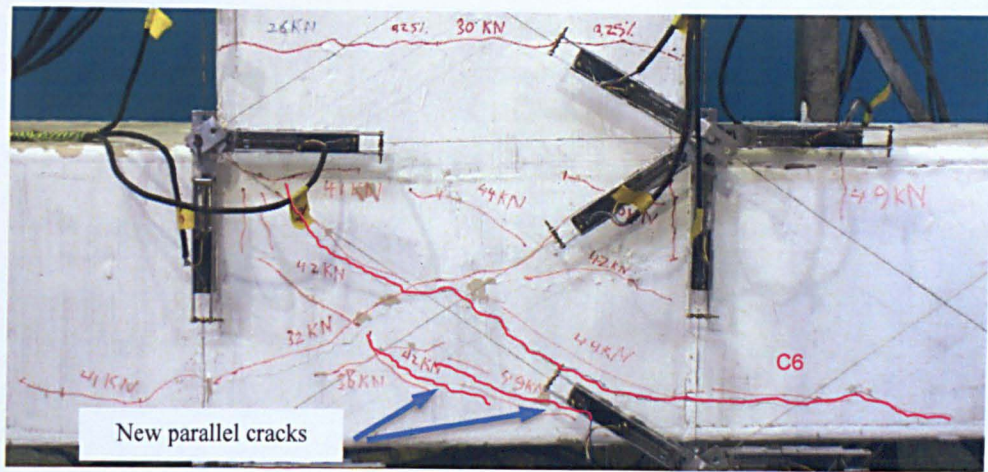


Figure B.29 Specimen JC-2 after three cycles at 0.75% drift

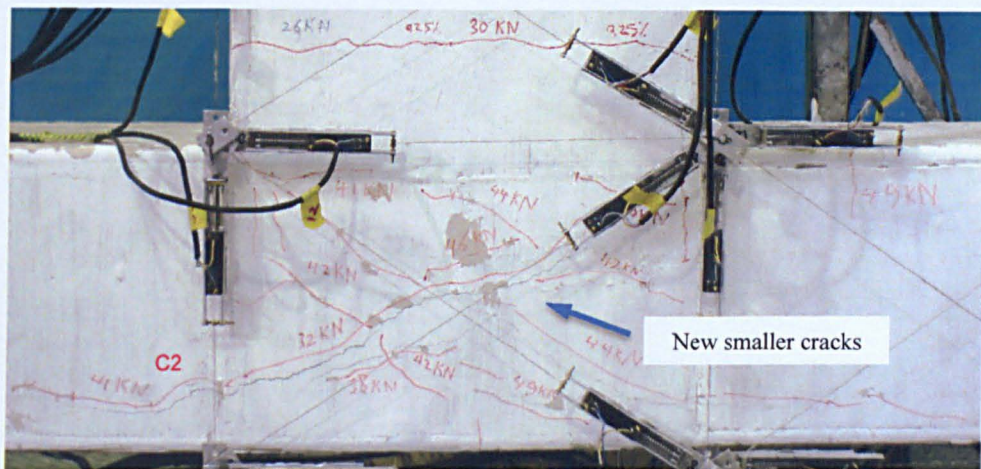
As the test continued to the second and third cycles, several new cracks formed in the joint area, whereas existing cracks extended and widened even further, as can be seen in Figure B.29. Figure B.24.c shows the exhibited crack pattern of specimen JC-2 at the end of the third cycle at 0.75% drift.

On the way to the first positive peak at 1.0% drift level, two new cracks almost parallel to the joint diagonal were observed. At the same time, the main diagonal joint crack C6 extended further into the top column following the path of the column longitudinal reinforcement, as shown in Figure B.30.a.

Similarly, during the second half of the same cycle, existing diagonal cracks especially C2 widened and extended further into the bottom column. In addition, several new smaller cracks formed around the joint centre, as can be seen in Figure B.30.b. The width of diagonal crack at the negative peak measured 2mm whereas only 1.5 mm at the positive peak.



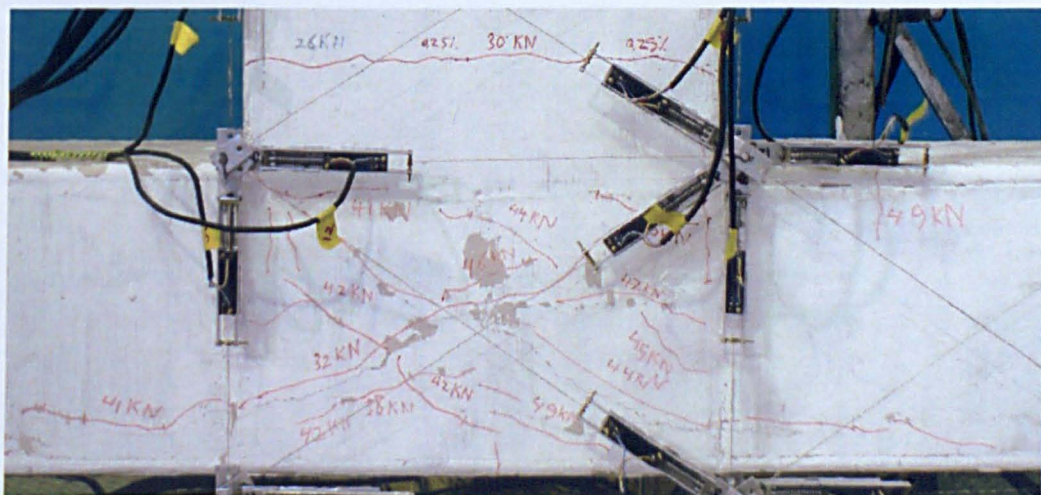
(a) Positive loading



(b) Negative loading

Figure B.30 Specimen JC-2 after one cycle at 1.0% drift

As the test continued to the second and third cycle, no further damage was observed, as can be seen in Figure B.31. In addition, when the specimen was brought to 0% drift level, by the end of the third cycle, residual cracks as wide as 1 mm were observed. Figure B.24.d shows the crack pattern of specimen JC-2 after three cycles at 1.0% drift.

**Figure B.31 Specimen JC-2 after three cycles at 1.0% drift**

Specimen JC-2 was heavily damaged during the 2.0% drift cycles. The existing joint cracks increased in width and intersected at the centre of the joint. In addition, the main diagonal cracks extended further into the top and bottom columns following the path of the column longitudinal reinforcement. The extensive damage caused concrete flaking around the intersected diagonal cracks at the centre of the joint, as can be seen in Figure B.34.

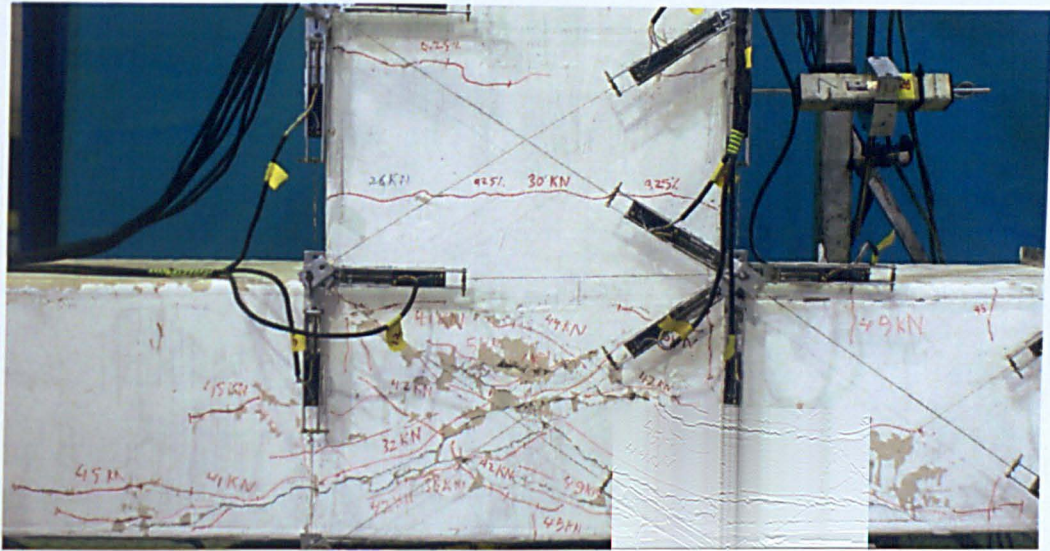
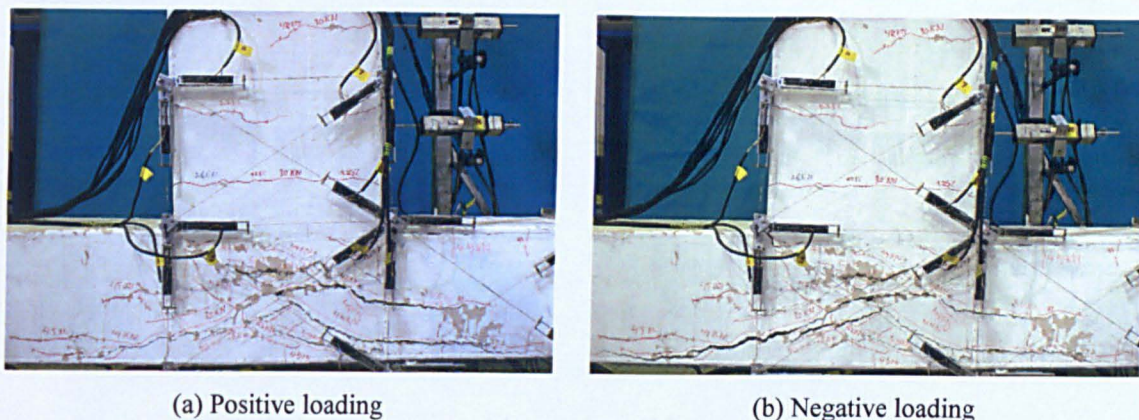


Figure B.34 Specimen JC-2 after three cycles at 2.0% drift

As the test continued, the observed damage increased with each cycle causing a 19% loss in strength between the first and the second cycle, (see Figure B.25). Measured cracks at peaks ranged between 6 to 8 mm. Figure B.24.f shows the final observed crack pattern of specimen JC-2 after completing three cycles at 2.0% drift.

The specimen was severely damaged during the 3.0% drift cycles. The already existing central cracks opened widely causing extensive damage to the concrete core. In addition, the main diagonal cracks extended further into the top and bottom columns. The top column; however, suffered far greater damage, as in addition to the main longitudinal crack, another joint crack extended and penetrated the centre of the top column. The observed diagonal cracks at peaks measured around 10 to 12 mm. Figure B.35 shows specimen JC-2 after completing one cycle at 3.0% drift.

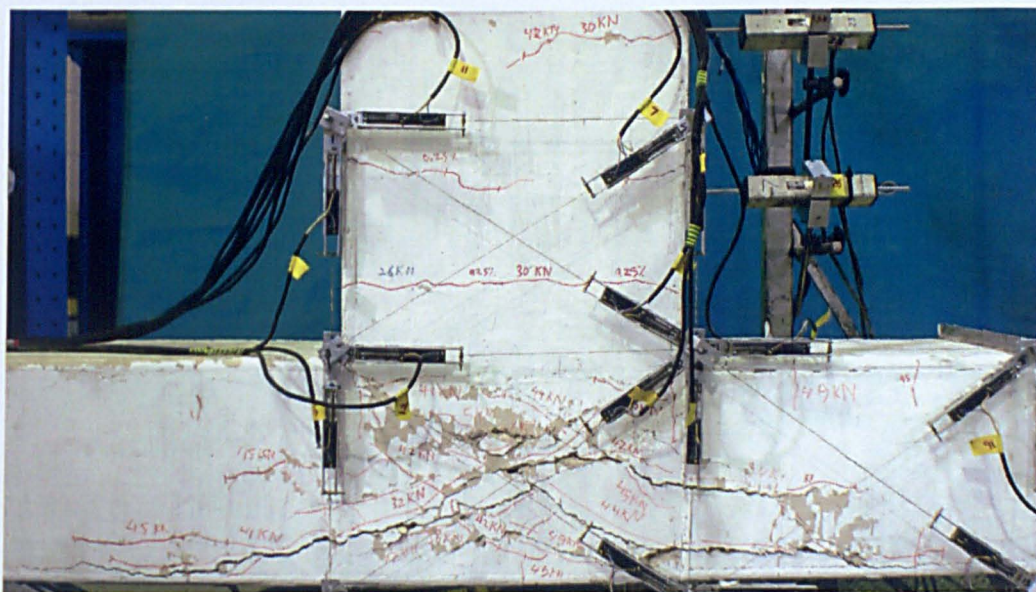


(a) Positive loading

(b) Negative loading

Figure B.35 Specimen JC-2 after one cycle at 3.0% drift

As the test continued, the specimen kept becoming weaker with each cycle leading to further loss in both strength and stiffness. The strength reduction was approximately 22% between the first and the second cycle, whereas the reduction between the first and the third cycle was around 30%, (see Figure B.25). At the end of the third cycle, the damage was so extensive that small pieces of concrete fell out from the centre of the joint. Figure B.36 shows concrete spalling of specimen JC-2 after completing three cycles at 3.0% drift.

**Figure B.36 Specimen JC-2 after three cycles at 3.0% drift**

During the 4.0% drift cycles, specimen JC-2 suffered further severe damage accompanied by continuous loss in both strength and stiffness. The total loss by the third cycle was 50% of the maximum lateral load capacity, as can be seen in Figure B.25. At the end of the third cycle, the specimen was severely damaged and suffering from extensive expansion in the core area. Figure B.37 shows the level of damage attained by specimen JC-2 after completing three cycles at 4.0% drift.

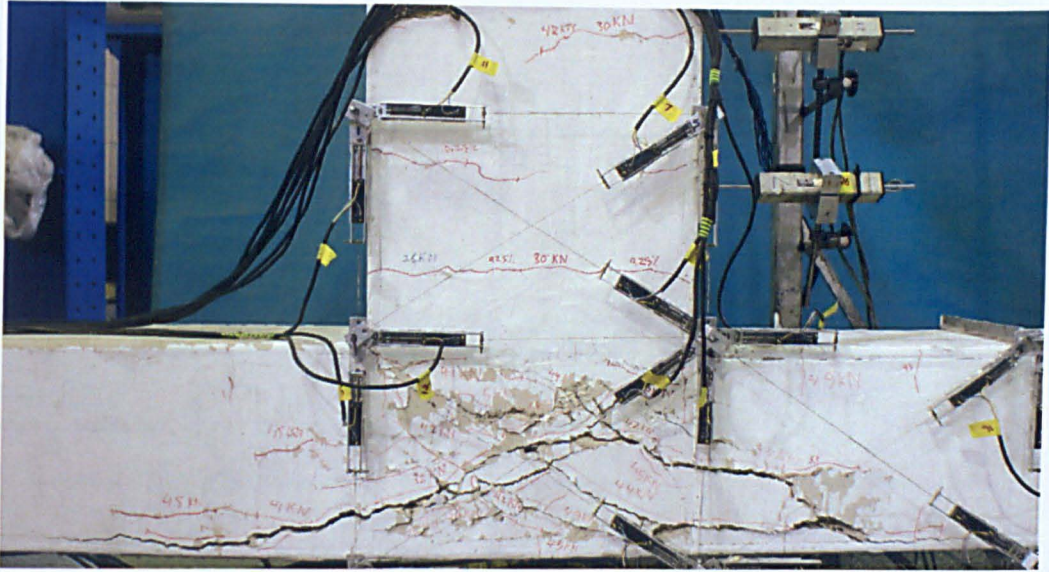


Figure B.37 Specimen JC-2 after three cycles at 4.0% drift

The test was continued by displacing the joint to the 5% drift level. Similarly to the previous drift level, the joint suffered further severe damage leaving the bottom concrete triangle barely hanging from the bottom longitudinal reinforcement.

After completing one full cycle, the specimen was near the point of total collapse. Therefore, for safety purposes, the test was stopped and concluded. Figure B.38 shows specimen JC-2 after completing one full cycle at 5.0% drift.

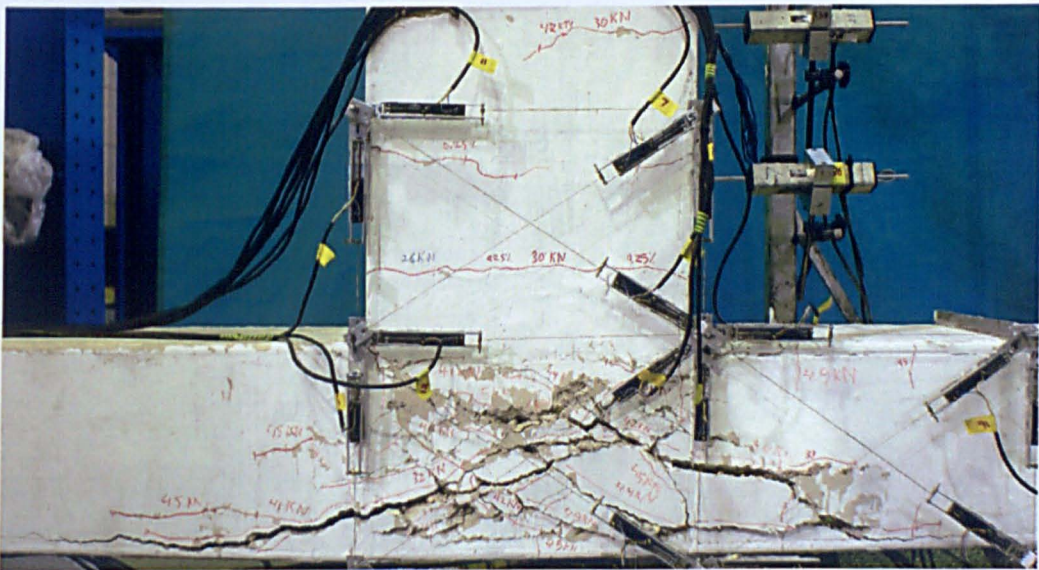


Figure B.38 Specimen JC-2 after one cycle at 5.0% drift

B.4 PERFORMANCE INDICATORS

B.4.1 Axial Load Capacity

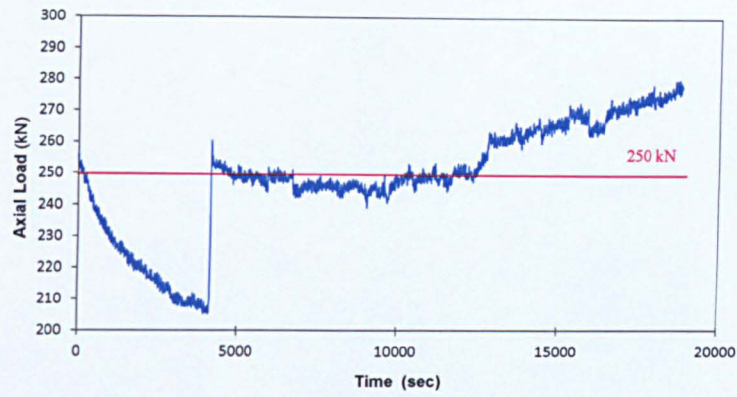


Figure B.39 Applied axial load history of specimen JA-3

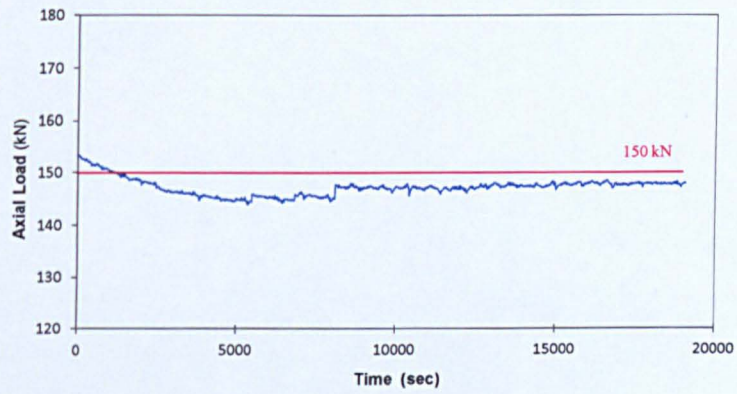


Figure B.40 Applied axial load history of specimen JB-1

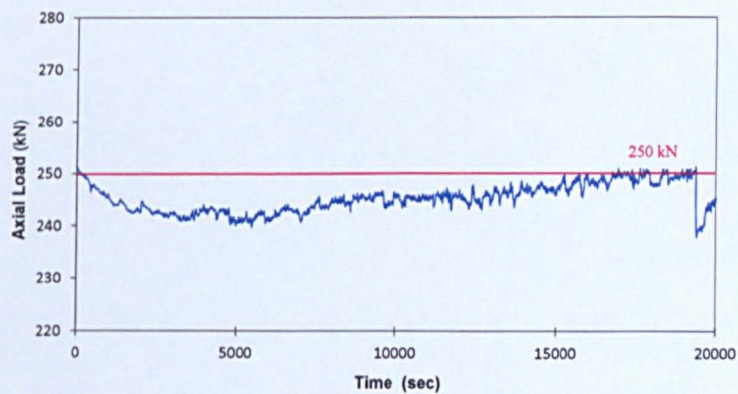


Figure B.41 Applied axial load history of specimen JB-2

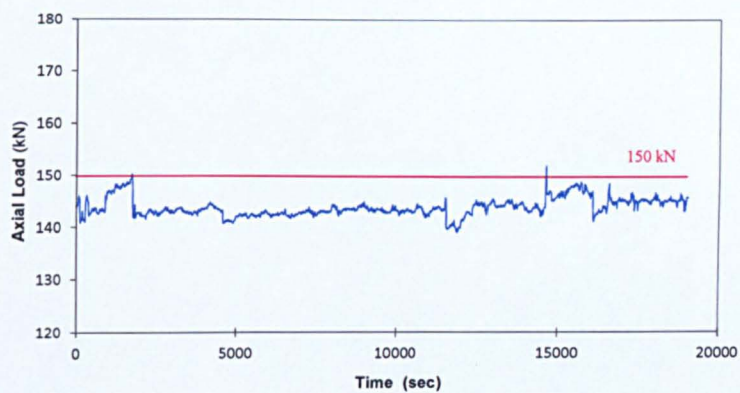


Figure B.42 Applied axial load history of specimen JC-1

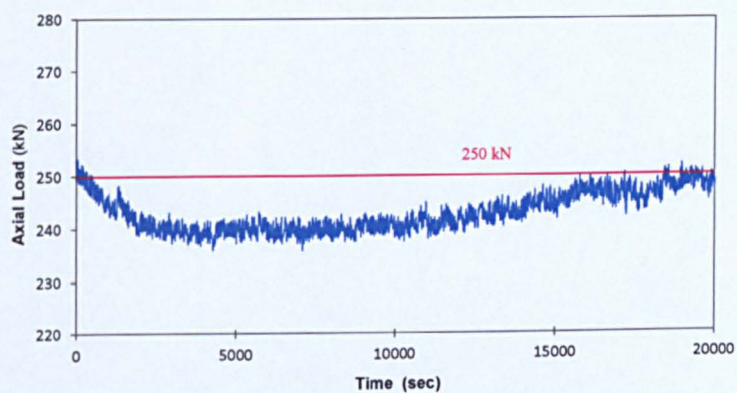


Figure B.43 Applied axial load history of specimen JC-2

B.4.2 Stiffness Degradation

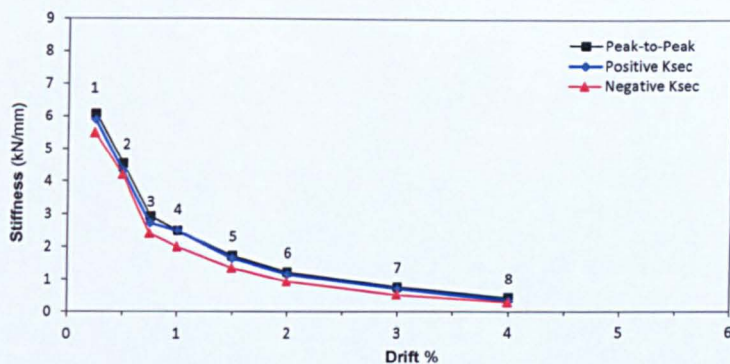


Figure B.44 Peak-to-peak and half-cycle secant stiffness degradation of specimen JB-1

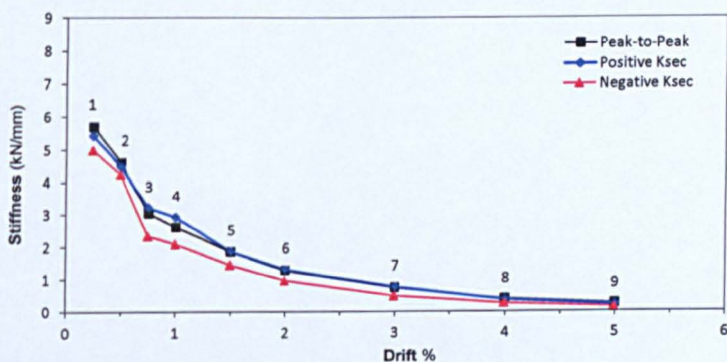


Figure B.45 Peak-to-peak and half-cycle secant stiffness degradation of specimen JB-2

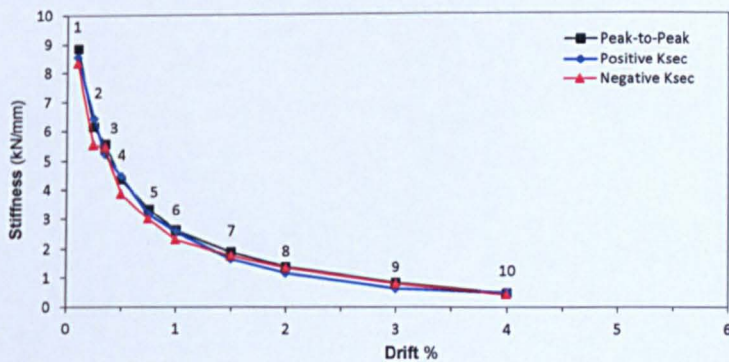


Figure B.46 Peak-to-peak and half-cycle secant stiffness degradation of specimen JC-1

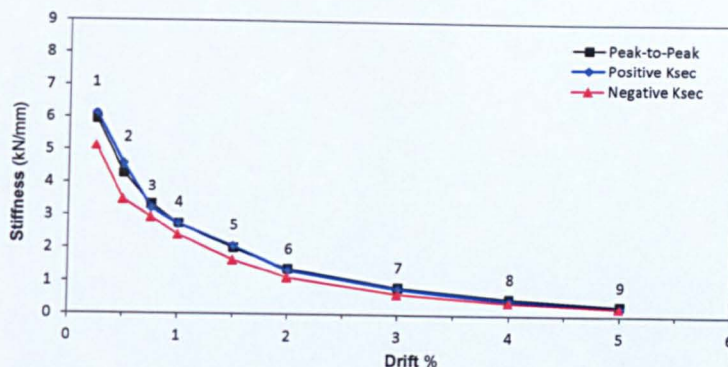


Figure B.47 Peak-to-peak and half-cycle secant stiffness degradation of specimen JC-2

B.4.3 Shear Stress-Strain Response Curve

Table B-1 Maximum measured joint shear stress-strain of groups B&C specimens

Specimen No.	Loading direction	Drift %	Shear stress (MPa)	γ ($\sqrt{\text{MPa}}$)	shear strain (Rad)	ASCE 41 ($\sqrt{\text{MPa}}$)
JB-1	+	1.59	2.9	0.52	0.0069	0.50
	-	-0.61	-2.4	-0.42	-0.0011	-0.50
JB-2	+	1.40	3.4	0.61	-	0.50
	-	-1.45	-2.5	-0.45	-	-0.50
JC-1	+	1.98	2.9	0.56	0.0067	0.50
	-	-1.39	-2.7	-0.52	-0.0051	-0.50
JC-2	+	1.49	3.2	0.56	0.0070	0.50
	-	-1.55	-2.8	-0.49	-0.0067	-0.50

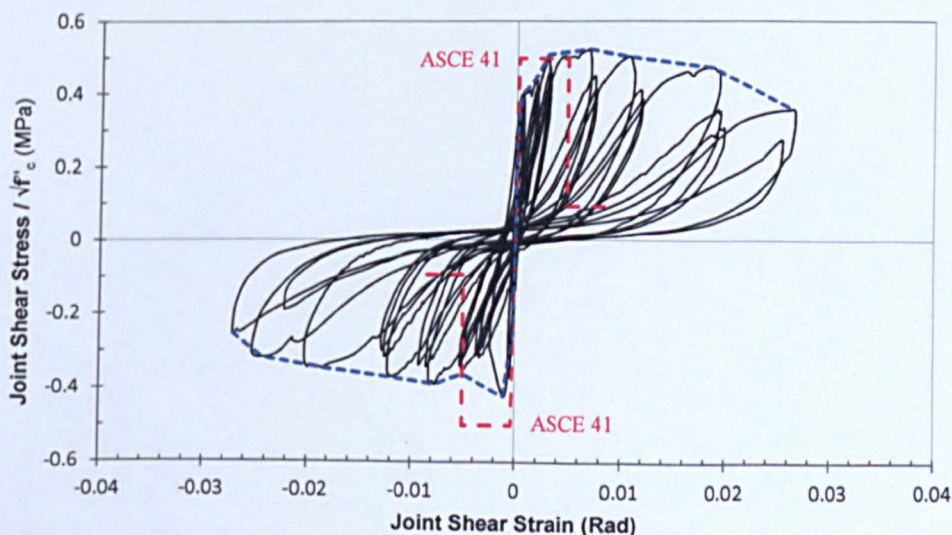


Figure B.48 Joint shear stress-shear strain of specimen JB-1

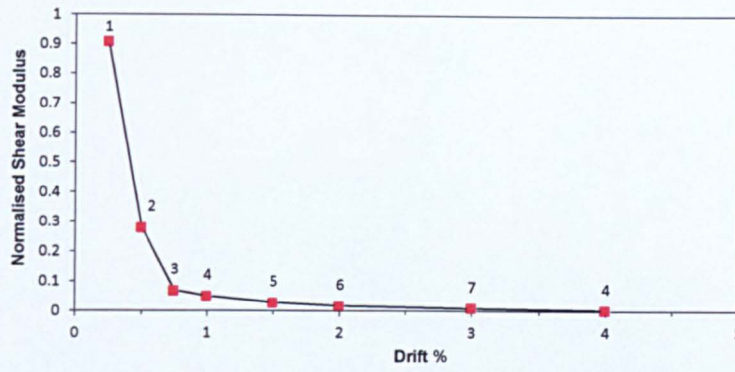


Figure B.49 Peak-to-peak Shear Modulus Degradation of specimen JB-1

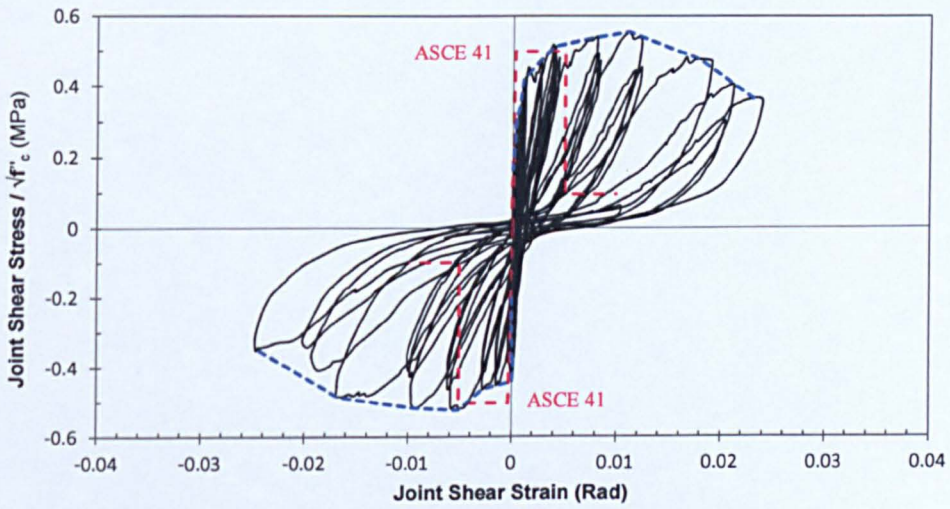


Figure B.50 Joint shear stress-shear strain of specimen JC-1

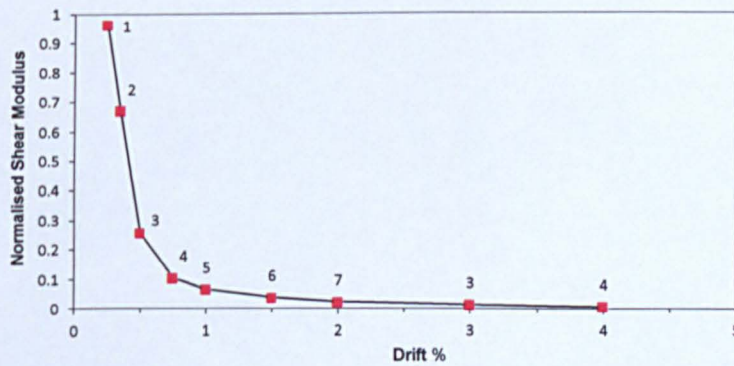


Figure B.51 Peak-to-peak Shear Modulus Degradation of specimen JC-1

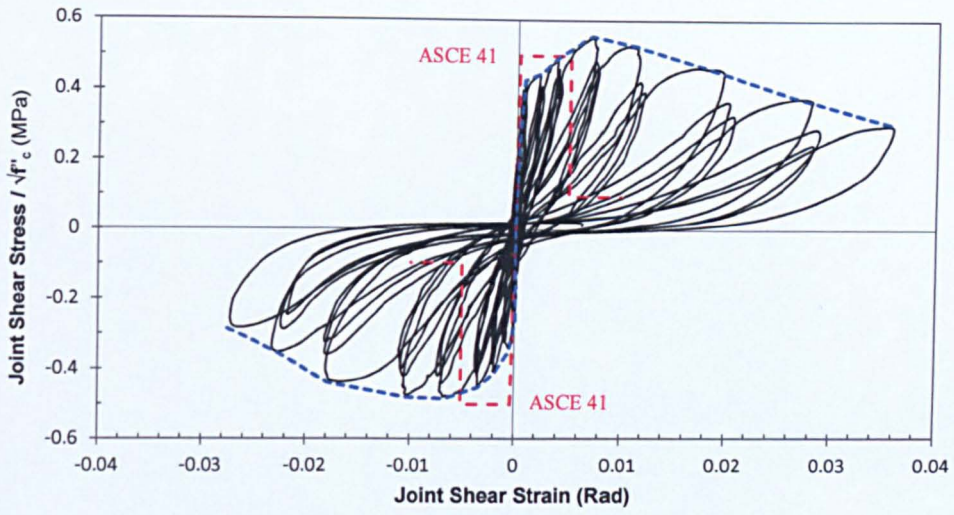


Figure B.52 Joint shear stress-shear strain of specimen JC-2

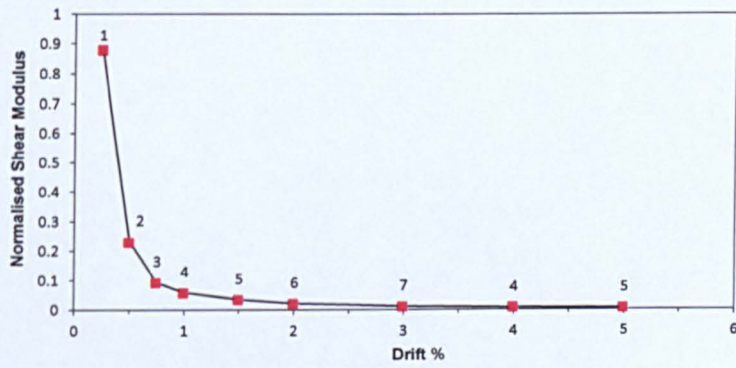


Figure B.53 Peak-to-peak Shear Modulus Degradation of specimen JC-2

B.4.4 Dissipated Energy

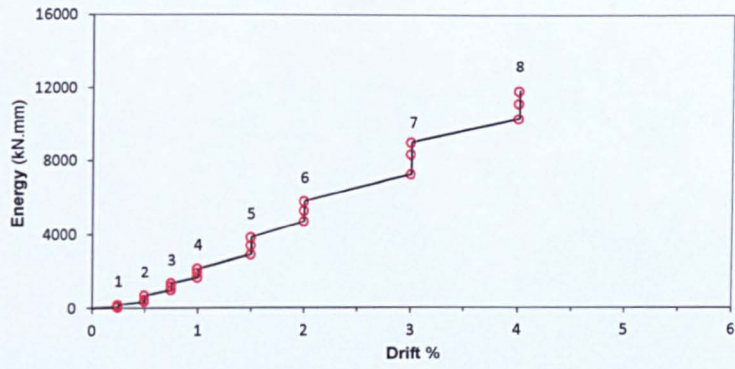


Figure B.54 Cumulative energy dissipation of specimen JB-1

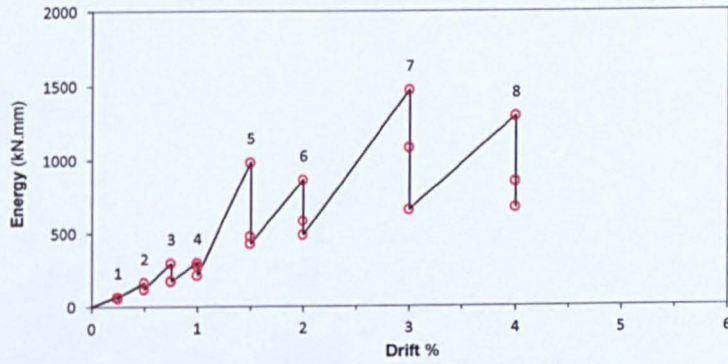


Figure B.55 Dissipated energy per cycle for specimen JB-1

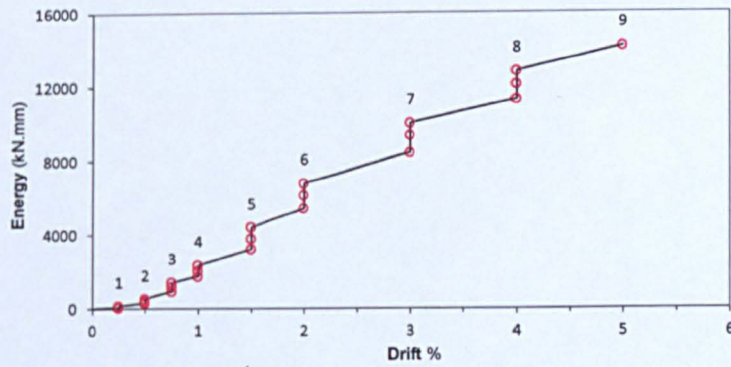


Figure B.56 Cumulative energy dissipation of specimen JB-2

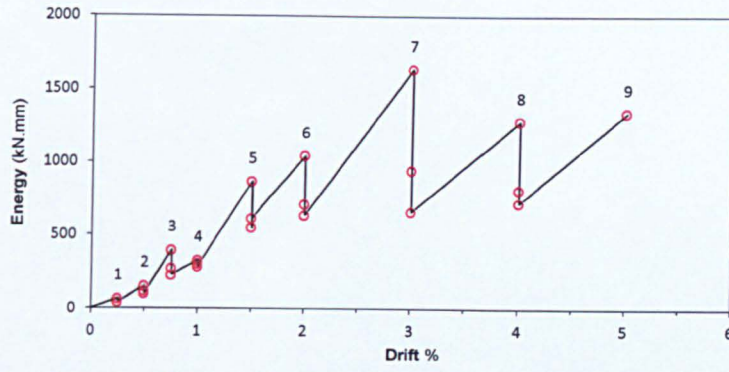


Figure B.57 Dissipated energy per cycle for specimen JB-2

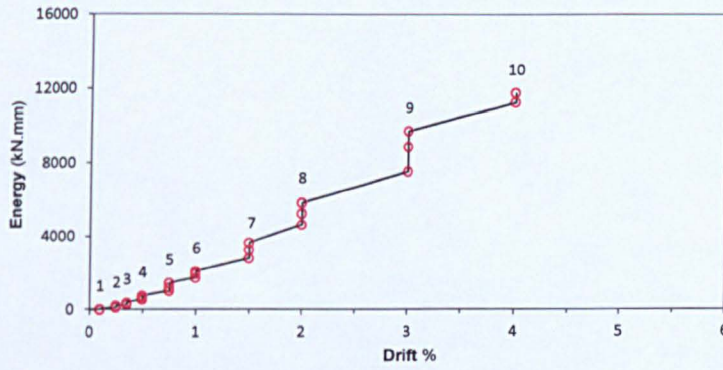


Figure B.58 Cumulative energy dissipation of specimen JC-1

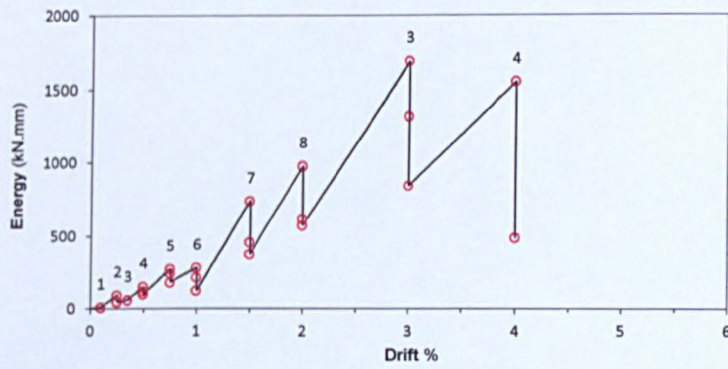


Figure B.59 Dissipated energy per cycle for specimen JC-1

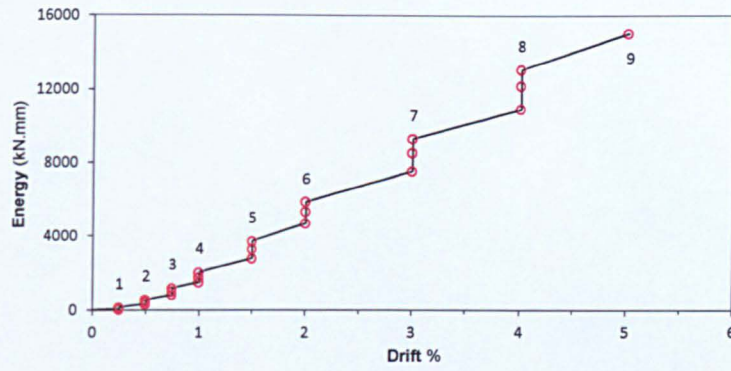


Figure B.60 Cumulative energy dissipation of specimen JC-2

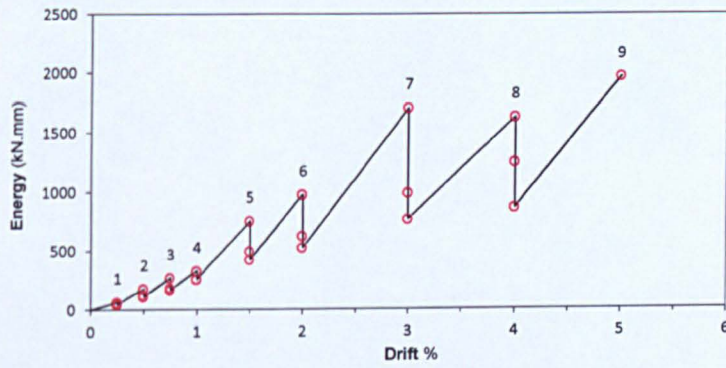


Figure B.61 Dissipated energy per cycle for specimen JC-2

B.5 BEAM BAR STRAINS

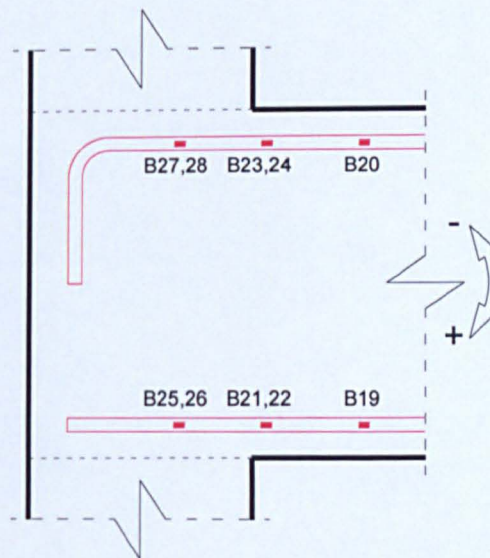


Figure B.62 Strain gauges of beam top and bottom bars of Group A specimens

B.5.1 SPECIMEN JA-2

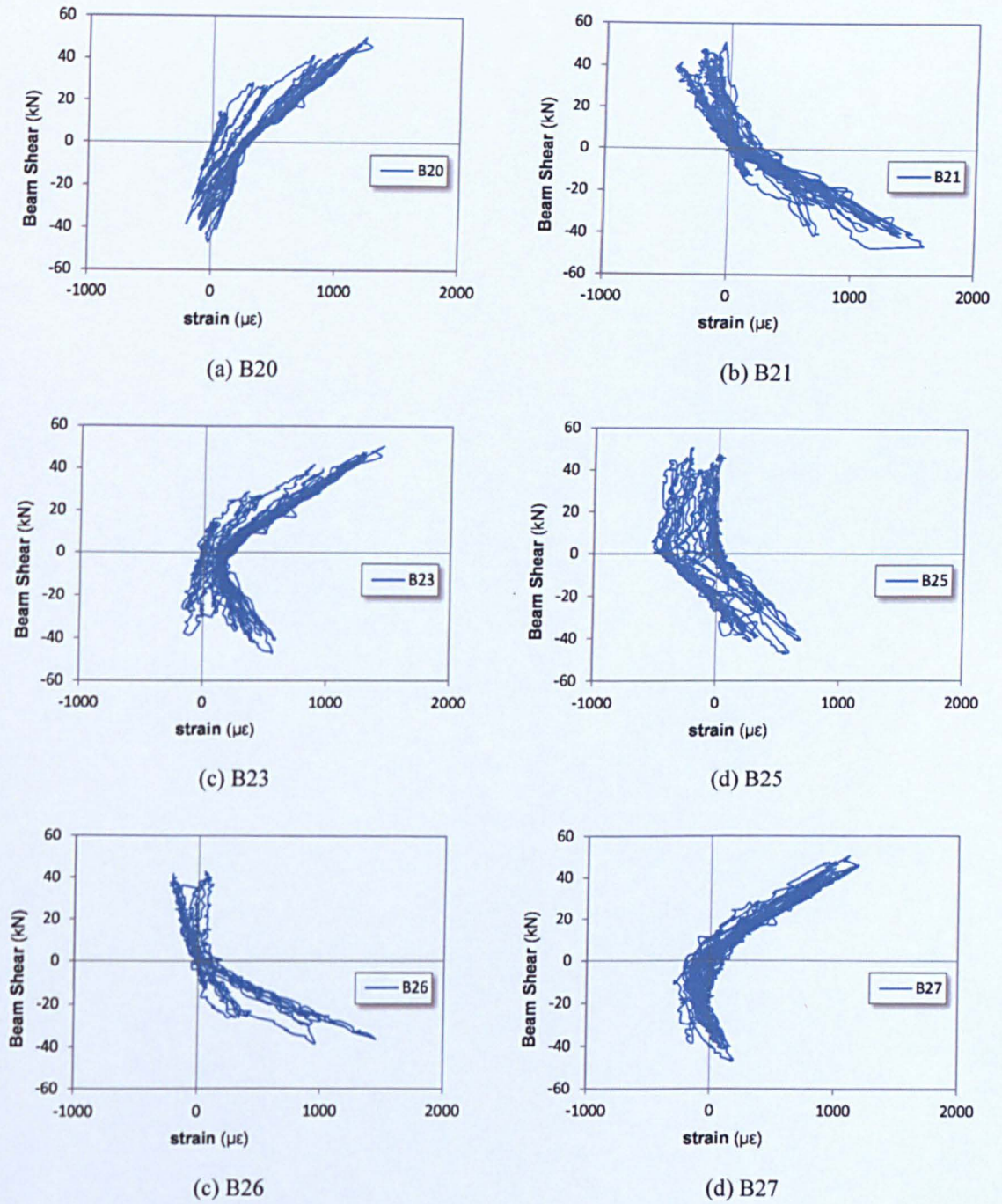


Figure B.63 Measured strains of beam top and bottom bars of specimen JA-2

B.5.2 SPECIMEN JA-3

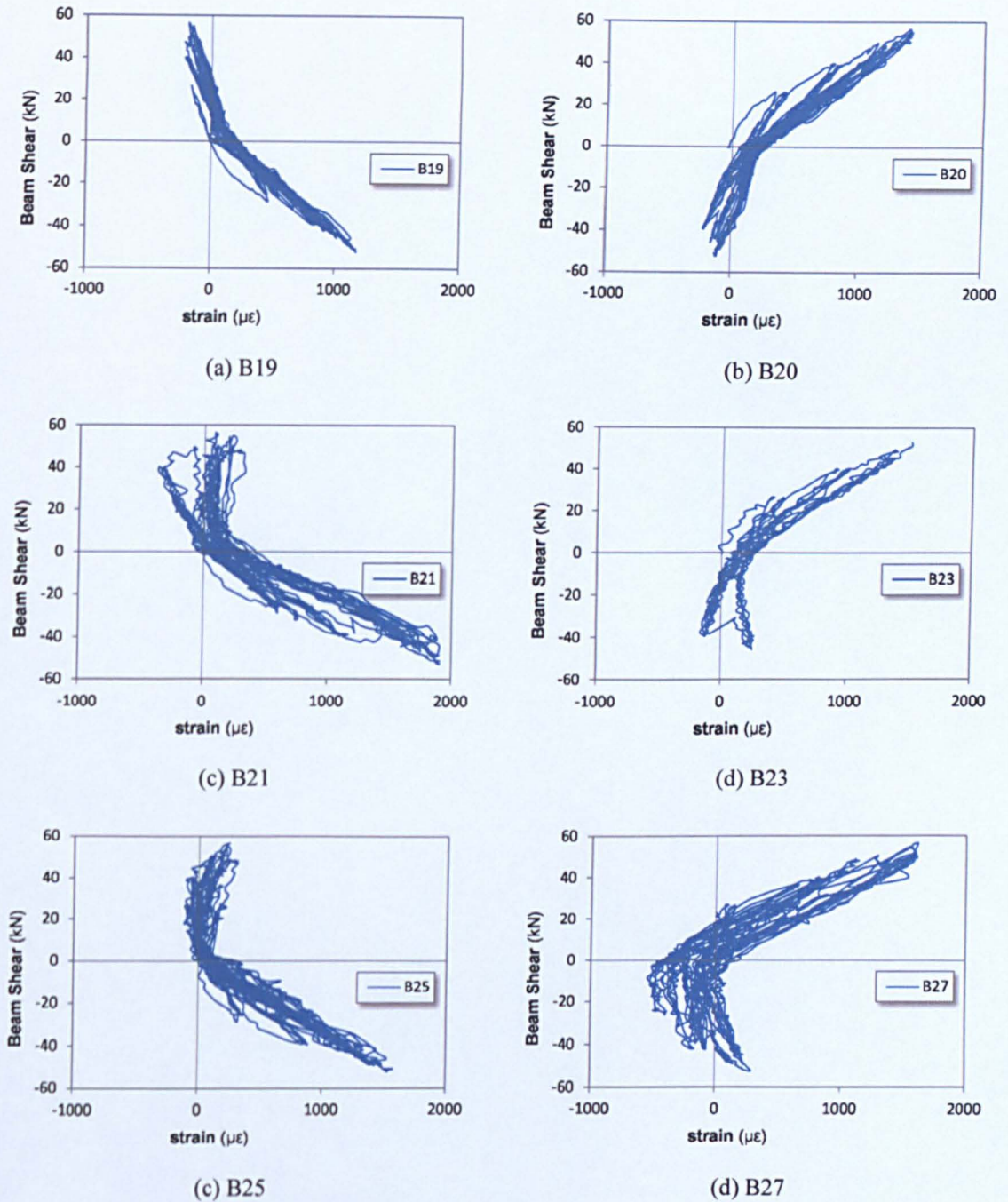
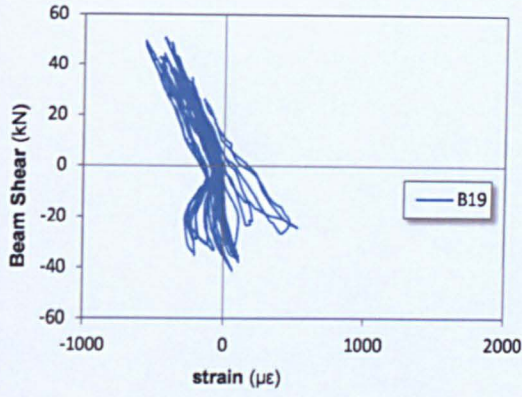
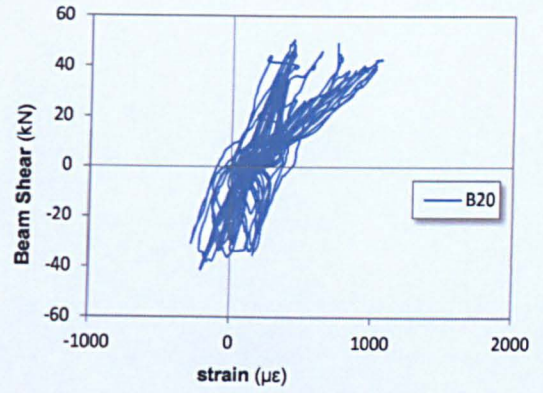


Figure B.64 Measured strains of beam top and bottom bars of specimen JA-3

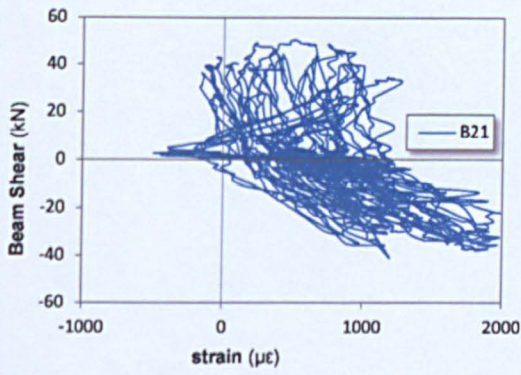
B.5.3 SPECIMEN JB-1



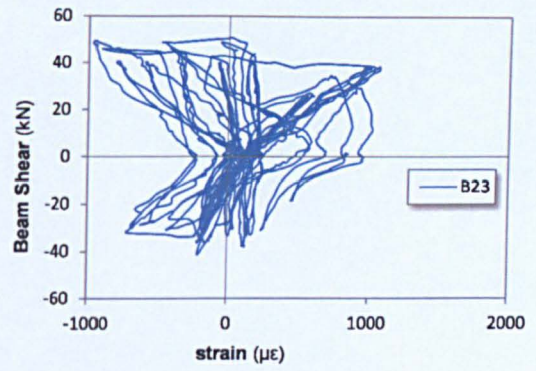
(a) B19



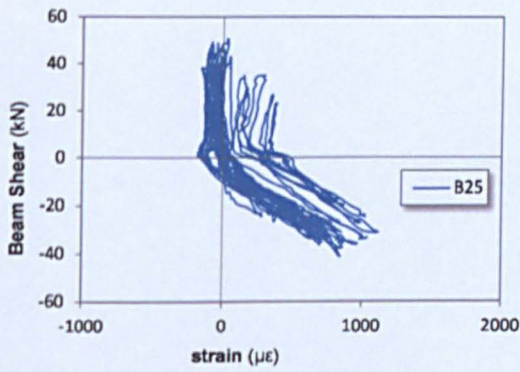
(b) B20



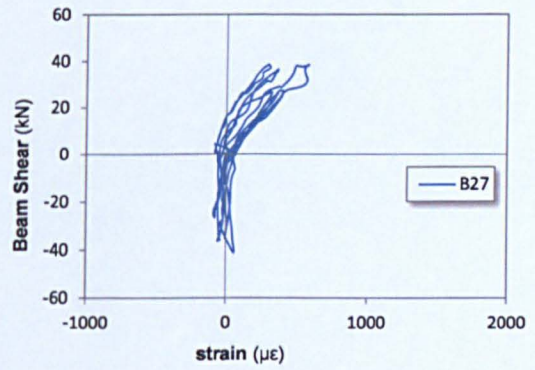
(c) B21



(d) B23



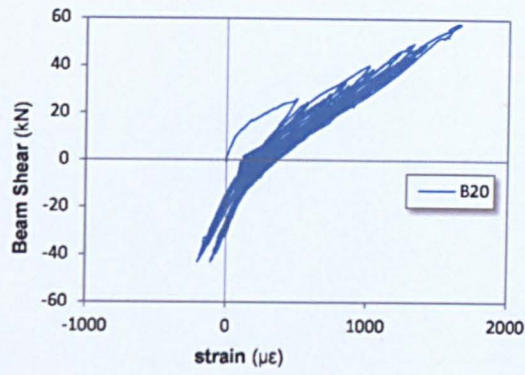
(c) B25



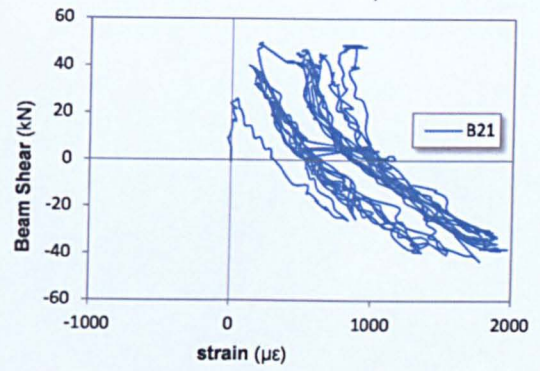
(d) B27

Figure B.65 Measured strains of beam top and bottom bars of specimen JB-1

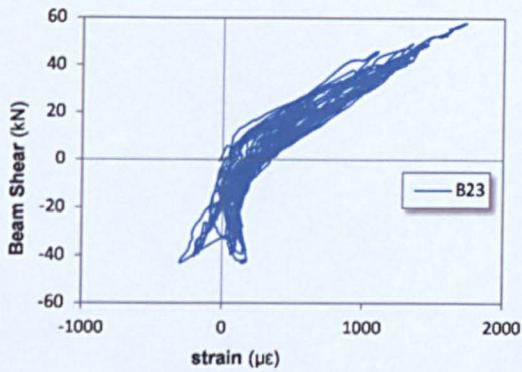
B.5.4 SPECIMEN JB-2



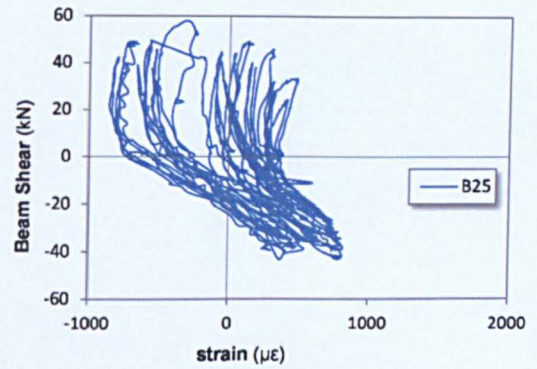
(a) B20



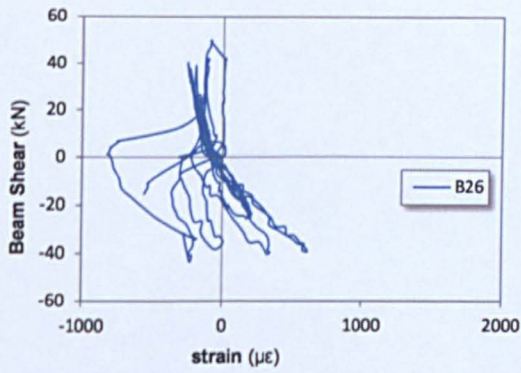
(b) B21



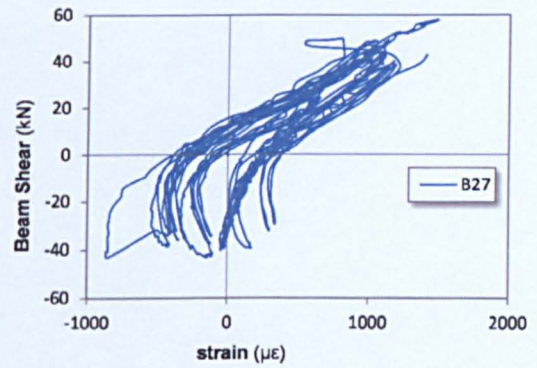
(c) B23



(d) B25

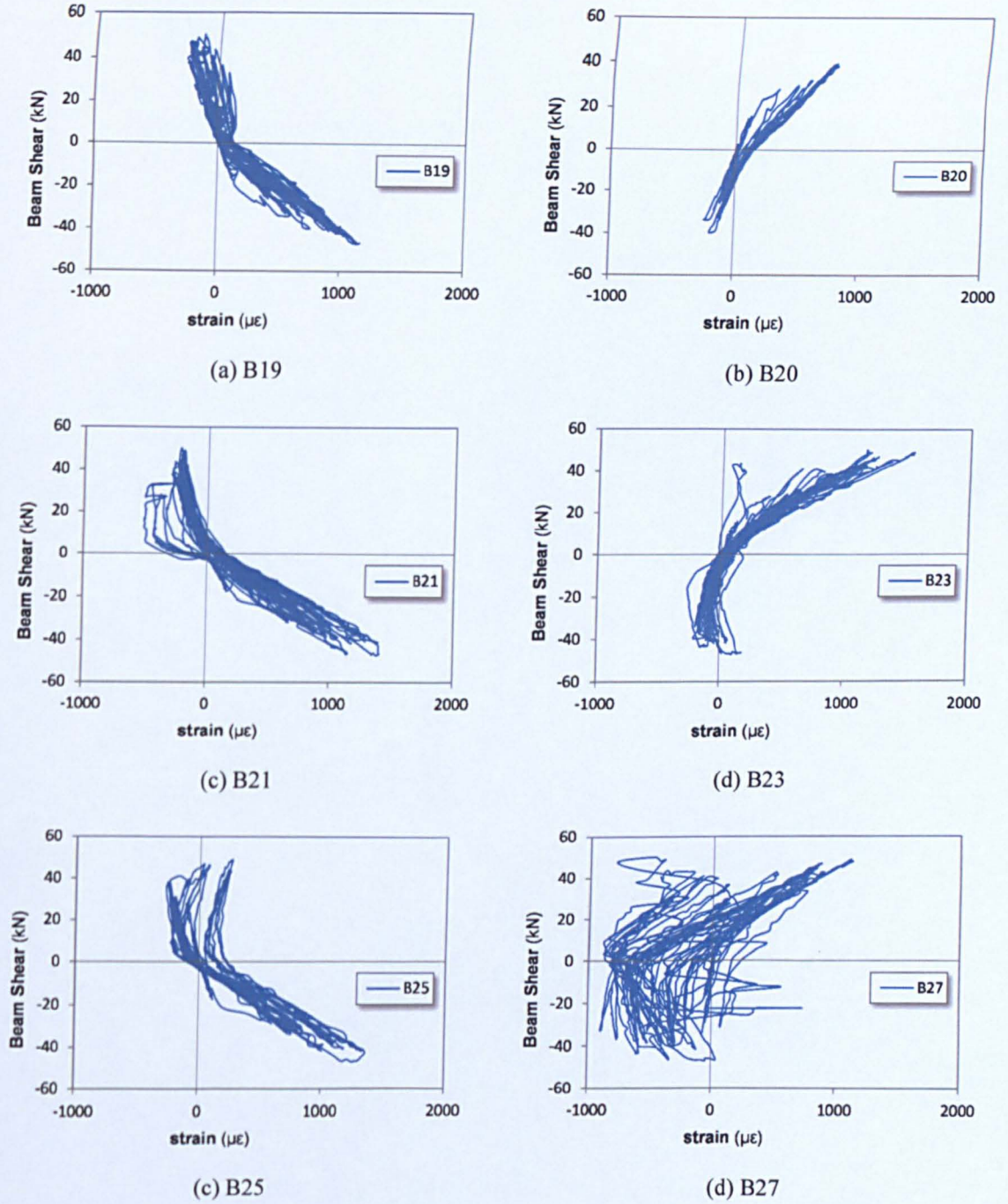


(c) B26

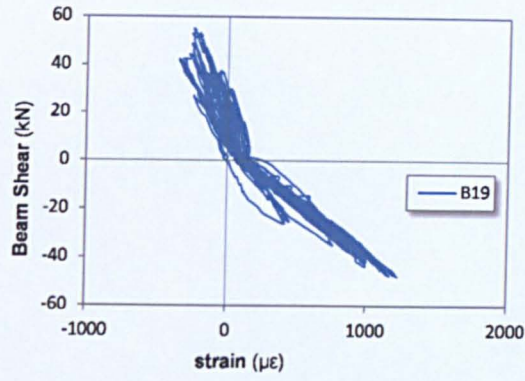


(d) B27

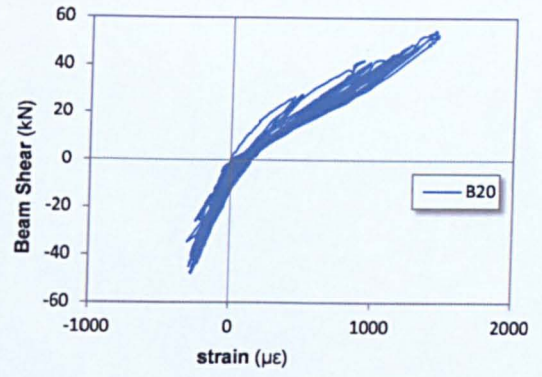
Figure B.66 Measured strains of beam top and bottom bars of specimen JB-2

B.5.5 SPECIMEN JC-1**Figure B.67 Measured strains of beam top and bottom bars of specimen JC-1**

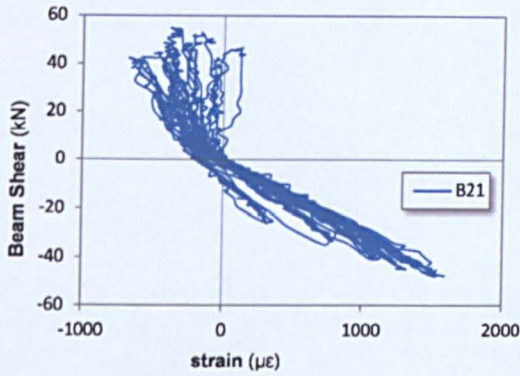
B.5.6 SPECIMEN JC-2



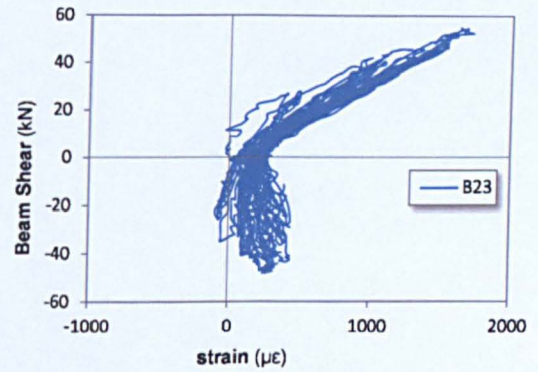
(a) B19



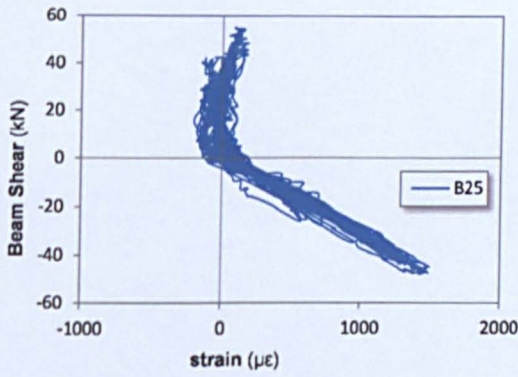
(b) B20



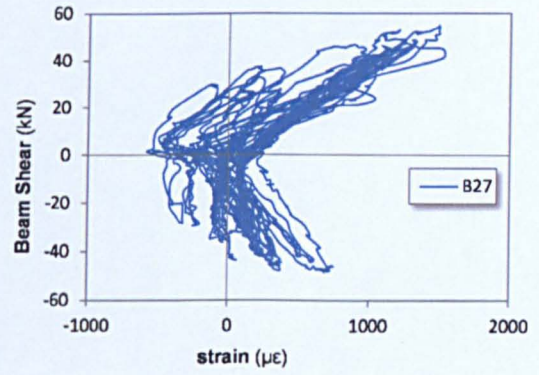
(c) B21



(d) B23



(c) B25



(d) B27

Figure B.68 Measured strains of beam top and bottom bars of specimen JC-2

B.6 COLUMN BAR STRAINS

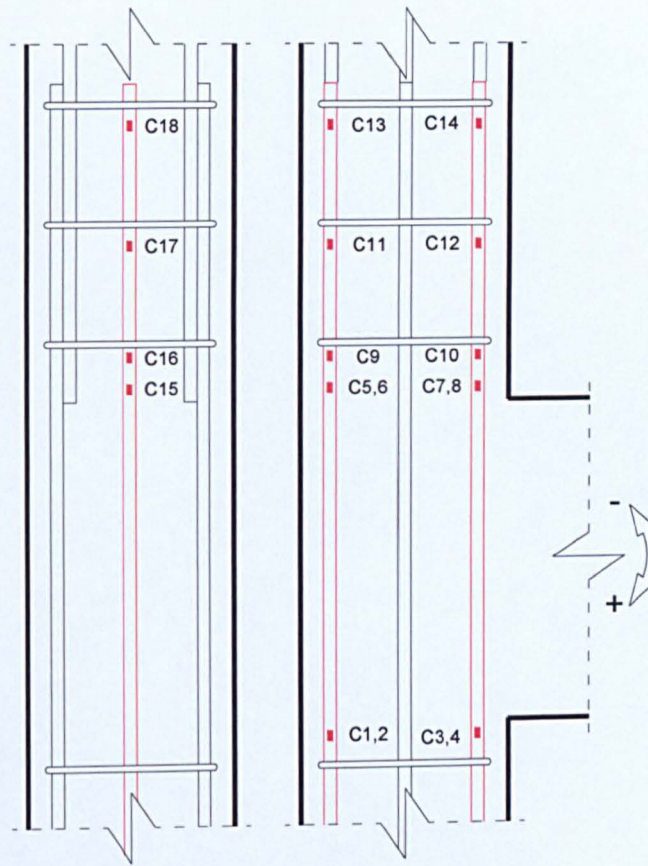
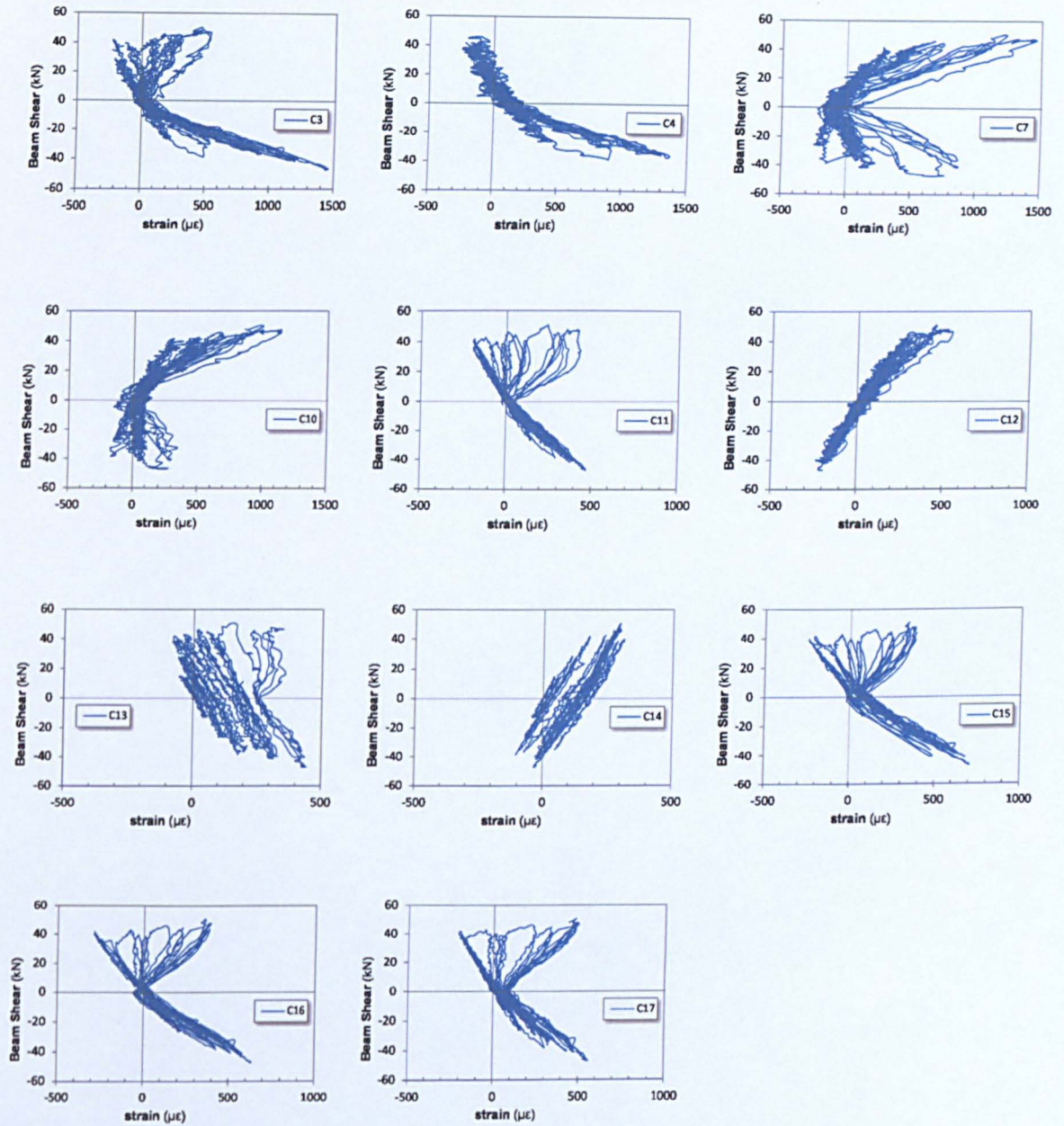
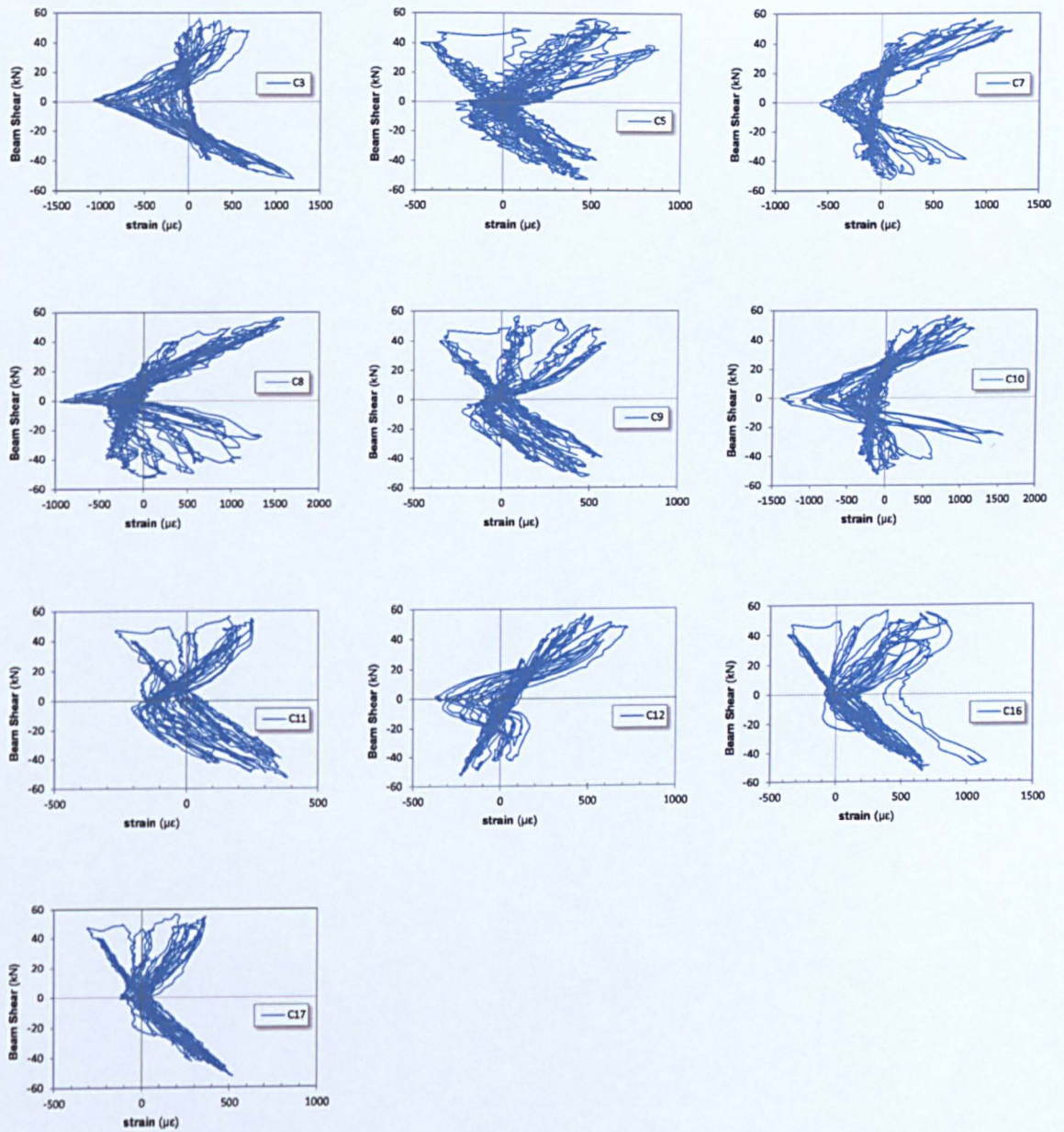


Figure B.69 Strain gauges of column bars

B.6.1 SPECIMEN JA-2**Figure B.70 Measured strains of column bars of specimen JA-2**

B.6.2 SPECIMEN JA-3**Figure B.71 Measured strains of column bars of specimen JA-3**

B.6.3 SPECIMEN JB-1

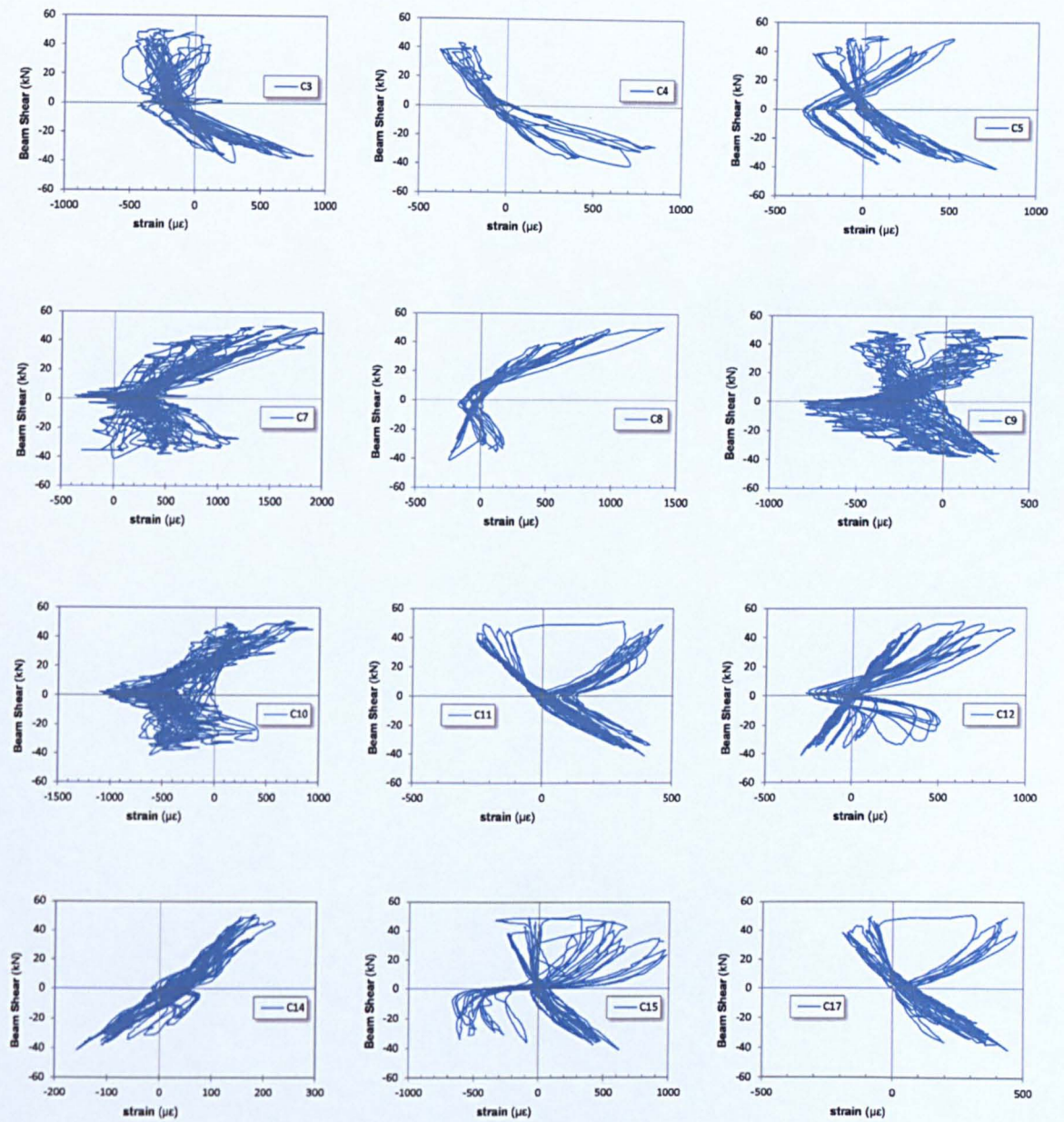
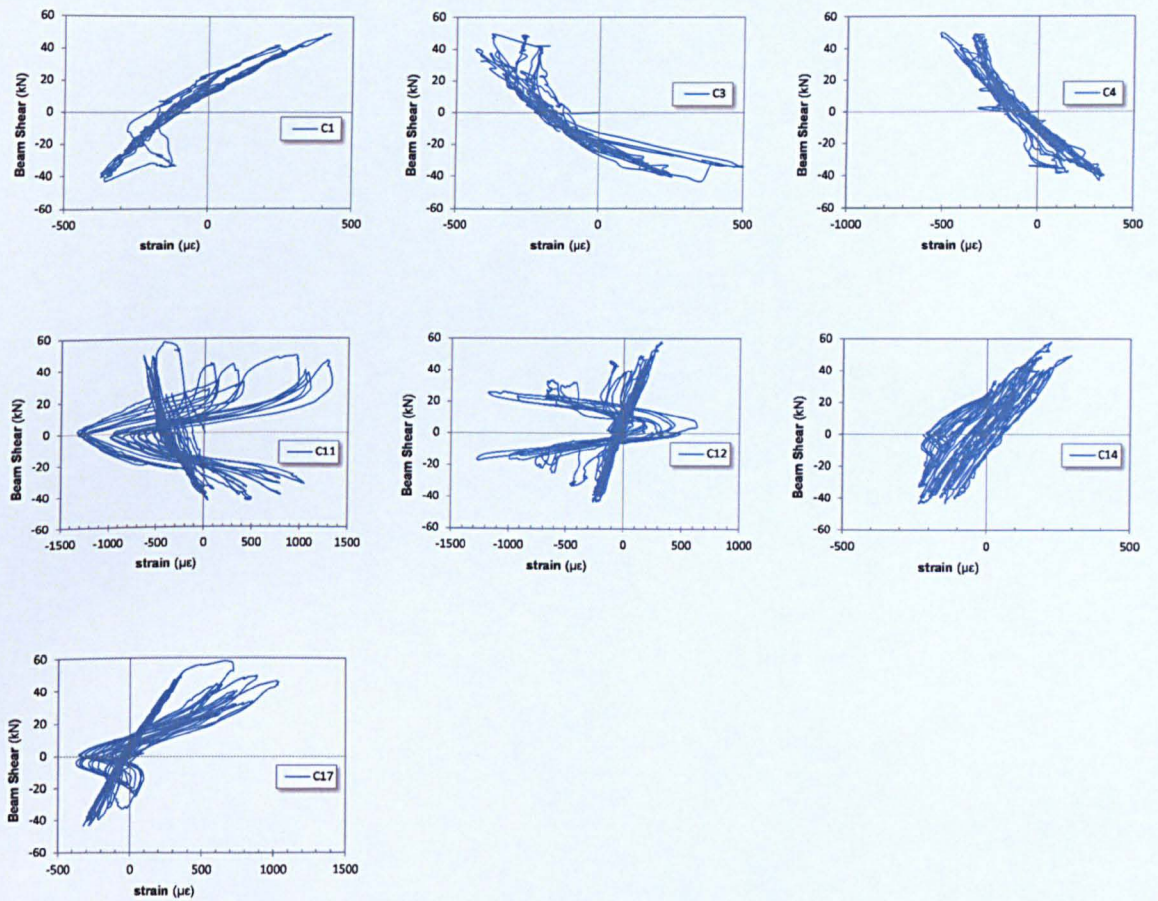
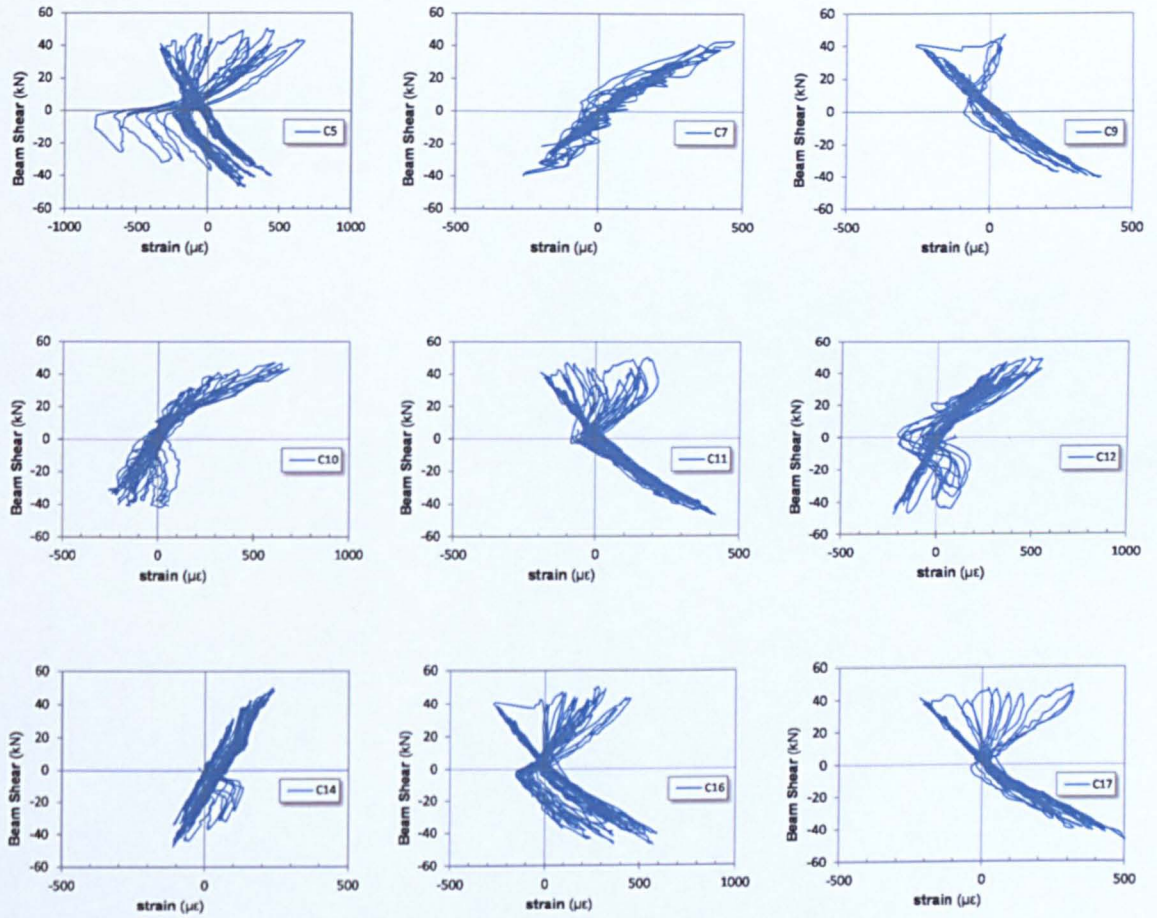


Figure B.72 Measured strains of column bars of specimen JB-1

B.6.4 SPECIMEN JB-2**Figure B.73 Measured strains of column bars of specimen JB-2**

B.6.5 SPECIMEN JC-1**Figure B.74 Measured strains of column bars of specimen JC-1**

B.6.6 SPECIMEN JC-2

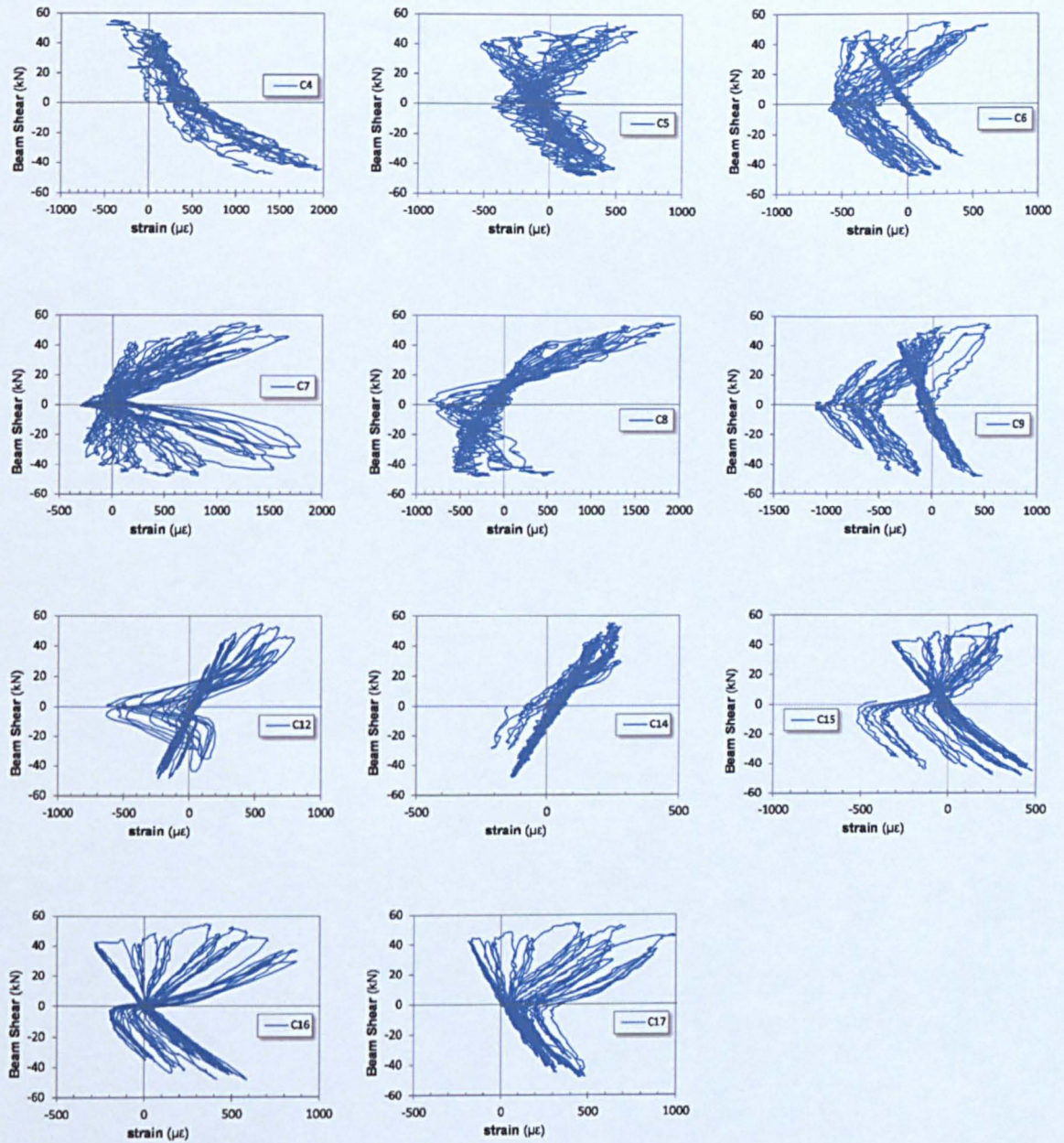


Figure B.75 Measured strains of column bars of specimen JC-2